



VNIVERSITAT
ID VALÈNCIA

**LOW TOXICITY METAL HALIDE
SEMICONDUCTORS FOR OPTOELECTRONICS
AND THERMOELECTRICS**

– PhD Thesis –

VNIVERSITAT ID VALÈNCIA
Doctorado en Nanociencia y Nanotecnología

Paz Sebastiá Luna

Directors:

Prof. Dr. Hendrik Jan Bolink

Dr. Francisco Palazón Huet

March 2023

Prof. Dr. Hendrik Jan Bolink, professor titular de la Universitat de València en l'Institut de Ciència Molecular (ICMol), i **Dr. Francisco Palazón Huet**, investigador Ramón y Cajal en la Universitat Politècnica de Cartagena, certifiquen que la memòria presentada per l'estudiant de doctorat Paz Sebastiá Luna, amb el títol “*Low toxicity metal halide semiconductors for optoelectronics and thermoelectrics*”, correspon a la seua Tesi Doctoral i ha sigut realitzada sota la seua direcció i tutoria, autoritzant mitjançant aquest escrit la presentació d'aquesta.

A Paterna (València), a 1 de Març de 2023.

Prof. Dr. Hendrik Jan Bolink

(Director i tutor)

Handwritten signature of Prof. Dr. Hendrik Jan Bolink in black ink, featuring a stylized, cursive script.

Dr. Francisco Palazón Huet

(Director)

Handwritten signature of Dr. Francisco Palazón Huet in black ink, featuring a stylized, cursive script that includes the name 'Palazon'.

A mis padres.

*“Que no tot en la vida és faena
Que morir és no viure lluitant”
ZOO*

Index

Index	7
Chapter 1: Introduction and aim of the thesis	11
1.1 Overview	13
1.2 Light-emitting diodes	14
1.2.1 Working principle	14
1.2.2 Requirements	16
1.3 Solar cells	16
1.3.1 Working principle	16
1.3.2 Requirements	18
1.4 Thermoelectric generators	19
1.4.1 Working principle	19
1.4.2 Requirements	22
1.4.3 Summary of requirements	23
1.5 Most common materials	24
1.5.1 LEDs	24
1.5.2 Solar cells	26
1.5.3 Thermoelectrics	28
1.6 Synthesis methods and thin film deposition	29
1.7 Aim of the thesis	31
Chapter 2: Methodology and characterization techniques	33
2.1 Mechanochemical synthesis	35
2.2 Thin film deposition	36
2.2.1 Spin coating	37
2.2.2 Single-source vacuum deposition (SSVD)	38
2.3 Characterization techniques	40
2.3.1 X-Ray diffraction (XRD)	40
2.3.2 X-Ray Photoelectron Spectroscopy (XPS)	41
2.3.3 Optical characterization	42
2.3.4 Scanning electron microscopy	44
2.3.5 Thermoelectrical characterization	45

Chapter 3: Solvent-Free Synthesis and Thin-Film Deposition of Cesium Copper Halides with Bright Blue Photoluminescence	51
3.1 Introduction	54
3.2 Experimental section	55
3.3 Results and discussion	58
3.4 Conclusions	70
3.5 Author contribution and acknowledgments	71
Chapter 4: Tuning the Optical Absorption of Sn-, Ge-, and Zn-Substituted Cs₂AgBiBr₆ Double Perovskites: Structural and Electronic Effects	73
4.1 Introduction	76
4.2 Experimental section	78
4.3 Results and discussion	81
4.4 Conclusions	91
4.5 Author contribution and acknowledgments	91
Chapter 5: Vacuum-Deposited Cesium Tin Iodide Thin Films with Tunable Thermoelectric Properties	93
Chapter 6: General outlook and conclusions	111
Chapter 7: Resum en valencià	115
7.1 Capítol 1: Introducció	117
7.1.1 Díodes emissors de llum	118
7.1.2 Cèl·lules solars	120
7.1.3 Generadors termoelèctrics	121
7.1.4 Most common materials	124
7.1.5 Mètodes de síntesis i deposició de pel·lícules fines	127
7.1.6 Objectius de la tesi	129
7.2 Capítol 3: Síntesi sense dissolvents i deposició en capa fina d'halurs de cesi i coure amb fotoluminescència blau brillant	130
7.2.1 Resum	130
7.2.2 Introducció	130
7.2.3 Conclusions	131
7.3 Capítol 4: Ajust de l'absorció òptica de les perovskites dobles Cs ₂ AgBiBr ₆ substituïdes per Sn, Ge i Zn: efectes estructurals i electrònics	132
7.3.1 Resum	132
7.3.2 Introducció	132
7.3.3 Conclusions	135

7.4 Capítol 5: Capes fines de iodur de cesi i estany depositades en buit amb propietats termoelèctriques modulables	136
7.4.1 Resum	136
7.4.2 Introducció	136
7.4.3 Conclusions	138
7.5 Capítol 6: Perspectives generals i conclusions	139
Appendix A	143
Appendix B	169
Appendix C	197
Appendix D	215
Appendix E	231
Appendix F	235
Appendix G	243
Acknowledgements	247

Chapter 1

Introduction and aim of the thesis

*“Donde nos llevó la imaginación
Donde con los ojos cerrados
Se divisan infinitos campos”*
Antonio Vega

1.1 Overview

Climate change is already a reality that affects the living conditions of millions of people every year and whose effects are already beginning to be felt in all parts of the world.^{1,2} One of the main causes is the uncontrolled release of greenhouse gases into the atmosphere, such as CO₂, methane or nitrous oxide, mainly caused by the burning of fossil fuels and biomass, *e.g.* wood or crop waste, for energy.³ Coal, gas, oil and biomass are currently the world's main sources of energy and account for more than three-quarters of global greenhouse gas emissions.^{4,5} To achieve a cleaner planet and preserve the environment and all its inhabitants, it is necessary to look for less harmful and polluting energy sources. Among the different alternatives, solar energy, which is included in the group of "renewable energies" and whose development began in recent decades, stands out. Solar energy is based, broadly speaking, on the conversion of energy from the sun's rays into electricity ready for consumption.

On the other hand, it is also possible to convert energy in the form of waste heat from different sources such as the sun, human body, or industrial processes to produce electricity. This is the main basis for thermoelectric power, which could in the future be combined with solar energy and position itself as a renewable and efficient energy source to completely replace polluting fossil fuels.⁶ Moreover, thermoelectric devices could be used in car engines, medical and wearable devices (or Internet of Things, IoT), residential smart-buildings and many other electronic devices.⁷

However, the search for new energy sources to reduce pollution and limit climate change should go hand in hand with other changes in society and our daily lives. As highlighted in the analysis carried out by Eurostat in 2020, 27 % of the final energy consumption in Europe was due to the residential sector. Households use this energy for several applications, such as heating/cooling spaces and water, cooking, or lighting. Of this share, 14.5 % represents the energy used for lighting only in the European Union (EU).⁸ Hence, the development and improvement of artificial light sources with eco-friendly and energy-efficient technologies must also be positioned as one of the fundamental steps towards the ecological transition.

To develop these devices, either for lighting purposes or for energy production, a crucial point is the development of new materials. Indeed, materials science plays a crucial role to obtain the desired properties for these fields, enabling the fine-tuning and

optimization of the materials properties to improve their efficiency and production costs.⁹⁻¹¹

In this thesis, we will focus our efforts on the search and study of new materials with potential application in these big research areas *i.e.* photovoltaics, thermoelectrics and eco-friendly lighting sources such as light-emitting diodes (LEDs), with the aim of fighting against climate change and supporting renewable and non-polluting energies. Furthermore, in view of their potential integration in these devices, we will study their deposition into thin films. In the following section, the operation of two types of optoelectronic devices, LEDs and solar cells, and of thermoelectric generators, will be introduced. Special emphasis will be placed on the requirements that materials must have in order to be suitable for these applications.

1.2 Light-emitting diodes

1.2.1 Working principle

LEDs are semiconductor devices that emit energy in the form of photons when supplied with an electric current. These devices are capable of emitting in a wide range of bands within the electromagnetic spectrum, from the infrared to the UV, depending on the chemical composition of the semiconductor material.^{12,13} High-performance devices can achieve almost 100 % electrical-to-optical conversion efficiency and lifetimes exceeding 50000 hours at competitive costs, making them nearly ideal light sources.^{12,14}

LEDs are solid-state lighting devices, which generate photons through a process called electroluminescence,¹³ the emission of light by a substance upon the application of an electric field.¹⁵ Generally, their basic operation principle is as follows: first, electronic charges are injected and transported into a thin-film semiconductor from the electrodes (electrons -negative charges- from the cathode and holes -positive charges- from the anode). Charges are transported within the active layer where they meet and can recombine following different pathways. In materials with low dielectric constant such as organic semiconductors, an electron and a hole are attracted to each other by electrostatic Coulomb interaction, forming a bound state called exciton. Once excitons are formed, they may recombine by the emission of a photon of the corresponding energy

(**Figure 1.1a**).¹⁶ In materials with a large dielectric constant, such as inorganic semiconductors and hybrid perovskites, the binding energy is small and recombination takes place directly from free carriers (**Figure 1.1b**).¹⁷ As a result, photons with energy equal to the semiconductor bandgap (energy difference between valence and conduction band) are emitted.

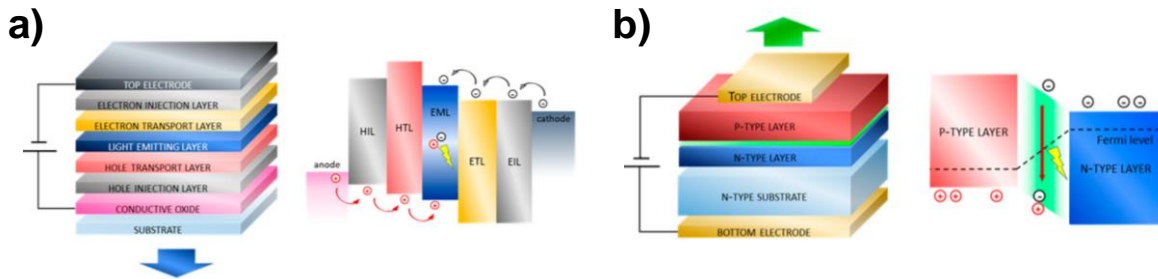


Figure 1.1. Device architecture and working mechanism of (a) an organic LED (OLED) and (b) inorganic LED. Illustrations are adapted from literature.¹⁸

The processes of charge injection, transport and recombination are separated in different layers, each optimized to carry out a specific task. OLEDs usually consist of a transparent substrate (glass), a transparent conductor (anode), a hole transport layer (HTL), a light emitting layer, an electron transport layer (ETL) and a metal cathode. In order to facilitate charge injection, additional hole and electron injection layers (HIL and EIL, respectively) can be placed in between the electrodes and the transport materials (**Figure 1.1a**).¹⁴ When an external voltage is applied, electrons are injected from the cathode into the lowest unoccupied molecular orbital (LUMO) of the adjacent material, while electrons are extracted from the highest occupied molecular orbital (HOMO) into the anode (which can also be viewed as hole injection from the anode into the semiconductor). These charge carriers move through the layers toward the emissive layer, where they form an exciton that may relax with the emission of light.¹⁶ On the contrary, in perovskite LEDs, another type of LED, a film of the emissive layer is sandwiched between an HTL and an ETL; charge carriers are injected, and move through the valence and conduction bands of the perovskite, and radiatively recombine emitting light (**Figure 1.1b**).¹⁹ This type of recombination can be highly efficient due to the direct bandgap characteristic of these semiconductors.

1.2.2 Requirements

One of the most important performance indicator for a LED is the external quantum efficiency (EQE), given by the ratio of emitted photons by the LED to the amount of charges (electrons) injected.²⁰ In order to achieve a high EQE, it is imperative for the emissive layer to have a high photoluminescence quantum yield (PLQY), defined as the ratio of emitted to absorbed photons.²¹ For an optimal PLQY from the thin films, homogeneous and high surface coverage are needed to prevent non-radiative losses from pinholes or uncovered areas of the surface.²² Moreover, high carrier mobilities, ensuring electrons and holes can reach each other without recombining, and long carrier lifetimes, related to a low trap density and long carrier diffusion lengths, are also required to achieve a high performing LED.²²⁻²⁴

1.3 Solar cells

1.3.1 Working principle

Photovoltaic solar cells convert light into electricity. Typically, they consist of a semiconducting material that absorbs the incoming photons with energies greater or equal to its bandgap energy. The energy absorbed is then used to excite an electron to the conduction band, leaving a hole behind at the valence band. If the materials have a high dielectric constant, which is assumed in this thesis, then the electron-hole pair (or exciton) is weakly bound and the charge carriers may be considered free charges at room temperature. To prevent their recombination, n-type and p-type selective layers for electrons and holes, respectively, are placed on both sides of the absorber so that they can only flow through one of them. Eventually, charge carriers are extracted with electrical contacts connected to an external circuit, performing thus work and creating a flow of electricity (**Figure 1.2**).^{25,26}

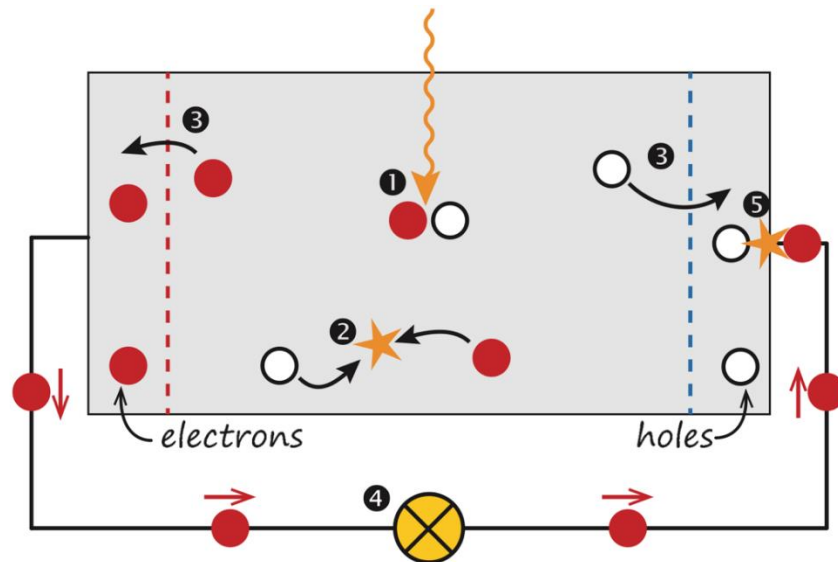


Figure 1.2. Basic working mechanism of a solar cell. (1) Generation of an electron and a hole upon the absorption of a photon. (2) A potential loss mechanism occurs when electrons and holes recombine. However, it is unlikely in efficient solar cells (3) Diffusion and drift of electrons and holes through the charge selective layers. (4) Extracted electrons travel through an external circuit generating a current. (5) Electrons that have passed through the circuit recombine with holes. Illustration adapted from literature.²⁶

There are two main architectures for thin film solar cells, depending on the deposition sequence of each component on a transparent glass substrate, *p-i-n* or *n-i-p* (**Figure 1.3**). Both consist of a transparent conductive oxide (TCO) as the base, on top of which a hole-transport layer (HTL, p-type), an absorber material, an electron-transport layer (ETL, n-type) and metallic electrodes are deposited. The position of the HTL and ETL is given by the device architecture (**Figure 1.3**).

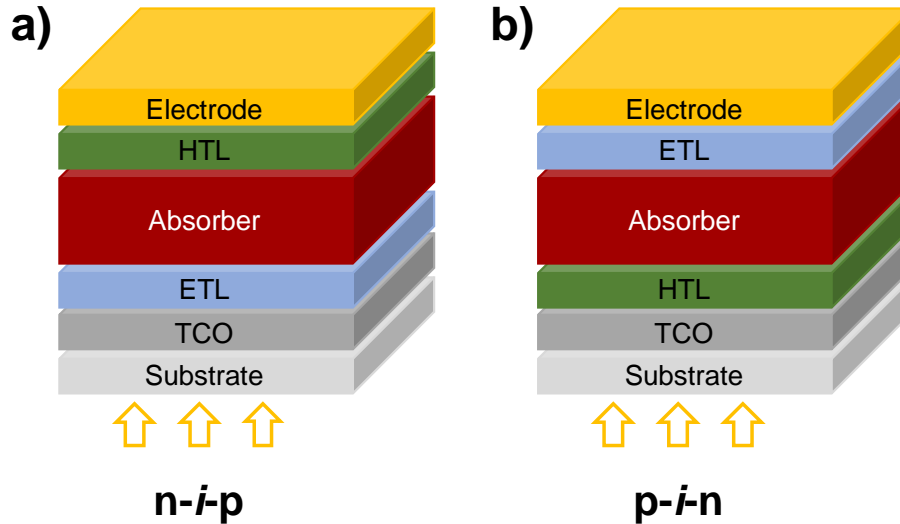


Figure 1.3. Schematic diagram of (a) planar n-i-p and (b) planar p-i-n solar cell architectures (not to scale). Yellow arrows indicate the direction of the sunlight.

1.3.2 Requirements

The characteristics of the materials needed to achieve highly efficient solar cells share some similarities with those described previously for LEDs (see Section 1.2.2). Ideally, absorbers for solar cells are direct bandgap semiconductors with high absorption coefficients in the whole range of wavelengths absorbed. A low exciton binding energy is also desired to ensure a spontaneous separation of the electrons and holes into free carriers upon illumination and thus prevent losses by recombination.²³

In order to enhance charge transport, materials with high carrier mobilities, long diffusion lengths and long carrier lifetimes are sought after.^{23,27} This ensures that free charges can be transported across the absorber and reach their corresponding electrodes before recombining. Note that this requirement is more important for solar cells than for LEDs, as the former typically require thicker films than the latter (hundreds of nanometers vs tens of nanometers) to ensure sufficient light absorption. For this purpose, homogenous thin films of the absorber without pinholes or defect states are also desirable.²⁸

1.4 Thermoelectric generators

1.4.1 Working principle

A thermoelectric generator (TEG) converts thermal energy, usually from waste heat, into electrical power.^{29,30} Its working principle is based on the Seebeck effect. It states that when a material is subjected to a temperature difference an electric potential difference proportional to the temperature gradient is created and can be converted into electricity.^{6,31}

A generic TEG is composed by a series of thermocouples, that is, a combination of p-type and n-type semiconductors connected both electrically (in series) and thermally (in parallel). When a temperature difference is applied, majority carriers considered as free charges (holes in a p-type semiconductor or electrons in an n-type semiconductor) diffuse from the hot side to the cold side, where charges possess less thermal energy; this is the microscopic basis of the Seebeck effect. This electrostatic potential drives a current through the device and it is used to power an electrical load through an external circuit (Figure 1.4).^{6,32,33}

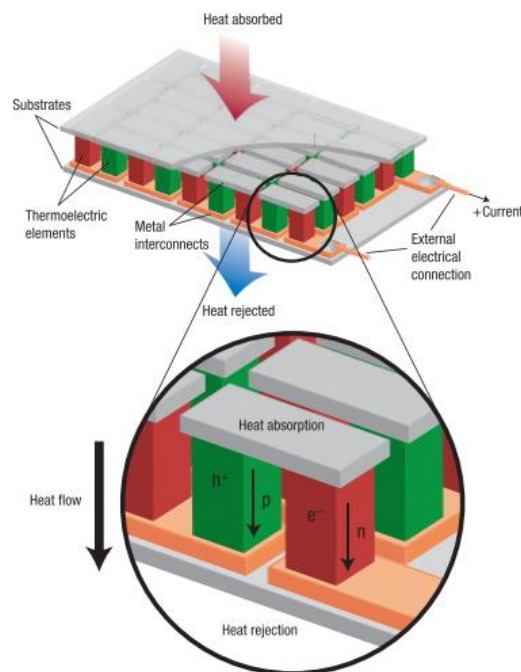


Figure 1.4. Schematic diagram of a thermoelectric device. Illustration adapted from literature.³²

The efficiency of a thermoelectric (TE) device is related to the figure-of-merit (ZT), defined as (**Equation 1.1**):

$$ZT = \frac{S^2 \sigma}{\kappa} T \quad (1.1)$$

which depends on the following key parameters: S is the Seebeck coefficient, σ is the electrical conductivity, κ is the thermal conductivity and T is the absolute temperature.^{29,34}

First, the Seebeck coefficient, S , or Seebeck voltage stands for the voltage produced in a material upon the application of a temperature gradient, as introduced before. The charge difference created produces an electric potential across the semiconductor. The Seebeck coefficient is thus defined as the ratio between the built-up electric potential (voltage) and the temperature difference. Thus, if the material is n-type, its sign will be negative due to the negative potential created by the negative charges accumulated (**Figure 1.5**). If, on the other hand, it were a p-type semiconductor, the accumulation of positive charges (holes) will create a positive build-up and the Seebeck coefficient will be positive.³⁵ However, the diffusion of the charge carriers towards the cold side is not infinite. The accumulation of charges on the cold end will create electrostatic repulsions and a density gradient that will push charges back to the hot end. Once the temperature gradient is counteracted by the density gradient and the electrostatic repulsions, there will not be a net flow of charges and the thermal equilibrium will be achieved.^{33,35} In this situation, as long as the temperature difference at both sides is maintained, the output voltage is also preserved.

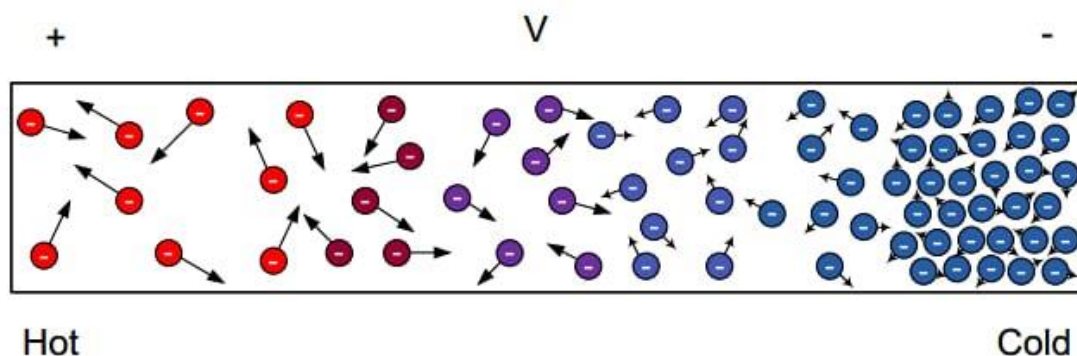


Figure 1.5. Illustration of an n-type semiconductor subjected to a temperature difference to show how electrons diffuse from the hot side to the cold side. Illustration adapted from literature.³³

Secondly, the electrical conductivity, σ , measures the ability of a material to transport weakly bound charged particles (electrons and holes) under the influence of an electric field.³⁵ It is often expressed as its reciprocal, the electrical resistivity, ρ . σ is directly dependant on the concentration of charge carriers (n), their mobility (μ) and the charge of the electron (e) (**Equation 1.2**).³¹

$$\sigma = n_e \mu_e e + n_h \mu_h e \quad (1.2)$$

For an n-type semiconductor, $n_e \gg n_h$, so that the second term of **Equation 1.2** can be neglected (and vice-versa for a p-type material). Thus, **Equation 1.2** can be simplified, being only dependent on the concentration and mobility of the majority charge carriers. Charge carrier concentration and charge mobilities are often estimated through Hall Effect measurements. The Hall Effect occurs when a magnetic field is applied perpendicular to a current flow in a semiconductor, producing a force, called Lorentz force, on the carriers that makes them move. This movement creates an electric field perpendicular to both the magnetic and the current flow that, in turn, creates a voltage known as the Hall voltage (R_H). As for the Seebeck coefficient, the sign of the Hall voltage is dependent on the sign of the majority charge carriers. Once R_H is known, it can be used to calculate the charge carrier concentration (n , **Equation 1.3**) and the charge mobility (μ , **Equation 1.4**).³⁶

$$n = \frac{1}{R_H} \quad (1.3)$$

$$\mu = \frac{R_H}{\rho} \quad (1.4)$$

Finally, the thermal conductivity, κ , measures the heat conduction in the semiconductor material through the charge carriers ($\kappa_{electronic}$) and the lattice vibrations (also known as phonons, $\kappa_{lattice}$) (**Equation 1.5**). $\kappa_{electronic}$ relates to the electrical conductivity, while $\kappa_{lattice}$ is affected by the crystalline structure of the material and its ability to spread lattice vibrations.³²

$$\kappa = \kappa_l + \kappa_e \quad (1.5)$$

1.4.2 Requirements

In order to maximize the performance of a thermoelectric device given by the figure-of-merit ZT , thermal and electrical properties need to be optimized. According to **Equation 1.1** it is paramount for a high performing TE material to have a high electrical conductivity, a large Seebeck coefficient to ensure an efficient conversion of heat into electricity and a low thermal conductivity to prevent thermal shorting.³⁰

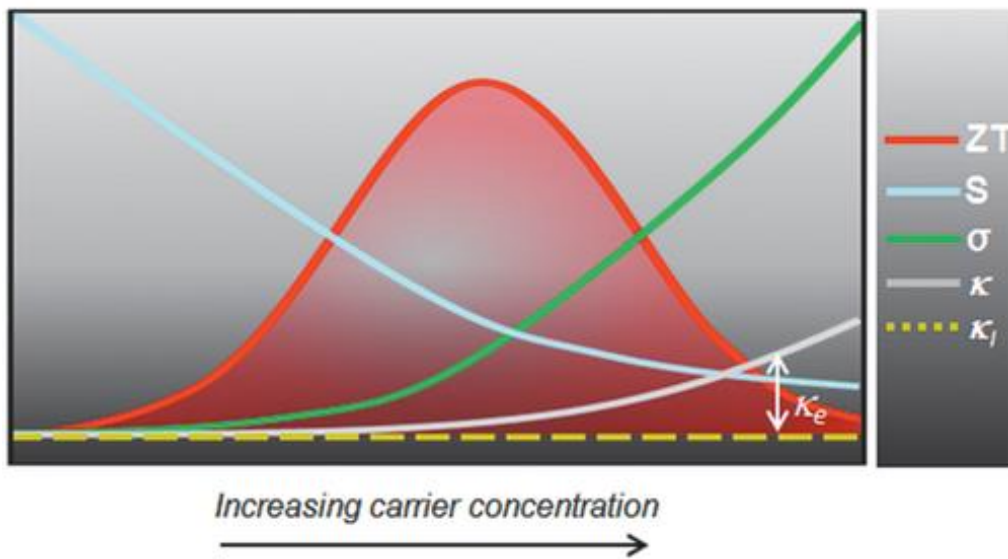


Figure 1.6. Illustration of the compromise between Seebeck coefficient, electrical conductivity, thermal conductivity, and thermal conductivity to achieve a high ZT . Illustration adapted from literature.³⁴

As many of these parameters present interdependency and different correlation to ZT (**Figure 1.6**), the choice of thermoelectric materials is challenging. Ideally, carrier concentrations between 10^{19} – 10^{21} cm^{-3} will help balancing the Seebeck coefficient and the electrical conductivity, which are usually present in heavily doped semiconductors or metals.³⁴ It is also desirable that there is just one single type of carrier to prevent cancelling out the Seebeck coefficient.³²

1.4.3 Summary of requirements

Thus, to choose the ideal material candidate for each of the aforementioned applications, they preferably need to meet the requirements summarized in **Table 1.1**.

Table 1.1. Summary of relevant properties that a material (or thin film) should meet for different applications. “Yes” implies that the property is important for the given application.

	LED	PV	TEG
Bandgap energy	Yes. Exact value strongly affects the color.	Yes. Tunable range (1-2 eV approx); around 1.2 eV is optimum for single junction.	No
High PLQY	Yes, crucial.	Yes, for high voltages.	No
High carrier concentration (doping)	No	No	Yes. Preferred just one type of charge carrier.
High surface coverage and homogeneity	Yes	Yes	Yes.
Low exciton binding energy	Not crucial.	Yes. To prevent recombination losses.	No
Strong light absorption	No. Materials will typically have strong absorption coefficients related to high PLQYs, but films may be very thin.	Yes	No
Low thermal conductivity	No	No	Yes

High electrical conductivity	No. Low charge carrier concentration desired.	No. Low charge carrier concentration desired.	Yes
Large Seebeck coefficient	No	No	Yes
High charge mobility	Yes	Yes	Yes
Long carrier lifetime	Yes	Yes	No
Long carrier diffusion length	Yes	Yes	Not crucial.

1.5 Most common materials

In this section, some of the most frequently used as well as currently under development materials as active layers for LEDs, solar cells and TEGs will be introduced, discussing possible improvements and alternatives to these.

1.5.1 LEDs

Currently, we find different types of LEDs, depending on the nature and physical state of the emissive material, *e.g.* organic LEDs (OLEDs), perovskite LEDs, quantum dots LEDs (QLEDs), etc.

Efficient OLEDs use a semiconducting host material and an emitting compound acting as a dopant as emissive layer. The host is generally an organic compound (either a small molecule or a polymer), while dopants in high-efficiency devices are an organometallic complex of metals such as iridium.¹⁶ In addition, the emission colour in OLEDs is relatively easy to tune, and they can be fabricated virtually on any substrate (glass, plastic, metal, etc.).^{13,15} However, OLEDs are relatively expensive (especially for lighting applications), due to the use of rare metals and complex device architecture. Moreover, their colour purity is lower as compared to other materials (such as quantum dots), due to the use of organic and/or organometallic emitters with wide emission bands.

Therefore, alternative emitters are being investigated, among which we find organic-inorganic (hybrid) perovskites. Perovskites have been widely studied for applications in photovoltaics, with record devices now achieving efficiencies close to silicon solar cells. Perovskite-LEDs (PeLEDs) have been developed only recently, but have also demonstrated their potential owing to their near-unity photoluminescence quantum yield and large bandgap (*i.e.* emission color) tunability.^{23,24,37}

Generally, the chemical formula of three-dimensional (3D) perovskites used for optoelectronics is ABX_3 , where A is a monovalent cation such as Cs^+ , methylammonium ($CH_3NH_3^+$) or formamidinium ($CH_3(NH_2)_2^+$); B is a divalent metal, normally Pb^{2+} or Sn^{2+} , and X is a halide (Cl^- , Br^- or I^-). In this ABX_3 -type structure, A-site cations occupy the cavity between four adjacent corner-sharing BX_6 metal halide octahedra (**Figure 1.7**).^{23,24} One of the main advantages of these materials is the rich diversity in properties owing to a large number of site substitution with other cations or anions.²²

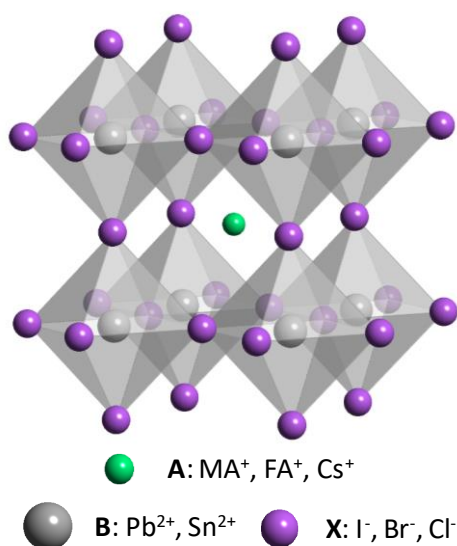


Figure 1.7. Schematic structure of ABX_3 perovskite.

One concern towards the widespread use of perovskite is the lead content, as it is toxic and environmentally harmful. In the European Union, the RoHS2 directive puts limits on the use of hazardous and heavy metals in consumable electronics, regulation that is expected to become stricter over time. For this reason, the development of lead-free halide perovskites with comparable performing features to the lead analogues is of great interest, as testified by the increasing number of publications on Pb-free materials.^{38,39}

One approach is to substitute Pb in the perovskite structure with another group 14 element, such as Sn or Ge. However, they are prone to oxidation when exposed to air, compromising the stability of the material. In order to overcome these problems, novel families of compounds based on Sb, Bi, Mn or employing double-cations, have been synthesized and tested in light-emitting devices.^{37,38} The development of this kind of compounds is still at the early stages but several of them have shown promising properties, such as the high PLQY reported for inorganic bismuth halides.³⁷

1.5.2 Solar cells

Technologies based on crystalline silicon (c-Si) dominate the current PV market, accounting for around 95% of worldwide PV production.⁴⁰ However, the development and efficiency improvement of silicon-based solar cells has been increasing rather slowly over the last decades (**Figure 1.8**, blue lines), approaching its expected efficiency limit of 29%.^{40,41} In order to overcome this efficiency barrier and continue the ascent, new generations of devices, such as tandem solar cells, are necessary. A tandem solar cell combines two different absorbers with different bandgaps to increase the sunlight absorption, reducing thermalization losses and consequently increasing the overall efficiency.

Alternative solar cells based on cadmium telluride, gallium arsenide, copper indium gallium selenide (CIGS) and copper zinc tin sulfide (CZTS) also entered the PV market, reaching efficiencies above 30% for GaAs (**Figure 1.8**).⁴⁰⁻⁴² Nonetheless, the toxicity of Cd and the scarcity and production costs of Ga, Te and In are major drawbacks in the development and commercialisation of these types of solar cells.^{40,42}

Amongst the emerging PV technologies, perovskite solar cells have gained attention in the last decade as a potential alternative to achieve highly-efficient solar cells. Maximum efficiencies achieved with perovskite solar cells have recently reached record values around 25.7%,⁴¹ very close to the values achieved with silicon. The simplest and most widely studied perovskite is methylammonium lead iodide (MAPbI₃, whose structure is shown in **Figure 1.7**) mainly due to its long charge carrier diffusion lengths and high absorption coefficients (see previous section for further information).⁴³

Notwithstanding, as previously discussed, the presence of Pb in their composition, a highly toxic metal that can cause severe neurological and behavioural effects in humans,^{44,45} limits their use in commercial PV modules. Due to these drawbacks, alternatives such as Sn²⁺ are being sought to replace Pb²⁺, for which promising results were expected. Unfortunately, tin halide perovskites are relatively unstable, due to the tendency of the metal to oxidize to Sn⁴⁺.⁴⁶ Therefore, current research lines are starting to investigate new photovoltaic materials based on Bi, Sb, Ge that could replace lead perovskites.^{45,46}

1.5.3 Thermoelectrics

Among the most widely used thermoelectric materials, we find Bi₂Te₃, Sb₂Te₃ and SnSe. The latter has a *ZT* of 3.1 (at 798 K), the highest reported value so far.^{32,47,48} Nevertheless, the scarceness, toxicity and high fabrication costs of these materials, especially for tellurides, represent a huge hindrance in their further development in thermoelectric generators.^{49,50} Besides, most of them are used in a single crystal state,^{32,47} which limits their integration in different devices architectures. Another major bottleneck comes from the temperature where their operational peak is reached, usually above 300 °C.⁵¹ It is paramount to decrease this minimum temperature required in order to widen the possible applications of TEGs such as to power small electronic devices like wearable sensors which may be interconnected in the so-called Internet of Things (IoT) and its many derivatives in industry, agriculture and wearable healthcare devices.⁷ Since the majority of these applications require room or moderate temperatures, TE materials with good performance below 100 °C are needed.⁵²

Organic semiconductors, such as poly(3,4-ethylenedioxythiophene) (PEDOT) or doped fullerene derivatives with oligoethylene–glycol (OEG) side chains have been

proposed for near room-temperature TE.^{9,53} While these are undoubtedly interesting alternatives, the use of such organic semiconductors present additional challenges: given the large size of the organic dopants (necessary to enhance electrical conductivity and hence ZT), their incorporation into the host material without disrupting the packing and creating additional energetic disorder is challenging.⁵³ Furthermore, polymers are often unsuitable for high-purity thin film deposition methods based on vacuum sublimation. Currently, some inorganic materials, such Ag_2Se or Cu_2Se , have shown good prospects for room-temperature applications, but a fine-tuning of the stoichiometry and deposition conditions are needed to achieve the best efficiencies, a process that can be costly and time-consuming.^{54,55} Hence, inorganic TE materials operating near room-temperature are sought after.

1.6 Synthesis methods and thin film deposition

The majority of these novel compounds, *i.e.* perovskites, are usually synthesized by solution processing (see Chapter 2 for further information), involving the use of high boiling point organic solvents, such as *N,N*-dimethylformamide (DMF) and dimethyl sulfoxide (DMSO), complicated crystallization steps and the waste of huge amounts of material.⁴⁵ Although the synthesis of the most used thermoelectric materials does not involve the use of solvents, they do need the application of high temperatures (usually above 700 K) and long synthesis times (from hours to days), notably increasing the energy demand of the procedure.⁵⁶ Given the scarcity of resources, money and time, it is necessary to look for new methods of preparing these materials.

In this line, mechanochemical methods, which consist of reacting the precursors by purely mechanical methods, are gaining attention in the last years for materials synthesis. In particular, the dry mechanochemical approach by ball milling of stoichiometric precursors can be classified within the “green chemistry”, as it does not involve the use of solvents, toxic compounds, high temperatures, and it avoids the waste of materials and derivatives during the process.⁵⁷

In short, the precursors required for the synthesis, together with a few grinding beads are placed inside appropriate grinding containers. These are placed in the ball mill in a horizontal position and then they are strongly shaken. Due to the fast movement of the containers the beads will move by inertia hitting with high energies against the

precursors and the walls of the vessel causing the precursors to react forming the product (see Chapter 2 for more information). This is a simple but very effective method to synthesize materials quickly in large quantities and with high phase-purity.⁵⁸ Proof of this is that the number of reports on mechanochemically synthesized compounds is continuously growing.⁵⁹⁻⁶¹

In order to apply these materials in optoelectronic and photovoltaic devices they need to be deposited into thin films. One of the attractive features of these novel compounds is the possibility to obtain high-quality thin-films with simple solution deposition methods. Solution-processing has been widely used to deposit all type of halide perovskites due to the simplicity and low cost of the method.²¹ Typically, the precursor compounds are dissolved in polar solvents such as DMF, DMSO or acetonitrile, and then deposited onto a substrate with different techniques such as blade coating, drop casting, spin-coating, etc. The latter, spin-coating, is one of the most used methods for deposition of perovskite films, where the solution is dropped onto the substrate and spun at high speed in order to obtain a flat and thin film.⁶²

Film formation relies on parameters like the concentration of the solution as well as the spin-coating speed and acceleration.²¹ In addition, it is also important to control the evaporation rate of the solvent, as it affects the crystallization of the materials and consequently the charge transport properties of the thin-film. Therefore, a post-annealing process is usually required to ensure the quantitative conversion of the materials into a polycrystalline film and to get rid of the solvent residues. However, all these parameters are difficult to control, leading to the spread of the properties from batch to batch, undermining the development of optoelectronic devices.

Thermal vacuum deposition methods offer some benefits to overcome these issues.⁶² Vacuum deposition has the advantage of better control over the film stoichiometry and thickness, leading to flat and homogeneous surfaces, with high purity. In addition, it enables the assembling of multilayer devices without any chemical interaction between the layers, as may happen with solution deposition processes.^{62,63} Co-sublimation has been successfully used for the deposition into thin film of a wide range of halide perovskites.^{63,64} It consists of the stoichiometric sublimation of the precursors of the perovskite inside a high-vacuum chamber, so they react to form a thin film of the desired composition, either directly after the sublimation or after a post-deposition annealing. Alternatively, it is also possible to sublime the pre-synthesized compound directly, which condenses and recrystallizes on the substrate placed above the source.

This technique is known as single-source vacuum deposition (SSVD) and it is advantageous because of its simplicity, good control of the stoichiometry of the material with reduced performance time. Applied to halide perovskites,⁶⁵ it could be also applied for the deposition of the compounds studied in this thesis.

1.7 Aim of the thesis

This thesis aims to investigate, synthesize, and characterize lead-free multinary metal halides (MMHs) with potential application in optoelectronics and thermoelectrics. The synthesis method must also meet the requirements of “green chemistry” to emphasize the sustainability and the low toxicity of the process. Hence, dry mechanochemistry by ball-milling is the preferred synthesis method for these new materials. In order to test their possible incorporation into optoelectronic and thermoelectric devices, their deposition into thin film by vacuum techniques is studied.

The thesis is structured as follows:

- **Chapter 3:** synthesis, thin film deposition and characterization of a series of ternary copper halides, CsCu_2X_3 and $\text{Cs}_3\text{Cu}_2\text{X}_5$ ($\text{X} = \text{Cl}, \text{Br}, \text{I}$), with a high PLQY in the blue, showing potential for LED fabrication.
- **Chapter 4:** synthesis, thin film deposition and characterization of the double perovskite $\text{Cs}_2\text{AgBiBr}_6$ and its doping with Sn, Zn and Ge. Study is accompanied by theoretical calculations to assess its application in photovoltaics.
- **Chapter 5:** synthesis, thin film deposition and characterization of the perovskite CsSnI_3 to discuss its use as a thermoelectric material for room temperature applications.

The materials presented here had previously been scarcely studied for the above-mentioned purposes. Given their ease of synthesis, low toxicity, and performance, they may represent a step forward in the research of new materials for optoelectronics and thermoelectrics.

Chapter 2

Methodology and characterization techniques

*“Esa noche canté
Al piano del amanecer todo mi repertorio.”*
Enrique Urquijo - Los Secretos

In this chapter the experimental procedures for the synthesis and characterization of the materials subject of concern of this thesis are introduced. A variety of materials were prepared through dry mechanochemical synthesis by ball milling and then transformed into thin films by different approaches. The characterization techniques used to investigate both powders and thin films are described.

2.1 Mechanochemical synthesis

As introduced in Chapter 1, one of the objectives within the scope of this thesis is the preparation of lead-free multinary metal halides (MMHs) via sustainable and green methods. Dry mechanochemical synthesis by ball milling was chosen because of its simplicity and speed in addition to not needing solvents. In the upcoming chapters (Chapters 3-5), three families of materials with different stoichiometries and crystalline phases will be presented: Cs-Cu-I, Cs-Ag-Bi-Br and Cs-Sn-I. Despite their obvious dissimilarities, the three of them can be easily synthesized by dry ball milling from their starting compounds.

Generally, stoichiometric amounts of the corresponding starting reagents were weighed on a microbalance placed inside a nitrogen-filled glovebox. All chemicals were stored under inert atmosphere and used as received without further purification. Once weighed, they were mixed and introduced inside a 10 mL zirconia ball mill jar together with 2 zirconia beads of 10 mm in diameter. Before closing the jars, a Teflon O-ring was placed in between the lid and the base of the jar for securing the joint (**Figure 2.1a**). Then, ball milling was performed with a MM-400 shaking ball mill from Retsch at a fixed frequency of 30 Hz for a certain amount of time (**Figure 2.1b**). Depending on the desired material, the duration of the ball milling cycle was optimized and modified accordingly (see Chapters 3-5). After the prefixed ball-milling time is elapsed, the powders were extracted from the ball mill jar by manual scratching of the zirconia walls with a metallic spatula. It must be noted that the preparation of the starting reagents, sealing and opening of the jars as well as the obtention of the final powders is carried out inside a nitrogen-filled glovebox. Avoiding contact of the materials with the atmosphere at any step of the synthesis is crucial to prevent their oxidation or degradation.

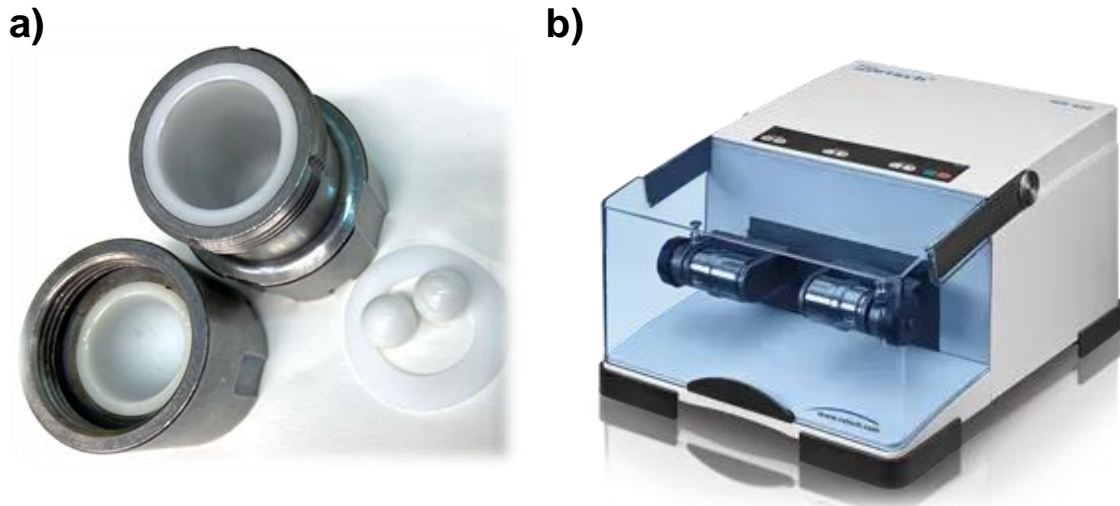


Figure 2.1. (a) 10 mL zirconia ball mill jar with two 10 mm zirconia beads and Teflon O-ring. (b) Mixer Mill MM-400 from Retsch. Picture taken from reference.⁶⁶

Upon the completion of the ball milling process, jars were cleaned in a fume-hood using a three-step procedure. They were rinsed and immersed in water inside an ultrasonic bath for 20 minutes. This step was repeated twice with dimethyl sulfoxide (DMSO) and isopropanol, respectively. If necessary, steps could be repeated to ensure proper cleaning. Finally, after drying in air overnight, they were ready to use again.

2.2 Thin film deposition

The implementation of the synthesized materials in most optoelectronics or thermoelectric devices such as light-emitting diodes (LEDs), solar cells or thermoelectric generators (TEGs) requires the deposition of the materials into thin films. In this thesis, two different deposition methods have been employed, solution processing and single-source vacuum deposition.

In both cases, glass substrates were thoroughly cleaned before the deposition. Standard cleaning procedure consisted of using subsequent sonication in water with soap, Milli-Q water, and 2-propanol baths. After drying with a N_2 flow, the substrates were placed in a UV ozone cleaner for 15 min. This process was followed independently of the deposition method chosen.

2.2.1 Spin coating

Spin coating is a widely used technique for depositing thin films because of its speed and low cost.⁶⁷ Nevertheless, solution processing faces several issues mainly coming from low reproducibility, limited substrate sizes and poor coverage of the film.⁶⁸ To enhance the coverage, the solubility of the materials in the precursor solution is usually increased. The choice of the solvent plays a key role in the solubility of the materials, affecting the final stoichiometry, phase, and morphology of the layer. Humidity control, rotation speed, solvent toxicity or re-dissolution of the films when depositing new layers on top increase the complexity of spin coating techniques.⁶⁷

In the case of MMHs, a certain amount of precursor powder is dissolved in organic solvents, such as *N,N*-dimethylformamide (DMF) or dimethyl sulfoxide (DMSO), up to a desired concentration. To ensure a more uniform film and get rid of aggregates or non-dissolved particles, solutions are filtered prior to their deposition. Next, a small portion of solution (in the order of a few μL) is deposited on top of a pre-cleaned substrate and spin coated at a fixed rotation speed for a certain amount of time, depending on the material (**Figure 2.2**). During spinning, the solution is spread all over the surface of the substrate forming a thin layer and the solvent starts to evaporate. However, in most cases, an annealing step after the deposition is required to help the drying of the film or to convert the material to the right phase.

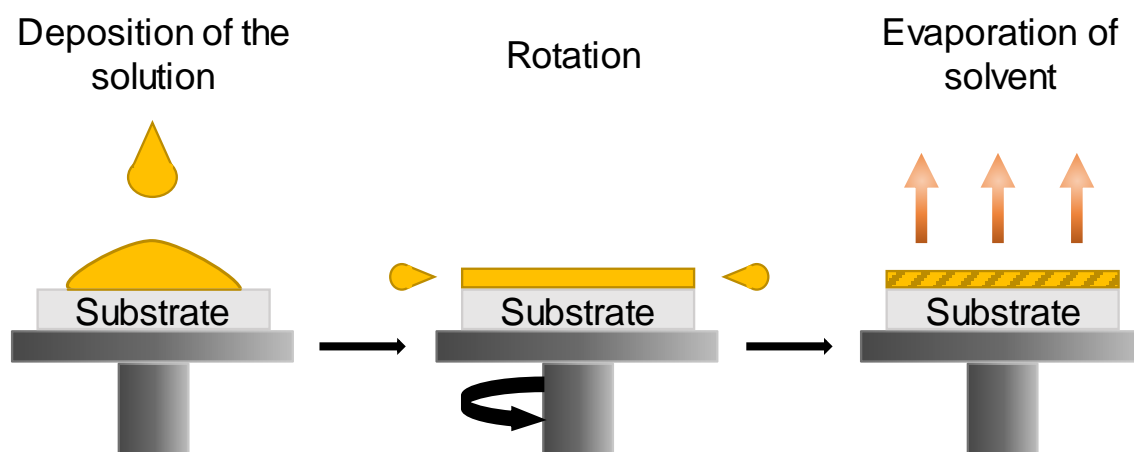


Figure 2.2. Schematic diagram of spin coating technique.

2.2.2 Single-source vacuum deposition (SSVD)

For obtaining high-efficiency optoelectronic devices, flat, homogeneous and pin-hole free thin films are required. Besides, Cs-containing perovskites, widely used for photovoltaics, present poor solubility in the most used solvents.^{65,69} Solution-based deposition methods inherently depend on the good miscibility of the materials and the formation of smooth, continuous, uniform films is, generally, challenging.⁷⁰ For these reasons, vapour deposition techniques stand out as a potential alternative.

Vacuum deposition methods offer enhanced control over the stoichiometry, thickness and morphology of the films.^{69,70} Among the several types of vacuum techniques available (e.g. co-evaporation, sequential deposition, single-source, etc), in this thesis single-source vacuum deposition (SSVD) has been chosen. It enables the direct deposition of the desired compounds pre-synthesized by ball milling without compromising their stoichiometry.

However, one of the main drawbacks of this technique is the high amount of electricity consumption and the potential incongruent melting and evaporation (decomposition of the presynthesized material).

In a typical SSVD, the mechanochemically synthesized material in powder form is loaded in a ceramic crucible (Creaphys GmbH) placed inside a high-vacuum chamber. Glass substrates are placed on the substrate holder, right above the material source. The evaporation chamber used in this thesis has room for three 3×3 cm substrates (see **Figure 2.3**). The chamber is then evacuated to a pressure below 8×10^{-6} mbar, a process that usually takes around 1 h 30 min – 2 h with the evaporator employed here. The evaporator is placed in air, outside a nitrogen-filled glovebox, which inevitably leads to the entrance of oxygen and moisture inside during sample loading. Their complete removal is what makes this process time-consuming and lasting for almost 2 h. Nevertheless, this does not have to be the case for all evaporators, as they can be placed inside a glovebox and, thus, reduce the amount of time needed for reaching high vacuum conditions.

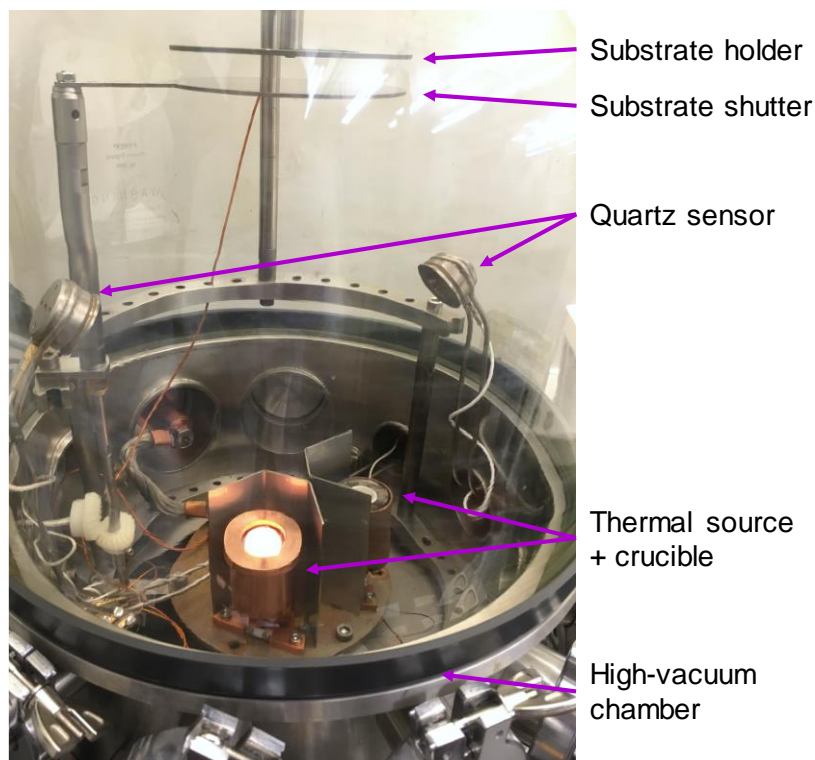


Figure 2.3. Basic components of the evaporator used for SSVD.

Once high-vacuum conditions are achieved, the substrate shutter is opened, and the rotation of the substrate holder is turned on. This will favor a homogeneous coverage of the substrate. Then, the material source is heated up to a certain temperature, dependent on the material and higher than the sublimation temperature of its individual components. The deposition of the material takes place slowly and can be followed and controlled by a quartz microbalance sensor placed above the source. The deposition finishes after the complete evaporation of the solid present in the crucible, indicated by a sudden drop of the evaporation rate.

To finish the evaporation, the substrate shutter is closed, the rotation is stopped and the source temperature is set to 0 °C to cool down the system. Later, the chamber is vented to atmospheric pressure and the substrates with a thin film with the same composition as the powders are obtained.

2.3 Characterization techniques

2.3.1 X-Ray diffraction (XRD)

In this thesis, X-ray diffraction was used to investigate the structure of the materials prepared. XRD is a bulk-sensitive technique commonly used to get microstructural information such as the crystal structure, crystal orientation, crystallite size or phase purity.⁷¹ XRD is based on Bragg's law (**Equation 2.1**), which relates the distance between atomic planes in a material to the position of the peaks in a diffractogram pattern. For a given crystalline material, whose atoms are arranged in an ordered manner in three dimensions, an incident X-ray beam is scattered (or diffracted) by the atoms in its path.⁷² The diffraction peak is thus formed when Bragg's law is fulfilled, that is, when the diffracted rays resulting from the interaction with the planes of atoms undergo constructive interference.⁷¹ Only when the phase shift between diffracted rays is equal to an integer multiple of the wavelength, the diffracted beams will still be in phase after the reflection, satisfying Bragg's law. **Equation 2.1** shows Bragg's law equation,

$$2d \sin \theta = n\lambda \quad (2.1)$$

where d stands for the distance between planes of atoms, θ is the angle of the incident X-ray beam with respect to the atomic plane, n is an integer number and λ is the wavelength of the X-ray.

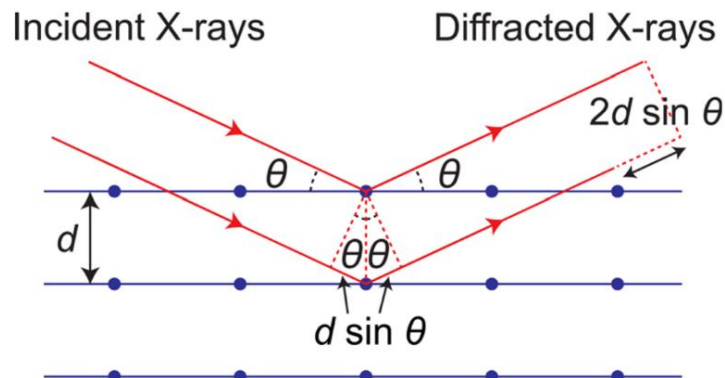


Figure 2.4. Schematic diagram of diffraction of X-rays according to Bragg's law. The illustration is adapted from reference.⁷¹

Most experiments shown in this thesis were acquired with an Empyrean diffractometer from Malvern Panalytical equipped with a Cu K α anode operated at 45 kV and 40 mA. Scans were measured in the $2\theta = 8^\circ - 60^\circ$ range in Bragg Brentano geometry. In this geometry, X-ray source and detector are placed at a fixed radius from the sample, fixed in a horizontal plane. Both source and detector are moved at the same time so that incident and diffracted beams impact and leave the sample at the same angle, θ .⁷¹

2.3.2 X-Ray Photoelectron Spectroscopy (XPS)

In this thesis, X-Ray photoelectron spectroscopy (XPS) has been employed to characterize the composition of the surface of the materials and the determination of the chemical state of the elements present. XPS is based on the photoelectric effect, which involves the irradiation of a sample with X-ray photons and the detection of the emitted photoelectrons (**Figure 2.5**). This process involves the energy transfer from the X-ray source to a core level electron, following the **Equation 2.2**,⁷³

$$h\nu = BE + KE + \phi_{spec} \quad (2.2)$$

where $h\nu$ stands for the energy of the X-ray, BE for the binding energy of the emitted electron, KE for the kinetic energy of the electron and ϕ_{spec} for the work function of the spectrometer. The binding energy of an electron depends on the element and the orbital from which it is ejected. It is independent on the X-ray energy source and useful for the determination of the sample composition.⁷⁴ Thus, the BE of an electron can be easily determined by the energy of the X-ray source, the known value of the spectrometer work function and the kinetic energy measured in the XPS experiment, as derived from **Equation 2.2**.

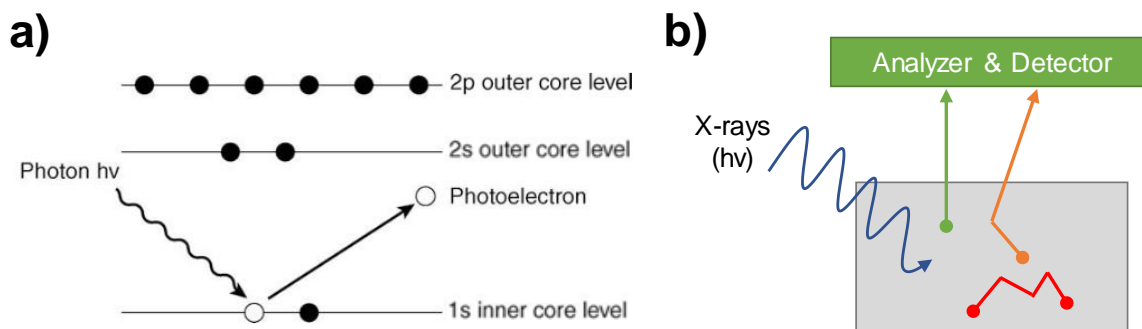


Figure 2.5. (a) Schematic diagram of the photoemission process that takes place in XPS. The illustration is adapted from reference.⁷⁴ (b) Schematic representation on how emitted electrons interact with the sample depending on how deep they are generated. The illustration is adapted from reference.⁷³

However, not all the electrons present in the sample can be detected by XPS. Although the X-rays can penetrate the sample in the order of microns, photoemitted electrons may face inelastic collisions in their way from the bulk to the surface and lose their kinetic energy before escaping. Hence, only electrons emitted from the surface or near (analysis depth $\sim 2 - 10$ nm) will have less scattering probability and will retain their kinetic energy, managing to escape from the surface and reach the detector.^{73,74} This depth limitation makes XPS a surface characterization technique.

XPS experiments in this thesis were acquired using a Thermo Scientific K-Alpha X-ray photoelectron spectrometer. Al K- α X-ray radiation was employed as the X-ray source. XPS data were analyzed with Thermo Advantage v5.9925 software.

2.3.3 Optical characterization

Ultraviolet-visible spectroscopy

Ultraviolet-visible spectroscopy (UV-Vis) refers to the amount of light from the ultraviolet-visible spectral region that is absorbed by a given material. When light from a certain wavelength and intensity (I_0) is passed through a material it can be partially absorbed and exits the sample with a modified intensity (I). The amount of light absorbed, or absorbance (A), is calculated by the Lambert-Beer law (**Equation 2.3**):

$$A = \log_{10} \left(\frac{I}{I_0} \right) \quad (2.3)$$

The absorbed light can also be translated into the amount of light transmitted through the sample, expressed in % of transmittance (T). **Equation 2.4** is derived from **Equation 2.3** to relate absorbance and transmittance:

$$A = \log_{10} \left(\frac{I}{I_0} \right) = \log_{10} T = \log_{10} \left(\frac{\%T}{100\%} \right) \quad (2.4)$$

It must be noted that the amount of light absorbed is dependent on the material and on its structure. If scans with incident light with all the wavelengths comprised in the UV-Vis region are acquired, a complete absorbance spectra of the material can be obtained.⁷⁵

In this thesis, two different measurement setups have been used depending on the state of the materials studied. On the one hand, when materials were in the powder state or in thin films where the surface was rough and inhomogeneous, light scattering, reflections or interferences play a key role in the measurement. In these cases, an integrating sphere was used to determine the optical properties (**Figure 2.6a**). An integrating sphere is internally covered with a diffuse and highly reflective material, usually Spectralon[®] that scatters the transmitted and scattered light equally inside the sphere. Then, the light reaches a photodetector coupled to the sphere, detecting a light intensity proportional to the total transmitted light and the scattered light.⁷⁶

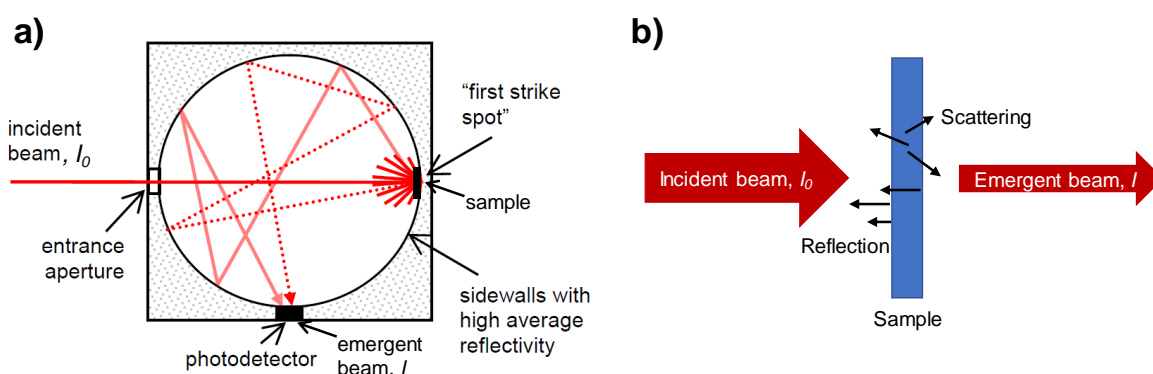


Figure 2.6. Schematic diagram of (a) integrating sphere and (b) transmission setup used for UV-Vis absorbance.

On the other hand, when samples are smooth and flat enough and they are deposited into thin films on top of a transparent substrate, the measurement setup can be simplified to a simple transmission configuration (**Figure 2.6b**). In this case, the substrate is placed on top of a flat horizontal holder with a small hole, where the transmitted light passes and that must be fully covered by the sample.

Photoluminescence spectroscopy

Photoluminescence spectroscopy measures the photoluminescence (PL) of a given material and, consequently, allows the study of different properties, such as PLQY, emission intensity, emission lifetime, Stokes shift, etc. In a common PL measurement, photons with a higher energy than the bandgap of the material are shined directly to the sample and the emission (at lower energy) spectrum is recorded (**Figure 2.7**). A low-pass filter is usually introduced in the reflected beam path between the sample and the detector in order to filter-out the high energy excitation light.

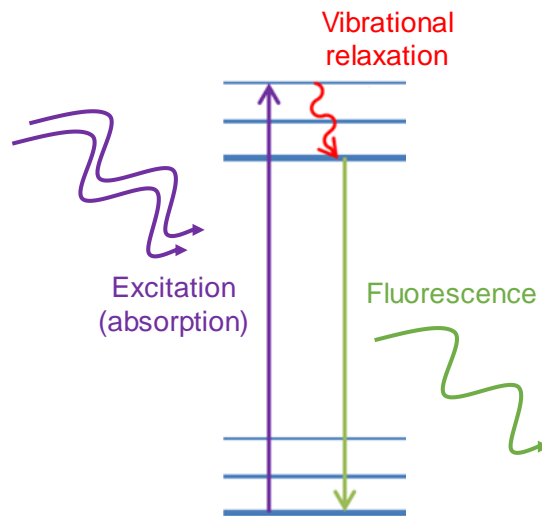


Figure 2.7. Jablonski diagram of fluorescence showing the radiative and non-radiative processes that can take place after the photon absorption.

2.3.4 Scanning electron microscopy

Scanning electron microscopy (SEM) produces images of a sample with a resolution around the nanometer scale by irradiating the surface with an electron beam. When this beam interacts with the sample, several electron signals are generated and

captured by the detectors. Among them, we can find backscattered electrons (BSE) and secondary electrons (SE). BSE are high energy electrons that originate from the bulk of the sample and provide compositional information (i.e., atoms in the sample with higher atomic number, Z , will produce more BSE and hence appear brighter). On the contrary, SE have lower energy as they are originated from the surface and provide topographic information.⁷⁷⁻⁷⁹ Information coming from both types of signals is used then to conform a high-quality image of the sample's surface.

X-rays are also generated when high energy electrons reach the sample. These X-rays are characteristic of the element from which they have been expelled and give compositional information. The detection of these X-rays and their assignment to each element is the basic principle of energy-dispersive X-ray (EDX) analysis.⁸⁰ This technique has been used in this thesis to gain insight in the sample composition and to calculate the atomic ratio of each element present.

2.3.5 Thermoelectrical characterization

For the thermoelectrical characterization, an all-in-one commercial equipment manufactured by LinseisTM was used to estimate the electrical conductivity, Seebeck coefficient, Hall coefficient and thermal conductivity at the same time. The basic measurement principle for each property is presented hereafter. Prior to the measurement, materials were deposited by vacuum sublimation as thin films (around 100 – 500 nm in thickness) on top of pre-structured measurement chips provided by LinseisTM (**Figure 2.8**). These chips are based on a silicon substrate covered by Al_2O_3 and platinum electrodes, each one used for a specific measurement.

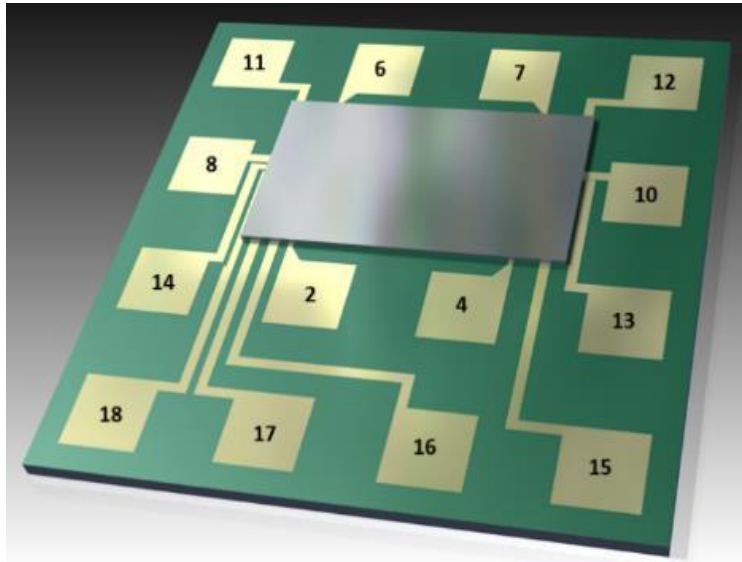


Figure 2.8. Schematic diagram of a measurement chip where the material has been deposited as thin film (grey area) and electrodes are labelled. The illustration is adapted from reference.⁸¹

Electrical conductivity

To determine the electrical conductivity, σ , the Van-der-Pauw method is employed, for which four electrodes connected at the corners of the sample are needed. In this method, the samples need to be flat and homogenous, with a known uniform thickness. A current is applied to two neighbour contacts and the drop in voltage occurred at the remaining two electrodes at the other edge of the sample is measured. After a changing positive/negative electrodes as well as current/voltage terminals, the electrical resistivity, ρ , is calculated via the Van-der-Pauw formula.^{82,83} The electrical conductivity is thus calculated as the reciprocal of the electrical resistivity.

Seebeck coefficient

The chip configuration needed for the Seebeck coefficient, S , measurement is shown in **Figure 2.9**. It consists of a heating stripe placed in a membrane below the sample thin film to which a current is applied to increase its temperature. This contact is known as the hot contact for the thermovoltage measurement and creates a temperature voltage across the stripe and, consequently, the sample. Located outside the membrane there is a contact that remains cooled at a specific temperature, acting as a cold contact.^{81,82} The temperature at each contact is measured by the voltage difference (or

thermoelectric voltage) created after the current applied by a thermocouple, following a similar procedure as for the electrical conductivity. The measurement carried out is under steady-state conditions, as it starts only when the temperature of the hot side is stable.⁸³

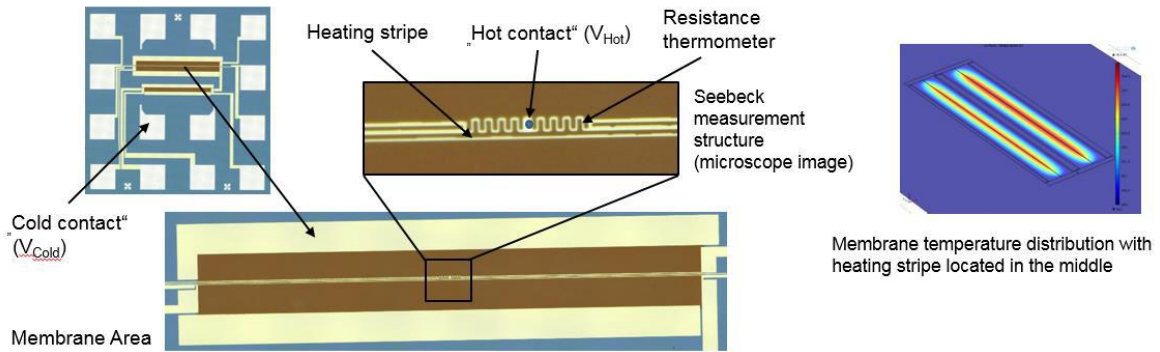


Figure 2.9. Configuration of the measurement chip for a Seebeck coefficient measurement. The illustration is adapted from reference.⁸¹

The Seebeck coefficient is thus calculated following the formula (Equation 2.5):

$$S = \frac{-V_{Th}}{\Delta T} = \frac{-(V_{Hot} - V_{Cold})}{T_{Hot} - T_{Cold}} \quad (2.5)$$

Where V_{Th} is the thermal voltage, ΔT is the temperature gradient, and V_{Hot} and V_{Cold} are the voltage of the hot and cold contacts, respectively. The Seebeck coefficient is usually expressed in volts/kelvin ($V K^{-1}$) or microvolts/kelvin ($\mu V K^{-1}$).⁸¹

Hall coefficient

For measuring the Hall coefficient, the system measures the change in the diagonal resistance of the sample with respect to a magnetic field applied perpendicularly (**Figure 2.10**).^{81,82}

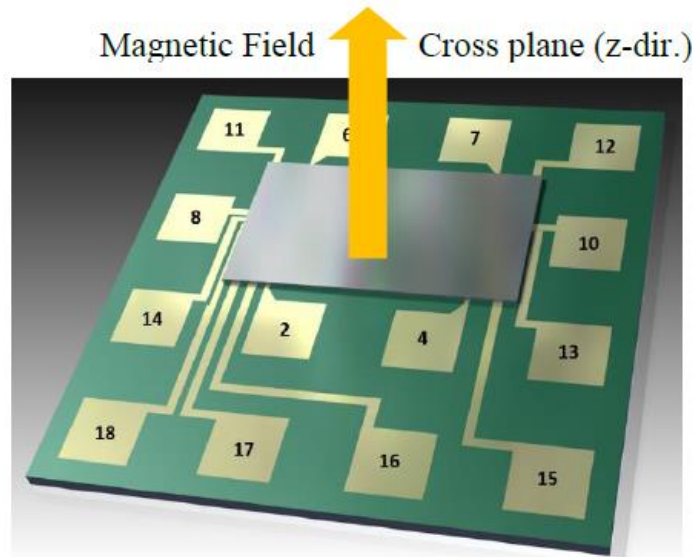


Figure 2.10. Layout of the measurement chip for the Hall coefficient calculation. The illustration is adapted from reference.⁸¹

Thermal conductivity

For measuring the thermal conductivity (λ), the 3 omega (3ω) method is followed and a similar membrane configuration than for the Seebeck coefficient is used. In this case, an alternating current with an angular frequency ω is applied to the hot stripe, a heat flux from the hotwire towards its surroundings is released. Then, the voltage drop across the wire due to the heating is transformed into the thermal conductivity by means of internal equations of the equipment defined by the manufacturer.^{81,82,84} This conversion is based on a differential measurement of the sample-covered chip and the empty chip measured separately (**Equation 2.6**). For this purpose, thermal conductivities of both empty and covered chips (λ_{Empty} and λ_{Sample} , respectively) together with the thickness of the sample/membrane (t_{Empty} and t_{Sample}) need to be taken into consideration.⁸¹

$$\lambda_{measured} * t_{measured} = \lambda_{Empty} * t_{Empty} + \lambda_{Sample} * t_{Sample} \quad (2.6)$$

Apart from conduction, losses from convection and radiation need to be taken into consideration. As the working pressure of the equipment is around 10^{-6} mbar (high vacuum), convection losses can be neglected. However, radiation losses are a crucial factor because of the setup configuration and need to be measured. For this purpose, the equipment incorporates a dual membrane correction, which evaluates and compares the

thermal conductivities of two different membranes with different areas. As a result of this correction, the accuracy of the measurement is considerably increased.⁸²

Chapter 3

Solvent-Free Synthesis and Thin-Film Deposition of Cesium Copper Halides with Bright Blue Photoluminescence

*“Faro que alumbras al mundo
Por encima de la tempestad
Devuélveme la esperanza y que brille mi estrella.”*
Revólver

Blue-luminescent materials show potential applications in lighting systems, such as the preparation of white light-emitting diodes. However, wide band gap blue emitters with high photoluminescence quantum yields (PLQYs) are typically more difficult to obtain as compared to green- or red-emitting ones. Here, we prepared two series of inorganic cesium copper halides, with the general formulas $\text{Cs}_3\text{Cu}_2\text{X}_5$ and CsCu_2X_3 ($\text{X} = \text{Cl}, \text{Br}, \text{I}$, and mixtures thereof) by dry mechanochemical synthesis at room temperature. We identified $\text{Cs}_3\text{Cu}_2\text{I}_5$ as the most promising material as its blue luminescence centered at 442 nm with a high PLQY ($> 40\%$) is maintained for several days in air ($\text{Cs}_3\text{Cu}_2\text{Cl}_5$ shows significantly higher PLQY, over 80% but is unstable in air). Based on this, we fabricated homogeneous and pinhole-free $\text{Cs}_3\text{Cu}_2\text{I}_5$ thin films by thermal single-source vacuum deposition. Crystalline phase and photoluminescence features are maintained in the thin films, demonstrating that these low-toxicity materials can be synthesized and processed by fully solvent-free routes for a widespread implementation in optoelectronic devices.

Reference:

Paz Sebastia-Luna, Javier Navarro-Alapont, Michele Sessolo, Francisco Palazon*, and Henk J. Bolink. Solvent-Free Synthesis and Thin-Film Deposition of Cesium Copper Halides with Bright Blue Photoluminescence. *Chemistry of Materials*, **2019**, *31*, 24, 10205–10210.

The content of this chapter was reproduced with permission from Chemistry of Materials. Full published paper and Supporting Information are attached at Appendix A.

3.1 Introduction

In the past decade, lead halide perovskites (LHPs) have emerged as promising materials for optoelectronics,^{11,22,85,86} but the necessity of replacing toxic Pb^{2+} ions by other more environmentally-friendly metals requires to search for different ternary and quaternary multinary metal halides (MMHs), with various stoichiometries and crystal structures.^{38,87} Among these, Cu(I)-based fully-inorganic ternary metal halides are particularly promising, especially for applications in light-emitting diodes (LEDs).^{16,88,89} Stable crystals with two different stoichiometries can be formed: CsCu_2X_3 and $\text{Cs}_3\text{Cu}_2\text{X}_5$ ($\text{X} = \text{Cl}, \text{Br}, \text{I}$, or mixtures thereof). The most common crystal structure of both compounds at room temperature is depicted in **Figure 3.1**.

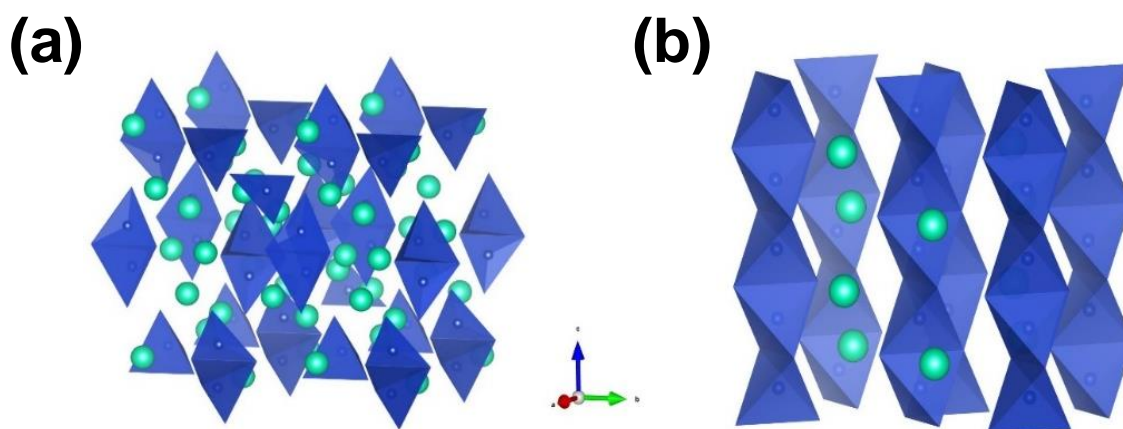


Figure 3.1. Crystal structures of $\text{Cs}_3\text{Cu}_2\text{Br}_5$ (a) and CsCu_2Br_3 (b), created with VESTA software based on crystallographic information files obtained in the Inorganic Crystal Structure Database (refs: 150297 and 49613). Green balls represent Cs^+ ions and blue polygons represent CuBr_4 tetrahedra.

Cu(I) is in tetrahedral coordination with the halides in both cases. However, $\text{Cs}_3\text{Cu}_2\text{X}_5$ is constituted by isolated dimers of CuX_4 whereas CsCu_2X_3 consists of side-sharing tetrahedra spatially arranged as wires. Based on these considerations, these structures may be referred to as 0D and 1D respectively.⁸⁹ To the best of our knowledge, only a few reports on these compounds exist.^{89–92} Furthermore, in the above-mentioned publications, the synthesis and thin film deposition of such MMHs was carried out either by solution processes in (toxic) organic solvents, such as DMF or DMSO, or by highly time- and energy-consuming thermal routes. Lately, solvent-free mechanochemical

synthesis (MCS) has been shown to be a very simple and efficient approach to synthesize different phase-pure multinary metal halides,^{58–61,65,93–96} as previously introduced in Chapters 1 and 2. In this work, MCS enables the formation of Cu(I) ternary inorganic halides of high quality. In particular, some of the as-synthesized compounds exhibit bright photoluminescence even as non-passivated bulk powders and are stable in air for several days. Furthermore, as-synthesized compounds can be deposited as thin films with good morphology, crystallinity, and photoluminescence. In order to do so, we employed single-source vacuum deposition (SSVD) which has recently proven to be an easy, fast and non-toxic (solvent-free) approach for the deposition of other inorganic as well as hybrid organic-inorganic halide compounds (see Chapter 2 for a detailed explanation).^{28,65,97}

3.2 Experimental section

Materials

Cesium chloride (CsCl, > 99%), cesium bromide (CsBr, > 99%), and cesium iodide (CsI, > 99%) were purchased from TCI. Copper(I) chloride (CuCl, $\geq 99.999\%$), copper(I) bromide (CuBr, $\geq 99.999\%$), and copper(I) iodide (CuI, $\geq 99.999\%$) were purchased from Sigma-Aldrich. Dimethyl sulfoxide (DMSO) of reagent grade was purchased from Scharlau and *N,N*-dimethylformamide (DMF) from Fisher. All chemicals were stored in a nitrogen-filled glovebox and used as received without further purification.

Mechanochemical synthesis

As introduced in Chapter 2, stoichiometric amounts of CsX/CuX powders were mixed inside a nitrogen-filled glovebox. Then, approximately 3 g of the mixed precursor powders was introduced inside 10 mL zirconia ball mill jars with two zirconia beads of 10 mm in diameter. The jars were closed under nitrogen so that the powders were not exposed to air. Then, ball milling was performed with an MM-400 shaking ball mill from Retsch, at a frequency of 30 Hz for 99 min.

Thin-Film Deposition by Solution Processing

Deposition and characterization of the thin films were carried out inside a clean-room ISO 7 10000. Glass substrates were extensively cleaned using procedure explained in Chapter 2. Substrates were transferred to a nitrogen-filled glovebox (H_2O and $\text{O}_2 < 0.1$ ppm) for solution processing of the films. $\text{Cs}_3\text{Cu}_2\text{I}_5$ powders were dissolved into a mixed solvent containing DMF and DMSO with a volume ratio of 1:1 to a 0.7 M concentration. The solutions were then filtered with a 0.45 μm -pore size polytetrafluoroethylene filter. Thin films were deposited by spin coating at a speed of 3000 rpm for 60 s, followed by annealing on a hot plate at 100 °C for 60 min (see Chapter 2 for further information about spin coating process).

Single-Source Vacuum Deposition

In a typical deposition, an alumina thermal source (Creaphys GmbH) inside a home-made vacuum chamber was loaded with 0.5 g of mechanochemically synthesized $\text{Cs}_3\text{Cu}_2\text{I}_5$ powder. The chamber was then evacuated to a pressure of 8×10^{-6} mbar, and the source was rapidly heated to 600 °C with a ramp of 50 °C min^{-1} . The deposition is controlled by a quartz microbalance sensor and stopped after the complete evaporation of the solid (see Chapter 2 for further information).

X-Ray Diffraction Characterization

X-ray diffraction was measured with a powder diffractometer model D8 Avance A25 Bruker brand equipped with $\text{CuK}\alpha$ anode. Single scans were acquired in the $2\theta = 10^\circ$ to 40° range with a step size of $2\theta = 0.025^\circ$, in Bragg-Brentano geometry in air. Whole powder pattern decompositions using the so-called Le Bail method, implemented in Fullprof software, were applied for the refinement of unit cell parameters.⁹⁸ Thompson-Cox-Hastings pseudo-Voigt line profile with refinable lineshape parameters are assumed for the fittings.⁹⁹

Optical Characterization

UV–visible absorption spectra of the films and powders were collected using a Jasco V-670 UV/vis/NIR spectrophotometer. The PL characteristics for powders were studied using a xenon lamp coupled to a monochromator as the excitation source and an integrated sphere coupled to a Hamamatsu C9920-02 spectrometer with a Hamamatsu PMA-11 optical detector in order to quantitatively determine the PL quantum yield (PLQY). For a typical analysis, three scans with an integration time of 100 ms were collected and averaged.

In this chapter, we will also study the excitation spectra of the synthesized materials. A fluorescence excitation spectrum of a given material is determined by fixing the emission wavelength using a monochromator and the excitation wavelength is scanned.¹⁰⁰ Prior to the excitation spectrum, an emission spectrum must be recorded to know the wavelength where the maximum emission is achieved. Once this wavelength is known, the excitation wavelengths are scanned across the desired excitation range and emission (at fixed wavelength) is recorded.^{101,102} Emission and excitation spectra were measured with a FluoroMax HORIBA-MTB spectrofluorometer equipped with a xenon light source coupled to a monochromator.

Scanning Electron Microscopy

The scanning electron microscopy (SEM) images were obtained using a Hitachi S-4800 scanning-electron microscope, operating at an accelerating voltage of 20 kV over platinum-metallized samples.

Thermal Characterization

Thermogravimetric analysis (TGA) was carried out with a TA Discovery TGA550 (TA Instruments) equipped with a continuous nitrogen flow. Measurements were performed with a ramp of 10 °C min⁻¹ from room temperature to 600 °C.

3.3 Results and discussion

We first synthesized a series of copper(I)-based inorganic compounds with the 1D structure CsCu_2X_3 ($\text{X} = \text{I}, \text{Br}, \text{Cl}$, and their mixtures). In short, the synthesis was carried out by simple dry ball milling of the corresponding CsX and CuX precursors in a 1:2 molar ratio in an inert atmosphere in order to avoid hydration and possible oxidation (see the Experimental Section for more details). **Figure 3.2** shows the X-ray diffractograms of all samples in the $10^\circ \leq 2\theta \leq 40^\circ$ range.

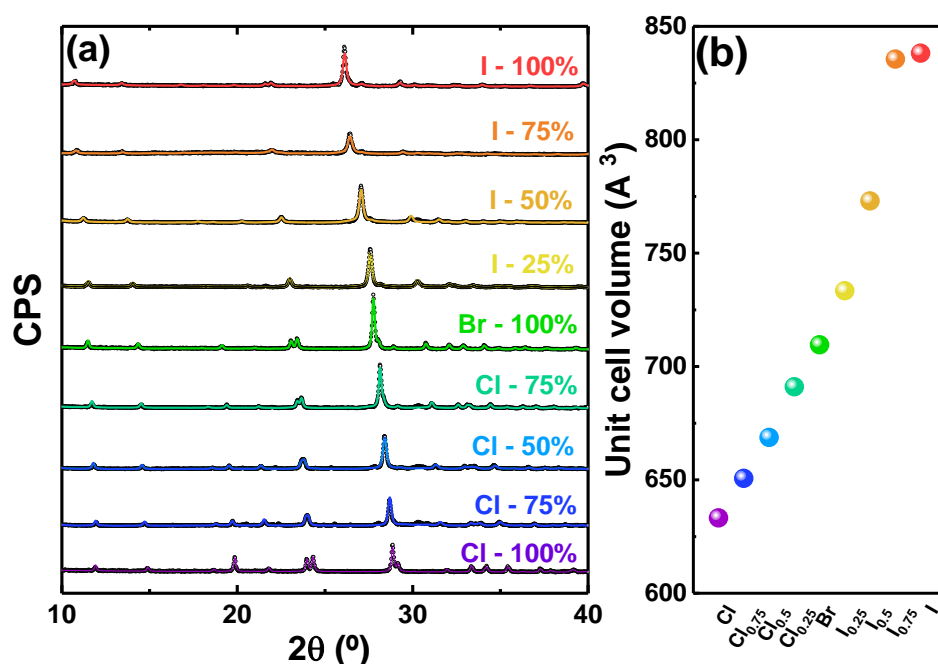


Figure 3.2. (a) XRD data (open circles) and fits (solid-colored lines) of different CsCu_2X_3 compounds. (b) Unit cell volume as derived from fits.

In order to compare the XRD results of our powders with the indexed patterns at the Inorganic Crystal Structure Database (ICSD), we performed whole powder pattern decompositions (WPPD) using the so-called Le Bail method. This method allows the refinement of the unit cell parameters and extract a calculated powder pattern that is compared to the experimental.⁹⁸ All diffractograms are fitted assuming single-phase compounds crystallized in the $Cmcm$ space group, with varying unit cell parameters (**Figure 3.2a** and **Table 3.1**). The space group, the same for all the halide combinations, together with the reference unit cell parameters used for the XRD fitting were extracted

from the ICSD database (CsCu₂Cl₃ ICSD code 49612; CsCu₂Br₃ ICSD code 49613 and CsCu₂I₃ ICSD code 38037).

Table 3.1. Lattice parameters derived from Le Bail fits of CsCu₂X₃ compounds (space group = *Cmcm*). Please note that the results are expressed without taking into account the number of significant digits.

X	a (Å)	b (Å)	c (Å)	α (°)	β (°)	γ (°)	V (Å³)
I	10.50438	13.11778	6.08282	90	90	90	838
I₇₅Br₂₅	10.47270	13.14974	6.06720	90	90	90	836
I₅₀Br₅₀	10.00890	12.91363	5.98059	90	90	90	773
I₂₅Br₇₅	9.78000	12.67451	5.91661	90	90	90	733
Br	9.87500	12.35396	5.81609	90	90	90	710
Cl₂₅Br₇₅	9.73313	12.29817	5.77289	90	90	90	691
Cl₅₀Br₅₀	9.58554	12.19961	5.71844	90	90	90	669
Cl₇₅Br₂₅	9.47997	12.09300	5.67565	90	90	90	651
Cl	9.50509	11.89780	5.59920	90	90	90	633

Unit cell volumes derived from the whole-pattern fit show a rather linear expansion from 633 Å³ (X = Cl) to 840 Å³ (X = I), as expected from the increased ionic radius when going from Cl⁻ to Br⁻ and to I⁻ (**Figure 3.2b**). In order to better appreciate the phase purity of the obtained compounds, experimental and fitted profiles are reproduced in higher resolution together with the calculated Bragg's reflections in the Supporting Information (**Figures S1–S9** at Supporting Information of Chapter 3). For monohalide compounds, the excellent quality of the fits is a strong indication of complete reaction and high phase purity. This observation also holds for most mixed-halide compounds, with a slightly worse match for Cl-rich mixed Br–Cl compounds (**Figures S7 and S8**). In these two cases, we cannot rule out a minor phase segregation between CsCu₂Br₃ and CsCu₂Cl₃ domains. Also, a broad peak around 2θ = 31° is observed in some samples, which can be attributed to zirconia debris originating from the grinding medium. As this does not appear on all samples, we conclude that it is not unavoidable and probably a further optimization of the synthesis conditions (powder-to-ball weight ratio

and previous use or not of the same grinding beads and jars) should result in a controllable elimination of these minor by-products.

To the best of our knowledge, there are no previous references on the thermal stability of these materials. Yet, thermal stability is crucial at least for two reasons: (i) to determine whether the materials would remain stable in standard operation conditions once implemented in devices and (ii) to determine whether they can be processed by thermal processes such as thermal vacuum deposition, without undergoing incongruent melting or vaporization. Thermal stability of these materials was studied by TGA. TGA is an analytical technique used to determine a material's thermal stability and its fraction of volatile components and moisture by monitoring the weight change that occurs as a sample is heated at a constant rate. The weight loss of the CsCu_2X_3 ($\text{X} = \text{Cl}, \text{Br}, \text{I}$) compounds as a function of temperature at atmospheric pressure is reported in **Figure 3.3**. Bromide and iodide samples present the highest thermal stabilities of the series, without any weight variation until approximately 490 °C and 360 °C, respectively. For the chloride species, the thermal behaviour is significantly different. A weight loss at around 185 °C was observed, followed by an increase around 400 °C. Based on literature, these two features can be ascribed first to oxidation of the Cu(I) halide to Cu_2O , followed by the oxidation of Cu(I) oxide to Cu(II) oxide ($\text{Cu}_2\text{O} \rightarrow \text{CuO}$).^{103–105} These transformations might occur in the presence of residual oxygen in the TGA column, even if the analyses were performed with a nitrogen flow. For bromide and iodide samples, no weight increase was observed, pointing to their higher stability towards oxidation in the experimental conditions.

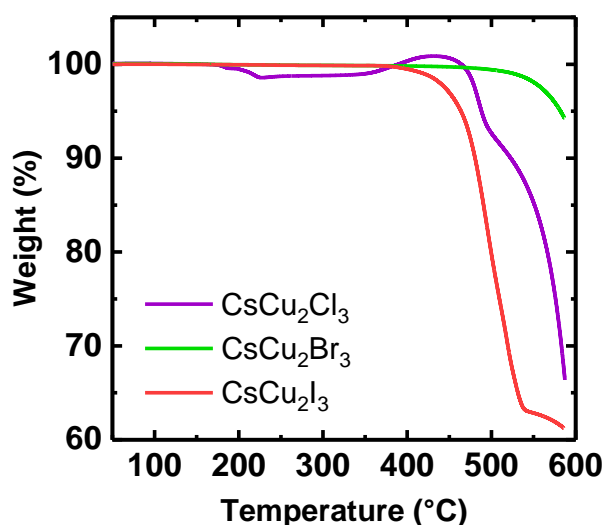


Figure 3.3. Thermogravimetric analysis (TGA) of the pure-halide CsCu_2X_3 compounds.

Optical absorption shows a tunable onset around 305 nm – 325 nm (see **Figure S11**), however, no PL could be detected with our setup. This is in line with the literature, where only one recent report demonstrates weak PL (5% PLQY) from surface-passivated colloidal nanorods with the same composition.¹⁰⁶

We also investigated the 0D structures $\text{Cs}_3\text{Cu}_2\text{X}_5$ ($\text{X} = \text{Cl}, \text{Br}, \text{I}$ and mixtures thereof). The application of these compounds for optoelectronics has been scarcely studied before, with only the pure-bromide, pure-iodide and mixed bromide-iodide species being reported.^{89,90,107} The pure-chloride compound, in contrast, has been only reported to define its structure.¹⁰⁸ Herein, we investigate the synthesis of the whole halide series by dry mechanochemistry and reveal their excellent optical quality.

Figures 3.4 and **S12–S20** show the XRD analysis of all $\text{Cs}_3\text{Cu}_2\text{X}_5$ compounds. For all mixed iodide–bromide samples (including the pure-bromide and the pure-iodide ones), diffractograms are fitted considering a *Pnma* space group with varying unit cell parameters (**Figure 3.4a**). This analysis holds for chloride-containing samples up to a chloride content of 75 % mol. As a result, we observe a clear trend on the unit cell volume with the ionic radius of the halide anion ($\text{Cl}^- < \text{Br}^- < \text{I}^-$; see **Figure 3.4b** and **Table 3.2**). Although *Pnma* is the expected space group for all $\text{Cs}_3\text{Cu}_2\text{I}_5$, $\text{Cs}_3\text{Cu}_2\text{Br}_5$, and $\text{Cs}_3\text{Cu}_2\text{Cl}_5$ based on ICSD (refs: 150298, 150297, and 150296, respectively), the diffractogram for $\text{Cs}_3\text{Cu}_2\text{Cl}_5$ is better fitted considering the space group *Cmcm*. Crystallization of $\text{Cs}_3\text{Cu}_2\text{Cl}_5$ in this space group was already reported by others.¹⁰⁸ Although the crystallization in one or the other space group is evident by the fits obtained in both cases, we could not elucidate what drives the crystallization in a given structure here. This, as will be detailed hereafter, has important consequences on the optical properties.

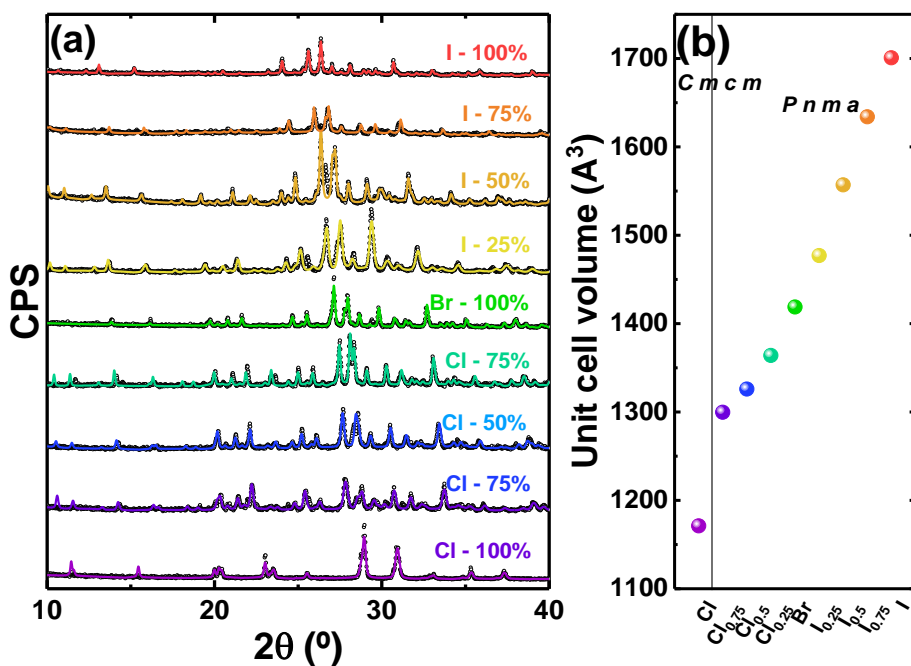


Figure 3.4. (a) XRD data (open circles) and fit (solid-colored lines) of different $\text{Cs}_3\text{Cu}_2\text{X}_5$ compounds. (b) Unit cell volume as derived from the fit.

Table 3.2. Lattice parameters derived from Le Bail fits of $\text{Cs}_3\text{Cu}_2\text{X}_5$ compounds (space group = *Pnma* for all compounds except for $\text{Cs}_3\text{Cu}_2\text{X}_5$ for which *Cmcm* is assumed).

X	a (\AA)	b (\AA)	c (\AA)	α ($^\circ$)	β ($^\circ$)	γ ($^\circ$)	V (\AA^3)
I	10.16984	11.64503	14.36164	90	90	90	1701
I ₇₅ Br ₂₅	9.61720	11.02493	13.66381	90	90	90	1634
I ₅₀ Br ₅₀	9.81536	11.32985	14.00074	90	90	90	1557
I ₂₅ Br ₇₅	9.70827	11.10062	13.70945	90	90	90	1477
Br	9.56618	10.92152	13.57964	90	90	90	1419
Cl ₂₅ Br ₇₅	9.41863	10.79131	13.42943	90	90	90	1364
Cl ₅₀ Br ₅₀	9.35090	10.68736	13.27232	90	90	90	1326
Cl ₇₅ Br ₂₅	9.28622	10.59379	13.22188	90	90	90	1300
Cl	15.42572	8.74765	8.67929	90	90	90	1171

By exposing these powders to air during 2 – 3 days, a change in their appearance is observed (see **Figure 3.5**). For the chloride sample, we see a change in color to yellow-

light green similar to that of Cu(II) chlorides in solution $[\text{CuCl}_4]^{2-}$,¹⁰⁹ a consequence of oxidation in the presence of moisture. Interestingly, the XRD pattern shows significant differences after air exposure (see **Figure 3.6**), which means that oxidation of the material affects the whole (“bulk”) sample. In the case of bromide, we see a change of color similar to that of copper(II) bromides in solution (purple), pointing again toward oxidation by moisture and the formation of $[\text{CuBr}_4]^{2-}$.^{110,111} Nonetheless, for this compound, it seems that the oxidation is only superficial, as no differences are observed by XRD (**Figure 3.6**). In the case of the iodide analogs, we do not observe any difference, which agrees with the very low stability of Cu(II) iodide compounds.^{112,113}

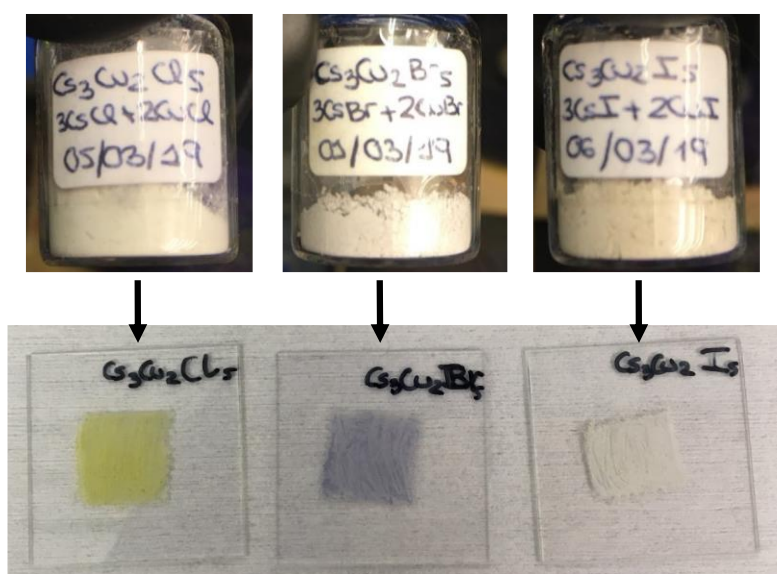


Figure 3.5. Comparison of the colour of the powders for $\text{Cs}_3\text{Cu}_2\text{X}_5$ when they are kept inside a nitrogen filled glovebox (up) and when they are exposed to air and moisture for 24 h (down).

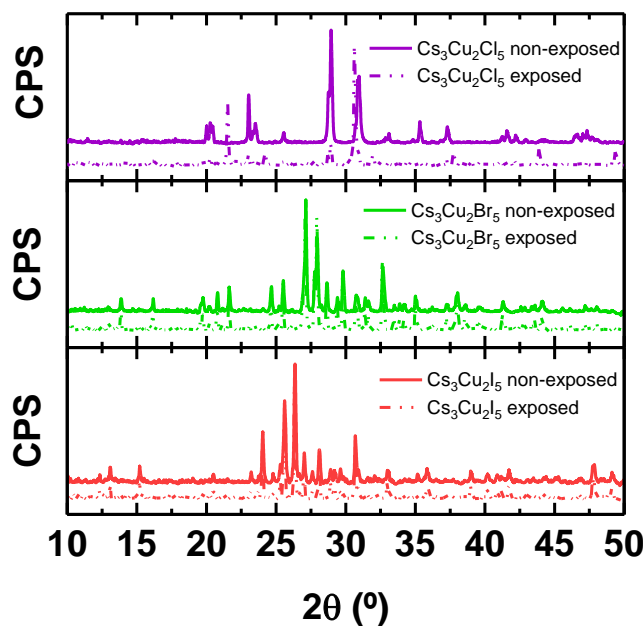


Figure 3.6. XRD of the as-prepared powders from ball milling synthesis for pure-halide $\text{Cs}_3\text{Cu}_2\text{X}_5$ compounds. Non-exposed to air powders are presented with a straight line and the exposed ones, with a dashed line.

The reason for the different reactivity against oxygen and moisture of these copper(I) halides is found in the strength of the atomic bonds and the redox potentials. For the whole halide series (Cl, Br and I), there is a well-known trend in stability in aqueous solution as follows: $\text{CuCl} < \text{CuBr} < \text{CuI}$.^{113,114} On the one hand, copper(I) is considered a soft acceptor ion that possesses a large number of *d*-electrons that can be easily dislocated, that is, it shows high polarizability. Consequently, copper(I) forms more favourably covalent bonds.¹¹⁵ The covalent character of the bond is thus strengthened when the most polarizable specie is bonded to copper(I). For the studied halides, iodide presents the highest polarizability of the three and is the most stable halide specie, being the breakage of the $\text{Cu}^{\text{I}}\text{-X}$ bond less favoured in the order $\text{I} < \text{Br} < \text{Cl}$.^{113,114} On the other hand, the redox potentials of the three halides show an increasing trend in the oxidizing character when going from iodide (0.54 V) to bromide (1.09 V) and to chloride (1.39 V), having Cl^- the highest redox potential of them. Thus, the oxidation of copper(I) to copper(II) is favoured in the case of the chloride species and less so for the iodide.¹¹⁶ The combination of these two factors makes the copper(I) chloride-containing specie the most sensitive species of the three to oxygen and moisture, being affected even in the bulk

(**Figure 3.6**). In contrast, the bromide form is only oxidized on the surface, whereas the iodide species is not at all affected.

To further confirm these observations, we carried out X-ray Photoelectron Spectroscopy (XPS) (**Figure S23**). While the Cu $2p$ spectra (**Figure S23a**) of $\text{Cs}_3\text{Cu}_2\text{Br}_5$ and $\text{Cs}_3\text{Cu}_2\text{I}_5$ show only a doublet for Cu $2p_{3/2}$ and Cu $2p_{1/2}$ peaks at binding energies (BEs) of 931.9 eV and 951.8 eV attributed to Cu(I), secondary high-BE peaks 933.9 eV and 953.8 eV are observed in $\text{Cs}_3\text{Cu}_2\text{Cl}_5$, which are ascribed to the oxidation of copper into Cu(II) species in this sample, as previously described.¹¹⁷ This is furthermore confirmed by the presence of strong satellite peaks around BE = 942 eV and BE = 962 eV, which is a clear sign of Cu(II).¹¹⁷

As for the 1D CsCu_2X_3 series, TGA of the pure-halide species was carried out. The thermal behavior was found to be similar to the 1D structures detailed above (see **Figure 3.7**). We observe again a weight increase in the chloride sample, which suggests oxidation of these compounds. This is also in line with the structural analysis and colour change discussed above, where we noted a more favored oxidation of the chloride samples. It must be noted, however, that all samples are stable until 250 °C, and even 350 °C (bromide) and 450 °C (iodide).

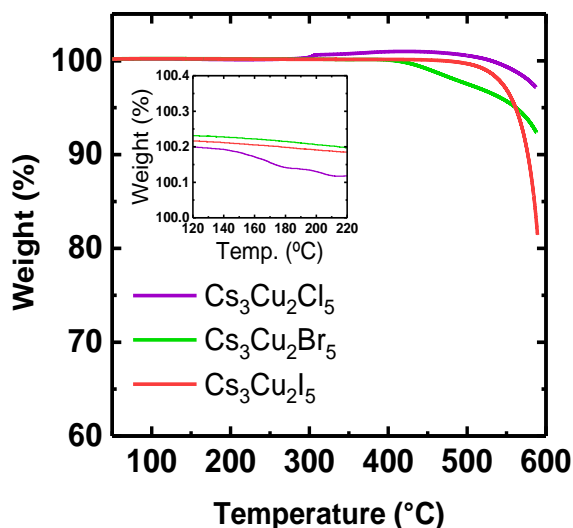


Figure 3.7. Thermogravimetric analysis (TGA) of the pure-halide $\text{Cs}_3\text{Cu}_2\text{X}_5$ compounds when they are kept inside a nitrogen filled glovebox. A special zoom is presented in the zone of first weight loss for chloride compound, which could correspond with the formation of Cu_2O .

Finally, we studied the optical properties of these materials (see **Figure 3.8**) by measuring the photoluminescence excitation (PLE) and emission (PL) spectra for the

whole $\text{Cs}_3\text{Cu}_2\text{X}_5$ series (see Experimental Section for further details). The wavelengths at the maximum PL intensity and corresponding PLQY for all samples are detailed in **Table 3.3** (note that the starting reagents do not show any noticeable PL under our measurement conditions as can be seen in **Figure S24**). Although the shifts in maximum excitation and emission wavelengths are not monotonic (see **Figure S26** for more details), there is an overall red-shift in the PL when decreasing the halide ionic radius (from I^- to Cl^-) together with a large Stokes shift (> 150 nm). This behavior is opposite to that observed from other MMHs such as LHPs or bismuth-based compounds.^{39,59,90,118,119} In fact, PL in those materials is a consequence of band-to-band radiative recombination, whereas for $\text{Cs}_3\text{Cu}_2\text{X}_5$ the PL originates from self-trapped excitons (STE) associated with a lattice deformation after the photoexcitation.^{90,120} STE efficiency depends, among others, on the structural distortion of the atomic framework and causes a large Stokes shift and a broad emission spectrum, as it is the case for these series.¹²¹ Upon photoexcitation, a reorganization of the excited state structure by Jahn-Teller distortion takes place. At the ground state, copper(I) shows a d^{10} closed-shell configuration with a favorable tetrahedral geometry (**Figure 3.1**) that becomes distorted in the excited state, after the formation of a $\text{Cu(II)-}d^9$ center.⁸⁹ This distortion elongates the bond on the z -axis while shortening the bond on the x - y -axis (**Figure 3.8a**).^{89,92} Thus, the Jahn-Teller effect contributes to the STE emission of $\text{Cs}_3\text{Cu}_2\text{X}_5$ and explains their unusual PL behavior (**Figure 3.8b**).^{120,121}

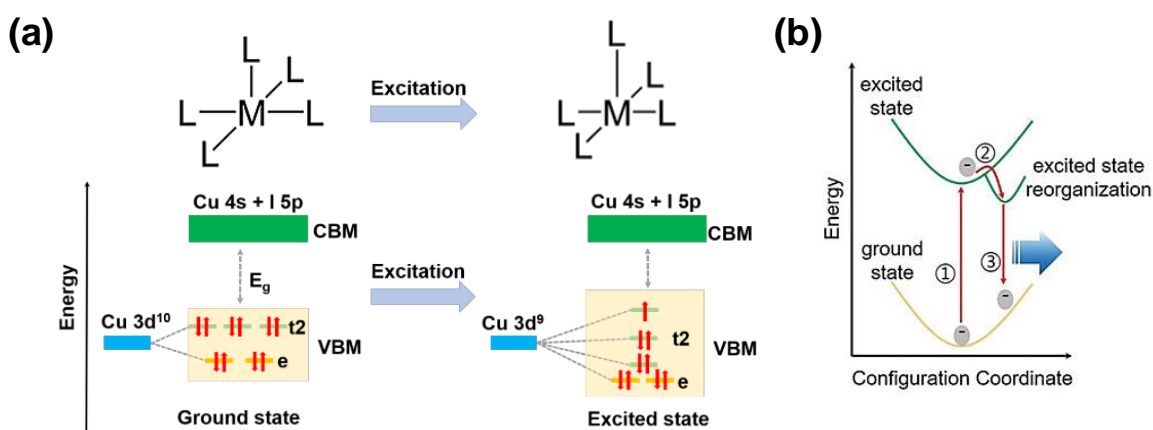


Figure 3.8. (a) Scheme of Jahn-Teller distortion on ground state and excited state of $\text{Cu(I)-}d^{10}$ and $\text{Cu(II)-}d^9$, respectively. Structure distortion for a generic ML_4 tetrahedral is shown. (b) Diagram for the STE formation on $\text{Cs}_3\text{Cu}_2\text{X}_5$. Pictures have been extracted from literature.⁸⁹

Furthermore, we observe markedly different optical features for Cl-rich compounds (75% and 100%), as compared to the rest of $\text{Cs}_3\text{Cu}_2\text{X}_5$ materials (**Figure 3.9**). Indeed, $\text{Cs}_3\text{Cu}_2\text{Cl}_5$ presents a significantly red-shifted PL spectrum with maximum emission wavelength around 516 nm (green), while iodide and bromide compounds typically show blue luminescence. This can be ascribed to the different crystalline phase of this compound as previously discussed (**Figure 3.2**). Interestingly $\text{Cs}_3\text{Cu}_2(\text{Cl}_{0.75}\text{Br}_{0.25})_5$ compounds exhibits dual excitation and emission properties (see solid and dashed lines in **Figure 3.9**) suggesting the coexistence of the *Cmcm* phase (as $\text{Cs}_3\text{Cu}_2\text{Cl}_5$) and *Pnma* phase (as $\text{Cs}_3\text{Cu}_2\text{Br}_5$). It is possible that this phase segregation is linked to halide segregation, though we were unable to elucidate this hypothesis.

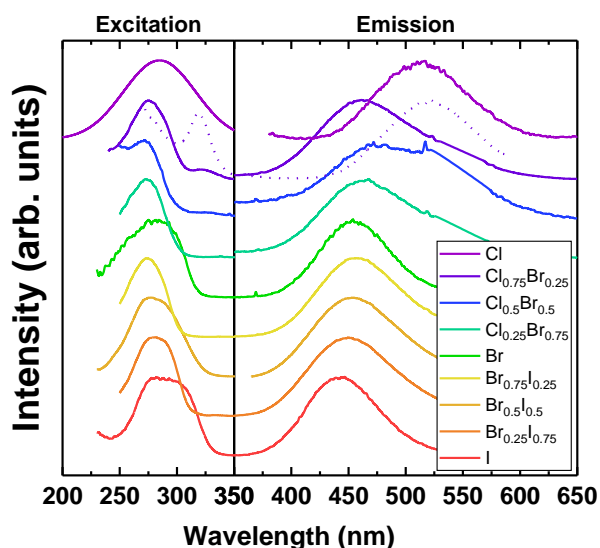


Figure 3.9. PLE (left) and PL (right) spectra of different $\text{Cs}_3\text{Cu}_2\text{X}_5$. X given in the legend. For $\text{Cs}_3\text{Cu}_2(\text{Cl}_{0.75}\text{Br}_{0.25})_5$ excitation spectrum corresponding to 516 nm emission and corresponding emission spectrum are presented as dashed lines, whereas excitation spectrum corresponding to emission at 450 nm and corresponding emission spectrum are presented as solid lines.

Table 3.3. PLQY and λ_{em} for $Cs_3Cu_2X_5$ compounds freshly prepared, exposed to air for 24 h, and thermally annealed. For mixed-halide compounds, as no benefit was observed for freshly prepared samples, stability in air or upon annealing was not assessed.

Compound	As-prepared		Air-exposed		Annealed	
	λ_{em} (nm)	PLQY (%)	λ_{em} (nm)	PLQY (%)	λ_{em} (nm)	PLQY (%)
$Cs_3Cu_2Cl_5$	516	78	528	3	525	81
$Cs_3Cu_2(Cl_{0.75}Br_{0.25})_5$	516	10	-	-	-	-
$Cs_3Cu_2(Cl_{0.5}Br_{0.5})_5$	470	3.6	-	-	-	-
$Cs_3Cu_2(Cl_{0.25}Br_{0.75})_5$	464	3.2	-	-	-	-
$Cs_3Cu_2Br_5$	455	14	456	3	457	19
$Cs_3Cu_2(Br_{0.75}I_{0.25})_5$	456	11	-	-	-	-
$Cs_3Cu_2(Br_{0.5}I_{0.5})_5$	452	15	-	-	-	-
$Cs_3Cu_2(Br_{0.25}I_{0.75})_5$	450	11	-	-	-	-
$Cs_3Cu_2I_5$	442	42	444	42	444	47

The PLQY of freshly-prepared pure-halides was found to be higher than that of all mixed-halide compounds (**Table 3.3**). Considering that the shift in the PL emission is minimal upon halide-mixing, no clear benefit (optical or structural) is obtained from mixed-compositions. Second, PLQY values of as-prepared pure-halide compounds are relatively high considering the simple synthesis conditions of dry ball-milling. Indeed, these values are comparable with those obtained from ligand-passivated quantum dots.⁹⁰ It is especially worth highlighting the high PLQY of 78% for $Cs_3Cu_2Cl_5$. We also observe that the PLQY of chloride and bromide compounds decreases significantly upon air exposure for 24h, while it is stable for $Cs_3Cu_2I_5$. This effect is ascribed to the moisture-induced oxidation discussed before (**Figures S21-S23**), which does not occur for copper iodide. Losses in PLQY from air-exposure of bromide and chloride samples can nevertheless be recovered by thermal annealing for 40 minutes at 170 °C, yielding PLQY values as high as 81% for $Cs_3Cu_2Cl_5$.

In view of the results and even though the chlorinated species is the most efficient in terms of PLQY, $Cs_3Cu_2I_5$ shows more promising optical features and stability than the others. Traditionally, highly efficient blue emitters have been difficult to prepare given

the large amount of energy required for the photon absorption and the possible presence of defect states within their bandgap that could suppress their emission.^{122,123}

In order to attempt to deposit it as thin film, as a first approach we dissolved the material in organic solvents and subsequently spin-coated it on a glass substrate followed by thermal annealing (see Experimental Section for details). The XRD pattern of spin-coated films show an excellent match with the reference ICSD pattern for bulk Cs₃Cu₂I₅ (**Figure S27**), suggesting that the structure is maintained upon thin film processing. Also, the PL signal centered at 438 nm (**Figure S28**) is very close to that of as-prepared bulk Cs₃Cu₂I₅ powders (**Table 3.3**). The blue luminescence is characterized by a PLQY of 19%, which is lower compared to that of the pristine bulk material. Although these results seem promising, it must be noted that dissolution of such inorganic metal halides in organic solvents is limited and as a result the film showed obvious inhomogeneities visible even to the naked eye (see **Figure S29**). Furthermore, using organic solvents for the thin film deposition partly defeats the purpose of using dry MCS for the original synthesis.

Therefore, we tested the deposition of Cs₃Cu₂I₅ by thermal single-source vacuum deposition. In short, as-synthesized powder materials are loaded in a ceramic crucible (source) inside a vacuum chamber. The source is then quickly heated to a high temperature by Joule effect causing the material to sublime and crystallize on the substrate, which is placed *ca.* 10 cm above the source (see Chapter 2 for details). No further thermal annealing or other post-deposition treatment is required. This method has previously been shown to be promising for the deposition of LHP thin films.^{65,97} The XRD signal of the film (**Figure 3.10a**) is well fitted considering the same space group as the bulk material. Interestingly, while all peaks present in the diffractogram of the film are present in the diffractogram of the powder sample (denoting that no impurity other than the expected Cs₃Cu₂I₅ phase is present) the reciprocal is not true (*i.e.*, several peaks present in the diffractogram of the powder sample are absent in the films'). Also, their relative intensities are varied. This, which is common for thin films of different compositions,¹²⁴ can be attributed to a preferential crystallographic orientation (crystallographic texture). The film thickness is measured to be 600 nm. Scanning Electron Microscopy (SEM) shows good homogeneity with grains of different sizes in the range of hundreds of nanometers (**Figure 3.10b**). The homogeneity can also be assessed by lower magnification images (**Figure S30**). Eventually, we note that the optical excitation and emission spectra of the thin film are nearly identical to the ones of

the starting bulk powders (**Figure 3.10c**). The PLQY of the vacuum-deposited film is 29%, higher than the film formed by solution-processing and close to the value of the starting material. Hence, it is evident that SSVD of mechanochemically-synthesized cesium copper halides leads to thin films of excellent morphology, crystallinity, and optical properties, paving the way to the implementation of these fully-dry approaches for low-toxicity optoelectronics.

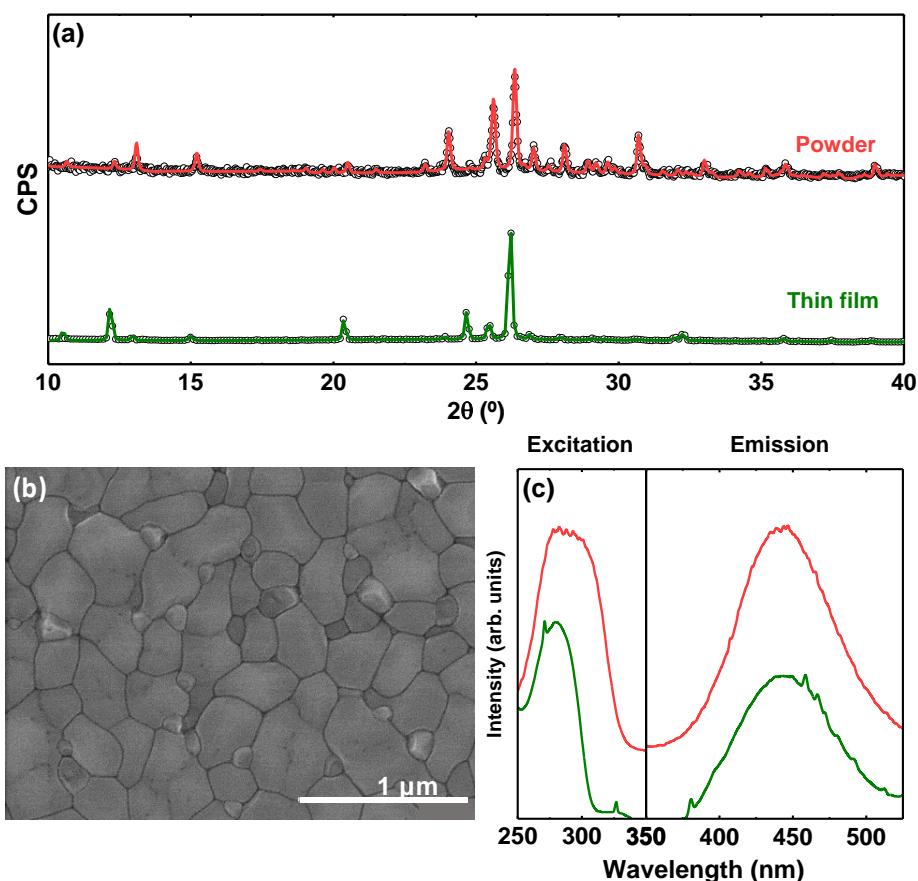


Figure 3.10. Characterization of SSVD $\text{Cs}_3\text{Cu}_2\text{I}_5$ thin film. (a) X-ray diffractogram with Le Bail fit in green. For an easy comparison, data and fit from bulk powder (see **Figure 3.4**) is reproduced here in red. (b) Scanning electron microscopy image. Scale bar is 1 micron (see lower magnifications in **Figure S30**). (c) Photoluminescence excitation and emission spectra in green. For an easy comparison, data from bulk powder (see **Figure 3.9**) is reproduced here in red.

3.4 Conclusions

In summary, we have demonstrated the synthesis of CsCu_2X_3 and $\text{Cs}_3\text{Cu}_2\text{X}_5$ ($\text{X} = \text{Cl}, \text{Br}, \text{I}$, and mixtures thereof) by simple solvent-free mechanochemistry. Pure-halide

Cs₃Cu₂X₅ compounds exhibit high PLQY in the blue-green region of the visible spectrum, making these very promising materials for lighting or deep-UV photodetectors. The green-emitting Cs₃Cu₂Cl₅ was synthesized with 78% PLQY (81% after air exposure and subsequent thermal annealing) albeit with poor stability in air. In contrast, the blue-emitting Cs₃Cu₂I₅ achieved stable PLQY exceeding 40% even when stored in air for several days. Differences in spectral features have been rationalized in terms of different crystalline structures as evidenced by the whole-pattern fitting of the XRD signal, while differences in air-stability can be explained by preferential oxidation mechanisms of Cu(I) halides to Cu(II) halides. Finally, we were able to process Cs₃Cu₂I₅ powders into homogeneous thin films by single-source vacuum deposition with excellent crystallinity and conserved optical features.

3.5 Author contribution and acknowledgments

In this chapter, Paz Sebastiá developed the main experiments (synthesis, spin-coating deposition and SSVD) and characterization steps, along with the writing of the manuscript. All the research was carried out at the Institute of Molecular Science (ICMol) of the University of Valencia.

The research leading to these results has received funding from the European Union Programme for Research and Innovation Horizon 2020 (2014-2020) under the Marie Skłodowska-Curie Grant Agreement PerovSAMs No. 747599), the Spanish Ministry of Science, Innovation and Universities (ex-MINECO) via the Unidad de Excelencia María de Maeztu MDM-2015-0538, MAT2017- 88821-R, and PCIN-2015-255, and the Generalitat Valenciana (Prometeo/2016/135). M.S. thanks the Spanish Ministry of Science Innovation and Universities (ex-MINECO) for his postdoctoral RyC contract. We acknowledge the European Union's Horizon 2020 research & innovation program under grant agreement No. 763977 of the PerTPV project. We thank Prof. Miguel Julve for fruitful discussions on the oxidation of copper halides.

Paz Sebastia-Luna, Javier Navarro-Alapont, Michele Sessolo, Francisco Palazon*, and Henk J. Bolink. Solvent-Free Synthesis and Thin-Film Deposition of Cesium Copper Halides with Bright Blue Photoluminescence. *Chemistry of Materials*, **2019**, *31*, 24, 10205–10210.

Chapter 4

Tuning the Optical Absorption of Sn-, Ge-, and Zn-Substituted $\text{Cs}_2\text{AgBiBr}_6$ Double Perovskites: Structural and Electronic Effects

*“Ese cristalito roto
Yo sentí como crujía
Antes de caerse al suelo
Ya sabía que se rompía.”*
Rosalía

Lead-free halide double perovskites (DPs) are highly tunable materials in terms of chemical composition and optical properties. One of the most widely reported DPs is $\text{Cs}_2\text{AgBiBr}_6$, which is envisaged as a promising absorber for photovoltaics. Nevertheless, its bandgap energy (around 1.9 – 2.3 eV) remains too large for common tandem solar cells. In this chapter, we report the mechanochemical synthesis of Sn-, Ge-, and Zn-substituted $\text{Cs}_2\text{AgBiBr}_6$ in powder form, whose bandgaps energies reach 1.55, 1.80, and 2.02 eV, respectively. These differences are rationalized through density functional theory (DFT)* calculations, demonstrating combined electronic and structural (disorder) effects introduced by the divalent metal cation substituents. Finally, we present the first vacuum-deposited thin films of the Sn-substituted DP, which also show a notable narrowing of the bandgap, and thus paves the way towards its implementation in photovoltaic solar cells.

**See Section 4.5 for author contributions.*

Reference:

Paz Sebastián-Luna, Joaquín Calbo, Nicolás Albiach-Sebastián, Michele Sessolo, Francisco Palazón, Enrique Ortí, Henk J Bolink. Tuning the Optical Absorption of Sn-, Ge-, and Zn-Substituted $\text{Cs}_2\text{AgBiBr}_6$ Double Perovskites: Structural and Electronic Effects. *Chemistry of Materials*, **2021**, 33, 20, 8028-8035.

The content of this chapter was reproduced with permission from Chemistry of Materials. Full published paper and Supporting Information are attached at Appendix B.

4.1 Introduction

Lead halide perovskites (LHPs), promising materials for future photovoltaics and other optoelectronic applications, follow the general formula $APbX_3$, where A stands for a monovalent cation (*e.g.* Cs^+ , $CH_3NH_3^+$, or $CH(NH_2)_2^+$) and X is a halide anion such as Cl^- , Br^- , or I^- (see Chapter 1 for more information). Despite the well-documented performances of lead-halide perovskite-based optoelectronics,^{125,126} the toxicity of Pb^{2+} ions hinders the widespread application of these materials.¹²⁷ By substituting $Pb(II)$ with a combination of $B(I)$ and $B(III)$ cations, while maintaining the same anion framework (see **Figure 4.1**), double perovskites (DPs) can be readily formed.

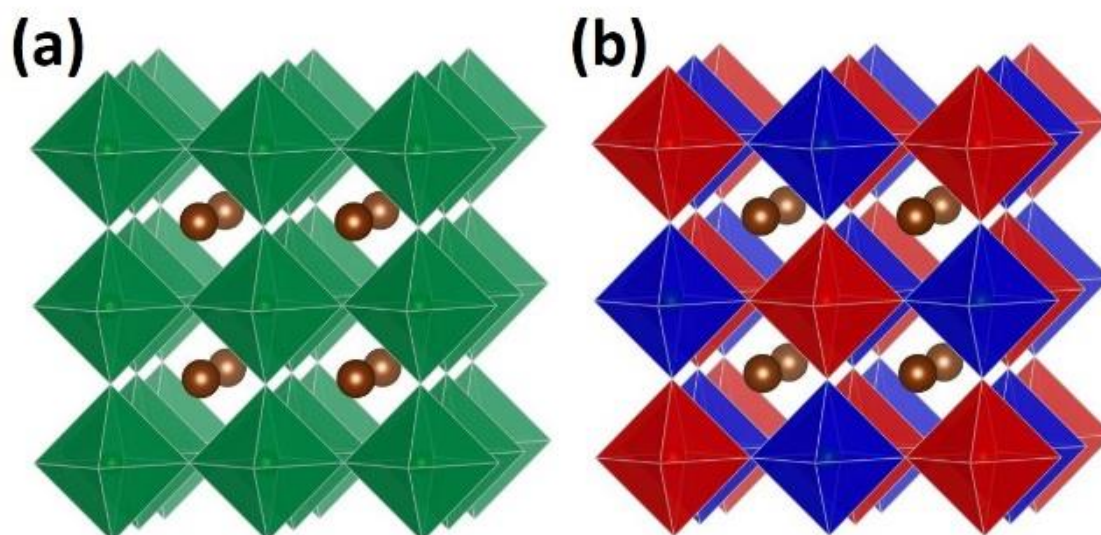


Figure 4.1. Comparison between the cubic structures of a perovskite $AB^{2+}X_3$ (a) and a double perovskite $A_2B^+B^{3+}X_6$ (b).

Halide double perovskites offer a wide range of properties that can compete directly with those of LHPs, such as their longer recombination lifetime at room temperature, higher heat and moisture stability, and lower toxicity.¹²⁸ Their chemical formula $A_2B^+B^{3+}X_6$, containing one monovalent (B^+) and one trivalent (B^{3+}) cation, shows the large variety of different atomic combinations that can be formed with this stoichiometry. $Cs_2NaInCl_6$, Cs_2KInCl_6 , $Cs_2AgInCl_6$, $Cs_2AgSbCl_6$, or $Cs_2NaBiCl_6$ are just a few examples of reported stable DPs.¹²⁹ Nevertheless, these chloride DPs typically have bandgap energies above 2.5 eV, which is too large for photovoltaic applications.¹³⁰ In this work, we focus on the double perovskite $Cs_2AgBiBr_6$, with an indirect bandgap of

1.95 eV, which is closer to a useful value in applications as wide-bandgap absorber in tandem devices.¹²⁸ Indeed, its performance in solar cells has been studied in literature, but the maximum reported power conversion efficiency (PCE) is only 2.84% with a maximum photocurrent on the order of 5 mA cm⁻².¹³¹ It has been suggested that this may be overcome by the use of thicker films to increase absorption.¹³² However, Cs₂AgBiBr₆ films have been reported to have a limited charge diffusion length, which in turn limits the performance of such thicker films as photovoltaic absorbers.¹³²

A more efficient absorption of visible light (through bandgap narrowing) is required to ensure future applications in photovoltaics of double perovskites. Partial B-site substitutions have been reported as a strategical route to tackle this issue. Karunadasa and coworkers have demonstrated a bandgap narrowing of *ca.* 0.5 eV by using monovalent and divalent cations with the same ns² electronic configuration as Bi(III), namely Tl(I) and Sn(II), altogether with an induced change in the bandgap nature from indirect to direct.^{133,134} Nevertheless, the addition of the highly-toxic Tl element, along with the slow solution-process synthesis and the lack of a clear substitution mechanism, could hinder the further development of this B-site substitution. Mitzi and co-workers also found a decrease in bandgap energy of around 0.3 eV by the addition of Sb(III), another element with an ns² valence electron configuration.¹³⁵ In contrast, addition of In(III), with a different electronic configuration (nd¹⁰, same as Ag(I)), was found to widen the bandgap.¹³⁵ From these results, a phenomenological rule seems to suggest that ns²-electronic-configuration substituents (Tl⁺, Sn²⁺, Sb³⁺) cause a decrease of the bandgap of Cs₂AgBiBr₆, while nd¹⁰ substituents lead to a bandgap increase. This observation led us to attempt such bandgap-tuning through simpler and faster synthetic methods,⁵⁸ along with the introduction of new substituents not previously reported experimentally, in particular Ge²⁺ and Zn²⁺, with ns² and nd¹⁰ electronic configurations, respectively.

Herein, we report the rapid dry mechanochemical synthesis of Sn²⁺, Ge²⁺, and Zn²⁺-substituted Cs₂AgBiBr₆, and their optical and structural characterization. Note that electronic levels directly introduced by the dopants might not be the only effect at play in tuning the absorption of Cs₂AgBiBr₆ (the term dopant is used herein in the general sense of substituent or additive, without any *a priori* implication on the concentration of free charges or the position of the Fermi level within the bandgap). Indeed, theoretical studies have shown that the degree of order or disorder in the structure, that is, the precise alternation of [AgBr₆]⁵⁻ and [BiBr₆]³⁻ octahedra or in contrast the existence of segregated [AgBr₆]⁵⁻ and [BiBr₆]³⁻ domains, can have a large influence on the bandgap. In particular,

Yang *et al.*¹³⁶ calculated that the bandgap energy may shrink from 1.93 eV for the fully-ordered structure (*i.e.*, perfectly alternating Ag and Bi) to only 0.44 eV for the fully-disordered one (*i.e.*, random distribution of Ag and Bi –not fully segregated–), with intermediate values closer to those experimentally observed for a partially-disordered structure. Furthermore, they showed that the addition of dopants led to a lower formation energy difference between the ordered and disordered structures. In other words, the lower bandgap observed for doped- $\text{Cs}_2\text{AgBiBr}_6$ could be not only directly linked to electronic effects as previously described but also to an increased disorder in the structure.

Hence, in order to rationalize the experimental results obtained with Sn(II), Ge(II), and Zn(II) additives, theoretical calculations are performed. Our results confirm a favorable neighboring substitution of the B-site doping cations, resulting in a bandgap reduction in going from referable $\text{Cs}_2\text{AgBiBr}_6$ to Ge^{2+} -doped and to Sn^{2+} -doped analogues. The mixing of the frontier occupied and unoccupied B^{2+} dopant orbitals in the valence and conduction band, respectively, accounts for a change in the electronic dimensionality of the double perovskite, which, together with structural octahedral deformations, leads to an indirect-direct transition of the bandgap.

Finally, Sn-based alloys are deposited as thin films by single-source vacuum deposition with different substituent loadings. We demonstrate thus the first DP thin films with increased visible absorption, which paves the way towards their implementation in photovoltaics and other thin-film based optoelectronic applications.

4.2 Experimental section

Materials

Cesium bromide (CsBr , > 99 %) was purchased from TCI. Bismuth bromide (BiBr_3 , $\geq 98\%$), and zinc bromide (ZnBr_2 , 99.999%) were purchased from Sigma-Aldrich. Silver bromide (AgBr , > 99.998%) and tin(II) bromide (SnBr_2 , > 99.2%) were purchased from Alfa Aesar. Germanium(II) bromide (GeBr_2) was purchased from Biosynth. All chemicals were stored in a nitrogen-filled glovebox and used as received without further purification.

Mechanochemical synthesis

An experimental procedure similar to that reported in literature was followed.¹³⁷ Binary precursor salts (CsBr, AgBr, BiBr₃ as well as dopants SnBr₂, GeBr₂, and ZnBr₂) were introduced inside a 10 mL zirconia ball-mill jars with 2 zirconia beads of 10 mm in diameter. Powders were maintained in inert atmosphere since the jars were closed inside a nitrogen-filled glovebox. Ball-milling (BM) was performed with a MM-400 shaking ball-mill from Retsch, at a frequency of 30 Hz for 1 h and 5 h. Pure DP was synthesized from stoichiometric amounts of CsBr, AgBr, and BiBr₃. For the doped samples, calculations were made considering 1 mol of pure-DP as the basis; that is, *e.g.* for the 15%-doped samples, 0.15 mol of the dopant was added to 1 mol of Cs₂AgBiBr₆ (molar ratio 1:0.15).

Thin-film deposition by single-source vacuum deposition (SSVD)

In a typical deposition, an alumina thermal crucible (Creaphys GmbH) is placed inside a vacuum chamber and loaded with 350 mg of the as-synthesized Cs₂AgBiBr₆ powder (referred to as “BM DPP”, where “*p*” stands for pristine, as opposed to doped). Then, the chamber was evacuated to a pressure of 8×10^{-6} mbar and the source is rapidly heated to 550 °C. The deposition is stopped after the complete evaporation of the solid. An average film thickness of 550 nm is deposited, as measured with a mechanical profilometer.

For doped samples, three different starting powders were tested. On the one hand, the mechanochemically-synthesized 15% SnBr₂-doped double perovskite powder was used (BM DP:15% SnBr₂). On the other hand, for the other compositions, an extra amount of dopant is added and hand mixed with the ball-milled double perovskite powder, *i.e.*, 1 mol of the dopant was hand-mixed inside the evaporation crucible with 0.15 (or 1) mol of DP; the molar ratio is 1:0.15 (or 1:1) Cs₂AgBiBr₆:dopant. They are referred to in the text as “BM DPP+15% SnBr₂” or “BM DPP+100% SnBr₂”, respectively.

XRD characterization

X-ray diffraction was measured with a powder diffractometer Empyrean from Panalytical equipped with CuK α anode operated at 45 kV and 40 mA. Single scans were acquired in the $2\theta = 8$ to 60° range with a step size of $2\theta = 0.025^\circ$ in Bragg-Brentano geometry in air.

Optical characterization

UV-visible absorption spectra of the films and powders were collected using an integrating sphere coupled to an Avantes Avaspec-2048L optical detector (Avantes BV).

Scanning Electron Microscopy (SEM)

SEM images were acquired using a Phenom XL G2 Microscope from Thermo Fisher, operating at an acceleration voltage of 10 kV.

Theoretical calculations

Theoretical calculations were performed using the Density Functional Theory framework in three-dimensional periodic conditions. The starting crystal structure for Cs₂AgBiBr₆ double perovskite was extracted from Materials Project with a cubic crystal system and $Fm\bar{3}m$ space group.¹³⁸ Primitive, conventional, and $2 \times 2 \times 2$ lattices were considered in the calculations. In the $2 \times 2 \times 2$ supercell system, subsequent B-site cation substitutions of $\frac{1}{8}$ Ag⁺ and $\frac{1}{8}$ Bi³⁺ by $\frac{1}{4}$ Sn²⁺/Ge²⁺/Zn²⁺ (14% doping concentration) were performed. Minimum-energy crystal structures were obtained by full ion and lattice relaxation at the GGA PBEsol level of theory using a tier-1 numerical atomic orbital (NAO) basis set without applying any symmetry constraints. Sampling k-point grid was set to $6 \times 6 \times 6$, $4 \times 4 \times 4$, and $2 \times 2 \times 2$ for the primitive, conventional, and supercell lattices, respectively. Single-point calculations were further performed at the hybrid HSE06/tier-1 level of theory on the previously GGA PBEsol-optimized crystal structures to obtain the accurate band structures, projected density of states, and bandgap predictions. A general L – Γ – X k-path and k-grids up to $8 \times 8 \times 8$ for primitive, $4 \times 4 \times 4$

for conventional, and $3 \times 3 \times 3$ for supercell lattices were selected to explore the first Brillouin zone of the reciprocal space. Relativistic effects were considered by using the atomic ZORA approximation.¹³⁹ Crystal structure and frontier crystal orbital representations were done through the VESTA software.¹⁴⁰ All the calculations were performed by means of the efficient, accurate all-electron, full-potential electronic structure FHI-AIMS code package.¹³⁹

4.3 Results and discussion

Mechanochemical synthesis of $\text{Cs}_2\text{AgBiBr}_6$ is carried out as described elsewhere.¹³⁷ In short, inside a nitrogen-filled glovebox, a stoichiometric amount of CsBr, AgBr and BiBr_3 is introduced inside a 10 mL zirconia ball-mill jar with two zirconia beads of 10 mm in diameter. The jars are sealed in nitrogen (see the Experimental Section and Chapter 2 for more details). After 1 h of grinding, the as-synthesized powder is nearly phase-pure $\text{Cs}_2\text{AgBiBr}_6$ (**Figure 4.2a**) with a bandgap energy (E_g) of 1.94 eV (**Figure 4.2b**). This value is in general agreement with previous literature reports, which present a considerable scattering in values around 1.7 – 2.3 eV (with most references reporting values in the 2.0 – 2.2 eV range).^{128,134,135,141–144} This mismatch of bandgap values for the $\text{Cs}_2\text{AgBiBr}_6$ double perovskite in literature was previously noticed and studied by Yang and co-workers.¹³⁶ Their first-principles calculations point towards the different arrangement of Ag^+ and Bi^{3+} ions as the cause of the bandgap variation. By introducing different levels of cation disorder on the sub-lattice of Ag-Bi, the band alignment of the whole structure is modified, going from a wider indirect bandgap for the highly-ordered structure to a narrower direct bandgap for the disordered cation substructure. The ordering of the structure may be tuned by synthetic conditions.^{144,145} Herein, the rapid dry ball-milling mechanochemical approach employed is hypothesized to lead to a partially-disordered structure, according to the relatively low bandgap value of 1.94 eV with regards to most experimental reports.

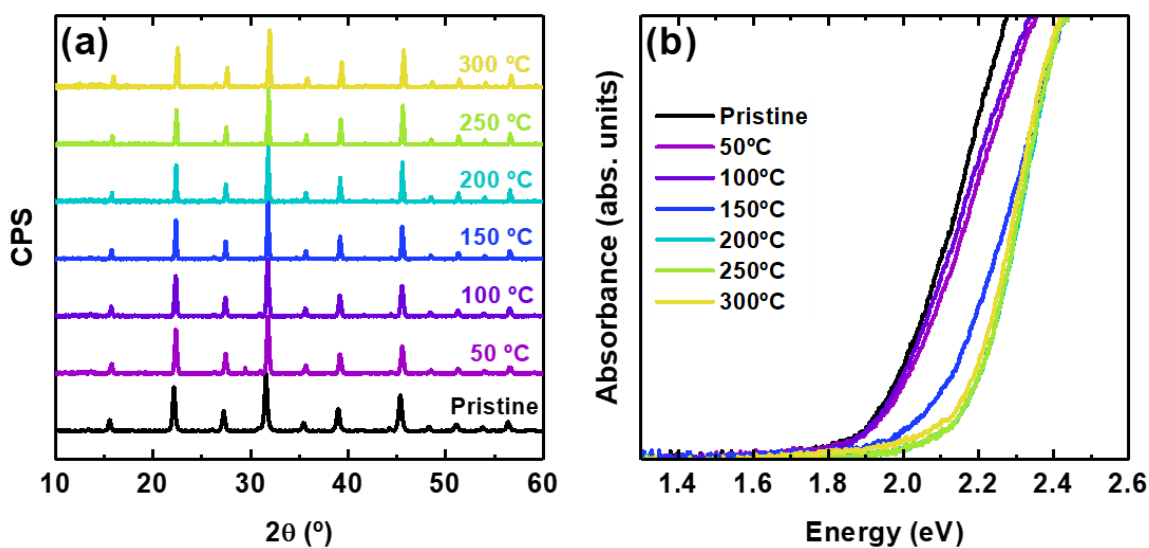


Figure 4.2. XRD diffractograms of $\text{Cs}_2\text{AgBiBr}_6$ samples after post-synthesis annealing at different temperatures (a), and UV-Vis absorption onset to estimate the bandgap (b).

When the as-synthesized powders are thermally annealed at different temperatures for 15 minutes, the absorption edge is found to blue-shift by up to 250 meV (**Figure 4.2b**). These results suggest that, as the annealing temperature increases, the double-perovskite structure undergoes a conversion from a less-ordered structure towards a higher-ordered arrangement of the cations. These changes, which are likely to occur at the atomic scale, are not detectable by X-ray diffraction within the limits of our instrumentation. In contrast, the similar diffraction pattern for all samples presented in **Figure 4.2a**, demonstrates the stability of the $\text{Cs}_2\text{AgBiBr}_6$ DP without any noticeable degradation into other binary or ternary phases.

These results highlight the fact that, without any alloying or doping with extrinsic elements, the bandgap of $\text{Cs}_2\text{AgBiBr}_6$ can be tuned by synthesis and post-synthesis conditions. Nevertheless, even after a long milling process of 5 h, it appears to be difficult to reach E_g values below approximately 1.8 eV (see **Figure 4.3**). Thus, in order to obtain lower bandgap energies, we focused on the incorporation of extra ions into the double perovskite structure. In this case, we incorporated Sn^{2+} , Ge^{2+} , and Zn^{2+} in the mechanochemical synthesis of $\text{Cs}_2\text{AgBiBr}_6$, and evaluated their effect on the optical absorption of the final compound.

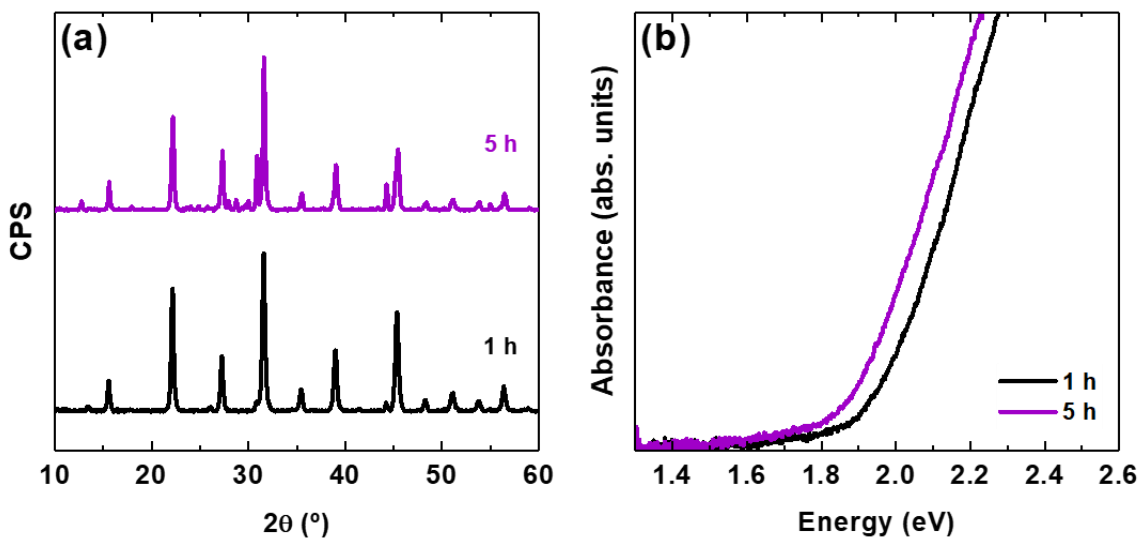


Figure 4.3. (a) XRD diffractograms of $\text{Cs}_2\text{AgBiBr}_6$ samples ball-milled during 1 h and 5 h. (b) UV-Vis absorption onset to estimate the bandgap.

In accordance to previous results with different additives,^{133–135} we observe a trend in the bandgap shift according to the electronic configuration of the additive (ns^2 for Sn^{2+} and Ge^{2+} or nd^{10} for Zn^{2+}), in view of the different onset of the UV-Vis absorption spectra presented in **Figure 4.4**. By incorporating small amounts of Sn(II) , the absorption of the double perovskite can be significantly red-shifted. Following the previously optimized procedure for the $\text{Cs}_2\text{AgBiBr}_6$ dry mechanochemical synthesis (see Experimental Section for more details), Sn is incorporated in the double perovskite structure and modifies its optical properties, as can be seen by the different colors of the powders (**Figure S2**). In **Figure 4.4a**, the red-shift in the UV-Vis absorption is clearly observed, reducing the bandgap energy from 1.94 eV for the pure-DP to 1.55 eV for the highly-substituted samples (see **Table S2**). It is worth mentioning that E_g have been extracted from the Tauc plot, since the direct linear extrapolation of the absorbance spectra may be misleading (**Figure 4.4d-f**). Frequently, doped materials show sub-band gap absorption states that might have a negative influence in the estimation of the bandgap directly from the UV-Vis spectra. In this case, a Tauc plot considering a direct allowed transition has been used to determine the bandgap energies. The choice of a direct transition is based on several reasons: (i) The Tauc plot of the pristine $\text{Cs}_2\text{AgBiBr}_6$ with an indirect transition gives rise to a similar bandgap value compared with the direct transition (**Figure S3**). (ii) For the doped species the Tauc plot considering an indirect transition does not show the expected linear behavior (**Figure S3**), which can be

considered as experimental evidence of a direct bandgap. (iii) As it will be discussed below, theoretical calculations confirm not only the reduction in the bandgap but also the transition from indirect to direct upon doping.

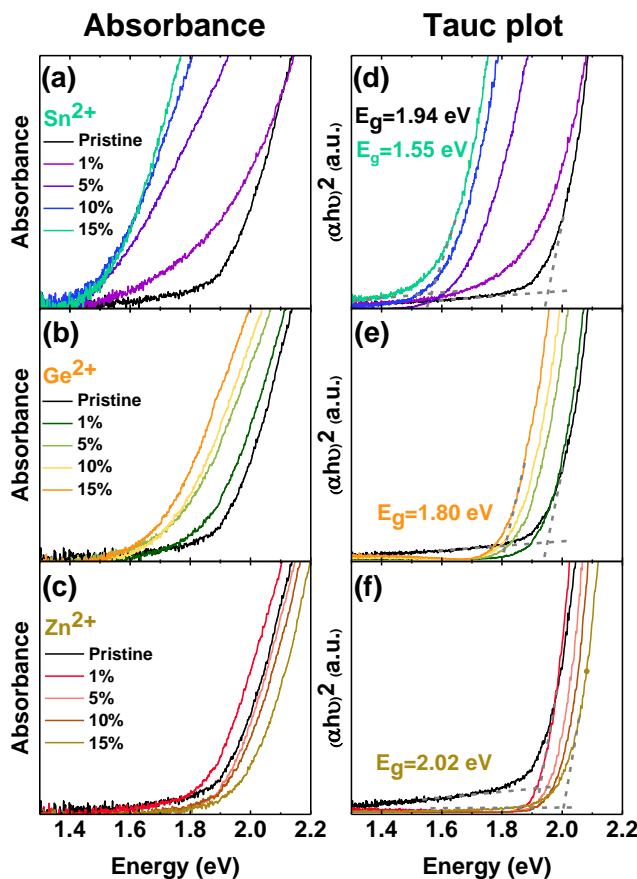


Figure 4.4. UV-Vis absorption onset to estimate the bandgap of SnBr₂- (a), GeBr₂- (b), and ZnBr₂- (c) doped double perovskite. Panels (d, e, f) show the Tauc plot considering a direct allowed transition for the aforementioned dopants, respectively. The estimated bandgaps for the pristine and 15%-doped species are given.

In the same line, the addition of small amounts of Ge(II) also caused a red shift in the absorption of the double perovskite (**Figure 4.4b**). In this case, the bandgap modification is progressive and smoother than for Sn-substituted samples, reaching a bandgap of 1.80 eV (see **Figure 4.4e** and **Table S3**), ideal for the fabrication of tandem solar cells with silicon. This result is also in line with previous calculations where a large reduction in the bandgap was predicted by Sn(II) or Ge(II) doping.¹⁴⁶ On the other hand, when incorporating ZnBr₂, the absorption onset is slightly blue-shifted compared to Cs₂AgBiBr₆, and the bandgap increases to 2.02 eV for the sample with the highest ZnBr₂ incorporation (**Figure 4.4c** and **Table S4**).

Notwithstanding the changes in the optical properties, the final structure of the double perovskite is maintained after the incorporation of the additives, without noticeable byproduct phases or particular broadening/narrowing of the diffraction peaks in the XRD characterization (**Figures S4–S6**). On the contrary, the incorporation of Sn^{4+} and Ge^{4+} does not lead to a shift in the bandgap (**Figure S7**), suggesting that M(IV)-type cations do not enter the double perovskite structure, as the M(II)-type do. This was previously seen by others.¹³⁴

To gain more insight into the structural and electronic effects upon doping, we performed a series of theoretical calculations based on density functional theory. The reference double perovskite $\text{Cs}_2\text{AgBiBr}_6$ is predicted with an indirect bandgap of 2.15 eV (**Table S4**), in relatively good accord with the experimental value of 1.94 eV and with recently reported data.¹⁴⁶ The valence band maximum (VBM) is described mainly by the p orbitals of Br, whereas the conduction band minimum (CBM) is predominantly contributed by the p orbitals of Bi. A primitive unit cells was modeled to assess the effect of B-cation substitution in a 14% ratio (see Experimental Section for details), similar to the highest level of doping experimentally achieved (15%). We considered two doping motifs by substituting either neighboring or distant Ag^+ and Bi^{3+} atoms (**Figure 4.5** and **Table S5**).

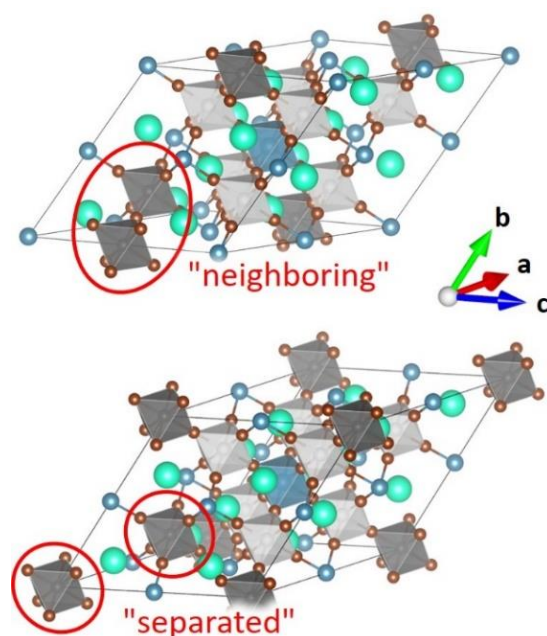


Figure 4.5. Cells with “neighboring” and “separated” B-cation substitutions in the double perovskite $\text{Cs}_2\text{Ag}_{(1-a)}\text{Bi}_{(1-a)}\text{X}_{2a}\text{Br}_6$ where $X = \text{Sn}, \text{Ge}, \text{Zn}$ and $a = \frac{1}{8}$. Color coding: Cs in light

green, Bi in dark blue (coordination octahedra are not shown for clarity), Br in brown, substituted B-cation octahedra in dark gray, and Ag-cation octahedra in light gray.

Theoretical calculations indicate that the “neighboring” substitution is preferred over the “separated” disposition, with energy differences of 0.07, 0.18, and 0.51 eV for Sn²⁺, Ge²⁺, and Zn²⁺ doping, respectively. These results are in good accord with a recent theoretical study in which the thermodynamic stability of Sn²⁺/Ge²⁺ B-cation substitution is assessed in the conventional unit cell of Cs₂AgBiBr₆.¹⁴⁶ With a focus on the most stable “neighboring” substituted double perovskites, band structure calculations on the cell show a significant decrease in the bandgap in going from pristine Cs₂AgBiBr₆ (2.13 eV) to Ge²⁺-doped (1.81 eV) and Sn²⁺-doped (1.63 eV) structures (**Figure 4.6**), in very good correlation with the experimental results. Although the major contribution to the VBM (Br-*p*) and CBM (Bi-*p*) does not change with respect to the reference Cs₂AgBiBr₆, the *s* and *p* orbitals of Sn and Ge significantly participate in the frontier bands of the doped material. Importantly, the nature of the bandgap changes from indirect to direct upon doping (**Figures S9** and **S11**), which can be explained by the mixing of the *s* orbital of the doping element (Sn or Ge) with the Br *p* orbital in the VBM, and of the Sn/Ge *p* orbital with the Bi *p* orbital in the CBM (**Figure 4.6**), in accord with previous suggestions.¹⁴⁶ Moreover, a significant distortion along with a tilting of the B-site octahedra is predicted upon doping (see **Figures S16** and **S17**). The reduction of the bandgap found experimentally and confirmed theoretically after ns² B-site doping therefore implies a significant geometry deformation accompanied by a change in the electronic dimensionality of the double perovskite, rather than a simple inclusion of frontier, discrete defect states by Sn²⁺ or Ge²⁺.¹⁴⁷

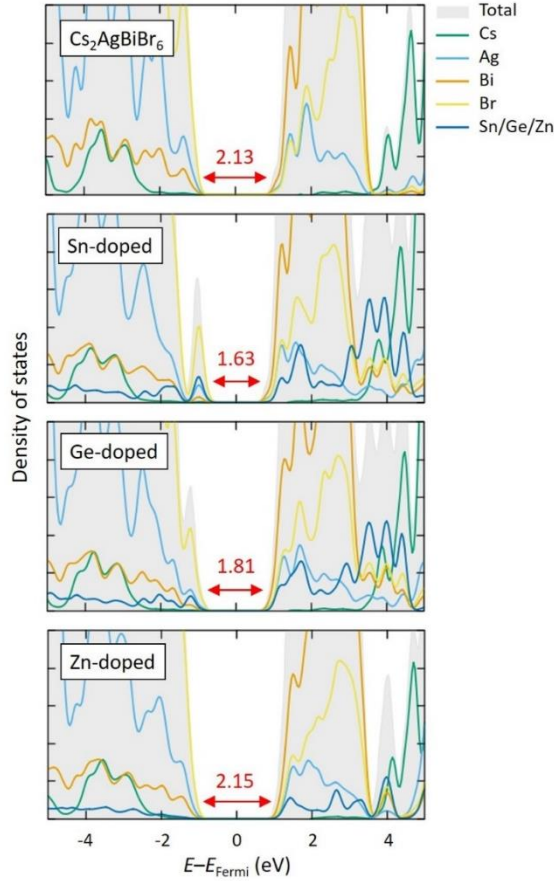


Figure 4.6. Atom-projected density of states calculated for the supercell of $\text{Cs}_2\text{AgBiBr}_6$ and its doped analogues. The bandgap is indicated in eV.

In contrast to ns^2 doping, $nd^{10} \text{Zn}^{2+}$ B-cation substitution leads to a negligible change in the bandgap (2.15 eV) with respect to $\text{Cs}_2\text{AgBiBr}_6$ (**Figure 4.6**). In this case, the relatively deep energy levels of $nd^{10} \text{Zn}^{2+}$ do not interact with the VBM, whose nature is described by the Br p and Ag d orbitals, as in the case of the undoped DP. The unoccupied Zn $4s^0$ orbitals are located slightly higher in energy from the CBM and weakly interact with the Bi p and Ag s orbitals. The Zn–Br distances are significantly distorted out of a perfect octahedron (**Figure S17**); however, this geometry deformation does not introduce frontier defect states within the bandgap.

Considering the experimental and theoretical results reported so far, Sn stands out as the best option to significantly reduce the bandgap of $\text{Cs}_2\text{AgBiBr}_6$. However, the implementation of these materials in most optoelectronic devices such as solar cells or light-emitting diodes requires their deposition as thin films. Single-source vacuum deposition (SSVD) has been demonstrated to be a fast and reproducible method compatible with a wide range of materials for obtaining thin, smooth, and homogeneous

films.^{28,65,148,149} In this technique, the presynthesized powder materials are placed inside a ceramic crucible in a vacuum chamber. When the crucible is heated at a prefixed temperature under high-vacuum conditions, the materials sublime and deposit on top of a substrate, placed right above the material source. Eventually, thin films with the same composition as the starting materials are deposited onto the substrates (see Chapter 2 for further information).

To the best of our knowledge, SSVD has been employed successfully by others to deposit pure, wide-bandgap, $\text{Cs}_2\text{AgBiBr}_6$, but it has never been used to prepare thin films of the doped, low-bandgap compositions.^{69,150} We first optimized the conditions for the deposition of the undoped DP presynthesized by dry ball-milling (see Experimental Section for further details). As-deposited films do not show the expected diffractogram and optical absorption of $\text{Cs}_2\text{AgBiBr}_6$ (**Figure 4.7**). Similar to what was described in previous reports, we also observed that the as-prepared films presented XRD peaks corresponding to undesirable side phases such as $\text{Cs}_3\text{Bi}_2\text{Br}_9$, with a preferential orientation along the *c*-axis as one can see by the main peaks at $2\theta = 8.7^\circ$ and 26.3° corresponding to the (001) and (003) planes, respectively (**Figure 4.7a**).^{69,151} This is also in accordance with the observed wide bandgap (**Figure 4.7b**).

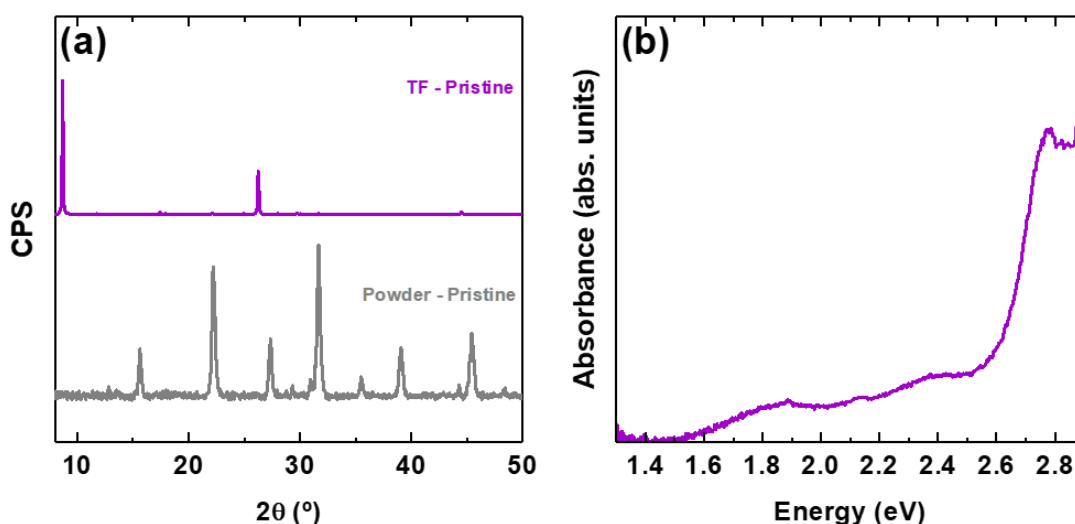


Figure 4.7. XRD diffractogram (a) and absorbance (b) of SSVD thin film (TF) as-deposited $\text{Cs}_2\text{AgBiBr}_6$ (without annealing), showing a predominance of $\text{Cs}_3\text{Bi}_2\text{Br}_9$ phase. More details in the main text.

After being annealed at a high temperature (250°C), these unwanted byproducts vanish to yield the expected $\text{Cs}_2\text{AgBiBr}_6$ phase (**Figure 4.8a**; black diffractogram termed

“BM DPp”). This transformation is also linked to important changes in morphology, as observed by SEM (**Figure 4.8c,d**). The as-deposited film shows a heterogeneous morphology with anisotropic domains of different sizes. After annealing, the morphology becomes much more homogeneous, with close-packed grains or domains ~ 500 nm in typical size. High-resolution X-ray photoelectron spectra of Cs $3d$, Ag $3d$, Bi $4f$, and Br $3d$ signals are presented in **Figure S20**. Quantitative analysis of the thin film, based on these spectra, yields atomic percentages of 20.3%, 10.4%, 9.2%, and 60.1% for Cs, Ag, Bi, and Br, respectively. This highlights the nearly stoichiometric transfer of the preformed $\text{Cs}_2\text{AgBiBr}_6$ material by SSVD. Indeed, within instrumental and analysis error, the values are very close to the expected composition. Thin films of the pristine double perovskite present a E_g of 2.35 eV (**Figure 4.8b**), in agreement with previous reports of this material.^{152,153}

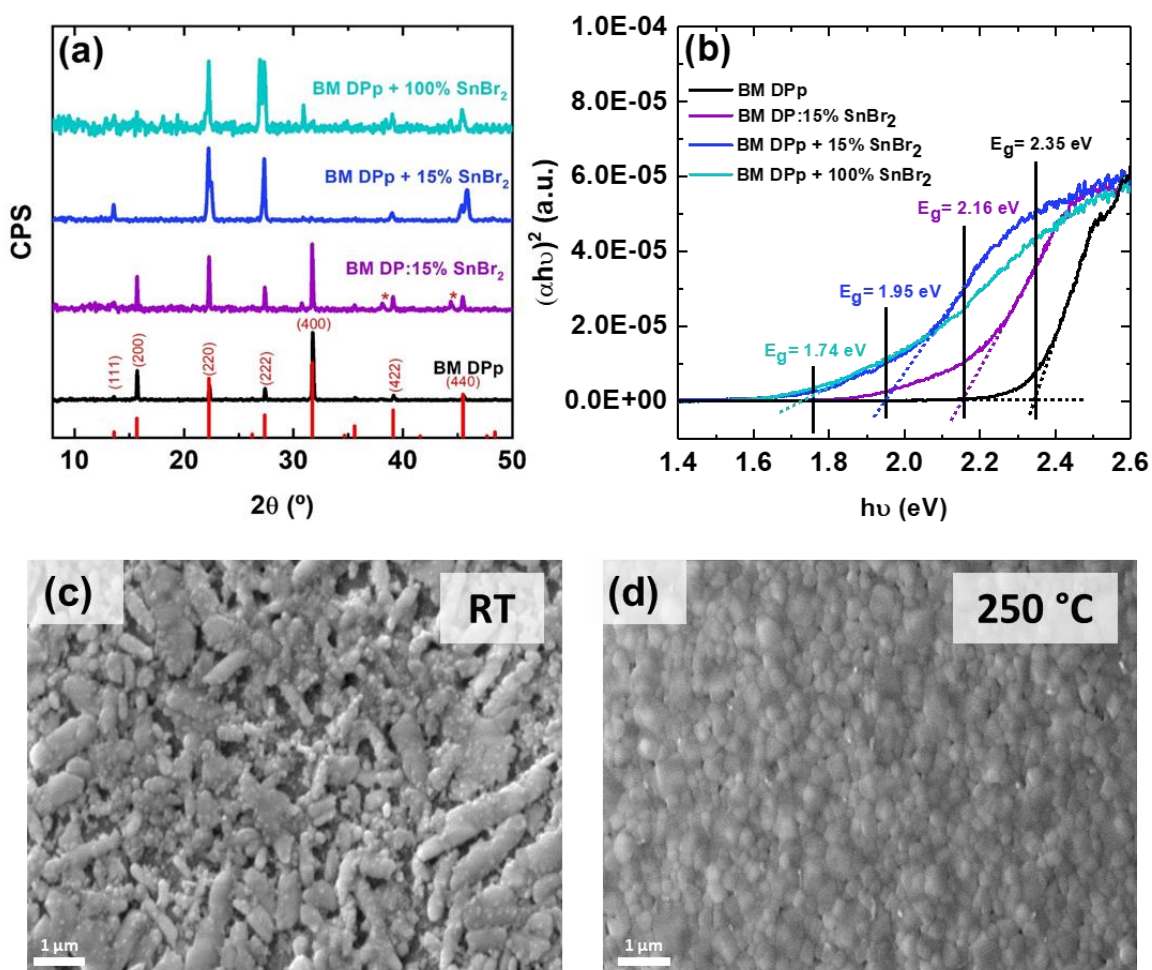


Figure 4.8. (a) XRD diffractograms of SSVD thin films of pristine and Sn-doped $\text{Cs}_2\text{AgBiBr}_6$ samples after annealing at 250 °C. Red asterisks indicate the interfering peaks from the Al

platform of the XRD setup. “BM DPp” refers to the deposition of pure ball-milled $\text{Cs}_2\text{AgBiBr}_6$; “BM DP:15% SnBr_2 ” to ball-milled doped $\text{Cs}_2\text{AgBiBr}_6$:15% SnBr_2 ; “BM DPp+15% SnBr_2 ” to pure ball-milled $\text{Cs}_2\text{AgBiBr}_6$ with an extra 15% of SnBr_2 added and manually mixed in the crucible; “BM DPp+100% SnBr_2 ” to pure ball-milled $\text{Cs}_2\text{AgBiBr}_6$ with an extra 100% of SnBr_2 added and manually mixed in the crucible. (b) Tauc plot of post-annealed Sn-doped thin-films considering a direct allowed transition. (c) SEM images of pristine DP thin-films at room temperature and (d) annealed at 250 °C (scale 1 μm).

Finally, we tested the SSVD of Sn-substituted DP. The SSVD of presynthesized 15% Sn-doped powder (DP:15% SnBr_2) after annealing at 250 °C led to a slight red-shift of the absorption onset in regard to the pristine composition (**Figure 4.8b** and **Figure S21**). Nevertheless, according to the XRD diffractograms, the overall structure is kept constant, following the same pattern as the annealed pure double perovskite thin films (**Figure 4.8a**).

To achieve thin films with a narrower bandgap, more SnBr_2 was added to the pure DP inside the evaporation crucible (this is, without previously ball-milling these mixtures), we explored two different ratios (see Experimental Section). When 15% SnBr_2 was added to the non-doped DP (DPp+15% SnBr_2), there is a further red-shift of the absorption onset of the thin films, achieving an E_g of 1.95 eV (**Figure 4.8b**). Elemental analysis derived from XPS (**Figure S22**) reveals that in both cases the molar fraction of Sn(II) present in the films is similar and around 5% (independent of whether 15% SnBr_2 is added before or after ball-milling). However, the bandgap shift is accompanied by changes in crystallinity (**Figure 4.8a**). Indeed, the diffractogram of this sample with SnBr_2 added during the evaporation corresponds to the expected $\text{Cs}_2\text{AgBiBr}_6$ double perovskite phase, albeit with a preferential orientation perpendicular to the (220) and (222) planes (see **Figure S23**). If the amount of SnBr_2 added is increased to a DP:Sn molar ratio of 1:1 (DPp+100% SnBr_2), a thin film with a 1.74 eV bandgap was obtained after annealing (**Figure 4.8b**) with a crystallinity similar to that of the 15% added film previously discussed (**Figure 4.8a**). Elemental and chemical analysis (**Figure S22**) shows that this drastic addition of 100% in the evaporation crucible leads to an increase in the tin atomic percentage to only 9.5%. Hence, it seems that the process is somehow limited and excess SnBr_2 is lost in the evaporation, not incorporated into the crystalline film. It is also worth mentioning that such an important addition of SnBr_2 leads to the formation of different Sn species, as evidenced by the secondary, low-binding

energy component in the XPS Sn $3d_{5/2}$ spectra (see **Figure S22**). These results demonstrate that it is possible to obtain homogeneous thin films with the double perovskite crystal structure of $\text{Cs}_2\text{AgBiBr}_6$ and a tunable bandgap through the insertion of tin bromide in a fully dry process.

4.4 Conclusions

We have studied the bandgap tuning of the $\text{Cs}_2\text{AgBiBr}_6$ double perovskite synthesized by solvent-free approaches through two different routes: (i) *via* postsynthesis thermal annealing and (ii) *via* the introduction of different dopants in the structure. The first method demonstrated that an increase in the annealing temperature leads to a widening of the bandgap, from 1.94 eV for the pristine form to 2.16 eV when annealing at 300 °C. The reason for this phenomenon may reside in the increase in the Ag–Bi lattice ordering upon annealing, which triggers an increase in the bandgap of the double perovskite. In contrast, the incorporation of SnBr_2 and GeBr_2 into the DP yielded a remarkable red-shift in the absorption onset (1.55 and 1.80 eV, respectively). The addition of ZnBr_2 , instead, induced a slight increase in the bandgap. The underlying reason for these changes was studied through density functional theory calculations, indicating that Sn^{2+} and Ge^{2+} change the electronic dimensionality of the double perovskite by mixing their occupied *s* orbitals in the VBM and their unoccupied *p* orbitals in the CBM. This, in combination with structural octahedral deformations, leads to a significant reduction of the bandgap, in agreement with the experimental results, and to an indirect-to-direct transition in the nature of the gap. Finally, Sn-doped DP thin films were deposited by single-source vacuum deposition. Different dopant concentrations were studied, revealing the possibility of tuning the absorption properties in thin films. These results pave the way to the implementation of cation-substituted $\text{Cs}_2\text{AgBiBr}_6$ thin films in next-generation optoelectronic devices.

4.5 Author contribution and acknowledgments

In this chapter, Paz Sebastián developed the synthesis, SSVD and characterization steps of the double perovskite powders and films, along with the writing of the

manuscript. Theoretical calculations and modelling were carried out by Dr. Joaquín Calbo and Prof. Enrique Ortí. All the research was performed at the Institute of Molecular Science (ICMol) of the University of Valencia.

The research leading to these results has received funding from the Spanish Ministry of Science and Innovation and European Feder Funds (Projects PGC2018-099568-B-I00, PID2020-119748GA-I00, PCI2019-111829-2, and CEX2019-000919-M) and the Generalitat Valenciana (IDIFEDER/2018/061 and PROMETEO/2020/077). P. S. thanks the Spanish Ministry of Universities for her pre-doctoral grant (FPU18/01732). F. P. and M. S. thank the Spanish Ministry of Science for their Juan de la Cierva and Ramón y Cajal contracts, respectively.

Paz Sebastián-Luna, Joaquín Calbo, Nicolás Albiach-Sebastián, Michele Sessolo, Francisco Palazón, Enrique Ortí, Henk J Bolink. Tuning the Optical Absorption of Sn-, Ge-, and Zn-Substituted Cs₂AgBiBr₆ Double Perovskites: Structural and Electronic Effects. *Chemistry of Materials*, **2021**, 33, 20, 8028-8035.

Chapter 5

Vacuum-Deposited Cesium Tin Iodide Thin Films with Tunable Thermoelectric Properties

*“Una aventura es más divertida
Si huele a peligro.”*
Romeo Santos

Most current thermoelectric materials have important drawbacks, such as toxicity, scarcity, and peak operating temperatures above 300 °C. Herein, we report the thermoelectric properties of different crystalline phases of Sn-based perovskite thin films. The 2D phase, Cs₂SnI₄, is obtained through vacuum thermal deposition and easily converted into the black β phase of CsSnI₃ (B-β CsSnI₃) by annealing at 150 °C. B-β CsSnI₃ is a p-type semiconductor with a figure-of-merit (*ZT*) ranging from 0.021 to 0.033 for temperatures below 100 °C, which makes it a promising candidate to power small electronic devices such as wearable sensors which may be interconnected in the so-called Internet of Things. The B-β phase is stable in nitrogen, whereas it spontaneously oxidizes to Cs₂SnI₆ upon exposure to air. Cs₂SnI₆ shows a negative Seebeck coefficient and an ultralow thermal conductivity. However, the *ZT* values are one order of magnitude lower than for B-β CsSnI₃ due to a considerably lower electrical conductivity.

Reference:

Paz Sebastiá-Luna, Unnati Pokharel, Bas A. H. Huisman, L. Jan Anton Koster, Francisco Palazón, Henk J Bolink. Vacuum-Deposited Cesium Tin Iodide Thin Films with Tunable Thermoelectric Properties. *ACS Applied Energy Materials*, **2022**, 5, 8, 10216-10223.

The content of this chapter was reproduced with permission from ACS Applied Energy Materials. Full published paper and Supporting Information are attached at Appendix C.

5.1 Introduction

Thermoelectric generators (TEGs) represent a very promising source of renewable energy, as they directly convert (waste) heat into electricity.^{9,32} Thermoelectric materials are typically characterized by the figure-of-merit, ZT (**Equation 1.1**),

$$ZT = \frac{S^2 \sigma}{\kappa} \quad (1.1)$$

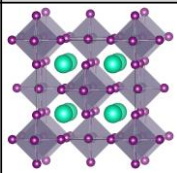
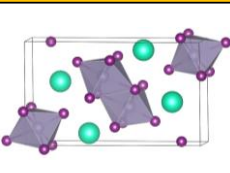
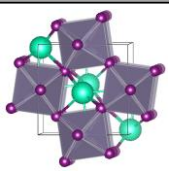
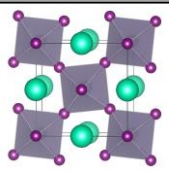
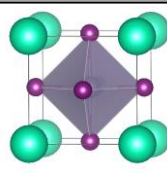
which depends on the following key parameters: S is the Seebeck coefficient, σ is the electrical conductivity, κ is the thermal conductivity and T is the absolute temperature. Thus, to maximize the ZT value of a given material, a large Seebeck coefficient, high electrical conductivity and low thermal conductivity are required.^{31,32}

As introduced previously in Chapter 1, inorganic TE materials operating near room-temperature are sought after. In the search for alternative materials that are easy to process, metal halide perovskites, such as $\text{CH}_3\text{NH}_3\text{PbI}_3$, FASnI_3 or CsSnI_3 , have emerged in recent years as potential thermoelectric materials. Indeed, ultralow thermal conductivity ($< 0.5 \text{ W m}^{-1} \text{ K}^{-1}$) and acceptable Seebeck coefficients have been demonstrated.^{34,154,155} Sn-based halide perovskites surpass their Pb counterparts in thermoelectric performance because of the self-oxidation of Sn^{2+} to Sn^{4+} , acting as a self-doping mechanism that enhances their electrical conductivity.¹⁵⁵ Besides, their toxicity is reduced due to the absence of Pb in their composition. In this work, we focus on CsSnI_3 , which furthermore contains Cs instead of an organic cation, offering much higher thermal stability than organic-inorganic perovskites.¹⁵⁶ It must be noted that Cs is up to three orders of magnitude more abundant on Earth crust than Bi or Te, which are common elements for current thermoelectrics.⁵² In fact, when comparing abundance and yearly production, it is worth noting that Cs is one of the most “underproduced” elements with scope for increased production.¹⁵⁷ With regards to toxicity, cesium has 40 known isotopes, of which radioactive ^{137}Cs is the most toxic and dangerous. In this work, we use its most stable isotope, ^{133}Cs , with a much lower toxicity.¹⁵⁸ Therefore, CsSnI_3 emerges as a promising alternative to most current thermoelectric compounds such as PbTe , Bi_2Te_3 or Sb_2Te_3 with regards to element abundance and toxicity.

CsSnI_3 is known to have four different polymorphs, two of them existing at room temperature (**Table 5.1**)^{159,160}: A yellow phase, Y CsSnI_3 , with an orthorhombic one-

dimensional double-chain structure and an orthorhombic three-dimensional perovskite that is black in colour, B- γ CsSnI₃. Based on the literature, annealing Y CsSnI₃ to 150 °C under an inert atmosphere yields a black cubic perovskite (B- α), which upon cooling back below 150 °C transforms into a black tetragonal phase (B- β), and into the black orthorhombic phase B- γ when it is cooled below 80 °C. Exposing B- γ CsSnI₃ to air for a short period of time triggers the transformation into Y CsSnI₃, as this phase is thermodynamically more stable in ambient conditions.^{159,160} Eventually, upon prolonged exposure to air, Y CsSnI₃ evolves to Cs₂SnI₆, a vacancy-ordered double perovskite that contains oxidized Sn⁴⁺ rather than Sn²⁺ ions.¹⁶¹ Previous reports have studied the thermoelectric properties of CsSnI₃ thin films. Saini *et al.* prepared films grown by solution process in DMSO:DMF mixtures and using toluene as anti-solvent, followed by thermal annealing reaching a ZT of 0.137 at room temperature.¹⁶² Kontos *et al.* studied the effect of SnF₂-doping onto spin-coated CsSnI₃ films, revealing a change in the electrical resistance upon the exposure to air of the samples.¹⁶⁰ In the same line, Liu *et al.* reached a ZT around 0.14 in SnCl₂-doped CsSnI₃ films deposited by a sequentially-evaporation method.¹⁶³ Nevertheless, this performance is only achieved upon the introduction of additional SnCl₂ into the structure and after exposure of the films to air and humidity for 6 minutes, while longer exposure time was found to diminish the ZT again.¹⁶³ Kanatzidis and coworkers studied the thermal and transport properties of a series of CsSnBr_{3-x}I_x perovskites, obtaining a ZT for CsSnI₃ of 0.025 at 300 K that reaches a maximum of 0.15 at 550 K. These results were achieved with bulk (6 × 6 × 1.5 mm) crystals sintered at 923 K for periods of more than 24 h.¹⁶⁴ In summary, these results demonstrate the potential of CsSnI₃ thin films for TE. However, the aforementioned protocols include complex solvent processing, need of external dopants or additives, high temperature synthesis and/or are very sensitive to air and humidity. More robust and simpler routes are therefore sought after.

Table 5.1. Existing Different Phases and Structures of the Cs–Sn–I System, Their Crystal Structures, and Ambient Conditions for Each Phase Transition.^a

Phase	Cs_2SnI_6	$\gamma \text{ CsSnI}_3$	$\text{B-}\gamma \text{ CsSnI}_3$	$\text{B-}\beta \text{ CsSnI}_3$	$\text{B-}\alpha \text{ CsSnI}_3$
Crystal structure					
Crystal system	Cubic	Orthorhombic	Orthorhombic	Tetragonal	Cubic
Formation	300 K Air (\approx hours)	300 K Air (\approx sec)	300 K N_2	< 425 K Air/ N_2	> 425 K Air/ N_2

^a Transition temperatures are taken from the literature.^{159,160}

Here, we focus our research on the study of vacuum deposition of CsSnI_3 thin films, via single source thermal evaporation of pre-synthesized dry powders. Thermal vacuum deposition shows better thickness control, higher throughput and higher reproducibility compared to solution processing.^{63,165} Remarkably, the as-synthesized film presents the two-dimensional structure characteristic of Cs_2SnI_4 , a phase only theoretically reported so far. Its electrical conductivity is very low but can be increased by several orders of magnitude upon annealing and consequent conversion to $\text{B-}\beta \text{ CsSnI}_3$, achieving a maximum ZT of 0.033.

5.2 Experimental section

Materials

Cesium iodide (CsI , > 99 %) was purchased from TCI. Tin(II) iodide (SnI_2 , 99.999%) was purchased from Alfa Aesar. All chemicals were stored in a nitrogen-filled glovebox and used as received without further purification.

Mechanochemical synthesis

Stoichiometric amounts of CsI and SnI_2 were introduced inside a 10 mL zirconia ball-mill jars with 2 zirconia beads of 10 mm in diameter inside a nitrogen-filled

glovebox. Ball-milling (BM) was performed with a MM-400 shaking ball-mill from Retsch, at a frequency of 30 Hz for 30 minutes. See Chapter 2 for further information.

Thin-film deposition by single-source vacuum deposition (SSVD)

In a typical deposition, an alumina thermal crucible (Creaphys GmbH) was placed inside a vacuum chamber, and the as-synthesized CsSnI₃ powder was loaded. Then, the chamber was evacuated to a pressure of 7×10^{-6} mbar, and the source was rapidly heated to 500 °C. The deposition was stopped after the complete evaporation of the solid. The sample film thickness was measured with a mechanical profilometer (Ambios XP200). Results shown in the main text are obtained from thin films of B- β CsSnI₃ and Cs₂SnI₆ with a film thickness of 210 nm ($\pm 0.5\%$) and 540 nm ($\pm 0.2\%$), respectively. The reason a thicker film was deposited to evaluate Cs₂SnI₆ is that the conductivity is lower than for CsSnI₃, and therefore the overall conductance of the film falls below the limit of detection of the instrumental setup if a 210 nm film is employed. The thickness evaluation is performed on the relevant phase right before thermoelectric characterization to ensure accurate conductivity assessment. It must be noted, however, that the 540 nm thickness of the Cs₂SnI₆ film is obtained from a precursor B- β CsSnI₃ film of 515 nm, meaning that a $\sim 5\%$ thickness increase occurs upon phase transition.

XRD characterization

X-ray diffraction was measured with a powder diffractometer Empyrean from Panalytical equipped with CuK α anode operated at 45 kV and 40 mA. Single scans were acquired in the $2\theta = 8$ to 60° range with a step size of $2\theta = 0.01^\circ$ in Bragg-Brentano geometry in air. A sealed dome sample holder (Anton Paar) was used for measurements in N₂.

Optical characterization

UV–vis absorption spectra of the films are acquired in a transmission configuration coupled to an Avantes Avaspec-2048L optical detector (Avantes BV). Photoluminescence measurements were performed inside a nitrogen-filled glovebox by

using a MatchBox laser as an excitation source at 515 nm coupled to an Avantes Avaspec-2048L optical detector. For a typical analysis, one scan with an integration time of 3 s was collected.

Scanning Electron Microscope (SEM)

SEM images were obtained using a Phenom XL G2Microscope from Thermo Fisher, at an operating acceleration voltage of 10 kV. EDX data was acquired using a Hitachi S-4800 Scanning-Electron Microscope.

Thermoelectric properties measurement

Electrical conductivity, thermal conductivity, Seebeck coefficient and Hall Effect were measured simultaneously on the same sample using a Thin Film Analyzer (TFA) from LinseisTM. The operation mechanism of this equipment is described in Chapter 2 and in literature.⁸² A home-built setup was employed to measure the Seebeck coefficient of $B\text{-}\beta$ CsSnI_3 and Cs_2SnI_6 thin-films for comparison. Seebeck coefficient of samples processed under same conditions were measured with both the setups to compare values.¹⁶⁶ All measurements were carried out under inert atmosphere. For error bar calculation, we have incorporated the error of the equipment provided by the manufacturer and the thickness measurement into consideration. Final errors are: $\pm 10\%$ for thermal conductivity, $\pm 6\%$ for electrical conductivity, $\pm 7\%$ for Seebeck coefficient and $\pm 9\%$ for Hall coefficient. ZT and charge mobility errors are calculated from the combination of these errors.

5.3 Results and discussion

Following the procedure described in the Experimental Section, synthesis of the CsSnI_3 was carried out via dry mechanochemical synthesis by ball-milling under nitrogen, thus preventing oxidation and degradation of Sn(II) in contact with the atmosphere. The synthesized CsSnI_3 is a black powder with a complex X-ray diffraction pattern (see **Figure S1**). When this diffraction pattern is compared with the known

patterns for the yellow phase (Y CsSnI₃, Inorganic Crystal Structure Database code 262927) and the black gamma phase (B- γ CsSnI₃, ICSD code 262926), it can be deduced that our as synthesized powder is a mixture of these two phases.

Once the powders were formed, thin films with thicknesses of few hundred nanometers (see Experimental Section for more details) were deposited via single-source vacuum deposition (SSVD) inside a high-vacuum chamber. SSVD has been previously shown by us and others to be a fast and reproducible method for depositing pure, stoichiometric materials.^{65,70,167} In our case, the SSVD of the ball-milled CsSnI₃ did not lead directly to the deposition of any of the previously mentioned CsSnI₃ phases, as the XRD diffractogram does not match with any of them (**Figure 5.1a**). On the contrary, the few and equally spaced peaks present are reminiscent of a 2D material. Indeed the main diffractogram signals can be well matched with a 2D phase isostructural to Cs₂Pb(I_{0.5}Cl_{0.5})₄ (**Figure S2**).¹⁶⁸ Thus, it is reasonable to ascribe this signal to the crystallization of the 2D phase Cs₂SnI₄ (**Figure S2**), whose main diffraction peaks correspond to the (00*l*) planes. To the best of our knowledge, this phase has only been theoretically reported because of its high instability.^{169,170} Indeed, we attempted the mechanochemical synthesis of Cs₂SnI₄ but a mixture of Y CsSnI₃ and B- γ CsSnI₃ was formed instead (**Figure S3**). The formation route of Cs₂SnI₄ upon the sublimation of CsSnI₃ powder still remains unclear to us. We hypothesize that, even if the 2D phase is unstable, the high energies supplied by the evaporation process allowed its formation. However, we cannot rule out the co-existence of Cs₂SnI₄ in the thin films together with CsSnI₃ phases. Indeed, minor peaks around $2\theta = 27.6^\circ$ and $2\theta = 29.2^\circ$ do not match the 2D structure and suggest traces of Y CsSnI₃ and B- γ CsSnI₃ (**Figure S2**). The preferential deposition of Cs₂SnI₄ took place in a reproducible manner at several evaporation batches of ball-milled CsSnI₃ (**Figure S4**), with slight differences in the presence of side phases that could be linked to variations in the air exposure. Elemental analysis by Energy Dispersive X-ray spectroscopy (EDX) shows a molar ratio of Cs:Sn:I 1:1.5:3.1, very close to the stoichiometry expected for a CsSnI₃-derived phase (1:1:3) with an excess of Sn ascribed to indium tin oxide (ITO) substrate. The absorption spectrum (**Figure 5.1b**) confirms the presence of, at least, two different species with different absorption intensities. The Tauc plot derived from the absorption spectrum reveals two bandgaps energies of 2.45 eV and 1.42 eV which are ascribed to Y CsSnI₃ (indirect transition) and Cs₂SnI₄ (direct transition) phases, respectively, very similar to the literature references (**Figure S5**).^{169,171}

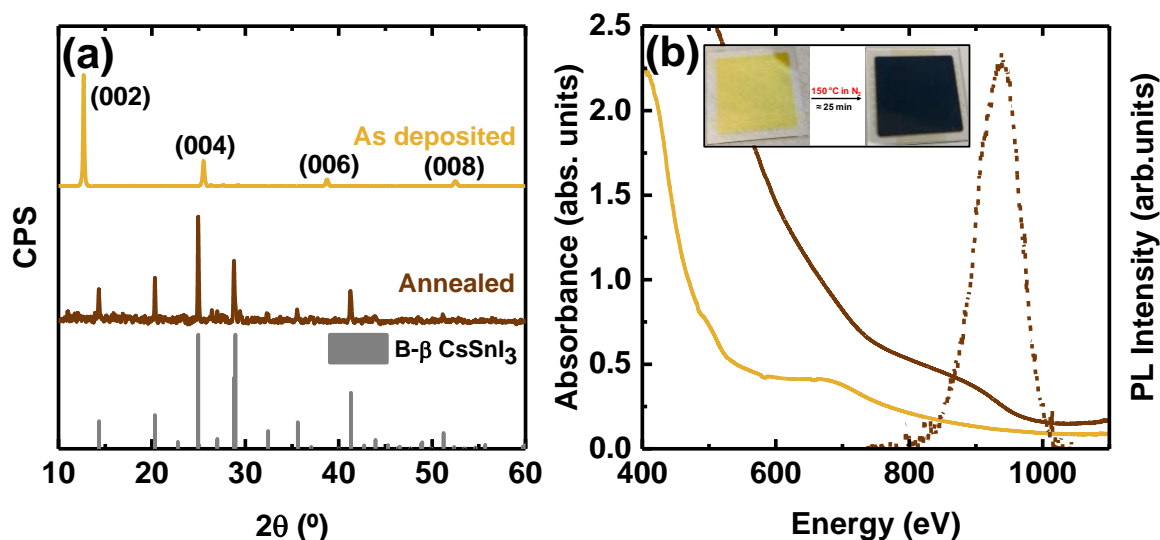


Figure 5.1. (a) XRD diffractograms and (b) absorbance (solid lines) and photoluminescence (dashed line) spectra of SSVD thin-films as-deposited and annealed for 25 min at 150 °C. Panel (a) shows the ICSD pattern for black beta phase of CsSnI₃ (code 262925) and the predicted main crystalline structure for both films. Predicted XRD planes of as-deposited thin-films were obtained from the fit presented in **Figure S2**.

A preliminary study of the electrical properties of the 2D phase revealed a very low conductivity (**Figure S6**). Such a low conductivity is detrimental for thermoelectric use, as it would lead to a very low ZT value. However, it was possible to convert the poorly-conductive Cs₂SnI₄ into the more conductive black beta phase of CsSnI₃ (B-β CsSnI₃) by thermal annealing at 150 °C under inert atmosphere (**Figure 5.1a**). **Figure 5.2** shows the XRD patterns resulting from in-situ annealing of Cs₂SnI₄ thin films up to 150 °C. Cs₂SnI₄ undergoes a gradual conversion to CsSnI₃, for which 25 minutes of annealing are required to form a pure black beta phase of CsSnI₃. This transformation is further evidenced by the increase in optical absorption of the thin-film in the 500-950 nm region (**Figure 5.1b**), causing a darkening of the film (note that both absorption spectra in **Figure 5.1b** are obtained from the same film –same thickness– and hence absorbance units directly relate to absorption coefficient of the given phase). The shift towards higher wavelengths translates into a narrowing of the bandgap. Assuming a direct bandgap for this material, we obtain a value of 1.30 eV from the absorption spectrum, (see Tauc plot in **Figure S8**). Contrary to Cs₂SnI₄ where no photoluminescence (PL) was detected, B-β CsSnI₃ shows infrared emission with the maximum at 937 nm (1.32 eV). This implies that there is only a very small Stokes shift. Both the bandgap energy deduced from

absorption and the maximum of the PL emission are in agreement with values reported previously.^{160,161,171,172} These properties make B- β CsSnI₃ also interesting for alternative applications such as light absorber for solar cells or as the emitter for near infrared light-emitting diodes.^{173,174}

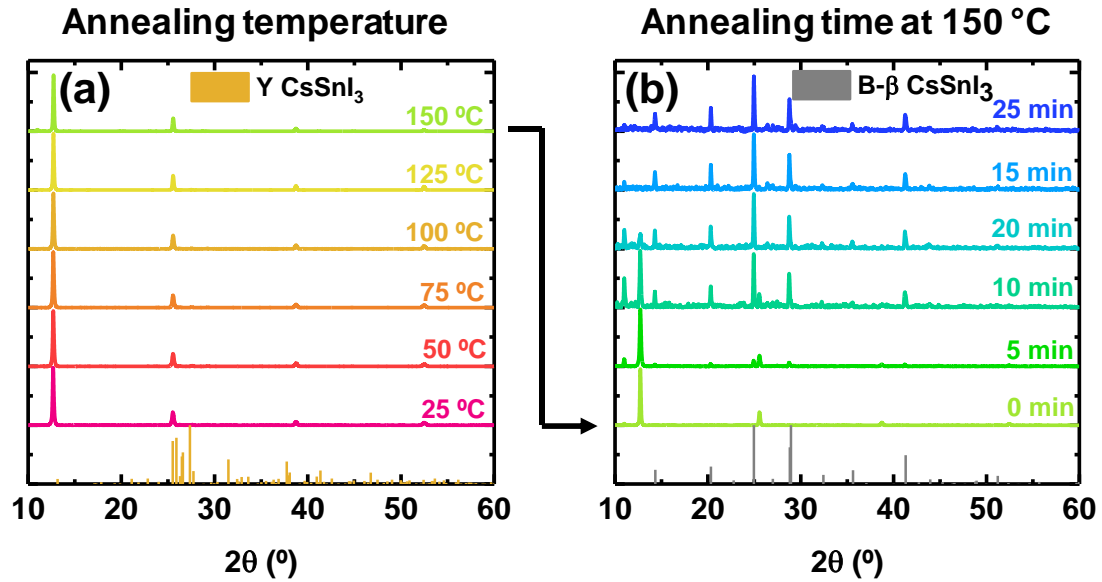


Figure 5.2. XRD diffractograms of (a) in-situ annealing of Cs₂SnI₄ thin films up to 150 °C and (b) effect of the annealing time at 150 °C until it is fully converted into the black beta phase of CsSnI₃.

The thermoelectric performance of B- β CsSnI₃ thin-films was then studied under an inert atmosphere through temperature-dependent measurements ranging from 25 °C to 100 °C (**Figure 5.3a**) with an integrated thin film analyzer from LinseisTM (see Experimental Methods).⁸² The electrical conductivity (σ) decreases with increasing temperature as expected for band-like charge transport. A maximum conductivity of $50 \pm 3 \text{ S cm}^{-1}$ at room temperature is obtained. This is seven orders of magnitude higher than the conductivity of the phase that was formed prior to annealing the film, Cs₂SnI₄. Hall effect measurements (**Figure 5.3b**) show that the B- β CsSnI₃ thin-films are a p-type semiconductor (positive Hall coefficient) with a charge carrier concentration (n) around $7 \cdot 10^{18} \text{ cm}^{-3}$ and hole mobility of $42 \pm 6 \text{ cm}^2 \text{V}^{-1} \text{s}^{-1}$ at room temperature. A temperature increase causes a sharp decrease in the charge carrier mobility in line with the observed decrease in the electrical conductivity whereas the carrier concentration remains virtually constant. It is known that the origin of the p-type conduction of B- β CsSnI₃ arises from its ability to accommodate Sn⁴⁺ ions and Sn vacancies due to oxidation which effectively

acts as self-doping and hence transit to a hole-doped state.¹⁷⁵ When increasing the temperature, holes delocalize and molecular vibrations increase to achieve a metal-like behaviour translating into a decrease in the electrical conductivity.^{159,164,176} Thus, the mean free path of electrons is reduced, and their mobility is also decreased. While this behavior is typical of a metal and not of an intrinsic semiconductor, we should stress that CsSnI₃ is effectively a self-doped semiconductor (not a metal, as it clearly presents a bandgap of 1.3 eV as shown in **Figure 5.1**). In the words of Chung et al.²⁰ “although stoichiometric CsSnI₃ is a semiconductor, the material is prone to intrinsic defects associated with Sn vacancies. This creates highly mobile holes which cause the materials to appear metallic.” We hypothesize that, as no phase transition took place here upon heating and samples were stored in nitrogen during measurement, the formation of new Sn⁴⁺ centers is avoided, so the carrier concentration is kept constant. These findings were previously reported by others as they did not consider phase transitions upon heating B- β CsSnI₃ to have an effect on the charge transport properties.¹⁵⁹

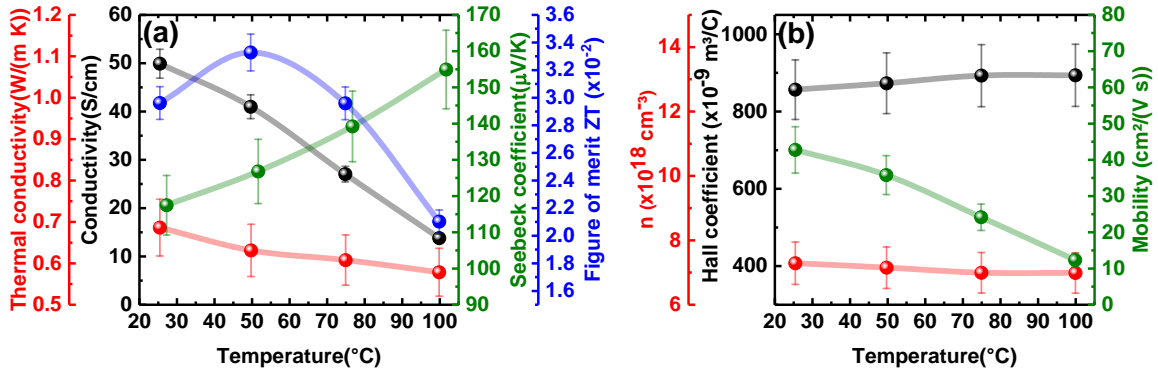


Figure 5.3. (a) Temperature dependence of electrical conductivity, σ (black line), thermal conductivity, κ (red line), Seebeck coefficient, S (green line) and figure-of-merit, ZT (blue line) of B- β CsSnI₃. (b) Temperature dependence of Hall coefficient (black line), charge carrier concentration of the bulk, n (red line) and charge mobility (green line) of B- β CsSnI₃. Errors bars come from measurement of film thickness and the deviation of the equipment (see Experimental Section). ZT and charge mobility error bars are originated from the combination of these errors.

On the other hand, the ultralow thermal conductivity (κ) detected in the whole range of temperatures is consistent with the ultralow lattice thermal conductivity reported for most halide perovskites.^{154,177} The cause of this phenomenon is ascribed to the phonon-phonon scattering inside the crystal lattice, which intensifies by increasing the temperature, hindering the thermal transport (decreasing κ).^{156,163,164} Such low thermal

conductivities are beneficial for the thermoelectric performance and are found in other materials such as MAPbI₃ or SnSe, whose ZT is one of the highest reported so far.^{34,178}

The positive Seebeck coefficient, S , as shown in **Figure 5.3a**, confirms that B- β CsSnI₃ is a p-type semiconductor, consistent with our Hall effect measurements and in corroboration with findings from others.^{159,179} S steadily rises up to $154 \pm 11 \mu\text{V K}^{-1}$ with increasing temperature, which agrees with the decrease in electrical conductivity and is comparable to other Sn-based perovskites.^{31,164} A similar value for S was determined independently with a different characterization methodology (see **Figure S9** and Experimental Section). The thermoelectric figure-of-merit, ZT , for our thin films (thickness = 300 nm) of B- β CsSnI₃ ranges from 0.021 to 0.033 in the temperature range studied (room temperature to 100 °C) and reaches its maximum (0.0333 ± 0.0013) at 50 °C, which is relevant for applications near room temperature.

When the B- β CsSnI₃ thin film is kept in inert atmosphere (**Figure 5.4a**), the black beta phase is preserved for at least 7 days. However, as mentioned, B- β CsSnI₃ spontaneously evolves to Cs₂SnI₆ upon exposure to air in 2 days or less (**Figure 5.4b**). This phase change is accompanied by a decrease in the film homogeneity and the formation of pinholes spread all over the film surface, as SEM images evidence (**Figure 5.5**). The poor morphology is likely attributed to an irregular oxidation from B- β CsSnI₃ to Cs₂SnI₆, which could be avoided by controlling the atmosphere composition and deposition process.^{180,181} After one week in air we observe the formation of some small amount of CsI, indicating some degradation of this Cs₂SnI₆ structure and a low stability of the phase when exposed to air for long periods. In contrast, **Figure S11** shows that the XRD diffraction pattern after heating to 150 °C in ambient conditions remains unchanged, revealing the high thermal stability of Cs₂SnI₆. This finding was previously confirmed by other authors who performed thermogravimetric analysis (TGA), showing no decomposition until 515 K.¹⁸²

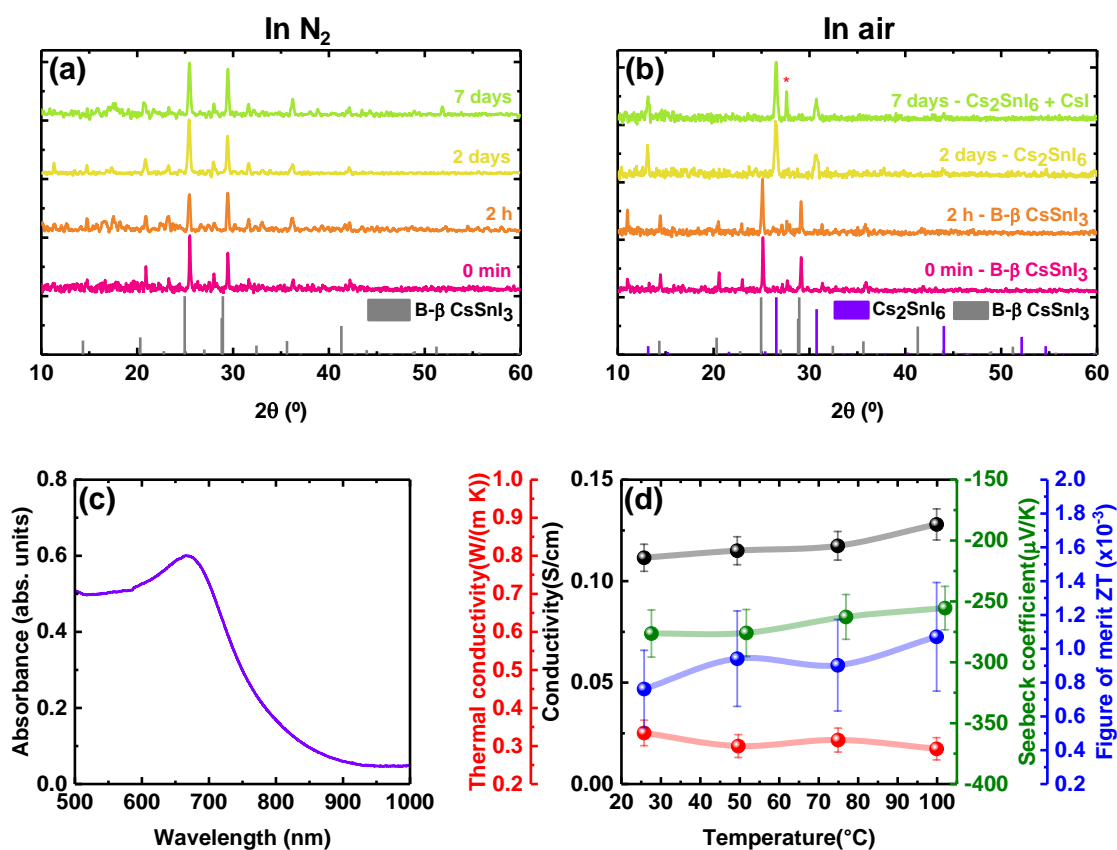


Figure 5.4. XRD diffractograms of the evolution of Cs₂SnI₆ thin films exposed to (a) air and (b) N₂ for 1 week. Red asterisk stands for the main XRD peak of CsI, a by-product of the degradation. (c) UV-Vis absorbance spectrum of Cs₂SnI₆. (d) Temperature dependence of electrical conductivity, σ (black line), thermal conductivity, κ (red line), Seebeck coefficient, S (green line) and figure-of-merit, ZT (blue line) of Cs₂SnI₆ thin films. See error bar calculation in Figure 5.3a.

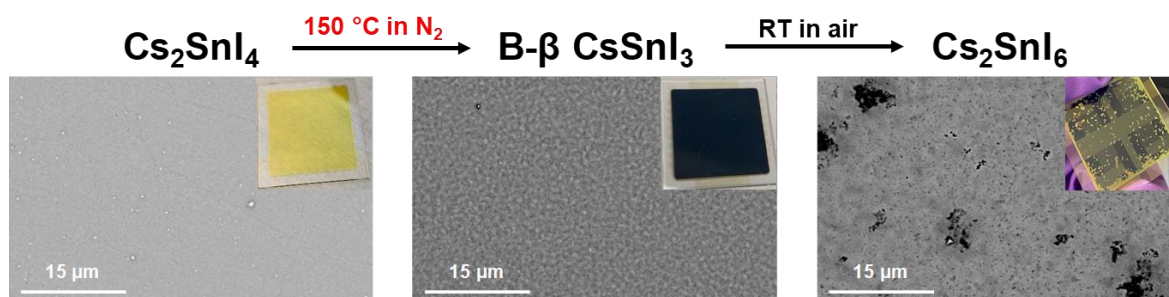


Figure 5.5. SEM images of Cs₂SnI₄, B-β CsSnI₃ and Cs₂SnI₆ thin films at 10000x magnification. Insets with the appearance of each thin film are included.

The conversion of B-β CsSnI₃ to Cs₂SnI₆ leads to a change of the optical properties of the thin films. The shape and the intensity of the optical absorbance is completely different from the B-β CsSnI₃ phase (Figure 5.4c). The absorption spectra

has an overall strongly reduced absorbance compared to that of the B- β CsSnI₃ phase.^{183,184} A direct bandgap of 1.49 eV can be estimated from the Tauc plot (**Figure S12**), in line with previous reports for this phase.^{94,161,185} No significant PL was detected for this material, which could be ascribed to a high non-radiative recombination rate of the films induced by the formation of trap states.^{180,184,186}

Figure 5.4d shows the temperature dependence of the thermoelectric performance of Cs₂SnI₆ thin films. We observe a conductivity around 0.1 S cm⁻¹ in the whole temperature range, in line with other reported values.¹⁸¹ This is 2 orders of magnitude lower than that observed previously for B-beta CsSnI₃ (**Figure 5.3**). An ultralow thermal conductivity is also found for Cs₂SnI₆, together with a negative Seebeck coefficient over the whole range of temperatures, indicating that electrons are the dominant charge carriers (n-type conduction). The n-type character of the compound comes from the presence of iodine vacancies and tin interstitials inside the lattice, defects easily formed in this double perovskite.^{182,186} With our home-built setup, measurements run on a different day and on a different sample yielded a Seebeck coefficient at 25 °C of -514 μ V K⁻¹ (**Figure S13**), which is considerably higher in absolute value, although in the same order of magnitude as what was obtained from the analysis using the thin-film analyzer. We hypothesize that the difference of Seebeck values arises from a dissimilar oxidation level of the layers. It seems plausible that variations in the atmosphere, *e.g.* oxygen concentration, moisture or temperature, during the oxidation of B- β CsSnI₃ to Cs₂SnI₆ may cause a different degree of oxidation affecting the charge transport mechanisms and, thus, the thermoelectric performance. We should also note that the oxidation in air from CsSnI₃ to Cs₂SnI₆ is likely accompanied by formation of SnO₂ which may be amorphous and hence not detected here by XRD. It is possible that this side-product also affects the overall thermoelectric properties of the film. Anyhow, the low electrical conductivity (two orders of magnitude lower than that of B- β CsSnI₃) leads to ZT values around 1×10^{-3} in the 25 °C – 100 °C range. The improvement of the electrical conductivity is, thus, paramount to boost the possibilities in TE of this material.

5.4 Conclusions

In conclusion, we report the thermal deposition of Cs₂SnI₄ directly from the SSVD of ball-milled CsSnI₃ powder. Absorption spectra of these thin films reveal the

presence of the 2D perovskite ($E_g = 1.42$ eV) together with traces of γ CsSnI₃ ($E_g = 2.45$ eV). Their electrical conductivity is found to be extremely low but rises almost 7 orders of magnitude after annealing for 25 min at 150 °C, when the B- β CsSnI₃ phase is formed. B- β CsSnI₃ shows ultralow thermal conductivity and p-type conduction corroborated from Seebeck and Hall measurements. Its electrical conductivity decreases when increasing the temperature, caused by the reduction in charge mobility. In the temperature range studied (RT – 100 °C) and without exposure to air or further external doping, the maximum ZT achieved is 0.0333 ± 0.0013 at 50 °C. The black beta phase is conserved in nitrogen for more than 7 days but oxidizes into Cs₂SnI₆ upon exposure to air for a few hours. Cs₂SnI₆ has a lower electrical conductivity, an ultralow thermal conductivity, and a larger absolute Seebeck coefficient, reaching a ZT of 0.0011 ± 0.0003 (100 °C) (see **Table 5.2** for summarized maximum values achieved). Hence, both B- β CsSnI₃ and Cs₂SnI₆ show potential for implementation in low-temperature operating TEGs when the conductivity of these materials can be controllably improved.

Table 5.2. Comparison of maximum electrical conductivity (σ_{max}), thermal conductivity (κ_{max}), Seebeck coefficient (S_{max}), and figure-of-merit ZT (ZT_{max}) for the three species studied in this work.^a

Phase	σ_{max} (S cm ⁻¹)	κ_{max} (W m ⁻¹ K ⁻¹)	S_{max} (μ V K ⁻¹)	ZT_{max}
Cs ₂ SnI ₄	2.47×10^{-6} at 25 °C	ND	ND	ND
B- β CsSnI ₃	50 ± 3 at 25 °C	0.69 ± 0.07 at 25 °C	154 ± 11 at 100 °C	0.0333 ± 0.0013 at 50 °C
Cs ₂ SnI ₆	0.128 ± 0.007 at 100 °C	0.33 ± 0.03 at 25 °C	-255 ± 18 at 100 °C	0.0011 ± 0.0003 at 100 °C

^a Temperatures at which they are achieved are given. ND stands for non-detected.

5.5 Author contribution and acknowledgments

In this chapter, Paz Sebastiá developed the synthesis, SSVD, optical, XRD characterization steps, and thermoelectric study, along with the writing of the manuscript. Bas A. H. Huisman carried out PL measurements. All these experiments were performed at the Institute of Molecular Science (ICMol) of the University of Valencia. Electrical conductivity and Seebeck coefficient measurements with alternative setup were carried out by Unnati Pokharel at the University of Groningen.

The research leading to these results has received funding from the European Research Council (ERC) under the European Union's Horizon 2020 research and innovation programme (Grant agreement No. 834431). Authors acknowledge support from the Comunitat Valenciana (IDIFEDER/2018/061 and PROMETEU/2020/077), as well as by the Ministry of Science and Innovation (MCIN), and the Spanish State Research Agency (AED): Project PCI2019-111829-2 funded by MCIN/AEI/10.13039/501100011033 and by the European Union; Project CEX2019-000919-M funded by MCIN/AEI/10.13039/501100011033 Dutch Research Council (NWO, FOM Focus Group "Next Generation Organic Photovoltaics") P. S. thanks the Spanish Ministry of Universities for her pre-doctoral grant (FPU18/01732 and EST19/00295). F. P. acknowledges funding from the Ramón y Cajal program of the Spanish Ministry of Science (RYC2020-028803-I).

Paz Sebastiá-Luna, Unnati Pokharel, Bas A. H. Huisman, L. Jan Anton Koster, Francisco Palazón, Henk J Bolink. Vacuum-Deposited Cesium Tin Iodide Thin Films with Tunable Thermoelectric Properties. *ACS Applied Energy Materials*, **2022**, *5*, 8, 10216-10223.

Chapter 6

General outlook and conclusions

*“Ya me cansé de discusiones
De vivir demasiado deprisa
No te quiero sumisa, te quiero libre
Subir esa montaña y sentir la brisa.”*
Los Chikos del Maíz

The main goal of this thesis was the search and development of inorganic and low-toxicity (in particular lead-free) compounds with possible applications in optoelectronics and thermoelectrics to replace the most frequently used and/or currently developed materials in these fields. Given the sustainable approach of the applications of these materials, we have sought to emphasize it even more by employing solvent-free green synthesis and deposition methods. For this reason, dry mechanochemical synthesis by ball milling and single source vacuum deposition have been the preferred methods for the three families of materials presented herein. In particular, the following achievements can be highlighted:

- **Chapter 3:** two series of copper-based compounds with the formula CsCu_2X_3 and $\text{Cs}_3\text{Cu}_2\text{X}_5$ ($\text{X} = \text{Cl}, \text{Br}, \text{I}$, and mixtures thereof) have been synthesized with demonstrated potential for light-emitting devices, at least based on the latter. By changing the halide, it has been possible to tune the emission wavelength, ranging from the green for the Cl-pure to the blue for the I-pure species. Among them, the most emissive one is $\text{Cs}_3\text{Cu}_2\text{Cl}_5$, with a PLQY around 80% centred at 516 nm (green emission). However, $\text{Cs}_3\text{Cu}_2\text{I}_5$, with a PLQY exceeding 40% at 442 nm (blue emission), is arguably the most interesting of all of them due to the scarceness of highly efficient blue light emitting diodes. It has been shown that it keeps its outstanding performance even after the exposure to air and after its deposition into a thin film, either by solution processing or by thermal vacuum deposition. This work is, therefore, especially relevant for proposing highly efficient and low toxicity alternatives for LEDs, which can even be combined with each other to produce white light, a topic that is proposed for future work.
- **Chapter 4:** to widen the photovoltaic applications of the double perovskite $\text{Cs}_2\text{AgBiBr}_6$ it was needed to narrow its bandgap (1.94 eV, indirect), considered too wide for single-junction and tandem solar cells. This was attempted following two different approaches. First, the annealing of the as-synthesized powders led to a bandgap widening, up to 2.16 eV, contrary to pursued. Second, the introduction of different dopants into the structure by means of the mechanochemical synthesis was tested. The incorporation of different amounts of SnBr_2 and GeBr_2 red-shifted the absorption onset considerably (up to 1.55 and 1.80 eV, respectively) and a modification of the bandgap nature (from indirect to

direct). On the contrary, the introduction of ZnBr_2 did not lead to a bandgap reduction but to an increase, up to 2.02 eV. Density Functional Theory (DFT) calculations were performed to understand the underlying reason of the different behaviour of the dopants once incorporated into the structure, which was related to the mixing of the orbitals participating in the bonding. Thin films of Sn-doped $\text{Cs}_2\text{AgBiBr}_6$ were deposited by SSVD and showed the possibility of bandgap tuning. Hence, this work has significant relevance since it opens the door for the bandgap reduction of this double perovskite and its utilization in efficient PV devices.

- **Chapter 5:** in this chapter, three different species within the system Cs-Sn-I are studied for thermoelectrics. The direct SSVD of ball-milled CsSnI_3 yields a barely reported 2D perovskite, Cs_2SnI_4 . Cs_2SnI_4 was previously only theoretically predicted but this work represents the first experimental proof of the existence of this phase. However, its electrical conductivity around $10^{-6} \text{ S cm}^{-1}$ is found to be too low for this purpose. A significantly more conductive phase, black beta CsSnI_3 (B- β CsSnI_3), forms upon annealing at 150 °C of the 2D perovskite and yields an electrical conductivity around 50 S cm^{-1} near room temperature. This phase is a p-type semiconductor that achieves a maximum figure-of-merit ZT of 0.033 at 50 °C, comparable to other room-temperature TE materials and stable under inert conditions for more than 7 days. Cs_2SnI_6 forms when the black beta phase is exposed to air but has lower electrical conductivity (0.128 S cm^{-1}), reaching a ZT_{max} of 0.0011. The performance of these materials, nevertheless, is still low compared to the current TE materials but could be boosted when the electrical conductivity is increased. Once improved, they could serve as a real alternative to the current low-temperature operating TEGs.

Overall, the work developed in this thesis represents a step forward in two different research fields, optoelectronics and thermoelectrics, which are gaining increasing attention in the last years because of the higher concern about sustainability and renewable energies. This thesis paves the way towards the implementation of the proposed materials in LEDs, solar cells and TEGs.

Chapter 7

Resum en valencià

*“Tornar a nàixer, tornar a ser un xiquet
Tindrè el secret de la vida eterna
Que fores tu l'únic govern que em governa.”*
Aspencat

7.1 Capítol 1: Introducció

El canvi climàtic és ja una realitat que afecta les condicions de vida de milions de persones cada any i els efectes del qual ja comencen a notar-se en totes les parts del món.^{1,2} Una de les principals causes és l'emissió incontrolada de gasos d'efecte d'hivernacle a l'atmosfera, com ara CO₂, metà o òxid nítrós, provocada principalment per la crema de combustibles fòssils i biomassa, per exemple fusta o residus de cultius, per a obtenir energia.³ El carbó, el gas, el petroli i la biomassa són actualment les principals fonts d'energia del món i són responsables de més de tres quarts parts de les emissions globals de gasos d'efecte d'hivernacle.^{4,5} Per a aconseguir un planeta més net i preservar el medi ambient i a tots els seus habitants, és necessari buscar fonts d'energia menys nocives i contaminants. Entre les diferents alternatives destaca l'energia solar, inclosa en el grup de "energies renovables" i el desenvolupament de les quals es va iniciar en les últimes dècades. L'energia solar es basa, a grans trets, en la conversió de l'energia dels raigs del sol en electricitat llesta per al consum.

D'altra banda, també és possible convertir l'energia en forma de calor residual procedent de diferents fonts, com el sol, el cos humà o els processos industrials, per a produir electricitat. Aquesta és la base principal de l'energia termoelèctrica, que en el futur podria combinar-se amb l'energia solar i posicionar-se com una font d'energia renovable i eficient per a substituir per complet als combustibles fòssils contaminants.⁶ A més, els dispositius termoelèctrics podrien utilitzar-se en motors d'automòbils, dispositius mèdics i *wearables* (o Internet de les coses, IoT), edificis residencials intel·ligents i molts altres dispositius electrònics.⁷

No obstant això, la cerca de noves fonts d'energia per a reduir la contaminació i limitar el canvi climàtic ha d'anar juntament amb altres canvis en la societat i en la nostra vida quotidiana. Com es destaca en l'anàlisi realitzada per Eurostat en 2020, el 27% del consum final d'energia a Europa es va deure al sector residencial. Les llars utilitzen aquesta energia per a diverses aplicacions, com la calefacció/refrigeració d'espais i aigua, la cuina o la il·luminació. D'aquest percentatge, el 14,5% representa l'energia utilitzada per a la il·luminació només a la Unió Europea (UE).⁸ D'aquí ve que el desenvolupament i la millora de les fonts de llum artificial amb tecnologies ecològiques i energèticament eficients haja de situar-se també com un dels passos fonamentals cap a la transició ecològica.

Per a desenvolupar aquests dispositius, ja siga amb finalitats d'il·luminació o de producció d'energia, un punt crucial és el desenvolupament de nous materials. De fet, la ciència dels materials exerceix un paper crucial per a obtenir les propietats desitjades per a aquests camps, permetent l'ajust i l'optimització de les propietats dels materials per a millorar la seua eficiència i els costos de producció. Recentment s'estan desenvolupant tot tipus de materials inorgànics i orgànics amb l'objectiu d'integrar-los en aquesta mena d'estructures, de manera que puguen fins i tot escalar-se a processos industrials més complexos sense afectar les seues propietats i prestacions.⁹⁻¹¹

En aquesta tesi, centrarem els nostres esforços en la cerca i estudi de nous materials amb potencial aplicació en aquestes tres grans àrees d'investigació com són la fotovoltaica, la termoelèctrica i les fonts d'il·luminació ecològiques com els díodes emissors de llum (LEDs), amb l'objectiu de lluitar contra el canvi climàtic i donar suport a les energies renovables i no contaminants. A més, en vista de la seua potencial integració en aquests dispositius, estudiarem la seua deposició en làmines primes. En la següent secció, s'introduirà el funcionament de dos tipus de dispositius optoelectrònics, els LED i les cèl·lules solars, i dels generadors termoelèctrics. Es posarà l'accent principalment en els requisits que han de reunir els materials per a ser adequats per a aquesta mena d'aplicacions.

7.1.1 Díodes emissors de llum

Funcionament

Els LEDs són dispositius semiconductors que emeten energia en forma de fotons quan reben corrent elèctric. Aquests dispositius són capaços d'emetre en una àmplia gamma de bandes dins de l'espectre electromagnètic, des de l'infraroig fins a l'ultraviolat, depenent de la composició química del material semiconductor.^{12,13} Els dispositius d'alt rendiment poden aconseguir una eficiència de conversió elèctrica-òptica de quasi el 100% i una vida útil superior a 50000 hores a costos competitius, la qual cosa els converteix en fonts de llum quasi ideals.^{12,14}

Els LEDs generen fotons a través d'un procés denominat electroluminescència,¹³ que consisteix en l'emissió de llum per una substància en aplicar un corrent elèctric.¹⁵ En general, el seu principi bàsic de funcionament és el següent: en primer lloc, s'injecten

càrregues electròniques i es transporten a un semiconductor des dels elèctrodes (electrons -càrregues negatives- des del càtode i buits -càrregues positives- des de l'ànode). Les càrregues es transporten dins de la capa activa, on es troben i poden recombinar-se seguint camins diferents. En materials amb baixa constant dielèctrica, com els semiconductors orgànics, un electró i un buit s'atrauen entre si per interacció electroestàtica de Coulomb, formant un estat lligat denominat excitó. Una vegada formats els excitons, poden recombinar-se mitjançant l'emissió d'un fotó de l'energia corresponent (**Figura 1.1a**).¹⁶ En els materials amb una constant dielèctrica gran, com els semiconductors inorgànics i les perovskites híbrides, l'energia d'enllaç és xicoteta i la recombinació té lloc directament a partir de portadors lliures (**Figura 1.1b**).¹⁷ S'emeten fotons amb una energia igual a la de la banda prohibida del semiconductor (diferència d'energia entre la banda de valència i la de conducció).

Els processos d'injecció, transport i recombinació de càrregues se separen en diferents capes, cadascuna optimitzada per a fer una tasca específica. Els OLED solen constar d'un substrat transparent (vidre), un conductor transparent (ànode), una capa de transport de buits (HTL), una capa emissora de llum, una capa de transport d'electrons (ETL) i un càtode metàl·lic. Per a facilitar la injecció de càrrega, poden col·locar-se capes addicionals d'injecció de buits i electrons (HIL i EIL, respectivament) entre els elèctrodes i els materials de transport (**Figura 1.1a**).¹⁴ Quan s'aplica una tensió externa, els electrons s'injecten des del càtode cap a l'orbital molecular més desocupat (LUMO) del material adjacent, mentre que també s'extrauen electrons des de l'orbital molecular més alt ocupat (HOMO) fins a l'ànode. Aquests portadors de càrrega es mouen a través de les capes cap a la capa emissiva, on formen un excitó que pot relaxar-se amb l'emissió de llum.¹⁶ Per contra, en un LED de perovskita, una pel·lícula de la capa emissiva s'intercala entre una HTL i una ETL; els portadors de càrrega s'injecten i es mouen a través de les bandes de valència i conducció de la perovskita, i es recombinen radiativament emetent llum (**Figura 1.1b**).¹⁹ Aquest tipus de recombinació pot ser molt eficient a causa de la característica de banda prohibida directa d'aquests semiconductors.

Requeriments

Un dels indicadors de rendiment més importants d'un LED és l'eficiència quàntica externa (EQE), que ve donada per la relació entre els fotons emesos pel LED i la quantitat de càrregues (electrons) injectades.²⁰ Per a aconseguir una EQE elevada, és

imprescindible que la capa emissiva tinga un alt rendiment quàntic de fotoluminescència (PLQY), definit com la relació entre els fotons emesos i els absorbits.²¹ Perquè el PLQY de les pel·lícules primes siga òptim, és necessari que la cobertura de la superfície siga homogènia i elevada, a fi d'evitar pèrdues no radiatives per forats o zones no cobertes de la superfície.²² A més, per a aconseguir un LED d'alt rendiment també es requereixen mobilitats de portador de càrregues elevades, que garantisquen que els electrons i els buits puguin arribar als seus elèctrodes corresponents sense recombinar-se, i temps de vida llargs, relacionats amb una baixa densitat de paranys i longituds de difusió llargues.²²⁻²⁴

7.1.2 Cèl·lules solars

Funcionament

Les cèl·lules solars converteixen la llum en electricitat. Solen consistir en un material semiconductor que absorbeix els fotons entrants amb energies superiors o iguals a la seua energia de banda prohibida. L'energia absorbida s'utilitza llavors per a excitar un electró a la banda de conducció, deixant un buit en la banda de valència. Si els materials tenen una constant dielèctrica elevada, com se suposa en aquesta tesi, el parell electró-buit (o excitó) està feblement lligat i els portadors de càrrega poden considerar-se càrregues lliures a temperatura ambient. Per a evitar la seua recombinació, es col·loquen capes selectives de tipus n i tipus p per a electrons i buits, respectivament, a banda i banda de l'absorbidor, de manera que només puguin fluir a través d'una d'elles. Finalment, els portadors de càrrega s'extrauen amb contactes elèctrics connectats a un circuit extern, realitzant així treball i creant un flux d'electricitat (**Figura 1.2**).^{25,26}

Les arquitectures més comuns per a una cèl·lula solar, depenent de la seqüència de deposició de cada component sobre un substrat de vidre transparent, són p-i-n o n-i-p (**Figura 1.3**). Ambdues consisteixen en un substrat conductor transparent com a base, sobre el qual es depositen una capa de transport de buits (HTL, tipus p), un material absorbent, una capa de transport d'electrons (ETL, tipus n) i elèctrodes metàl·lics amunt. La posició de la HTL i la ETL ve donada per l'arquitectura del dispositiu (**Figura 1.3**).

Requeriments

Les característiques dels materials necessaris per a aconseguir cèl·lules solars altament eficients comparteixen algunes similituds amb les descrites anteriorment per als LEDs (vegeu l'Apartat 7.1.1). Idealment, els absorbidors de les cèl·lules solars són semiconductors de banda prohibida directa amb alts coeficients d'absorció en tota la gamma de longituds d'ona absorbides. També es desitja una energia d'enllaç dels electrons i buits baixa per a garantir una separació espontània d'aquests com a portadors lliures després de la il·luminació i evitar pèrdues per recombinació.²³

Per a millorar el transport de càrregues, es busquen materials amb altes mobilitats, llargues longituds de difusió i llargs temps de vida dels portadors de càrrega.^{23,27} Això garanteix que les càrregues lliures puguin transportar-se a través de l'absorbidor i arribar als seus elèctrodes corresponents abans de recombinar-se. Observe's que aquest requisit és més important per a les cèl·lules solars que per als LED, ja que les primeres solen requerir pel·lícules més gruixudes que els segons (centenars de nanòmetres enfront de desenes de nanòmetres) per a garantir una absorció suficient de la llum. Per a això, també és desitjable que les pel·lícules primes de l'absorbidor siguin homogènies, sense forats ni estats defectuosos.²⁸

7.1.3 Generadors termoeleèctrics

Funcionament

Un generador termoeleèctric (TEG) converteix l'energia tèrmica, normalment calor residual, en energia elèctrica.^{29,30} El seu principi de funcionament es basa en l'efecte Seebeck. Segons aquest, quan un material se sotmet a una diferència de temperatura, es crea una diferència de potencial elèctric proporcional al gradient de temperatura que pot convertir-se en electricitat.^{6,31}

Un TEG genèric està compost per una sèrie de termoparells, és a dir, una combinació de semiconductors tipus p i tipus n connectats tant elèctricament (en sèrie) com tèrmicament (en paral·lel). Quan s'aplica una diferència de temperatura, els portadors majoritaris considerats càrregues lliures (buits en un semiconductor de tipus p o electrons en un semiconductor de tipus n) es difonen del costat calent al costat fred, on les càrregues

posseeixen menys energia tèrmica; aquesta és la base microscòpica de l'efecte Seebeck. Aquest potencial electroestàtic impulsa un corrent a través del dispositiu i s'utilitza per a alimentar una càrrega elèctrica a través d'un circuit extern (**Figura 1.4**).^{6,32,33}

L'eficiència d'un dispositiu termoelèctric (TE) està relacionada amb la figura de mèrit (ZT), definida en l'**Equació 1.1**, que depèn dels següents paràmetres clau: S és el coeficient Seebeck, σ és la conductivitat elèctrica, κ és la conductivitat tèrmica i T és la temperatura absoluta.^{29,34}

En primer lloc, el coeficient Seebeck, S , representa la tensió produïda en un material en aplicar un gradient de temperatura, com s'ha introduït anteriorment. La diferència de càrrega creada produeix un potencial elèctric a través del semiconductor. El coeficient Seebeck es defineix com la relació entre el potencial elèctric (tensió) acumulat i la diferència de temperatura. Així, el seu signe serà negatiu a causa del potencial negatiu creat per les càrregues negatives acumulades, en el cas d'un tipus n (**Figura 1.5**). Si, per contra, es tractara d'un semiconductor de tipus p, l'acumulació de càrregues positives (buits) crearà una acumulació positiva i el coeficient Seebeck serà positiu.³⁵ No obstant això, la difusió dels portadors de càrrega cap al costat fred no és infinita. L'acumulació de càrregues en l'extrem fred crearà repulsions electroestàtiques i un gradient de densitat que espantarà les càrregues cap a l'extrem calent. Una vegada que el gradient de temperatura siga contrarestat pel gradient de densitat i les repulsions electroestàtiques, no hi haurà un flux net de càrregues i s'aconseguirà l'estat estacionari.^{33,35}

En segon lloc, la conductivitat elèctrica, σ , mesura la capacitat d'un material per a transportar partícules carregades feblement lligades (electrons i buits) sota la influència d'un camp elèctric.³⁵ Sovint s'expressa com el seu recíproc, la resistivitat elèctrica, ρ . σ depèn directament de la concentració de portadors de càrrega (n), la seua mobilitat (μ) i la càrrega de l'electró (e) (**Equació 1.2**).³¹

Per a un semiconductor de tipus n, $n_e \gg n_h$, de manera que el segon terme de l'**Equació 1.2** pot menysprear-se (i viceversa per a un material de tipus p). Així doncs, l'**Equació 1.2** pot simplificar-se, ja que només depèn de la concentració i la mobilitat dels portadors de càrrega majoritaris. La concentració de portadors de càrrega i les mobilitats de càrrega solen estimar-se mitjançant mesuraments de l'efecte Hall. L'efecte Hall es produeix quan s'aplica un camp magnètic perpendicular a un flux de corrent en un semiconductor, produint una força sobre els portadors que fa que es moguen. Aquest moviment crea un camp elèctric perpendicular tant al flux magnètic com al de corrent que, al seu torn, crea un voltatge conegut com a voltatge Hall (R_H). Com en el cas del

coeficient Seebeck, el signe de la tensió Hall depén del signe dels portadors de càrrega majoritaris. Una vegada conegut el R_H , pot utilitzar-se per a calcular la concentració de portadors de càrrega (n , **Equació 1.3**) i la mobilitat de càrrega (μ , **Equació 1.4**).³⁶

Finalment, la conductivitat tèrmica, κ , mesura la conducció de calor en el material semiconductor a través dels portadors de càrrega ($\kappa_{electrònica}$) i les vibracions de la xarxa (també conegudes com a fonons, κ_{red}) (**Equació 1.5**). $\kappa_{electrònica}$ està relacionada amb la conductivitat elèctrica, mentre que κ_{red} es veu afectada per l'estructura cristal·lina del material i la seua capacitat per a propagar les vibracions de la xarxa.³²

Requeriments

Per a maximitzar el rendiment d'un dispositiu termoelèctric, donat per la figura de mèrit ZT , és necessari optimitzar les propietats tèrmiques i elèctriques. D'acord amb l'**Equació 1.1**, és fonamental aconseguir que un material TE d'alt rendiment tinga una conductivitat elèctrica alta, un coeficient de Seebeck gran per a garantir una conversió eficient de la calor en electricitat i una conductivitat tèrmica baixa per a evitar curtcircuits tèrmics.³⁰

Com molts d'aquests paràmetres presenten interdependència i diferent correlació amb ZT (**Figura 1.6**), l'elecció dels materials termoelèctrics és un desafiament. Idealment, concentracions de portadors entre 10^{19} i 10^{21} cm^{-3} ajuden a equilibrar el coeficient de Seebeck i la conductivitat elèctrica i solen ser presents en metalls o semiconductors molt dopats.³⁴ També serà desitjable l'existència d'un sol tipus de portador per a evitar anul·lar el coeficient de Seebeck.³²

Resum de requeriments

Per tant, per a elegir el material candidat ideal per a cadascuna de les aplicacions abans esmentades, idealment han de complir amb els requisits resumits en la **Taula 1.1**.

7.1.4 Most common materials

En aquesta secció, es presentaran alguns dels materials més utilitzats i actualment en desenvolupament com a capes actives per a LEDs, cèl·lules solars i TEGs, discutint possibles millores i alternatives a aquests.

LEDs

Actualment trobem diferents tipus de LEDs, depenent de la naturalesa i estat físic del material emissor, p.e. LEDs orgànics (OLED), LEDs amb perovskita, LEDs de punts quàntics (QLED), etc.

Els OLEDs eficients utilitzen un material amfitrió semiconductor i un compost emissor que actua com a dopant com a capa emissiva. L'hoste és generalment un compost orgànic (ja siga una molècula xicoteta o un polímer), mentre que els dopants en dispositius d'alta eficiència són un complex organometàl·lic de metalls com l'iridi.¹⁶ A més, el color d'emissió en els OLEDs és relativament fàcil d'ajustar i es poden fabricar pràcticament en qualsevol substrat (vidre, plàstic, metall, etc.).^{13,15} No obstant això, els OLEDs són relativament cars (especialment per a aplicacions d'il·luminació), a causa de l'ús de metalls rars i l'arquitectura complexa del dispositiu. A més, la seua puresa de color és menor en comparació amb altres materials (com els punts quàntics), a causa de l'ús d'emissors orgànics i/o organometàl·lics amb bandes d'emissió àmplies.

Per això, s'estan investigant emissors alternatius, entre els quals trobem les perovskites orgànic-inorgàniques (híbrides). Les perovskites han sigut àmpliament estudiades per a aplicacions en energia fotovoltaica, amb dispositius rècord que ara aconseguixen eficiències pròximes a les cèl·lules solars de silici. Els LEDs de perovskita (PeLEDs) s'han desenvolupat recentment, però també han demostrat el seu gran potencial gràcies al seu rendiment quàntic de fotoluminescència pròxim a la unitat i la possibilitat de modificar la seua banda prohibida o *bandgap* (és a dir, color d'emissió).^{23,24,37}

En general, la fórmula química de les perovskites tridimensionals (3D) utilitzades per a l'optoelectrònica és ABX_3 , on A és un catió monovalent com Cs^+ , metilamoni ($CH_3NH_3^+$) o formamidini ($CH_3(NH_2)_2^+$); B és un metall divalent, normalment Pb^{2+} o Sn^{2+} , i X és un halur (Cl^- , Br^- or I^-). En aquesta estructura de tipus ABX_3 , els cations del lloc A ocupen la cavitat entre quatre octaedres adjacents d'halogenurs metàl·lics BX_6 que

comparteixen les cantonades (**Figura 1.7**).^{23,24} Una dels principals avantatges d'aquests materials és la rica diversitat de propietats a causa d'una gran nombre de substitució del lloc amb altres cations o anions.²²

Una de les preocupacions davant l'ús generalitzat de la perovskita és el seu contingut en plom, ja que és tòxic i perjudicial per al medi ambient. A la Unió Europea, la directiva RoHS2 limita l'ús de metalls perillosos i pesats en productes electrònics consumibles. Per aquest motiu, el desenvolupament de perovskites d'halur sense plom amb característiques de rendiment comparables a les dels compostos de plom és de gran interès, com testifica el creixent nombre de publicacions sobre materials sense Pb.^{38,39}

Un enfocament consisteix a substituir el Pb en l'estructura de la perovskita per altres elements del grup 14, com el Sn o el Ge. No obstant això, són propensos a l'oxidació quan s'exposen a l'aire, la qual cosa compromet l'estabilitat del material. Per a superar aquests problemes, s'han sintetitzat noves famílies de compostos basats en Sb, Bi, Mn o que empen doubles cations, i s'han provat en dispositius emissors de llum.^{37,38} El desenvolupament d'aquesta mena de compostos encara es troba en una fase inicial, però diversos d'ells han mostrat propietats prometedores, com l'elevat PLQY registrat per als halurs de bismut inorgànics.³⁷

Cèl·lules solars

Les tecnologies basades en silici cristal·lí (c-Si) dominen el mercat fotovoltaic actual i representen al voltant del 95% de la producció fotovoltaica mundial.⁴⁰ No obstant això, el desenvolupament i la millora de l'eficiència de les cèl·lules solars basades en silici semblen haver augmentat amb bastant lentitud en els últims anys (**Figura 1.8**, línies blaves), acostant-se al seu límit d'eficiència esperat del 29%.^{40,41} Per a superar aquesta barrera d'eficiència i continuar l'ascens, es necessiten noves generacions de dispositius, com les cèl·lules solars en tàndem. Aquestes combinen dos absorbents diferents amb diferents bandes prohibides per a augmentar l'absorció de la llum solar i, en conseqüència, augmentar l'eficiència general.

Les cel·les solars alternatives basades en telurur de cadmi, arsenur de gal·li, selenur de coure, indi i gal·li (CIGS) i sulfur de coure, zinc i estany (CZTS) també van ingressar al mercat fotovoltaic, aconseguint eficiències superiors al 30% per a GaAs (**Figura 1.8**).⁴⁰⁻⁴² Però, la toxicitat del Cd i l'escassetat i els costos de producció de Ga,

Ti In són grans inconvenients en el desenvolupament i comercialització d'aquesta mena de cèl·lules solars.^{40,42}

Entre les tecnologies fotovoltaïques emergents, les cèl·lules solars de perovskita han acaparat l'atenció en les últimes dècades com a alternativa potencial per a aconseguir cèl·lules solars d'alta eficiència. Les eficiències màximes aconseguides amb cèl·lules solars de perovskita han aconseguit recentment valors rècord entorn del 25,7%,⁴¹ molt prop dels valors aconseguits amb el silici. La perovskita més simple i més àmpliament estudiada és el iodur de plom i metilamoni (MAPbI₃, l'estructura del qual es mostra en la **Figura 1.7**) degut principalment a les seues llargues longituds de difusió de portadors de càrrega i als seus alts coeficients d'absorció (vegeu la secció anterior per a més informació).⁴³

No obstant això, com s'ha comentat anteriorment, la presència de Pb en la seua composició, un metall altament tòxic que pot causar greus efectes neurològics i de comportament en humans,^{44,45} limita el seu ús en mòduls fotovoltaïcs comercials. A causa d'aquests inconvenients, s'estan buscant alternatives com el Sn²⁺ per a substituir al Pb²⁺, del qual s'esperaven resultats prometedors. Desgraciadament, les perovskites d'halur d'estany són relativament inestables, a causa de la tendència del metall a oxidar-se a Sn⁴⁺.⁴⁶ Per tant, les línies d'investigació actuals estan començant a investigar nous materials fotovoltaïcs basats en Bi, Sb, Ge que podrien substituir a les perovskites de plom.^{45,46}

Termoelèctrica

Entre els materials termoelèctrics més utilitzats es troben el Bi₂Te₃, el Sb₂Te₃ i el SnSe, presentant aquest últim un *ZT* de 3.1 (a 798 K), el valor més alt registrat fins hui.^{32,47,48} No obstant això, l'escassetat, toxicitat i alts costos de fabricació d'aquests materials, especialment en el cas dels telururs, suposen un gran obstacle per al seu desenvolupament.^{49,50} A més, la majoria d'ells s'utilitzen en estat monocristal·lí,^{32,47} el que limita la seua integració en diferents arquitectures de dispositius. Un altre obstacle important prové de la temperatura a la qual aconsegueixen el seu punt màxim de funcionament, normalment per damunt dels 300 °C.⁵¹ És fonamental reduir aquesta temperatura mínima necessària per a ampliar les possibles aplicacions dels TEG, com alimentar xicotets dispositius electrònics com a sensors portàtils que poden estar

interconnectats (Internet de les coses o IoT) i els seus nombrosos derivats en la indústria, l'agricultura i els dispositius sanitaris portàtils.⁷ Atés que la majoria d'aquestes aplicacions requereixen temperatures ambient o moderades, es necessiten materials amb un bon rendiment per davall dels 100 °C.⁵²

S'han proposat semiconductors orgànics, com el poli(3,4-etilendioxitiófé) (PEDOT) o derivats del fullere dopats amb cadenes laterals de oligoetilenglicol (OEG) per a la termoelèctrica a baixa temperatura.^{9,53} Encara que no hi ha dubte que es tracta d'alternatives interessants, l'ús d'aquests semiconductors orgànics presenta reptes addicionals: donat la gran grandària dels dopants orgànics (necessaris per a millorar la conductivitat elèctrica i, per tant, la *ZT*), la seua incorporació al material hoste sense alterar l'empaquetament i crear un desordre energètic addicional és tot un repte.⁵³ A més, els polímers solen ser inadequats per als mètodes de deposició de pel·lícules fines d'alta puresa basats en la sublimació al buit. En l'actualitat, alguns materials inorgànics, com Ag₂Se o Cu₂Se, han mostrat bones perspectives per a aplicacions a temperatura ambient, però és necessari ajustar l'estequiometria i les condicions de deposició per a aconseguir les millors eficiències, un procés que pot ser costós i portar molt de temps.^{54,55} Per tant, es busquen materials termoelèctrics inorgànics que funcionen prop de la temperatura ambient.

7.1.5 Mètodes de síntesis i deposició de pel·lícules fines

La majoria d'aquests compostos nous solen sintetitzar-se normalment mitjançant processament en dissolució (vegeu el Capítol 2 per a més informació), la qual cosa implica l'ús de dissolvents orgànics d'alt punt d'ebullició, com la N,N-dimetilformamida (DMF) i el dimetilsulfòxid (DMSO), complicats passos de cristallització i el desaprofitament d'enormes quantitats de material.⁴⁵ Donada l'escassetat de recursos, diners i temps, és necessari buscar nous mètodes de preparació d'aquests materials.

En aquesta línia, els mètodes mecanoquímics, que consisteixen a fer reaccionar els precursors per mètodes purament mecànics, estan guanyant atenció en els últims anys per a la síntesi de materials. En particular, l'enfocament mecanoquímic en sec per molta de boles dels precursors estequiomètrics pot classificar-se dins de la "química verda", ja que no implica l'ús de dissolvents, compostos tòxics, altes temperatures, i evita el desaprofitament de materials i derivats durant el procés.⁵⁷

De forma resumida, els precursors necessaris per a la síntesi, juntament amb algunes perles de molta, es col·loquen dins de recipients de molta adequats. Aquests es col·loquen en el molí de boles en posició horitzontal i, a continuació, s'agiten fortament. A causa del ràpid moviment dels recipients, les perles es mouren per inèrcia colpejant amb altes energies contra els precursors i les parets del recipient fent que els precursors reaccionen formant el producte (veure Capítol 2 per a més informació). Es tracta d'un mètode senzill però molt eficaç per a sintetitzar materials ràpidament en grans quantitats i amb gran puresa de fase.⁵⁸ Prova d'açò és que el nombre d'informes sobre compostos sintetitzats mecanoquímicament no deixa de créixer.⁵⁹⁻⁶¹

Per a aplicar aquests materials en dispositius optoelectrònics i fotovoltaics és necessari depositar-los en pel·lícules fines. Un dels atractius d'aquests nous compostos és la possibilitat d'obtenir pel·lícules fines d'alta qualitat amb mètodes senzills de deposició en solució. El processament en solució s'ha utilitzat àmpliament per a depositar tot tipus de materials, incloses les perovskites, a causa de la simplicitat i el baix cost del mètode.²¹ Normalment, els compostos precursors es dissolen en dissolvents polars com DMF, DMSO o acetonitril, i després es depositen sobre un substrat amb diferents tècniques com el *blade coating*, *drop casting*, *spin-coating*, etc. Aquest últim, el *spin-coating*, és un dels mètodes més utilitzats per a la deposició de pel·lícules de perovskita, en el qual la solució es deixa caure sobre el substrat i es fa girar a gran velocitat per a obtenir una pel·lícula plana i fina.⁶²

La formació de la pel·lícula depèn de paràmetres com la concentració de la solució, la velocitat de centrifugat i l'acceleració.²¹ A més, també és important controlar la velocitat d'evaporació del dissolvent, ja que afecta la cristallització dels materials i, en conseqüència, a les propietats de transport de càrrega de la pel·lícula fina. Per tant, sol ser necessari un procés posterior per a garantir la conversió quantitativa dels materials en una pel·lícula policristalina i per a eliminar els residus de dissolvent. No obstant això, tots aquests paràmetres són difícils de controlar, la qual cosa dona lloc a un creixement de la pel·lícula no reproduïble i incontrolable, perjudicant el desenvolupament de dispositius optoelectrònics.

Els mètodes de deposició tèrmica en buit ofereixen alguns avantatges per a superar aquests problemes.⁶² La deposició en buit té l'avantatge de controlar millor l'estequiometria i la grossària de la pel·lícula, la qual cosa dona lloc a superfícies planes i homogènies, de gran puresa. A més, permet assemblar dispositius multicapa sense cap interacció química entre les capes, com pot ocórrer amb els processos de deposició en

solució.^{62,63} La deposició en buit de font única (SSVD) consisteix en la sublimació tèrmica directa d'un compost pre-sintetitzat en una càmera d'alt buit, on el material es condensa i recristal·litza en un substrat col·locat per damunt de la font. Aquest mètode és avantatjós per la seua simplicitat, bon control de l'estequiometria del material amb un temps de realització reduït. Tenint en compte els bons resultats que ha mostrat aquesta tècnica aplicada a les perovskites d'halur,⁶⁵ també podria aplicar-se per a la deposició dels compostos estudiats ací.

7.1.6 Objectius de la tesi

Aquesta tesi té com a objectiu investigar, sintetitzar i caracteritzar materials inorgànics de baixa toxicitat (en particular lliures de Pb) amb potencial aplicació en optoelectrònica i termoelèctrica. El mètode de síntesi també ha de complir els requisits de la "química verda" per a emfatitzar la sostenibilitat i la no toxicitat del procés. D'ací ve que la mecanoquímica en sec per molta de boles siga el mètode de síntesi preferit per a aquests nous materials. Amb la finalitat de comprovar la seua possible incorporació a dispositius optoelectrònics i termoelèctrics, s'estudia la seua deposició en làmines primes mitjançant tècniques de buit.

La tesi s'estructura com segueix:

- **Capítol 3:** síntesi, deposició en capa prima i caracterització d'una sèrie d'halurs ternaris de coure, CsCu_2X_3 i $\text{Cs}_3\text{Cu}_2\text{X}_5$ ($\text{X} = \text{Cl}, \text{Br}, \text{I}$), amb un elevat PLQY blau, mostrant potencial per a la fabricació de LEDs.
- **Capítol 4:** síntesi, deposició en capa fina i caracterització de la perovskita doble $\text{Cs}_2\text{AgBiBr}_6$ i el seu dopat amb Sn, Zn i Ge. L'estudi s'acompanya de càlculs teòrics per a avaluar la seua aplicació en fotovoltaica.
- **Capítol 5:** síntesi, deposició en capa fina i caracterització de la perovskita CsSnI_3 per a analitzar el seu ús com a material termoelèctric per a aplicacions a temperatura ambient.

Els materials ací presentats havien sigut escassament estudiats amb anterioritat per als fins esmentats. Donada la seua facilitat de síntesi, baixa toxicitat i rendiment, poden representar un pas avant en la investigació de nous materials per a optoelectrònica i termoelèctrica.

7.2 Capítol 3: Síntesi sense dissolvents i deposició en capa fina d'halurs de cesi i coure amb fotoluminescència blau brillant

7.2.1 Resum

Els materials luminescents blaus tenen aplicacions potencials en sistemes d'il·luminació, com la preparació de díodes emissors de llum blanca. No obstant això, els emissors blaus de banda ampla amb alts rendiments quàntics de fotoluminescència (PLQY) solen ser més difícils d'obtenir que els emissors verds o rojos. En aquest treball hem preparat dues sèries d'halurs inorgànics de cesi i coure, amb les fórmules generals $\text{Cs}_3\text{Cu}_2\text{X}_5$ i CsCu_2X_3 ($\text{X} = \text{Cl}, \text{Br}, \text{I}$ i les seues mescles) mitjançant síntesi mecanoquímica en sec a temperatura ambient. Identifiquem el $\text{Cs}_3\text{Cu}_2\text{I}_5$ com el material més prometedor, ja que manté la luminescència blava centrada en 442 nm amb un elevat PLQY ($> 40\%$) després de diversos dies en l'aire (el $\text{Cs}_3\text{Cu}_2\text{Cl}_5$ mostra un PLQY significativament major, superior al 80%, però és inestable en l'aire). Basant-nos en això, fabriquem pel·lícules primes de $\text{Cs}_3\text{Cu}_2\text{I}_5$ homogènies i sense forats mitjançant deposició tèrmica al buit d'una sola font. La fase cristal·lina i les característiques de fotoluminescència es mantenen en les pel·lícules primes, la qual cosa demostra que aquests materials de baixa toxicitat es poden sintetitzar i processar per rutes totalment lliures de dissolvents per a una aplicació generalitzada en dispositius optoelectrònics.

7.2.2 Introducció

En l'última dècada, les perovskites d'halur de plom han sorgit com a materials prometedors per a l'optoelectrònica,^{11,22,85,86} però la necessitat de substituir els ions tòxics Pb^{2+} per altres metalls més respectuosos amb el medi ambient requereix la cerca de diferents halurs metàl·lics ternaris i quaternaris, amb diverses estequiometries i estructures cristal·lines.^{38,87} Entre ells, els halurs metàl·lics ternaris totalment inorgànics basats en Cu(I) són especialment prometedors, sobretot per a aplicacions en díodes emissors de llum (LED).^{16,88,89} Poden formar-se cristalls estables amb dues estequiometries diferents: CsCu_2X_3 i $\text{Cs}_3\text{Cu}_2\text{X}_5$ ($\text{X} = \text{Cl}, \text{Br}, \text{I}$, o mescles dels mateixos).

En la **Figura 3.1** es representa l'estructura cristal·lina més comuna de tots dos compostos a temperatura ambient.

El Cu(I) es troba en coordinació tetraèdrica amb els halurs en tots dos casos. No obstant això, el $\text{Cs}_3\text{Cu}_2\text{X}_5$ està constituït per dímers aïllats de CuX_4 , mentre que el CsCu_2X_3 consisteix en tetraedres de costats compartits disposats espacialment com a fils. Basant-nos en aquestes consideracions, aquestes estructures poden denominar-se 0D i 1D respectivament.⁸⁹ Pel que sabem, només existeixen uns pocs informes sobre aquests compostos.⁸⁹⁻⁹² A més, en les publicacions esmentades, la síntesi i deposició en capa fina d'aquests es va dur a terme mitjançant processos de dissolució en dissolvents orgànics (tòxics), com DMF o DMSO, o mitjançant rutes tèrmiques que consumeixen molt temps i energia. Últimament, la síntesi mecanoquímica sense dissolvents (MCS) ha demostrat ser un mètode molt senzill i eficient per a sintetitzar diferents halurs metàl·lics multinaris de fase pura,^{58-61,65,93-96} com s'ha presentat prèviament en els Capítols 1 i 2. En aquest treball, la MCS permet la formació d'halurs inorgànics ternaris de Cu(I) d'alta qualitat. En particular, alguns dels compostos sintetitzats presenten una fotoluminescència brillant fins i tot com a pols no passivats i són estables en aire durant diversos dies. A més, els compostos sintetitzats poden depositar-se com a pel·lícules fines amb bona morfologia, cristal·linitat i fotoluminescència. Per a això, fem la deposició en buit de font única (SSVD), que recentment ha demostrat ser un mètode fàcil, ràpid i no tòxic (sense dissolvents) per a la deposició d'altres compostos d'halurs inorgànics i híbrids orgànic-inorgànics (vegeu el Capítol 2 per a una explicació detallada).^{28,65,97}

7.2.3 Conclusions

En resum, hem demostrat la síntesi de CsCu_2X_3 i $\text{Cs}_3\text{Cu}_2\text{X}_5$ ($\text{X} = \text{Cl}, \text{Br}, \text{I}$ i les seues mescles) mitjançant síntesi mecanoquímica senzilla sense dissolvents. Els compostos d'halur pur $\text{Cs}_3\text{Cu}_2\text{X}_5$ presenten una elevada PLQY a la regió blava-verd de l'espectre visible, la qual cosa els converteix en materials molt prometedors per a il·luminació o fotodetectors d'UV profund. El $\text{Cs}_3\text{Cu}_2\text{Cl}_5$ emissor verd es va sintetitzar amb un 78% de PLQY (81% després d'exposició a l'aire i posterior recuita tèrmica), encara que amb poca estabilitat en l'aire. En canvi, el $\text{Cs}_3\text{Cu}_2\text{I}_5$ emissor de blau va aconseguir un PLQY estable superior al 40% fins i tot quan es va emmagatzemar en aire durant diversos dies. Les diferències en les característiques espectrals s'han racionalitzat

en termes de diferents estructures cristal·lines, com demostra l'ajust de tot el patró del senyal de XRD, mentre que les diferències en l'estabilitat a l'aire poden explicar-se per mecanismes d'oxidació preferencials dels halurs de Cu(I) a halurs de Cu(II). Finalment, hem sigut capaços de transformar pólvores de $\text{Cs}_3\text{Cu}_2\text{I}_5$ en làmines primes homogènies mitjançant deposició al buit d'una sola font amb excel·lent cristal·linitat i característiques òptiques conservades.

7.3 Capítol 4: Ajust de l'absorció òptica de les perovskites dobles $\text{Cs}_2\text{AgBiBr}_6$ substituïdes per Sn, Ge i Zn: efectes estructurals i electrònics

7.3.1 Resum

Les perovskites dobles (DP) d'halur sense plom són materials altament modificables en termes de composició química i propietats òptiques. Una de les més conegudes és la $\text{Cs}_2\text{AgBiBr}_6$, que es considera un prometedor absorbent per a l'energia fotovoltaica. No obstant això, la seua energia de banda prohibida (entorn de 1.9 – 2.3 eV) continua sent massa gran per a les cèl·lules solars en tàndem. En aquest capítol es presenta la síntesi mecanoquímica de $\text{Cs}_2\text{AgBiBr}_6$ substituïts amb Sn-, Ge- i Zn en forma de pols, amb energies de *bandgap* de 1.55, 1.80 i 2.02 eV, respectivament. Aquestes diferències es racionalitzen mitjançant càlculs de Teoria del Funcional de la Densitat (DFT), demostrant efectes electrònics i estructurals combinats (desordre) introduïts pels substituents del catió metàl·lic divalent. Finalment, presentem les primeres làmines primes depositades en buit de la DP substituïda amb Sn, que també mostren un notable estrenyiment del *bandgap*, la qual cosa aplanava el camí cap a la seua aplicació en cèl·lules solars fotovoltaïques.

7.3.2 Introducció

Les perovskites d'halur de plom, materials prometedors per a futurs sistemes fotovoltaïcs i altres aplicacions optoelectròniques, segueixen la fórmula general APbX_3 , on A representa un catió monovalent (per exemple, Cs^+ , CH_3NH_3^+ , or $\text{CH}(\text{NH}_2)_2^+$) i X és

un anió halur com Cl^- , Br^- , o I^- (vegeu el Capítol 1 per a més informació). Malgrat les prestacions ben documentades de l'optoelectrònica basada en perovskites d'halur de plom,^{125,126} la toxicitat dels ions Pb^{2+} dificulta l'aplicació generalitzada d'aquests materials.¹²⁷ Substituint el Pb(II) per una combinació de cations B(I) i B(III), però mantenint el mateix marc aniònic (vegeu la **Figura 4.1**), es poden formar fàcilment perovskites dobles (DP).

Les perovskites dobles d'halur ofereixen una àmplia gamma de propietats que poden competir directament amb les de plom, com el seu major temps de vida a temperatura ambient, major estabilitat a la calor i a la humitat, i menor toxicitat.¹²⁸ La seua fórmula química $\text{A}_2\text{B}^+\text{B}^{3+}\text{X}_6$, que conté un catió monovalent (B^+) i un altre trivalent (B^{3+}), mostra la gran varietat de combinacions atòmiques diferents que poden formar-se amb aquesta estequiometria. $\text{Cs}_2\text{NaInCl}_6$, $\text{Cs}_2\text{KInCl}_6$, $\text{Cs}_2\text{AgInCl}_6$, $\text{Cs}_2\text{AgSbCl}_6$, o $\text{Cs}_2\text{NaBiCl}_6$ són només alguns exemples de DP estables.¹²⁹ No obstant això, aquestes DP de clorur solen tindre energies de banda prohibida superiors a 2.5 eV, que és massa gran per a aplicacions fotovoltaïques.¹³⁰ En aquest treball, ens centrem en la perovskita doble $\text{Cs}_2\text{AgBiBr}_6$, amb un *bandgap* indirecte de 1.95 eV, que s'acosta més a un valor útil en aplicacions com a absorbent d'ampli *bandgap* en dispositius en tàndem.¹²⁸ De fet, en la bibliografia s'ha estudiat el seu rendiment en cèl·lules solars, però la màxima eficiència de conversió de potència (PCE) registrada és només del 2.84% amb una fotocorrent màxima de l'ordre de 5 mA cm^{-2} .¹³¹ S'ha suggerit que això podria superar-se mitjançant l'ús de pel·lícules més gruixudes per a augmentar l'absorció.¹³² No obstant això, s'ha informat que les pel·lícules de $\text{Cs}_2\text{AgBiBr}_6$ tenen una longitud de difusió de càrrega limitada, la qual cosa al seu torn limita el rendiment d'aquestes pel·lícules més gruixudes com a absorbents fotovoltaïcs.¹³²

Es requereix una absorció més eficaç de la llum visible (mitjançant l'estrenyiment de la banda prohibida) per a garantir les futures aplicacions fotovoltaïques de les perovskites dobles. Les substitucions parcials del lloc B s'han descrit com una via estratègica per a abordar aquesta qüestió. Karunadasa i col·laboradors han demostrat un estrenyiment del *bandgap* d'uns 0.5 eV utilitzant cations monovalents i divalents amb la mateixa configuració electrònica ns^2 que el Bi(III), a saber, Tl(I) i Sn(II), juntament amb un canvi induït en la naturalesa del *bandgap* d'indirecte a directe.^{133,134} No obstant això, l'addició de l'element Tl, altament tòxic, juntament amb la lenta síntesi en procés de dissolució i la falta d'un mecanisme de substitució clar, podria obstaculitzar el desenvolupament futur d'aquesta substitució del lloc B. Mitzi i col·laboradors també van

descobrir una disminució de l'energia de la banda prohibida d'uns 0.3 eV per l'addició de Sb(III), un altre element amb una configuració electrònica de valència ns^2 .¹³⁵ En canvi, es va descobrir que l'addició de In(III), amb una configuració electrònica diferent (nd^{10} , igual que Ag(I)), ampliava la banda prohibida.¹³⁵ A partir d'aquests resultats, una regla fenomenològica sembla suggerir que els substituents de configuració electrònica ns^2 (Tl^+ , Sn^{2+} , Sb^{3+}) provoquen una disminució del *bandgap* del $Cs_2AgBiBr_6$, mentre que els substituents nd^{10} condueixen a un augment del *bandgap*. Aquesta observació ens va portar a intentar ajustar el *bandgap* mitjançant mètodes sintètics més senzills i ràpids,⁵⁸ juntament amb la introducció de nous substituents dels quals no s'havia informat experimentalment, en particular Ge^{2+} i Zn^{2+} , amb configuracions electròniques ns^2 and nd^{10} , respectivament.

En aquest treball es descriu la síntesi mecanoquímica ràpida en sec de $Cs_2AgBiBr_6$ substituït per Sn^{2+} , Ge^{2+} , i Zn^{2+} , així com la seua caracterització òptica i estructural. Note's que els nivells electrònics introduïts directament pels dopants podrien no ser l'únic efecte en joc a l'hora de modificar l'absorció del $Cs_2AgBiBr_6$ (el terme dopant s'utilitza ací en el sentit general de substituent o additiu, sense cap implicació a priori sobre la concentració de càrregues lliures o la posició del nivell de Fermi dins del *bandgap*). De fet, els estudis teòrics han demostrat que el grau d'ordre o desordre en l'estructura, és a dir, l'alternança precisa d'octaedres $[AgBr_6]^{5-}$ i $[BiBr_6]^{3-}$ o, per contra, l'existència de dominis $[AgBr_6]^{5-}$ i $[BiBr_6]^{3-}$ segregats, pot tindre una gran influència en la banda prohibida. En particular, Yang et al.¹³⁶ van calcular que l'energia del *bandgap* pot reduir-se de 1.93 eV per a l'estructura totalment ordenada (és a dir, Ag i Bi perfectament alternats) a només 0.44 eV per a la totalment desordenada (és a dir, distribució aleatòria de Ag i Bi -no totalment segregada-), amb valors intermedis més pròxims als observats experimentalment per a una estructura parcialment desordenada. A més, van demostrar que l'addició de dopants conduïa a una menor diferència d'energia de formació entre les estructures ordenada i desordenada. En altres paraules, el menor *bandgap* observat per al $Cs_2AgBiBr_6$ dopat no sols podria estar directament relacionat amb els efectes electrònics descrits anteriorment, sinó també amb un major desordre en l'estructura.

Per tant, per a racionalitzar els resultats experimentals obtinguts amb additius de Sn(II), Ge(II) i Zn(II), es realitzen càlculs teòrics. Els nostres resultats confirmen una substitució veïna favorable dels cations dopants del lloc B, la qual cosa dona lloc a una reducció del *bandgap* en passar del $Cs_2AgBiBr_6$ referible als anàlegs dopats amb Ge^{2+} i amb Sn^{2+} . La mescla dels orbitals fronterers ocupats i desocupats del dopant B^{2+} en la

banda de valència i de conducció, respectivament, explica un canvi en la dimensionalitat electrònica de la perovskita doble que, juntament amb les deformacions estructurals octaèdriques, condueix a una transició indirecta-directa del *bandgap*.

Finalment, els aliatges basats en Sn es depositen com a pel·lícules primes mitjançant deposició en buit d'una sola font amb diferents càrregues de substituents. D'aquesta manera, vam demostrar les primeres pel·lícules primes de DP amb una major absorció en el visible, la qual cosa aplanava el camí cap a la seua aplicació en fotovoltaica i altres aplicacions optoelectròniques basades en pel·lícules primes.

7.3.3 Conclusions

Hem estudiat l'ajust del *bandgap* de la perovskita doble $\text{Cs}_2\text{AgBiBr}_6$ sintetitzada per mètodes sense dissolvents a través de dues rutes diferents: (i) mitjançant recuita tèrmica postsíntesi i (ii) mitjançant la introducció de diferents dopants en l'estructura. El primer mètode va demostrar que un augment de la temperatura de recuita condueix a un eixamplament del *bandgap*, de 1.94 eV per a la forma prístina a 2.16 eV quan es recou a 300 °C. La raó d'aquest fenomen pot residir en l'augment de l'ordenament de la xarxa Ag-Bi després de la recuita, que provoca un augment del *bandgap* de la perovskita doble. Per contra, la incorporació de SnBr_2 i GeBr_2 a la DP va produir un notable desplaçament al roig en l'inici de l'absorció (1.55 i 1.80 eV, respectivament). En canvi, l'addició de ZnBr_2 va induir un lleuger augment del *bandgap*. La raó subjacent d'aquests canvis es va estudiar mitjançant càlculs de DFT, indicant que el Sn^{2+} i Ge^{2+} canvien la dimensionalitat electrònica de la perovskita doble mesclant els seus orbitals *s* ocupats en la VBM i les seues orbitals *p* desocupats en la CBM. Això, en combinació amb deformacions estructurals octaèdriques, condueix a una reducció significativa del *bandgap*, d'acord amb els resultats experimentals, i a una transició indirecta a directa en la naturalesa del *gap*. Finalment, es van depositar pel·lícules primes de DP dopades amb Sn mitjançant deposició en buit d'una sola font. Es van estudiar diferents concentracions de dopant, revelant la possibilitat de sintonitzar les propietats d'absorció en pel·lícules primes. Aquests resultats aplanen el camí per a l'aplicació de pel·lícules primes de $\text{Cs}_2\text{AgBiBr}_6$ substituïdes per cations en dispositius optoelectrònics de pròxima generació.

7.4 Capítol 5: Capes fines de iodur de cesi i estany depositades en buit amb propietats termoelèctriques modulables

7.4.1 Resum

La majoria dels materials termoelèctrics actuals presenten importants inconvenients, com la seua toxicitat, escassetat i temperatures màximes de funcionament superiors a 300 °C. En aquest treball es presenten les propietats termoelèctriques de diferents fases cristal·lines de pel·lícules primes de perovskita basades en Sn. La fase 2D, Cs₂SnI₄, s'obté mitjançant deposició tèrmica en buit i es converteix fàcilment en la fase β negra de CsSnI₃ (B-β CsSnI₃) mitjançant recuita a 150 °C. El B-β CsSnI₃ és un semiconductor de tipus p amb una figura de mèrit (*ZT*) que oscil·la entre 0.021 i 0.033 per a temperatures inferiors a 100 °C, la qual cosa ho converteix en un candidat prometedor per a alimentar xicotets dispositius electrònics, com a sensors portàtils que poden estar interconnectats en la denominada Internet de les Coses. La fase B-β és estable en nitrogen, mentre que s'oxida espontàniament a Cs₂SnI₆ en exposar-se a l'aire. El Cs₂SnI₆ mostra un coeficient Seebeck negatiu i una conductivitat tèrmica ultrabaixa. No obstant això, els valors *ZT* són un ordre de magnitud inferiors als de B-β CsSnI₃ a causa d'una conductivitat elèctrica considerablement menor.

7.4.2 Introducció

Els generadors termoelèctrics (TEGs) representen una font molt prometedora d'energia renovable, ja que converteixen directament la calor (residual) en electricitat.^{9,32} Els materials termoelèctrics solen caracteritzar-se per la figura de mèrit, *ZT* (**Equació 1.1**), que depèn del coeficient Seebeck, la conductivitat elèctrica, la conductivitat tèrmica i la temperatura absoluta. Així, per a maximitzar el valor *ZT* d'un material donat, es requereix un coeficient Seebeck gran, una conductivitat elèctrica alta i una conductivitat tèrmica baixa.^{31,32}

Com s'ha presentat anteriorment en el Capítol 1, es busquen materials termoelèctrics inorgànics que funcionen prop de la temperatura ambient. En la cerca de materials alternatius que siguin fàcils de processar, les perovskites d'halurs metàl·lics, com CH₃NH₃PbI₃, FASnI₃ o CsSnI₃, han sorgit en els últims anys com a potencials

materials termoelèctrics. De fet, s'ha demostrat una conductivitat tèrmica ultrabaixa ($< 0.5 \text{ W m}^{-1} \text{ K}^{-1}$) i coeficients Seebeck acceptables.^{34,154,155} Les perovskites d'halur basades en Sn superen a les seues homòlogues de Pb en rendiment termoelèctric a causa de l'autooxidació de Sn^{2+} a Sn^{4+} , actuant com un mecanisme d'autodopatge que millora la seua conductivitat elèctrica.¹⁵⁵ A més, la seua toxicitat es redueix a causa de l'absència de Pb en la seua composició. En aquest treball, ens centrem en CsSnI_3 , que a més conté Cs en lloc d'un catió orgànic, oferint una estabilitat tèrmica molt major que les perovskites orgànic-inorgàniques.¹⁵⁶ Cal tindre en compte que el Cs és fins a tres ordres de magnitud més abundant en l'escorça terrestre que el Bi o el Te, que són elements comuns per als termoelèctrics actuals.⁵² De fet, en comparar l'abundància i la producció anual, cal destacar que el Cs és un dels elements més "infraproducts" i amb marge per a augmentar la seua producció.¹⁵⁷ Quant a la toxicitat, el cesi té 40 isòtops coneguts, dels quals el radioactiu ^{137}Cs és el més tòxic i perillós. En aquest treball, utilitzem el seu isòtop més estable, ^{133}Cs , amb una toxicitat molt de menor.¹⁵⁸ Per tant, CsSnI_3 sorgeix com una alternativa prometedora a la majoria dels compostos termoelèctrics actuals, com PbTe , Bi_2Te_3 o Sb_2Te_3 , pel que fa a l'abundància d'elements i la toxicitat.

Se sap que el CsSnI_3 té quatre polimorfs diferents, dos d'ells existents a temperatura ambient (**Taula 5.1**)^{159,160}: una fase groga, Y CsSnI_3 , amb una estructura ortoròmbica unidimensional de doble cadena i una perovskita ortoròmbica tridimensional de color negre, $\text{B-}\gamma \text{ CsSnI}_3$. Segons la bibliografia, la recuita de Y CsSnI_3 a $150 \text{ }^\circ\text{C}$ en atmosfera inerta dona lloc a una perovskita cúbica negra ($\text{B-}\alpha$), que en refredar-se de nou per davall de $150 \text{ }^\circ\text{C}$ es transforma en una fase tetragonal negra ($\text{B-}\beta$), i en la fase ortoròmbica negra $\text{B-}\gamma$ quan es refreda per davall de $80 \text{ }^\circ\text{C}$. L'exposició de $\text{B-}\gamma \text{ CsSnI}_3$ a l'aire durant un breu període de temps desencadena la transformació en Y CsSnI_3 , ja que aquesta fase és termodinàmicament més estable en condicions ambientals.^{159,160} Finalment, després d'una exposició prolongada a l'aire, Y CsSnI_3 evoluciona a Cs_2SnI_6 , una perovskita doble ordenada amb vacants que conté ions Sn^{4+} oxidats en lloc de Sn^{2+} .¹⁶¹ En informes anteriors s'han estudiat les propietats termoelèctriques de les làmines primes de CsSnI_3 . Saini et al. van preparar pel·lícules crescudes mitjançant un procés de dissolució en mescles DMSO:DMF i utilitzant tolué com a antisolvent, seguit d'una recuita tèrmica que va aconseguir un ZT de 0.137 a temperatura ambient.¹⁶² Kontos et al. van estudiar l'efecte del dopat amb SnF_2 en pel·lícules de CsSnI_3 recobertes per *spin-coating*, revelant un canvi en la resistència elèctrica després de l'exposició a l'aire de les mostres.¹⁶⁰ En la mateixa línia, Liu et al. van aconseguir una ZT entorn de 0.14 en

pel·lícules de CsSnI_3 dopades amb SnCl_2 i depositades mitjançant un mètode d'evaporació seqüencial.¹⁶³ No obstant això, aquest rendiment només s'aconsegueix després de la introducció de SnCl_2 addicional en l'estructura i després de l'exposició de les pel·lícules a l'aire i a la humitat durant 6 minuts, mentre que es va observar que un temps d'exposició més llarg disminuïa de nou la ZT .¹⁶³ Kanatzidis i col·laboradors van estudiar les propietats tèrmiques i de transport d'una sèrie de perovskites del tipus $\text{CsSnBr}_{3-x}\text{I}_x$, obtenint un ZT per a CsSnI_3 de 0.025 a 300 K que aconsegueix un màxim de 0.15 a 550 K. Aquests resultats es van aconseguir amb cristalls ($6 \times 6 \times 1,5$ mm) sinteritzats a 923 K durant períodes de més de 24 h.¹⁶⁴ En resum, aquests resultats demostren el potencial de les pel·lícules fines de CsSnI_3 per a TE. No obstant això, els protocols esmentats inclouen complexos processaments amb dissolvents, necessitat de dopants o additius externs, síntesis a alta temperatura i/o són molt sensibles a l'aire i la humitat. Per tant, es busquen rutes més robustes i senzilles.

La nostra investigació se centra en l'estudi de la deposició al buit de pel·lícules fines de CsSnI_3 mitjançant l'evaporació tèrmica en una sola font de pólvores seques presintetitzats. La deposició tèrmica en buit mostra un millor control de la grossària, un major rendiment i una major reproducibilitat en comparació amb el processament en solució.^{63,165} Cal destacar que la pel·lícula sintetitzada presenta l'estructura bidimensional característica del Cs_2SnI_4 , una fase de la qual fins ara només s'havia informat teòricament. La seua conductivitat elèctrica és molt baixa, però pot incrementar-se en diversos ordres de magnitud després de la recuita i la consegüent conversió a $\text{B-}\beta$ CsSnI_3 , aconseguint un ZT màxim de 0.033.

7.4.3 Conclusions

En conclusió, informem de la deposició tèrmica de Cs_2SnI_4 directament a partir de la SSVD de pols de CsSnI_3 sintetitzat per molt amb boles. Els espectres d'absorció d'aquestes pel·lícules primes revelen la presència de la perovskita 2D ($E_g = 1.42$ eV) juntament amb traces de γ CsSnI_3 ($E_g = 2.45$ eV). La seua conductivitat elèctrica és extremadament baixa, però augmenta quasi 7 ordres de magnitud després de la recuita durant 25 min a 150 °C, quan es forma la fase $\text{B-}\beta$ CsSnI_3 . $\text{B-}\beta$ CsSnI_3 mostra una conductivitat tèrmica ultrabaixa i una conducció de tipus p corroborada pels mesuraments de Seebeck i Hall. La seua conductivitat elèctrica disminueix en augmentar la

temperatura, causada per la reducció de la mobilitat de càrrega. En el rang de temperatures estudiat (RT – 100 °C) i sense exposició a l'aire ni dopatge extern addicional, el ZT màxim aconseguit és de 0.0333 ± 0.0013 a 50 °C. La fase beta negra es conserva en nitrogen durant més de 7 dies, però s'oxida a Cs_2SnI_6 en exposar-la a l'aire durant unes hores. El Cs_2SnI_6 té una conductivitat elèctrica menor, una conductivitat tèrmica ultrabaixa i un coeficient Seebeck absolut major, aconseguint un ZT de 0.0011 ± 0.0003 (100 °C) (vegeu la **Taula 5.2** per als valors màxims aconseguits). Per tant, tant B - β CsSnI_3 com Cs_2SnI_6 mostren potencial per a la seua implementació en TEGs operatius a baixa temperatura quan la conductivitat d'aquests materials puga millorar-se de manera controlable.

7.5 Capítol 6: Perspectives generals i conclusions

L'objectiu principal d'aquesta tesi ha sigut la cerca i desenvolupament de compostos inorgànics i de baixa toxicitat (en particular lliures de plom) amb possibles aplicacions en optoelectrònica i termoelèctrica per a substituir als materials més utilitzats i/o desenvolupats actualment en aquests camps. Donat l'enfocament sostenible de les aplicacions d'aquests materials, hem volgut emfatitzar-lo encara més emprant mètodes de síntesi i deposició ecològics i lliures de dissolvents. Per aquesta raó, la síntesi mecanoquímica en sec per molta de boles i la deposició al buit de font única han sigut els mètodes preferits per a les tres famílies de materials ací presentades. En particular, cal destacar els següents assoliments:

- **Capítol 3:** s'han sintetitzat dues sèries de compostos a base de coure amb la fórmula CsCu_2X_3 i $\text{Cs}_3\text{Cu}_2\text{X}_5$ ($X = \text{Cl}, \text{Br}, \text{I}$, i mescles dels mateixos) amb potencial demostrat per a dispositius emissors de llum, almenys basats en aquests últims. Canviant l'halur, ha sigut possible sintonitzar la longitud d'ona d'emissió, que va des del verd per a l'espècie pura de Cl fins al blau per a l'espècie pura de I. Entre elles, la més emissiva és $\text{Cs}_3\text{Cu}_2\text{Cl}_5$, amb un PLQY al voltant del 80% centrat en 516 nm (emissió verda). No obstant això, el $\text{Cs}_3\text{Cu}_2\text{I}_5$, amb un PLQY superior al 40% a 442 nm (emissió blava), és possiblement el més interessant de tots ells a causa de l'escassetat de díodes emissors de llum blava altament eficients. S'ha demostrat que manté les seues extraordinàries prestacions fins i tot després de l'exposició a l'aire i després de la seua deposició en pel·lícula prima, ja siga per

processament en dissolució o per deposició tèrmica en buit. Aquest treball és, per tant, especialment rellevant per a proposar alternatives altament eficients i de baixa toxicitat per als LED, que fins i tot poden combinar-se entre si per a produir llum blanca, tema que es proposa per a futurs treballs.

- **Capítol 4:** per a ampliar les aplicacions fotovoltaïques de la perovskita doble $\text{Cs}_2\text{AgBiBr}_6$ era necessari estretyar la seua banda prohibida (1.94 eV, indirecta), considerada massa ampla per a les cèl·lules solars d'unió simple. Això es va intentar seguint dos enfocaments diferents. En primer lloc, la recuita de les pols sintetitzades va conduir a un eixamplament del *bandgap*, fins a 2.16 eV, contràriament al perseguit. En segon lloc, es va provar la introducció de diferents dopants en l'estructura mitjançant la síntesi mecanoquímica. La incorporació de diferents quantitats de SnBr_2 i GeBr_2 va desplaçar considerablement l'inici de l'absorció (fins a 1.55 i 1.80 eV, respectivament) i va modificar la naturalesa del *bandgap* (d'indirecte a directe). Per contra, la introducció de ZnBr_2 no va produir una reducció del *bandgap* sinó un augment, fins a 2.02 eV. Es van realitzar càlculs de Teoria del Funcional de la Densitat (DFT) per a esbrinar la raó subjacent del diferent comportament dels dopants una vegada incorporats a l'estructura, que estava relacionada amb la mescla dels orbitals que participen en l'enllaç. Les pel·lícules primes de $\text{Cs}_2\text{AgBiBr}_6$ dopades amb Sn es van depositar mitjançant SSVD i van mostrar la possibilitat d'ajustar el *bandgap*. Per tant, aquest treball té una rellevància significativa ja que obri la porta a la reducció del *bandgap* d'aquesta perovskita doble i la seua utilització en dispositius fotovoltaïcs eficients.
- **Capítol 5:** en aquest capítol s'estudien tres espècies diferents dins del sistema Cs-Sn-I per a termoelèctrica. La SSVD directa de CsSnI_3 molt dona lloc a la deposició d'una perovskita 2D a penes coneguda, Cs_2SnI_4 . Anteriorment, el Cs_2SnI_4 només s'havia predit teòricament, però aquest treball representa la primera prova experimental de l'existència d'aquesta fase. No obstant això, la seua conductivitat elèctrica d'al voltant de $10^{-6} \text{ S cm}^{-1}$ resulta ser massa baixa per a aquest propòsit. No obstant això, una fase significativament més conductora, la beta negra CsSnI_3 (B- β CsSnI_3), es forma després de la recuita a 150 °C de la perovskita 2D i produeix una conductivitat elèctrica entorn de 50 S cm^{-1} prop de la temperatura ambient. Aquesta fase és un semiconductor de tipus p que aconsegueix una figura

de mèrit ZT màxima de 0.033 a 50 °C, comparable a la d'altres materials termoelèctrics a temperatura ambient i estable en condicions inertes durant més de 7 dies. El Cs_2SnI_6 es forma quan la fase β negra s'exposa a l'aire, però té una conductivitat elèctrica inferior (0.128 S cm^{-1}), aconseguint un ZT_{max} de 0.0011. No obstant això, el rendiment d'aquests materials continua sent baix en comparació amb els materials termoelèctrics actuals, però podria millorar-se en augmentar la conductivitat elèctrica. Una vegada millorats, podrien constituir una alternativa real als actuals TEG que funcionen a baixa temperatura.

En conjunt, el treball desenvolupat en aquesta tesi representa un pas avant en dos camps d'investigació diferents, l'optoelectrònica i la termoelèctrica, que estan guanyant cada vegada més atenció en els últims anys a causa de la major preocupació per la sostenibilitat i les energies renovables. Aquesta tesi aplanava el camí cap a l'aplicació dels materials proposats en LEDs, cèl·lules solars i TEGs.


Appendix A

Article: Solvent-Free Synthesis and Thin-Film
Deposition of Cesium Copper Halides with Bright
Blue Photoluminescence

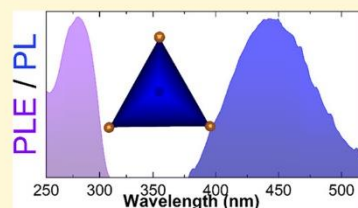
Solvent-Free Synthesis and Thin-Film Deposition of Cesium Copper Halides with Bright Blue Photoluminescence

Paz Sebastia-Luna,^{1b} Javier Navarro-Alapont, Michele Sessolo,^{1b} Francisco Palazon,^{1b*} and Henk J. Bolink^{1b}

Instituto de Ciencia Molecular, ICMol, Universidad de Valencia, C/ Catedrático J. Beltrán 2, 46980 Paterna, Spain

 Supporting Information

ABSTRACT: Nontoxic alternatives to lead halide perovskites are highly sought after for applications in optoelectronics. Blue-luminescent materials are especially demanded as they could be used to prepare white light-emitting diodes, with important potential applications in lighting systems. However, wide band gap blue emitters with high photoluminescence quantum yields (PLQYs) are typically more difficult to obtain as compared to green- or red-emitting ones. Here, we prepared two series of inorganic cesium copper halides, with the general formulas $\text{Cs}_3\text{Cu}_2\text{X}_5$ and CsCu_2X_3 ($\text{X} = \text{Cl}, \text{Br}, \text{I}$, and mixtures thereof) by dry mechanochemical synthesis at room temperature. X-ray diffraction demonstrates quantitative conversion of binary precursors into the desired ternary structures and good halide mixing in single-phase compounds. We identified $\text{Cs}_3\text{Cu}_2\text{I}_5$ as the most promising material as it maintains blue luminescence centered at 442 nm with a high PLQY (>40%) after several days in air ($\text{Cs}_3\text{Cu}_2\text{Cl}_5$ shows significantly higher PLQY, over 80% but is unstable in air). Based on this, we fabricated homogeneous and pinhole-free $\text{Cs}_3\text{Cu}_2\text{I}_5$ thin films by thermal single-source vacuum deposition. Crystalline phase and photoluminescence features are maintained in the thin films, demonstrating that these low-toxicity materials can be synthesized and processed by fully solvent-free routes for a widespread implementation in optoelectronic devices.



INTRODUCTION

In the past decade, lead halide perovskites (LHPs) have emerged as promising materials for optoelectronics.^{1–4} Driven by their thrust, there is a growing interest in developing alternative multinary metal halides (MMHs), of which LHPs represent a subclass. The necessity of replacing toxic Pb^{2+} ions with other more environmentally friendly metals requires the search for different ternary and quaternary MMHs, with various stoichiometries and crystal structures.^{5,6} Among these, Cu(I)-based fully inorganic ternary metal halides are particularly promising, especially for applications in light-emitting diodes.^{7–9} Stable crystals with two different stoichiometries can be formed: CsCu_2X_3 and $\text{Cs}_3\text{Cu}_2\text{X}_5$ ($\text{X} = \text{Cl}, \text{Br}, \text{I}$, or mixtures thereof). The most common crystal structure of both compounds at room temperature is depicted in Figure 1.

Cu(I) is in tetrahedral coordination with the halides in both cases. However, $\text{Cs}_3\text{Cu}_2\text{X}_5$ is constituted by isolated dimers of CuX_4 , whereas CsCu_2X_3 consists of side-sharing tetrahedra spatially arranged as wires. Based on these considerations, these structures may be referred to as 0D and 1D, respectively.⁹ To the best of our knowledge, only a few reports on these compounds exist.^{9–12} Furthermore, in the abovementioned publications, the synthesis and thin-film deposition of such MMHs was carried out either by solution processes in (toxic) organic solvents or by highly time- and energy-consuming thermal routes. Lately, solvent-free mechanochemical synthesis (MCS) has been shown to be a very simple and efficient approach to synthesize different phase-

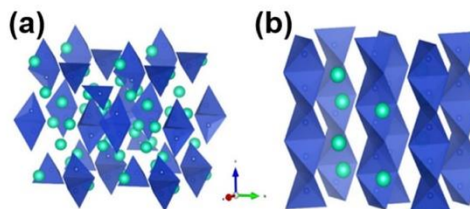


Figure 1. Crystal structures of $\text{Cs}_3\text{Cu}_2\text{Br}_5$ (left) and CsCu_2Br_3 (right), created with VESTA software based on crystallographic information files obtained in the Inorganic Crystal Structure Database (refs: 150297 and 49613). Green balls represent Cs^+ ions, and blue polygons represent CuBr_4 tetrahedra.

pure MMHs.^{13–22} This technique can be considered as *green chemistry*, as it does not involve the use of solvents, toxic compounds, and high temperatures, and it avoids the waste of materials and derivatives during the process.²³ Although the exact mechanisms and reaction kinetics happening during MCS are not fully elucidated, as this would require among others the possibility to monitor the process in situ through different characterization methods (something that is far from trivial experimentally),²⁴ we demonstrate that this process enables the formation of Cu(I) ternary inorganic halides of high quality. In particular, some of the as-synthesized

Received: September 22, 2019

Revised: November 20, 2019

Published: November 21, 2019

compounds exhibit bright photoluminescence (PL) even as nonpassivated bulk powders and are stable in air for several days. Furthermore, the as-synthesized compounds can be deposited as thin films with good morphology, crystallinity, and PL. In order to do so, we employed single-source vacuum deposition (SSVD) which has recently proven to be an easy, fast, and nontoxic (solvent-free) approach for the deposition of other inorganic and hybrid organic–inorganic halide compounds.^{18,25,26}

EXPERIMENTAL SECTION

Materials. Cesium chloride (CsCl, > 99%), cesium bromide (CsBr, > 99%), and cesium iodide (CsI, > 99%) were purchased from TCI. Copper(I) chloride (CuCl, ≥99.999%), copper(I) bromide (CuBr, ≥99.999%), and copper(I) iodide (CuI, ≥99.999%) were purchased from Sigma-Aldrich. Dimethyl sulfoxide (DMSO) of reagent grade was purchased from Scharlau and *N,N*-dimethylformamide (DMF) from Fisher. All chemicals were stored in a nitrogen-filled glovebox and used as received without further purification.

Mechanochemical Synthesis. Stoichiometric amounts of CsX/CuX powders were mixed inside a nitrogen-filled glovebox. Then, approximately 3 g of the mixed precursor powders was introduced inside 10 mL zirconia ball mill jars with two zirconia beads of 10 mm in diameter. The jars were closed under nitrogen so that the powders were not exposed to air. Then, ball milling was performed with an MM-400 shaking ball mill from Retsch, at a frequency of 30 Hz for 99 min.

Thin-Film Deposition by Solution Processing. Deposition and characterization of the thin films were carried out inside a clean-room ISO 7 10000. Glass substrates were extensively cleaned using subsequent sonication in water with soap, deionized water, and 2-propanol baths. After drying with a N₂ flow, the substrates were placed in a UV ozone cleaner for 15 min. Substrates were transferred to a nitrogen-filled glovebox (H₂O and O₂ < 0.1 ppm) for solution processing of the films. Cs₃Cu₂I₅ powders were dissolved into a mixed solvent containing DMF and DMSO with a volume ratio of 1:1 to a 0.7 M concentration. The solutions were then filtered with a 0.45 μm-pore size polytetrafluoroethylene filter. Thin films were deposited by spin-coating at a speed of 3000 rpm for 60 s, followed by annealing on a hot plate at 100 °C for 60 min.

Single-Source Vacuum Deposition. In a typical deposition, an alumina thermal source (Creaphys GmbH) inside a home-made vacuum chamber was loaded with 0.5 g of mechanochemically synthesized Cs₃Cu₂I₅ powder. The chamber was then evacuated to a pressure of 8 × 10⁻⁶ mbar, and the source was rapidly heated to 600 °C with a ramp of 50 °C/min. The deposition is controlled by a quartz microbalance sensor and stopped after the complete evaporation of the solid.

X-Ray Diffraction Characterization. X-ray diffraction (XRD) was measured with a powder diffractometer model D8 ADVANCE A25 Bruker brand equipped with a Cu Kα anode. Single scans were acquired in the 2θ = 10–40° range with a step size of 2θ = 0.025° in the Bragg–Brentano geometry in air. Whole powder pattern decompositions using the so-called Le Bail method, implemented in FullProf software, were applied for the refinement of unit cell parameters.¹ The Thompson–Cox–Hastings pseudo-Voigt line profile with refinable lineshape parameters is assumed for the fittings.²

Optical Characterization. UV–visible absorption spectra of the films and powders were collected using a Jasco V-670 UV/vis/NIR spectrophotometer (Jasco, Easton, USA). The PL characteristics for powders were studied using a xenon lamp coupled to a monochromator as the excitation source and an integrated sphere coupled to a Hamamatsu C9920-02 spectrometer with a Hamamatsu PMA-11 optical detector (Hamamatsu Photonics K.K.) in order to quantitatively determine the PL quantum yield (PLQY). For a typical analysis, three scans with an integration time of 100 ms were collected and averaged. Emission and excitation spectra were measured with a

FluoroMax HORIBA-MTB spectrofluorometer equipped with a xenon light source coupled to a monochromator.

Scanning Electron Microscopy. The scanning electron microscopy (SEM) images were obtained using a Hitachi S-4800 scanning-electron microscope, operating at an accelerating voltage of 20 kV over platinum-metallized samples.

Thermal Characterization. Thermogravimetric analysis (TGA) was carried out with a TA Discovery TGA550 (TA Instruments) equipped with a continuous nitrogen flow. Measurements were performed with a ramp of 10 °C/min from room temperature to 600 °C.

RESULTS AND DISCUSSION

We first synthesized a series of copper(I)-based inorganic compounds with the 1D structure CsCu₂X₃ (X = I, Br, Cl, and their mixtures). In short, the synthesis was carried out by simple dry ball milling of the corresponding CsX and CuX precursors in a 1:2 molar ratio in an inert atmosphere in order to avoid hydration and possible oxidation (see the Supporting Information for more details). Figure 2 shows the X-ray

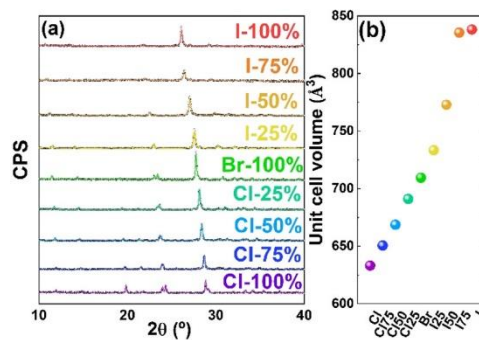


Figure 2. (a) XRD data (open circles) and fits (solid colored lines) of different CsCu₂X₃ compounds. (b) Unit cell volume as derived from fits.

diffraction patterns of all samples in the 10° ≤ 2θ ≤ 40° range. All diffraction patterns are fitted assuming single-phase compounds crystallized in the *Cmcm* space group, with varying unit cell parameters (Figure 2a and Table S1). Unit cell volumes derived from the whole-pattern fit show a rather linear expansion from 633 Å³ (X = Cl) to 840 Å³ (X = I), as expected from the increased ionic radius when going from Cl⁻ to Br⁻ and to I⁻ (Figure 2b). In order to better appreciate the phase purity of the obtained compounds, experimental and fitted profiles are reproduced in higher resolution together with the calculated Bragg's reflections in the Supporting Information (Figures S1–S9). For monohalide compounds, the excellent quality of the fits is a strong indication of complete reaction and high phase purity. This observation also holds for most mixed-halide compounds, with a slightly worse match for Cl-rich mixed Br–Cl compounds (Figures S7 and S8). In these two cases, we cannot rule out a minor phase segregation between CsCu₂Br₃ and CsCu₂Cl₃ domains. Also, a broad peak around 2θ = 31° is observed in some samples, which can be attributed to zirconia debris originating from the grinding medium. As this does not appear on all samples, we conclude that it is not unavoidable and probably a further optimization of the synthesis conditions (powder-to-ball weight ratio and previous use or not of the same grinding beads and jars)

should result in a controllable elimination of these minor byproducts.

Thermal stability of these materials was studied by TGA. To the best of our knowledge, there are no previous references on the thermal stability of these materials. Still, thermal stability is crucial at least for two reasons: (i) to determine whether the materials would remain stable in standard operation conditions once implemented in devices and (ii) to determine whether they can be processed by thermal processes such as thermal vacuum deposition, without undergoing incongruent melting or vaporization. The weight loss of the $\text{Cs}_3\text{Cu}_2\text{X}_5$ ($X = \text{Cl}, \text{Br},$ and I) compounds as a function of temperature at atmospheric pressure is reported in Figure S10. Bromide and iodide samples present the highest thermal stabilities of the series, without any weight variation until approximately 490 and 360 °C, respectively. For the chloride species, the thermal behavior is significantly different. A weight loss at around 185 °C was observed, followed by an increase around 400 °C. Based on the literature, these two features can be ascribed first to oxidation of the Cu(I) halide to Cu_2O , followed by the oxidation of Cu(I) oxide to Cu(II) oxide ($\text{Cu}_2\text{O} \rightarrow \text{CuO}$).^{27–29} These transformations might occur in the presence of residual oxygen in the TGA column, even if the analyses were performed with a nitrogen flow. For bromide and iodide samples, no weight increase was observed, pointing to their higher stability toward oxidation in the experimental conditions. Optical absorption shows a tunable onset around 305–325 nm (see Figure S11); however, no PL could be detected with our setup (see the Supporting Information for details). This is in line with the literature, where only one recent report demonstrates weak PL (5% PLQY) from surface-passivated colloidal nanorods with the same composition.¹¹

We also investigated the 0D structures $\text{Cs}_3\text{Cu}_2\text{X}_5$ ($X = \text{Cl}, \text{Br}, \text{I}$, and mixtures thereof). The application of these compounds for optoelectronics has been scarcely studied before, with only the pure-bromide, pure-iodide, and mixed bromide–iodide species being reported.^{9,10,12} The pure-chloride compound, in contrast, has been only reported to define its structure.³⁰ Herein, we investigate the synthesis of the whole halide series by dry mechanochemistry and reveal their excellent optical quality.

Figures 3 and S12–S20 show the XRD analysis of all $\text{Cs}_3\text{Cu}_2\text{X}_5$ compounds. For all mixed iodide–bromide samples (including the pure-bromide and the pure-iodide ones),

diffractograms are fitted considering a *Pnma* space group with varying unit cell parameters (Figure 3a). This analysis holds for chloride-containing samples up to a chloride content of 75 mol %. As a result, we observe a clear trend on the unit cell volume with the ionic radius of the halide anion ($\text{Cl}^- < \text{Br}^- < \text{I}^-$; see Figure 3b and Table S2). Although *Pnma* is the expected space group for all $\text{Cs}_3\text{Cu}_2\text{I}_5$, $\text{Cs}_3\text{Cu}_2\text{Br}_5$, and $\text{Cs}_3\text{Cu}_2\text{Cl}_5$ based on ICSD (refs: 150298, 150297, and 150296, respectively), the diffractogram for $\text{Cs}_3\text{Cu}_2\text{Cl}_5$ is better fitted considering the space group *Cmcm*. Crystallization of $\text{Cs}_3\text{Cu}_2\text{Cl}_5$ in this space group was already reported by others.³⁰ Although the crystallization in one or the other space group is evident by the fits obtained in both cases, we could not elucidate what drives the crystallization in a given structure here. This, as will be detailed hereafter, has important consequences on the optical properties.

By exposing these powders to air during 2–3 days, a change in their appearance is observed (see Figure S21). For the chloride sample, we see a change in color to yellow similar to that of Cu(II) chlorides in solution $[\text{CuCl}_4]^{2-}$,³¹ a consequence of oxidation in the presence of moisture. Interestingly, the XRD pattern shows significant differences after air exposure (see Figure S22), which means that oxidation of the material affects the whole (“bulk”) sample. In the case of bromide, we see a change of color similar to that of copper(II) bromides in solution, pointing again toward an oxidation by moisture and the formation of $[\text{CuBr}_4]^{2-}$.³¹ Nonetheless, for this compound, it seems that the oxidation is only superficial, as no differences are observed by XRD (Figure S22). In the case of the iodide analogues, we do not observe any difference, which agrees with the very low stability of Cu(II) iodide compounds.^{32,33} To further confirm these observations, we carried out X-ray photoelectron spectroscopy and X-ray-excited Auger electron spectroscopy (XAES; Figure S23). While the Cu 2p spectra (Figure S23a) of $\text{Cs}_3\text{Cu}_2\text{Br}_5$ and $\text{Cs}_3\text{Cu}_2\text{I}_5$ show only a doublet for Cu 2p_{3/2} and Cu 2p_{1/2} peaks at binding energies (BEs) of 931.9 and 951.8 eV attributed to Cu(I), secondary high-BE peaks 933.9 and 953.8 eV are observed in $\text{Cs}_3\text{Cu}_2\text{Cl}_5$, which are ascribed to the oxidation of copper into Cu(II) species in this sample, as previously described.³⁴ This is furthermore confirmed by the presence of strong satellite peaks around BE = 942 eV and BE = 962 eV, which is a clear sign of Cu(II).³⁴ Eventually, the higher kinetic energy of the Cu-LMM Auger peak in $\text{Cs}_3\text{Cu}_2\text{Cl}_5$ (Figure S23b) again confirms the oxidation of copper into Cu(II) in this material.³⁴ As for the 1D CsCu_2X_3 series, TGA of the pure-halide species was carried out. The thermal behavior was found to be similar to the 1D structures detailed above (see Figure S25). We observe again a weight increase in the chloride sample, which suggests oxidation of these compounds. This is also in line with the structural analysis and color change discussed above, where we noted a more favored oxidation of the chloride samples. It must be noted, however, that all samples are stable until 250 °C and even 350 °C (bromide) and 450 °C (iodide).

Finally, we studied the optical properties of these materials (see Figure 4) by measuring the PL excitation (PLE) and PL emission spectra for the whole $\text{Cs}_3\text{Cu}_2\text{X}_5$ series. The wavelengths at the maximum PL intensity and corresponding PLQY for all samples are detailed in Table 1 (note that the starting reagents do not show any noticeable PL under our measurement conditions as can be seen in Figure S24). Although the shifts in maximum excitation and emission

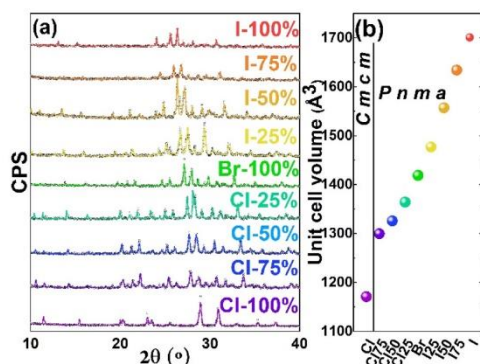


Figure 3. (a) XRD data (open circles) and fit (solid colored lines) of different $\text{Cs}_3\text{Cu}_2\text{X}_5$ compounds. (b) Unit cell volume as derived from the fit.

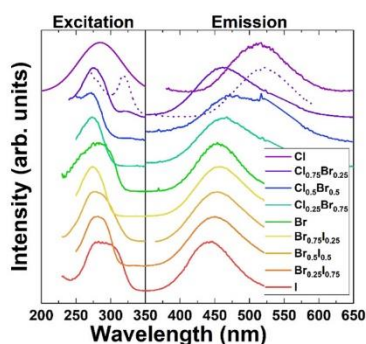


Figure 4. PLE (left) and PL emission (right) spectra of different $\text{Cs}_3\text{Cu}_2\text{X}_5$, X is given in the legend. For $\text{Cs}_3\text{Cu}_2(\text{Cl}_{0.75}\text{Br}_{0.25})_5$, the excitation spectrum corresponding to 516 nm emission and the corresponding emission spectrum are presented as dashed lines, whereas the excitation spectrum corresponding to emission at 450 nm and the corresponding emission spectrum are presented as solid lines.

Table 1. PLQY and λ_{em} for $\text{Cs}_3\text{Cu}_2\text{X}_5$ Compounds Freshly Prepared, Exposed to Air for 24 h, and Thermally Annealed^a

compound	as-prepared		air-exposed		annealed	
	λ_{em} (nm)	PLQY (%)	λ_{em} (nm)	PLQY (%)	λ_{em} (nm)	PLQY (%)
$\text{Cs}_3\text{Cu}_2\text{Cl}_5$	516	78	528	3	525	81
$\text{Cs}_3\text{Cu}_2(\text{Cl}_{0.75}\text{Br}_{0.25})_5$	516	10				
$\text{Cs}_3\text{Cu}_2(\text{Cl}_{0.5}\text{Br}_{0.5})_5$	470	3.6				
$\text{Cs}_3\text{Cu}_2(\text{Cl}_{0.25}\text{Br}_{0.75})_5$	464	3.2				
$\text{Cs}_3\text{Cu}_2\text{Br}_5$	455	14	456	3	457	19
$\text{Cs}_3\text{Cu}_2(\text{Br}_{0.75}\text{I}_{0.25})_5$	456	11				
$\text{Cs}_3\text{Cu}_2(\text{Br}_{0.5}\text{I}_{0.5})_5$	452	15				
$\text{Cs}_3\text{Cu}_2(\text{Br}_{0.25}\text{I}_{0.75})_5$	450	11				
$\text{Cs}_3\text{Cu}_2\text{I}_5$	442	42	444	42	444	47

^aFor mixed-halide compounds, as no benefit was observed for freshly prepared samples, stability in air or upon annealing was not assessed.

wavelengths are not monotonic (see Figure S26 for more details), there is an overall red shift in the PL when decreasing the halide ionic radius (from I^- to Cl^-). This behavior is opposite to that observed from other MMHs such as LHPs or bismuth-based compounds.^{10,16,35–37} In fact, PL in these materials is a consequence of band-to-band radiative recombination, whereas for $\text{Cs}_3\text{Cu}_2\text{X}_5$, the PL originates from self-trapped excitons induced by the strong charge localization within the 0D structure.¹⁰ Furthermore, we observe markedly different optical features for Cl-rich compounds (75 and 100%), as compared to the rest of $\text{Cs}_3\text{Cu}_2\text{X}_5$ materials (Figure 4). Indeed, $\text{Cs}_3\text{Cu}_2\text{Cl}_5$ presents a significantly red-shifted PL spectrum with a maximum emission wavelength of around 516 nm (green), while iodide and bromide compounds typically show blue luminescence. This can be ascribed to the different crystalline phases of this compound as previously discussed (Figure 2). Interestingly, $\text{Cs}_3\text{Cu}_2(\text{Cl}_{0.75}\text{Br}_{0.25})_5$ exhibits dual excitation and emission properties (see solid and dashed lines in Figure 4), suggesting the coexistence of the *Cmcm* phase (as $\text{Cs}_3\text{Cu}_2\text{Cl}_5$) and *Pnma* phase (as $\text{Cs}_3\text{Cu}_2\text{Br}_5$). It is possible that this phase segregation is linked to halide segregation, although we were unable to elucidate this hypothesis.

The PLQY of freshly prepared pure-halides was found to be higher than that of all mixed-halide compounds (Table 1). Considering that the shift in the PL emission is minimal upon halide mixing, no clear benefit (optical or structural) is obtained from mixed compositions. Second, PLQY values of the as-prepared pure-halide compounds are relatively high considering the simple synthesis conditions of dry ball milling. Indeed, these values are comparable with those obtained from ligand-passivated quantum dots.¹⁰ It is especially worth highlighting the high PLQY of 78% for $\text{Cs}_3\text{Cu}_2\text{Cl}_5$. We also observe that the PLQY of chloride and bromide compounds decreases significantly upon air exposure for 24 h, while it is stable for $\text{Cs}_3\text{Cu}_2\text{I}_5$. This effect is ascribed to the moisture-induced oxidation discussed before (Figures S21–S23), which does not occur for copper iodide. Losses in PLQY from air exposure of bromide and chloride samples can nevertheless be recovered by thermal annealing for 40 min at 170 °C, yielding PLQY values as high as 81% for $\text{Cs}_3\text{Cu}_2\text{Cl}_5$.

Given the promising optical features and stability of the pure-iodide compound in the powder state, we attempted to deposit it as thin film. In order to do so, as a first approach, we dissolved the material in organic solvents and subsequently spin-coated it on a glass substrate followed by thermal annealing (see the Supporting Information for details). The XRD pattern of spin-coated films shows an excellent match with the reference ICSD pattern for bulk $\text{Cs}_3\text{Cu}_2\text{I}_5$ (Figure S27), suggesting that the structure is maintained upon thin-film processing. Also, the PL signal centered at 438 nm (Figure S28) is very close to that of the as-prepared bulk $\text{Cs}_3\text{Cu}_2\text{I}_5$ powders (Table 1). The blue luminescence is characterized by a PLQY of 19%, which is lower compared to that of the pristine bulk material. Although these results seem promising, it must be noted that dissolution of such inorganic metal halides in organic solvents is limited, and as a result, the film showed obvious inhomogeneities visible even to the naked eye (see Figure S29). Furthermore, using organic solvents for the thin-film deposition partly defeats the purpose of using dry MCS for the original synthesis. Therefore, we tested the deposition of $\text{Cs}_3\text{Cu}_2\text{I}_5$ by thermal SSVD. In short, the as-synthesized powder materials are loaded in a ceramic crucible (source) inside a vacuum chamber. The source is then quickly heated to a high temperature, causing the material to sublime and crystallize on the substrate, which is placed ca. 10 cm above the source (see the Supporting Information for details). No further thermal annealing or other postdeposition treatments were performed. This method has previously been shown to be promising for the deposition of LHP thin films.^{18,25} The XRD pattern of the film (Figure 5a) is well fitted considering the same space group as the bulk material. Interestingly, while all peaks present in the diffractogram of the film are present in the diffractogram of the powder sample (denoting that no impurity other than the expected $\text{Cs}_3\text{Cu}_2\text{I}_5$ phase is present), the opposite is not true (i.e., several peaks present in the diffractogram of the powder sample are absent in the films). Also, their relative intensities are varied. This, which is common for thin films of different compositions,³⁸ can be attributed to a preferential crystallographic orientation (texture). The film thickness is measured to be 600 nm. SEM shows good homogeneity with grains of different sizes in the range of hundreds of nanometers (Figure 5b). The homogeneity can also be assessed by lower magnification images (Figure S30). Eventually, we note that the optical excitation and emission spectra of the thin film are nearly

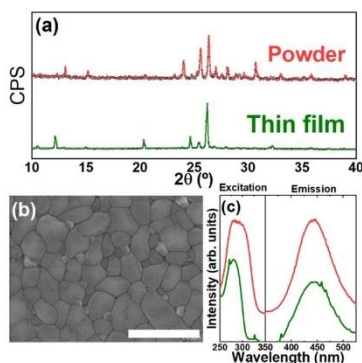


Figure 5. Characterization of SSVD $\text{Cs}_3\text{Cu}_2\text{I}_5$ thin film. (a) X-ray diffractogram with Le Bail fit in green. For an easy comparison, data and fit from bulk powder (see Figure 3) are reproduced here in red. (b) SEM image. Scale bar is $1\ \mu\text{m}$ (see lower magnifications in Figure S30). (c) PL excitation and emission spectra in green. For an easy comparison, data from bulk powder (see Figure 4) are reproduced here in red.

identical to the ones of the starting bulk powders (Figure 5c). The PLQY of the vacuum-deposited film is 29%, higher than that of the film formed by solution processing and close to the value of the starting material. Hence, it is evident that SSVD of mechanochemically synthesized cesium copper halides leads to thin films of excellent morphology, crystallinity, and optical properties, paving the way to the implementation of these fully dry approaches for low-toxicity optoelectronics.

CONCLUSIONS

In summary, we have demonstrated the synthesis of CsCu_2X_3 and $\text{Cs}_3\text{Cu}_2\text{X}_5$ ($\text{X} = \text{Cl}, \text{Br}, \text{I}$, and mixtures thereof) by simple solvent-free mechanochemistry. Pure-halide $\text{Cs}_3\text{Cu}_2\text{X}_5$ compounds exhibit a high PLQY in the blue-green region of the visible spectrum, making these very promising materials for lighting or deep-UV photodetectors. The green-emitting $\text{Cs}_3\text{Cu}_2\text{Cl}_5$ was synthesized with a 78% PLQY (81% after air exposure and subsequent thermal annealing), albeit with poor stability in air. In contrast, the blue-emitting $\text{Cs}_3\text{Cu}_2\text{I}_5$ achieved a stable PLQY exceeding 40% even when stored in air for several days. Differences in spectral features have been rationalized in terms of different crystalline structures as evidenced by the whole-pattern fitting of the XRD signal, while differences in air stability can be explained by preferential oxidation mechanisms of Cu(I) halides to Cu(II) halides. Finally, we were able to process $\text{Cs}_3\text{Cu}_2\text{I}_5$ powders into homogeneous thin films by SSVD with excellent crystallinity and conserved optical features. Future work will focus on the implementation of these films into different optoelectronic devices.

ASSOCIATED CONTENT

Supporting Information

The Supporting Information is available free of charge at <https://pubs.acs.org/doi/10.1021/acs.chemmater.9b03898>.

Thermal characterization (TGA); absorbance spectra of CsCu_2X_3 compounds; change in color of $\text{Cs}_3\text{Cu}_2\text{X}_5$ powders; XRD of nonexposed and exposed powders; variation in PLE and PL wavelengths of $\text{Cs}_3\text{Cu}_2\text{X}_5$ powders; XRD and PL spectra of solution-processed

thin films; and SEM image of thin film by SSVD of $\text{Cs}_3\text{Cu}_2\text{I}_5$ (PDF)

AUTHOR INFORMATION

Corresponding Author

*E-mail: francisco.palazon@uv.es

ORCID

Paz Sebastia-Luna: 0000-0001-6992-199X

Michele Sessolo: 0000-0002-9189-3005

Francisco Palazon: 0000-0002-1503-5965

Henk J. Bolink: 0000-0001-9784-6253

Author Contributions

The manuscript was written through contributions of all authors.

Notes

The authors declare no competing financial interest.

ACKNOWLEDGMENTS

The research leading to these results has received funding from the European Union Programme for Research and Innovation Horizon 2020 (2014–2020) under the Marie Skłodowska-Curie Grant Agreement PerovSAMs (no. 747599), the Spanish Ministry of Science, Innovation and Universities (ex-MINECO) via the Unidad de Excelencia María de Maeztu MDM-2015-0538, MAT2017-88821-R, and PCIN-2015-255, and the Generalitat Valenciana (Prometeo/2016/135). M.S. thanks the Spanish Ministry of Science Innovation and Universities (ex-MINECO) for his postdoctoral RyC contract. We acknowledge the European Union's Horizon 2020 research & innovation program under grant agreement no. 763977 of the PerTPV project. We thank Prof. Miguel Julve for fruitful discussions on the oxidation of copper halides.

REFERENCES

- Veldhuis, S. A.; Boix, P. P.; Yantara, N.; Li, M.; Sum, T. C.; Mathews, N.; Mhaisalkar, S. G. Perovskite Materials for Light-Emitting Diodes and Lasers. *Adv. Mater.* **2016**, *28*, 6804–6834.
- Kitai, A. Light Emitting Diodes. *Principles of Solar Cells, LEDs and Diodes*; John Wiley & Sons, Ltd: Chichester, 2011; Chapter 5, pp 215–252.
- Leijtens, T.; Bush, K. A.; Prasanna, R.; McGehee, M. D. Opportunities and Challenges for Tandem Solar Cells Using Metal Halide Perovskite Semiconductors. *Nat. Energy* **2018**, *3*, 828–838.
- Xing, J.; Zhao, Y.; Askerka, M.; Quan, L. N.; Gong, X.; Zhao, W.; Zhao, J.; Tan, H.; Long, G.; Gao, L.; et al. Color-Stable Highly Luminescent Sky-Blue Perovskite Light-Emitting Diodes. *Nat. Commun.* **2018**, *9*, 3541.
- Xu, L.-J.; Sun, C.-Z.; Xiao, H.; Wu, Y.; Chen, Z.-N. Green-Light-Emitting Diodes Based on Tetrabromide Manganese(II) Complex through Solution Process. *Adv. Mater.* **2017**, *29*, 1605739.
- Yang, T. C.-J.; Fiala, P.; Jeangros, Q.; Ballif, C. High-Bandgap Perovskite Materials for Multijunction Solar Cells. *Joule* **2018**, *2*, 1421–1436.
- Bizzarri, C.; Spuling, E.; Knoll, D. M.; Volz, D.; Bräse, S. Sustainable Metal Complexes for Organic Light-Emitting Diodes (OLEDs). *Coord. Chem. Rev.* **2018**, *373*, 49–82.
- Li, X.; Zhong, X.; Hu, Y.; Li, B.; Sheng, Y.; Zhang, Y.; Weng, C.; Feng, M.; Han, H.; Wang, J. Organic-Inorganic Copper(II)-Based Material: A Low-Toxic, Highly Stable Light Absorber for Photovoltaic Application. *J. Phys. Chem. Lett.* **2017**, *8*, 1804–1809.
- Jun, T.; Sim, K.; Iimura, S.; Sasase, M.; Kamioka, H.; Kim, J.; Hosono, H. Lead-Free Highly Efficient Blue-Emitting $\text{Cs}_3\text{Cu}_2\text{I}_5$ with OD Electronic Structure. *Adv. Mater.* **2018**, *30*, 1804547.

- (10) Roccanova, R.; Yangui, A.; Nhalil, H.; Shi, H.; Du, M.-H.; Saparov, B. Near-Unity Photoluminescence Quantum Yield in Blue-Emitting Cs₃Cu₂Br_{5-x}I_x (0 ≤ x ≤ 5). *ACS Appl. Electron. Mater.* **2019**, *1*, 269–274.
- (11) Cheng, P.; Sun, L.; Feng, L.; Yang, S.; Yang, Y.; Zheng, D.; Zhao, Y.; Sang, Y.; Zhang, R.; Wei, D.; et al. Colloidal Synthesis and Optical Properties of All-Inorganic Low-Dimensional Cesium Copper Halide Nanocrystals. *Angew. Chem., Int. Ed.* **2019**, *58*, 16087.
- (12) Zhang, Z.-X.; Li, C.; Lu, Y.; Tong, X.-W.; Liang, F.-X.; Zhao, X.-Y.; Wu, D.; Xie, C.; Luo, L.-B. Sensitive Deep Ultraviolet Photodetector and Image Sensor Composed of Inorganic Lead-Free Cs₃Cu₂I₅ Perovskite with Wide Bandgap. *J. Phys. Chem. Lett.* **2019**, *10*, 5343.
- (13) Prochowicz, D.; Sasaki, M.; Yadav, P.; Grätzel, M.; Lewiński, J. Mechanoperovskites for Photovoltaic Applications: Preparation, Characterization, and Device Fabrication. *Acc. Chem. Res.* **2019**, *52*, 3233–3243.
- (14) Rosales, B. A.; Wei, L.; Vela, J. Synthesis and Mixing of Complex Halide Perovskites by Solvent-Free Solid-State Methods. *J. Solid State Chem.* **2019**, *271*, 206–215.
- (15) Protesescu, L.; Yakunin, S.; Nazarenko, O.; Dirin, D. N.; Kovalenko, M. V. Low-Cost Synthesis of Highly Luminescent Colloidal Lead Halide Perovskite Nanocrystals by Wet Ball Milling. *ACS Appl. Nano Mater.* **2018**, *1*, 1300–1308.
- (16) El Ajjouri, Y.; Chirvony, V. S.; Vassilyeva, N.; Sessolo, M.; Palazon, F.; Bolink, H. J. Low-Dimensional Non-Toxic A₃Bi₂X₉ Compounds Synthesized by a Dry Mechanochemical Route with Tunable Visible Photoluminescence at Room Temperature. *J. Mater. Chem. C* **2019**, *7*, 6236–6240.
- (17) El Ajjouri, Y.; Chirvony, V. S.; Sessolo, M.; Palazon, F.; Bolink, H. J. Incorporation of Potassium Halides in the Mechanochemical Synthesis of Inorganic Perovskites: Feasibility and Limitations of Ion-Replacement and Trap Passivation. *RSC Adv.* **2018**, *8*, 41548–41551.
- (18) El Ajjouri, Y.; Palazon, F.; Sessolo, M.; Bolink, H. J. Single-Source Vacuum Deposition of Mechanochemical Inorganic Halide Perovskites. *Chem. Mater.* **2018**, *30*, 7423–7427.
- (19) El Ajjouri, Y.; Locardi, F.; Gélvez-Rueda, M. C.; Prato, M.; Sessolo, M.; Ferretti, M.; Grozema, F. C.; Palazon, F.; Bolink, H. J. Mechanochemical Synthesis of Sn(II) and Sn(IV) Iodide Perovskites and Study of Their Structural, Chemical, Thermal, Optical and Electrical Properties. *Energy Technol.* **2019**, 1900788.
- (20) Hong, Z.; Tan, D.; John, R. A.; Tay, Y. K. E.; Ho, Y. K. T.; Zhao, X.; Sum, T. C.; Mathews, N.; García, F.; Soo, H. S. Completely Solvent-Free Protocols to Access Phase-Pure, Metastable Metal Halide Perovskites and Functional Photodetectors from the Precursor Salts. *iScience* **2019**, *16*, 312–325.
- (21) Palazon, F.; El Ajjouri, Y.; Sebastia-Luna, P.; Lauciello, S.; Manna, L.; Bolink, H. J. Mechanochemical Synthesis of Inorganic Halide Perovskites: Evolution of Phase-Purity, Morphology, and Photoluminescence. *J. Mater. Chem. C* **2019**, *7*, 11406–11410.
- (22) Palazon, F.; El Ajjouri, Y.; Bolink, H. J. Making by Grinding: Mechanochemistry Boosts the Development of Halide Perovskites and Other Multinary Metal Halides. *Adv. Energy Mater.* **2019**, 1902499.
- (23) Anastas, P.; Eghbali, N. Green Chemistry: Principles and Practice. *Chem. Soc. Rev.* **2010**, *39*, 301–312.
- (24) Ban, V.; Sadikin, Y.; Lange, M.; Tumanov, N.; Filinchuk, Y.; Černý, R.; Casati, N. Innovative in Situ Ball Mill for X-Ray Diffraction. *Anal. Chem.* **2017**, *89*, 13176–13181.
- (25) Crane, M. J.; Kroupa, D. M.; Roh, J. Y.; Anderson, R. T.; Smith, M. D.; Gamelin, D. R. Single-Source Vapor Deposition of Quantum-Cutting Yb³⁺:CsPb(Cl_{1-x}Br_x)₃ and Other Complex Metal-Halide Perovskites. *ACS Appl. Energy Mater.* **2019**, *2*, 460.
- (26) Longo, G.; Gil-Escrig, L.; Degen, M. J.; Sessolo, M.; Bolink, H. J. Perovskite Solar Cells Prepared by Flash Evaporation. *Chem. Commun.* **2015**, *51*, 7376–7378.
- (27) Sierra-Avila, R.; Pérez-Alvarez, M.; Cadenas-Pliego, G.; Ávila-Orta, C. A.; Betancourt-Galindo, R.; Jiménez-Regalado, E.; Jiménez-Barrera, R. M.; Martínez-Colunga, J. G. Synthesis of Copper Nanoparticles Coated with Nitrogen Ligands. *J. Nanomater.* **2014**, *2014*, 1–8.
- (28) Van, K. V.; Habashi, F. Identification and Thermal Stability of Copper(I) Sulfate. *Can. J. Chem.* **1972**, *50*, 3872.
- (29) Li, J.; Shacham-Diamand, Y.; Mayer, J. W. Copper Deposition and Thermal Stability Issues in Copper-Based Metallization for ULSI Technology. *Mater. Sci. Rep.* **1992**, *9*, 1–51.
- (30) Mykhalichko, B. M.; Davydov, V. N.; Aksel'rud, L. G. Synthesis and Structure of Cs₃Cu₂Cl₅. *Russ. J. Inorg. Chem.* **1997**, *42*, 1011–1013.
- (31) Rizvi, M. A.; Akhoun, S. A.; Maqsood, S. R.; Peerzada, G. M. Synergistic Effect of Perchlorate Ions and Acetonitrile Medium Explored for Extension in Copper Redoximetry. *J. Anal. Chem.* **2015**, *70*, 633–638.
- (32) Margolis, L. A.; Schaeffer, R. W.; Yoder, C. H. The Synthesis and Analysis of Copper(I) Iodide. A First-Year Laboratory Project. *J. Chem. Educ.* **2001**, *78*, 235.
- (33) Burdett, J. K.; Sevov, S. Stability of the Oxidation States of Copper. *J. Am. Chem. Soc.* **1995**, *117*, 12788–12792.
- (34) Biesinger, M. C.; Lau, L. W. M.; Gerson, A. R.; Smart, R. S. C. Resolving Surface Chemical States in XPS Analysis of First Row Transition Metals, Oxides and Hydroxides: Sc, Ti, V, Cu and Zn. *Appl. Surf. Sci.* **2010**, *257*, 887–898.
- (35) Sun, J.; Yang, J.; Lee, J. I.; Cho, J. H.; Kang, M. S. Lead-Free Perovskite Nanocrystals for Light-Emitting Devices. *J. Phys. Chem. Lett.* **2018**, *9*, 1573–1583.
- (36) Shin, J.; Kim, M.; Jung, S.; Kim, C. S.; Park, J.; Song, A.; Chung, K.-B.; Jin, S.-H.; Lee, J. H.; Song, M. Enhanced Efficiency in Lead-Free Bismuth Iodide with Post Treatment Based on a Hole-Conductor-Free Perovskite Solar Cell. *Nano Res.* **2018**, *11*, 6283–6293.
- (37) Johansson, M. B.; Zhu, H.; Johansson, E. M. J. Extended Photo-Conversion Spectrum in Low-Toxic Bismuth Halide Perovskite Solar Cells. *J. Phys. Chem. Lett.* **2016**, *7*, 3467–3471.
- (38) Palazon, F.; Pérez-del-Rey, D.; Dänekamp, B.; Dreesen, C.; Sessolo, M.; Boix, P. P.; Bolink, H. J. Room-Temperature Cubic Phase Crystallization and High Stability of Vacuum-Deposited Methylammonium Lead Triiodide Thin Films for High-Efficiency Solar Cells. *Adv. Mater.* **2019**, *31*, 1902692.

Supporting Information for:

**Solvent-Free Synthesis and Thin-Film Deposition of Cesium
Copper Halides with Bright Blue Photoluminescence**

Paz Sebastián-Luna, Javier Navarro-Alapont, Michele Sessolo, Francisco Palazón,^{*} and
Henk J. Bolink

Instituto de Ciencia Molecular, ICMol, Universidad de Valencia, C/ Catedrático J.
Beltrán 2, 46980 Paterna, Spain

Table S1. Lattice parameters derived from Le Bail fits of CsCu_2X_3 compounds (space group = $Cmcm$).

X	a (Å)	b (Å)	c (Å)	α (°)	β (°)	γ (°)	V (Å³)
I	10.50438	13.11778	6.08282	90	90	90	838
I₇₅Br₂₅	10.47270	13.14974	6.06720	90	90	90	836
I₅₀Br₅₀	10.00890	12.91363	5.98059	90	90	90	773
I₂₅Br₇₅	9.78000	12.67451	5.91661	90	90	90	733
Br	9.87500	12.35396	5.81609	90	90	90	710
Cl₂₅Br₇₅	9.73313	12.29817	5.77289	90	90	90	691
Cl₅₀Br₅₀	9.58554	12.19961	5.71844	90	90	90	669
Cl₇₅Br₂₅	9.47997	12.09300	5.67565	90	90	90	651
Cl	9.50509	11.89780	5.59920	90	90	90	633

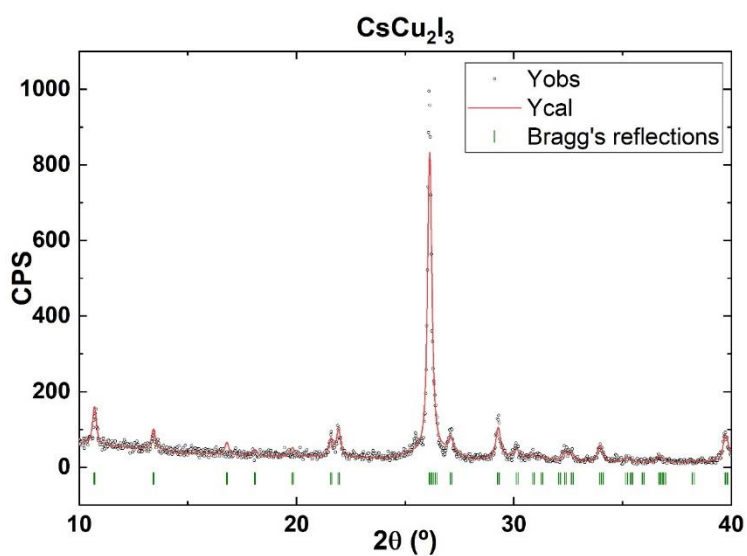


Figure S1. Experimental (open circles) and fitted (red line) diffractograms. Calculated Bragg's reflections position in green. Compound given in title.

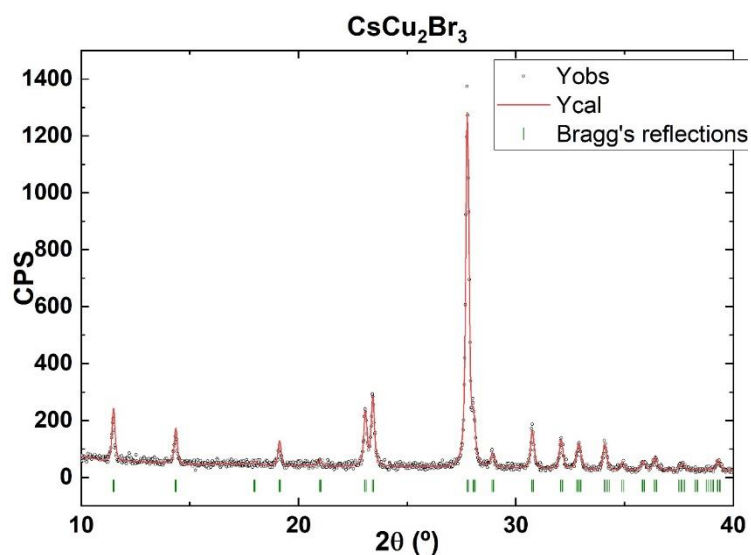


Figure S2. Experimental (open circles) and fitted (red line) diffractograms. Calculated Bragg's reflections position in green. Compound given in title.

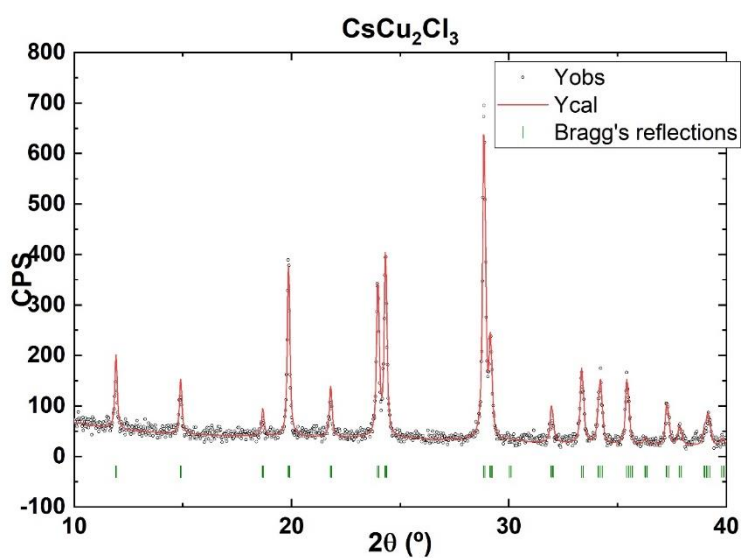


Figure S3. Experimental (open circles) and fitted (red line) diffractograms. Calculated Bragg's reflections position in green. Compound given in title.

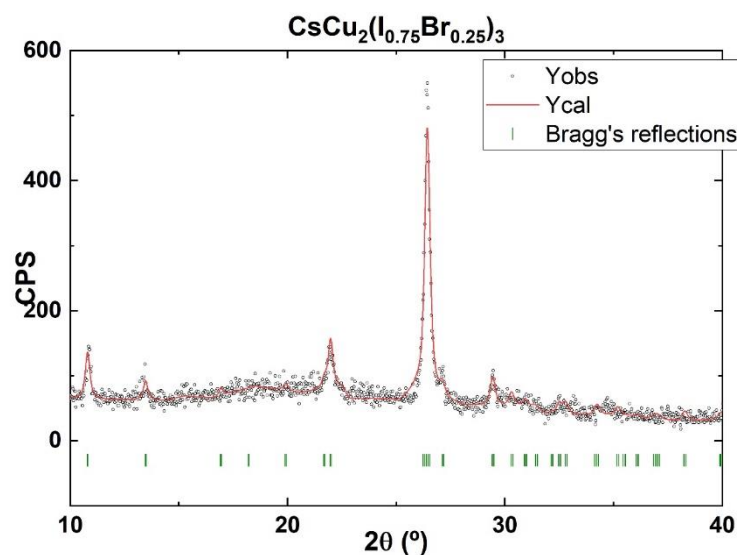


Figure S4. Experimental (open circles) and fitted (red line) diffractograms. Calculated Bragg's reflections position in green. Compound given in title.

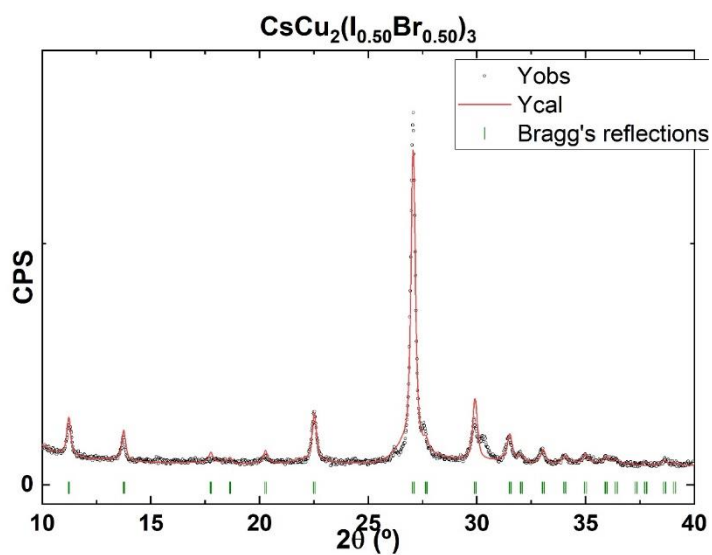


Figure S5. Experimental (open circles) and fitted (red line) diffractograms. Calculated Bragg's reflections position in green. Compound given in title.

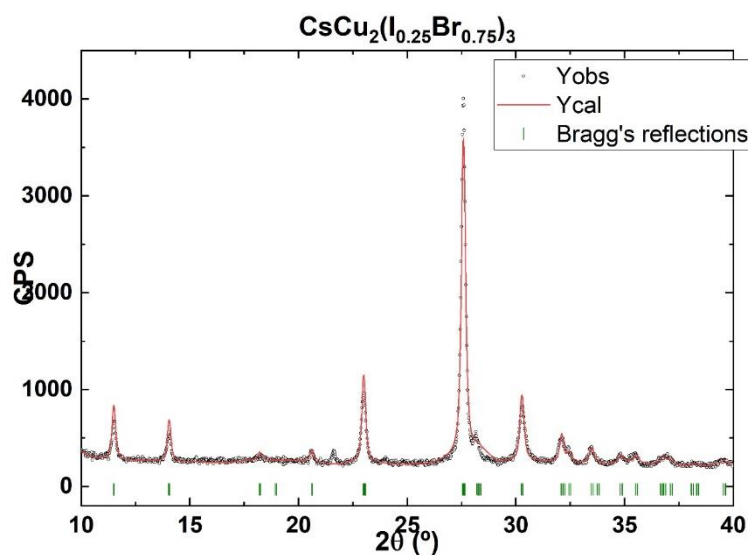


Figure S6. Experimental (open circles) and fitted (red line) diffractograms. Calculated Bragg's reflections position in green. Compound given in title.

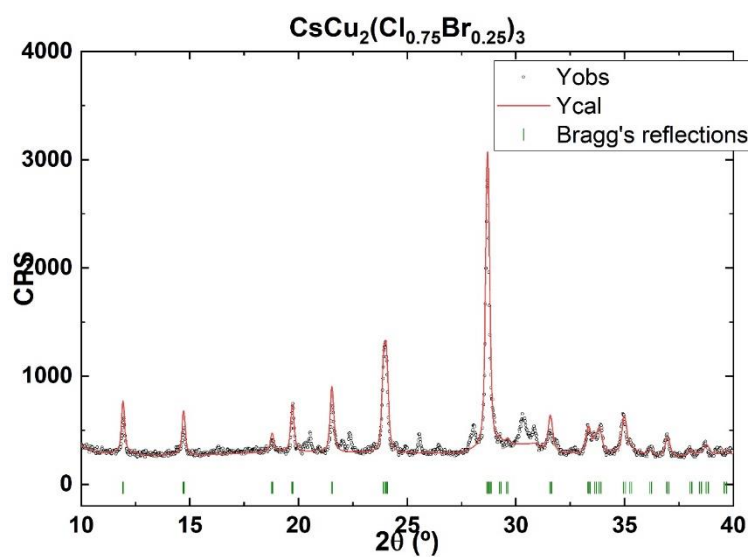


Figure S7. Experimental (open circles) and fitted (red line) diffractograms. Calculated Bragg's reflections position in green. Compound given in title.

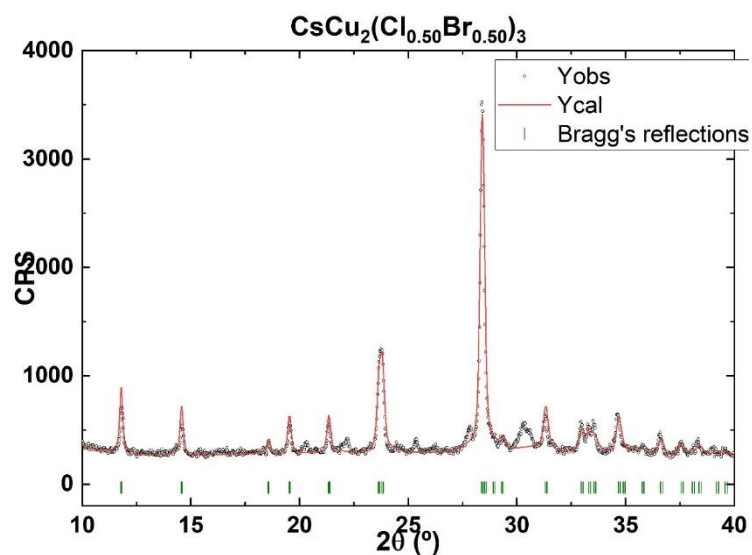


Figure S8. Experimental (open circles) and fitted (red line) diffractograms. Calculated Bragg's reflections position in green. Compound given in title.

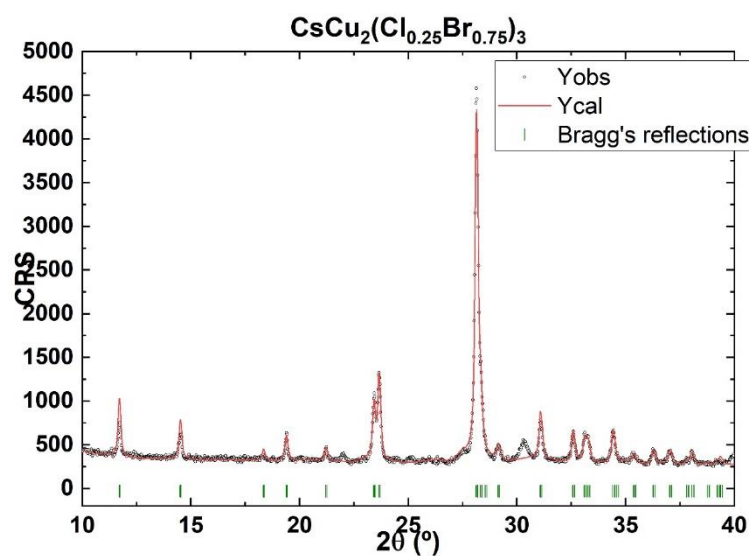


Figure S9. Experimental (open circles) and fitted (red line) diffractograms. Calculated Bragg's reflections position in green. Compound given in title.

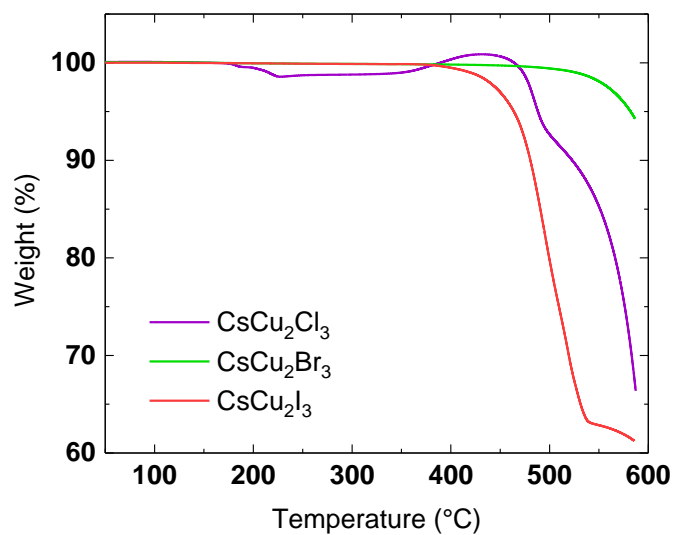


Figure S10. Thermogravimetric analysis (TGA) of the pure-halide CsCu_2X_3 compounds.

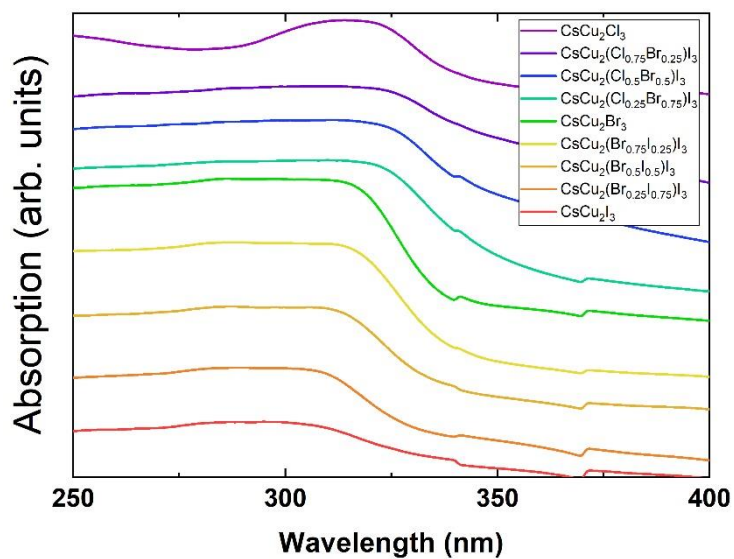


Figure S11. Normalized absorbance spectra of powders of all CsCu_2X_3 compounds.

Table S2. Lattice parameters derived from Le Bail fits of $\text{Cs}_3\text{Cu}_2\text{X}_5$ compounds (space group = $Pnma$ for all compounds except for $\text{Cs}_3\text{Cu}_2\text{X}_5$ for which $Cmcm$ is assumed).

X	a (Å)	b (Å)	c (Å)	α (°)	β (°)	γ (°)	V (Å³)
I	10.16984	11.64503	14.36164	90	90	90	1701
I₇₅Br₂₅	9.61720	11.02493	13.66381	90	90	90	1634
I₅₀Br₅₀	9.81536	11.32985	14.00074	90	90	90	1557
I₂₅Br₇₅	9.70827	11.10062	13.70945	90	90	90	1477
Br	9.56618	10.92152	13.57964	90	90	90	1419
Cl₂₅Br₇₅	9.41863	10.79131	13.42943	90	90	90	1364
Cl₅₀Br₅₀	9.35090	10.68736	13.27232	90	90	90	1326
Cl₇₅Br₂₅	9.28622	10.59379	13.22188	90	90	90	1300
Cl	15.42572	8.74765	8.67929	90	90	90	1171

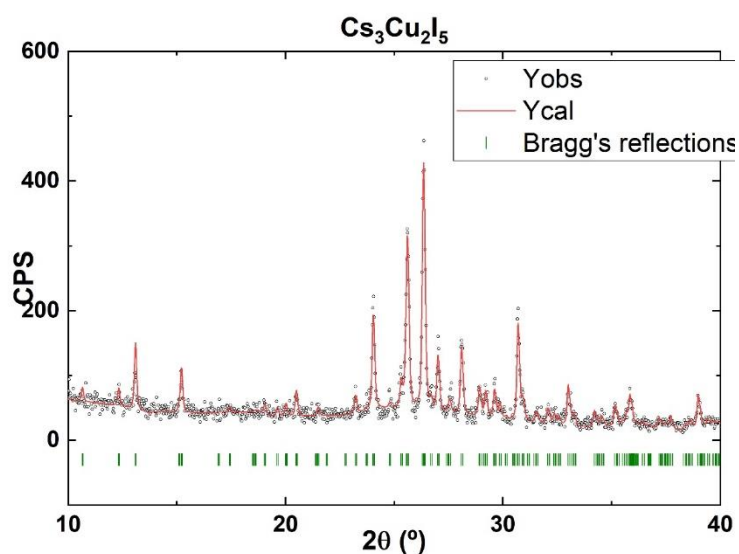


Figure S12. Experimental (open circles) and fitted (red line) diffractograms. Calculated Bragg's reflections position in green. Compound given in title.

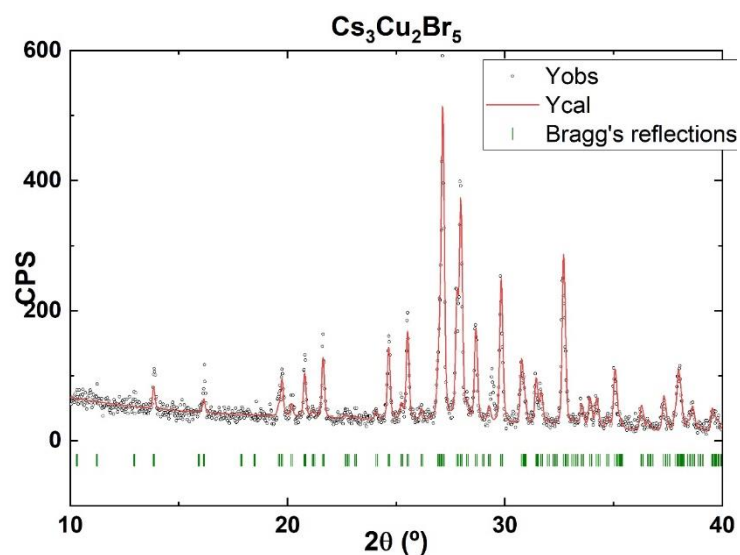


Figure S13. Experimental (open circles) and fitted (red line) diffractograms. Calculated Bragg's reflections position in green. Compound given in title.

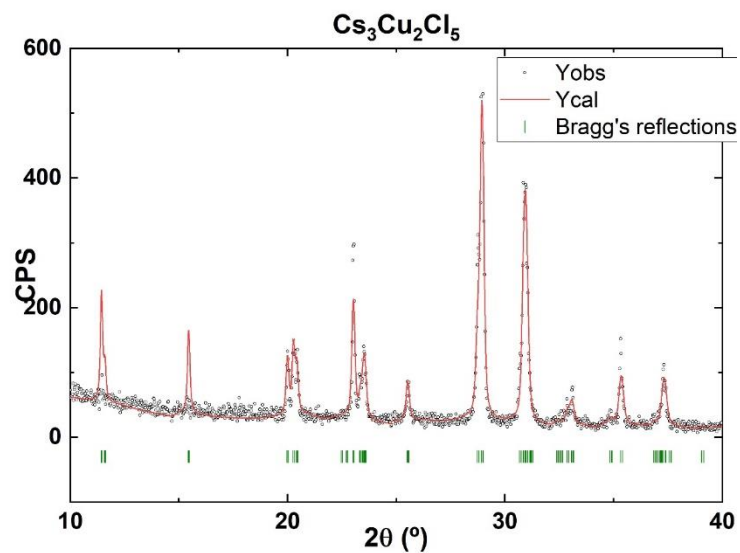


Figure S14. Experimental (open circles) and fitted (red line) diffractograms. Calculated Bragg's reflections position in green. Compound given in title.

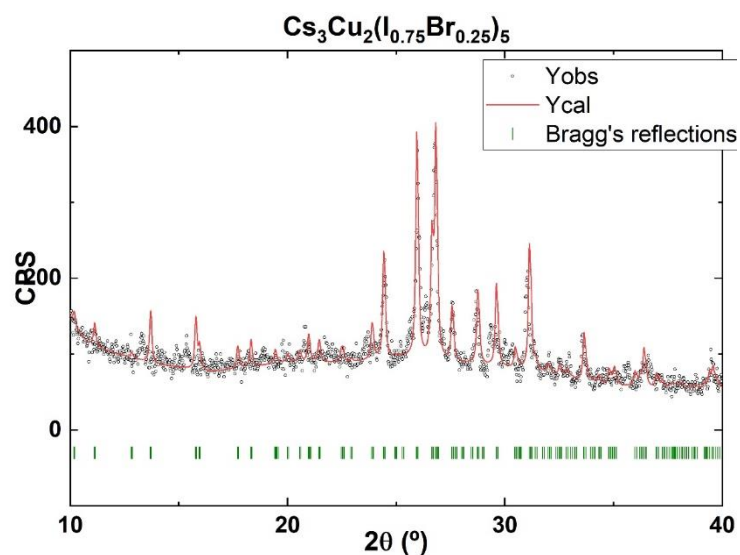


Figure S15. Experimental (open circles) and fitted (red line) diffractograms. Calculated Bragg's reflections position in green. Compound given in title.

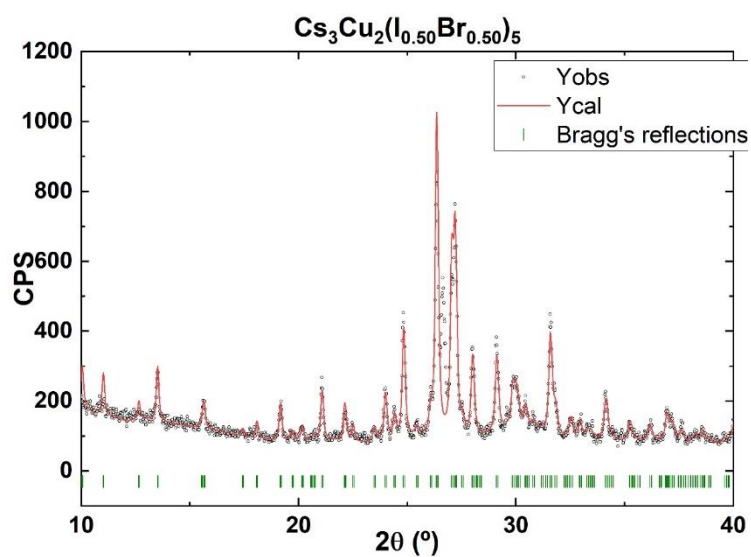


Figure S16. Experimental (open circles) and fitted (red line) diffractograms. Calculated Bragg's reflections position in green. Compound given in title.

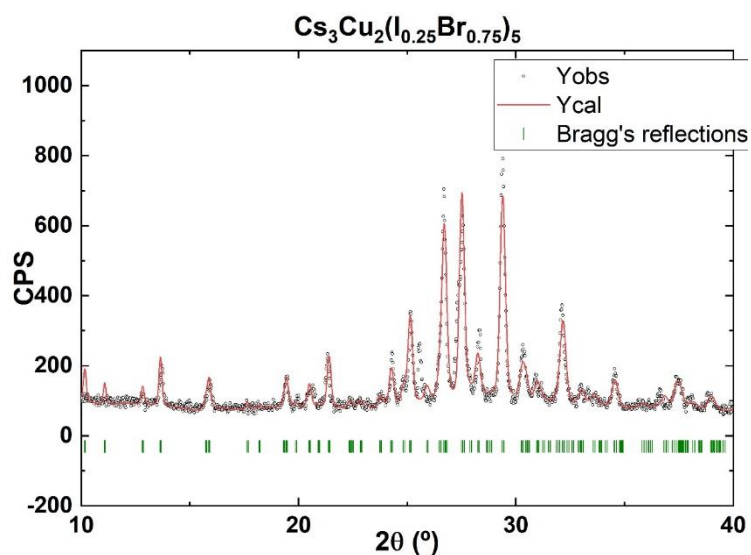


Figure S17. Experimental (open circles) and fitted (red line) diffractograms. Calculated Bragg's reflections position in green. Compound given in title.

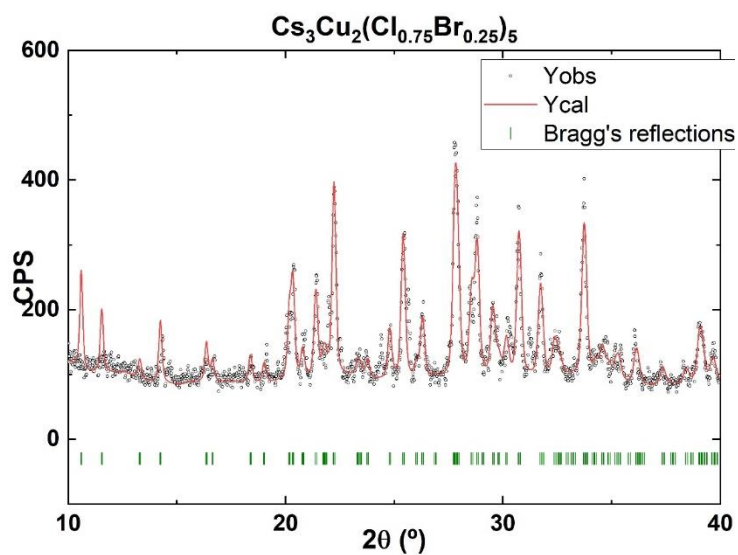


Figure S18. Experimental (open circles) and fitted (red line) diffractograms. Calculated Bragg's reflections position in green. Compound given in title.

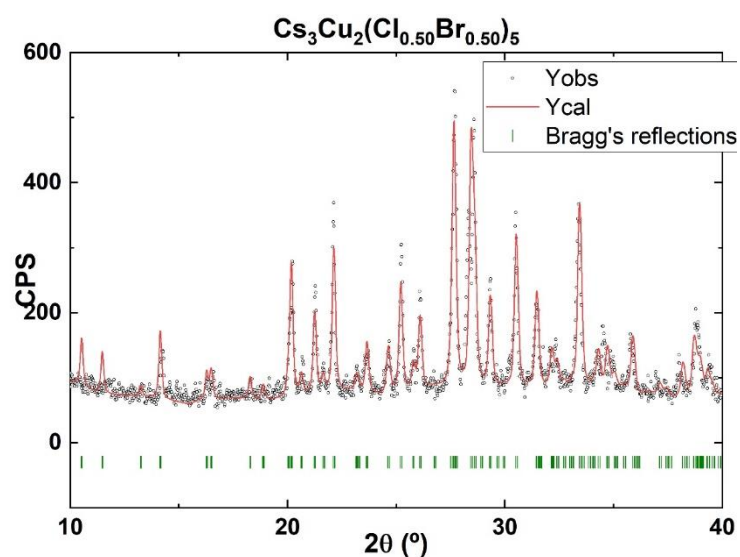


Figure S19. Experimental (open circles) and fitted (red line) diffractograms. Calculated Bragg's reflections position in green. Compound given in title.

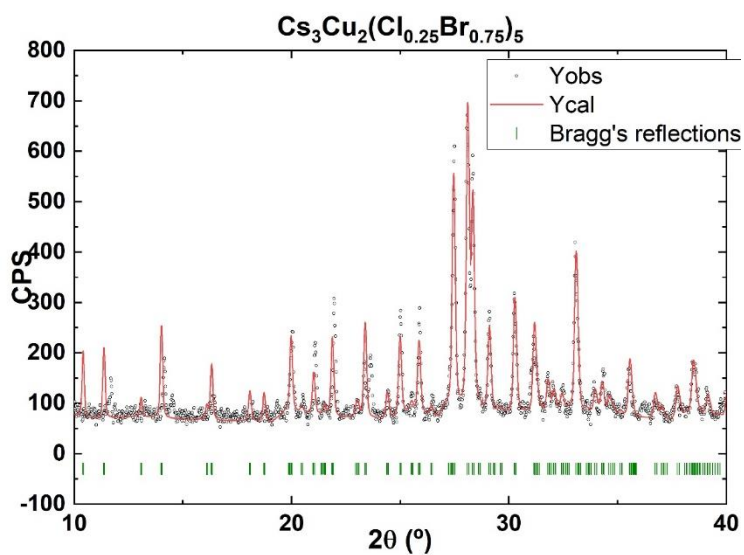


Figure S20. Experimental (open circles) and fitted (red line) diffractograms. Calculated Bragg's reflections position in green. Compound given in title.

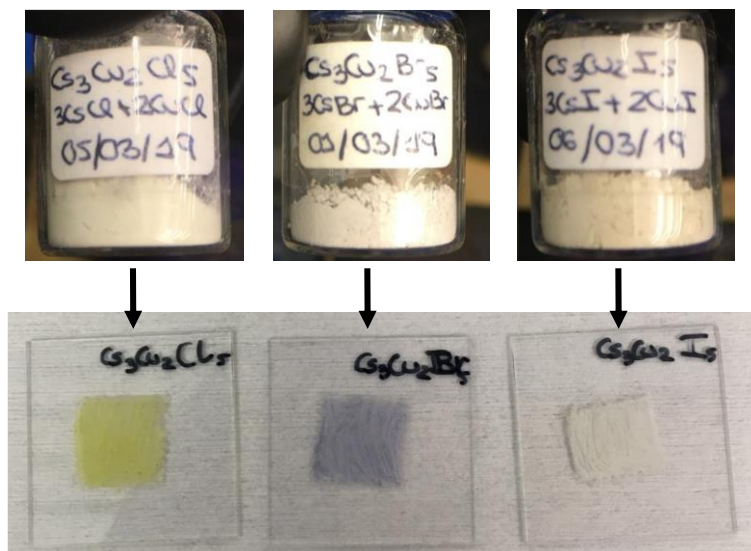


Figure S21. Comparison of the colour of the powders for $\text{Cs}_3\text{Cu}_2\text{X}_5$ when they are kept inside a nitrogen filled glovebox (up) and when they are exposed to air and moisture for 24 h (down).

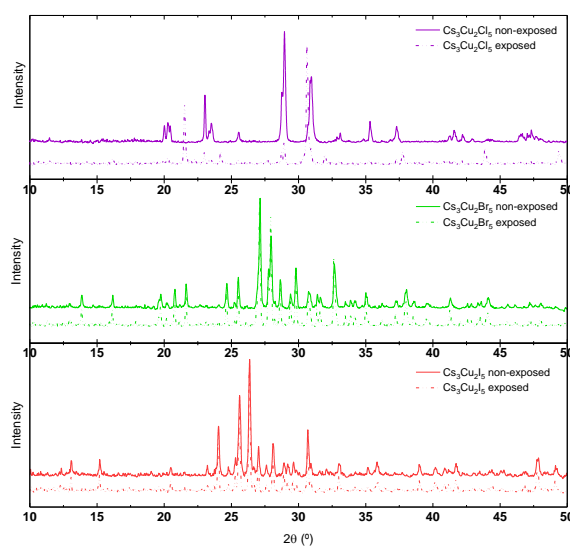


Figure S22. XRD of the as-prepared powders from ball milling synthesis for pure-halide $\text{Cs}_3\text{Cu}_2\text{X}_5$ compounds. Non-exposed to air powders are presented with a straight line and the exposed ones, with a dashed line.

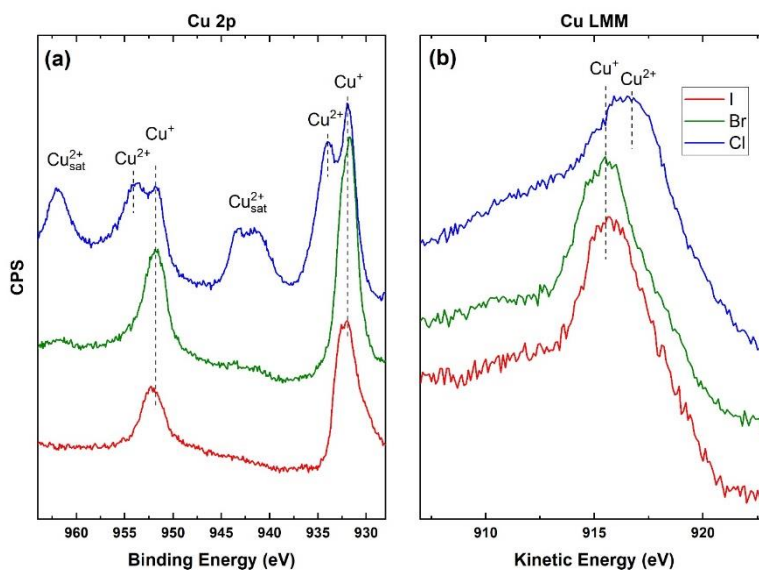


Figure S23. XPS (a) and XAES (b) characterization of $\text{Cs}_3\text{Cu}_2\text{X}_5$ ($\text{X}=\text{Cl}$, Br , and I). Clear indications of Cu(II) exist in the $\text{Cs}_3\text{Cu}_2\text{Cl}_5$ sample, demonstrating its lower stability in air.

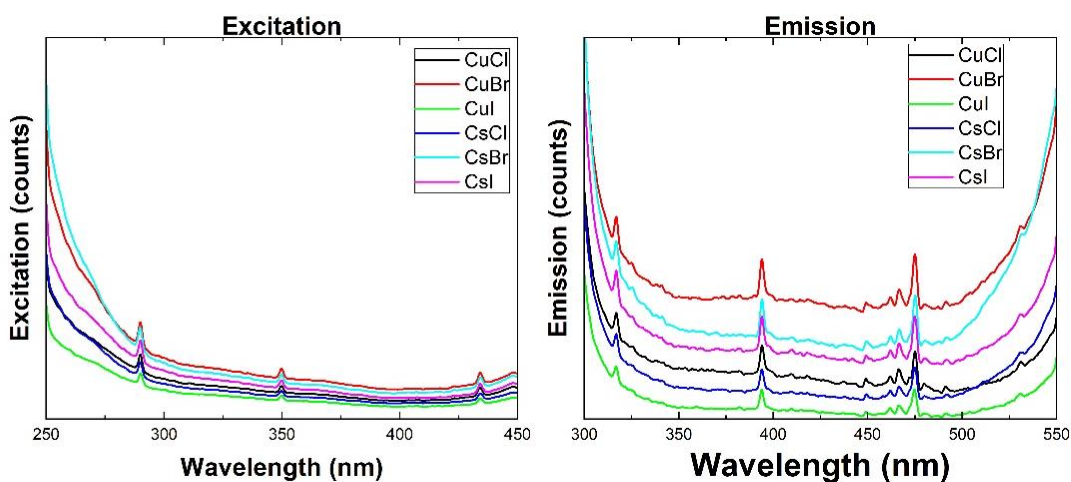


Figure S24. Excitation and emission spectra of starting reagents. Excitation spectra are acquired for an emission at 475 nm, while emission spectra are acquired with an excitation set at 290 nm. No significant PL is observed from the different chemicals in these conditions. Low-intensity, sample-independent features are attributed to the instrument. The “tails” at the lower and higher wavelengths represented here are due to the excitation source itself (first and second harmonic).

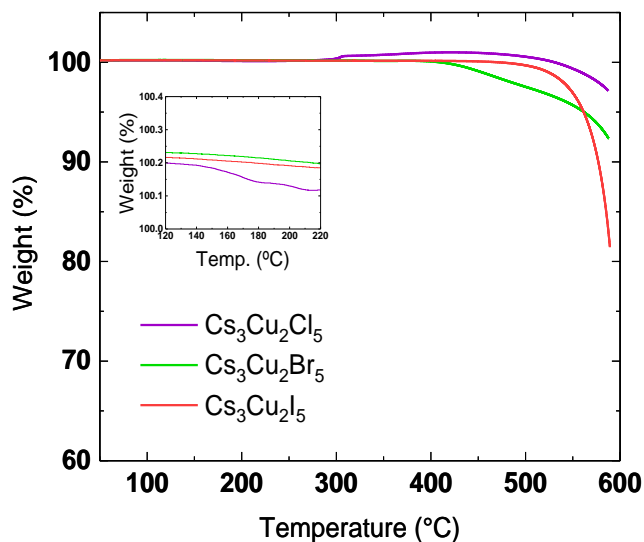


Figure S25. Thermogravimetric analysis (TGA) of the pure-halide $\text{Cs}_3\text{Cu}_2\text{X}_5$ compounds when they are kept inside a nitrogen filled glovebox. A special zoom is presented in the zone of first weight loss for chloride compound, which could correspond with the formation of Cu_2O .

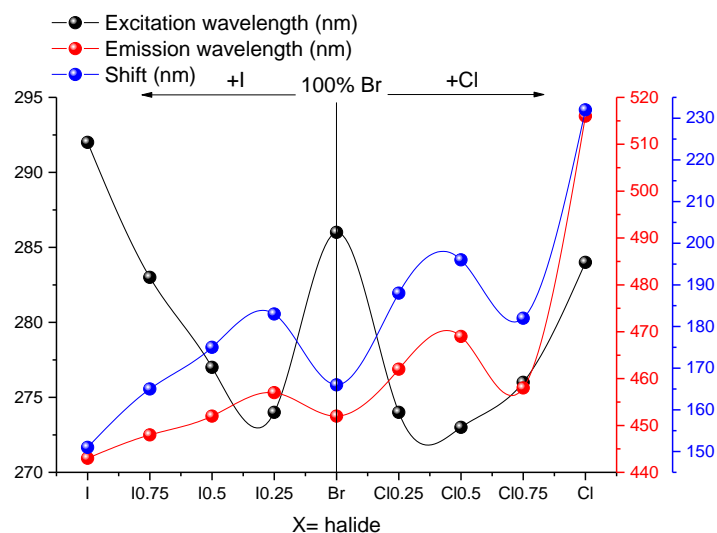


Figure S26. Variation in the emission (red) and excitation (black) wavelength trend for all the species synthesized of $\text{Cs}_3\text{Cu}_2\text{X}_5$ structure (non-exposed powders). In blue in shown the difference between emission and excitation wavelengths.

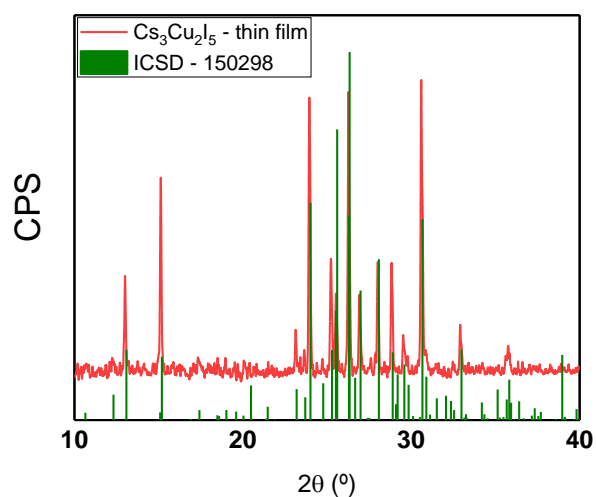


Figure S27. XRD of the thin-films by solution processes of ball-milled powders of Cs₃Cu₂I₅ (red line) and its reference bulk pattern from the Inorganic Crystal Structure Database (ICSD) (green columns).

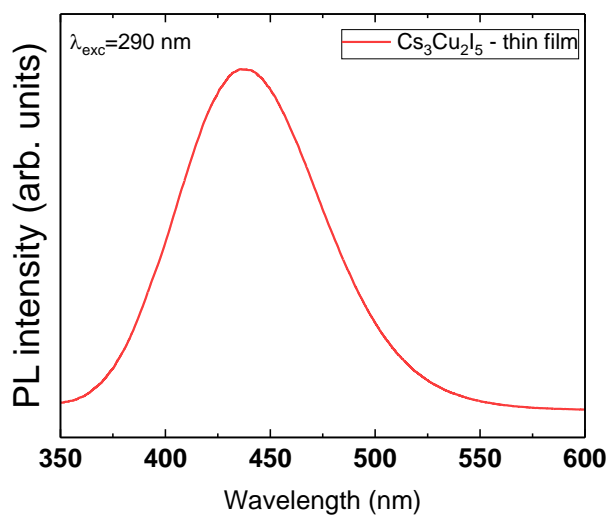


Figure S28. Photoluminescence spectra of thin-films by solution processing of Cs₃Cu₂I₅.

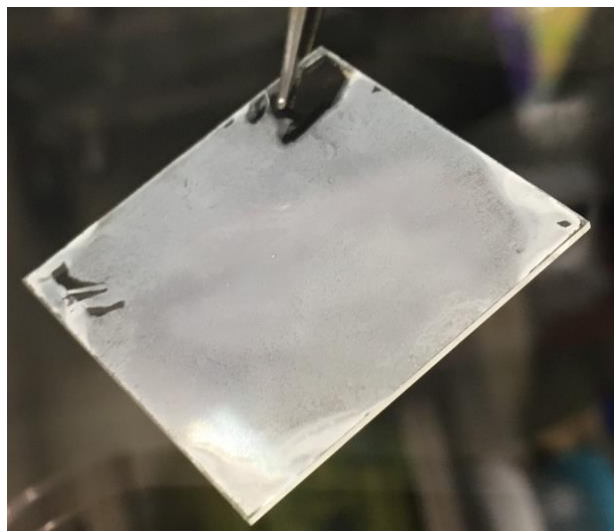


Figure S29. Photograph of spin-coated Cs₃Cu₂I₅ film showing obvious inhomogeneities. Substrate is 3 × 3 cm.

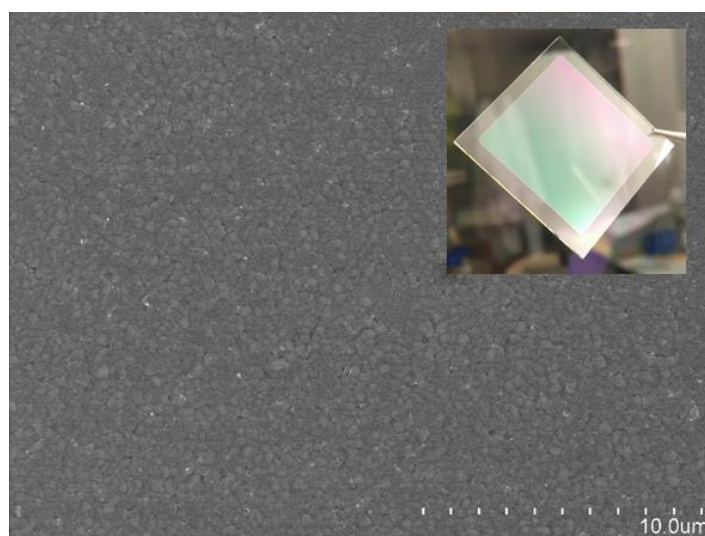


Figure S30. SEM image and photograph (inset) of SSVD-film of Cs₃Cu₂I₅ showing good homogeneity.

SUPPLEMENTARY REFERENCES:

- (1) Le Bail, A. Whole Powder Pattern Decomposition Methods and Applications: A Retrospection. *Powder Diffr.* **2005**, *20* (4), 316–326.
- (2) Thompson, P., Cox, D.E., Hasting, J. B. Rietveld Refinement of Deybe-Scherrer Synchrotron X-Ray Data from Al₂O₃. *J. App. Cryst.* **1987**, *20*, 79–83.

Appendix B

Article: Tuning the Optical Absorption of Sn-, Ge-, and Zn-Substituted $\text{Cs}_2\text{AgBiBr}_6$ Double Perovskites: Structural and Electronic Effects

Tuning the Optical Absorption of Sn-, Ge-, and Zn-Substituted Cs₂AgBiBr₆ Double Perovskites: Structural and Electronic Effects

Paz Sebastián-Luna, Joaquín Calbo, Nicolás Albiach-Sebastián, Michele Sessolo, Francisco Palazón,* Enrique Ortí, and Henk J. Bolink

Cite This: *Chem. Mater.* 2021, 33, 8028–8035

Read Online

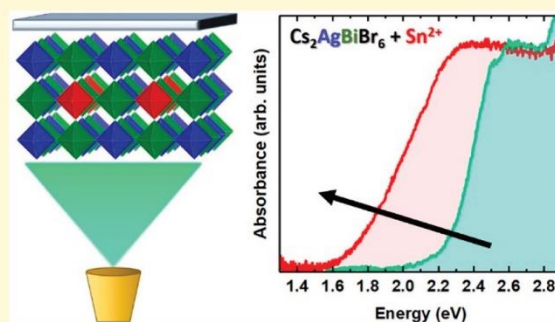
ACCESS |

Metrics & More

Article Recommendations

Supporting Information

ABSTRACT: Lead-free halide double perovskites (DPs) are highly tunable materials in terms of chemical composition and optical properties. One of the most widely reported DPs is Cs₂AgBiBr₆, which is envisaged as a promising absorber for photovoltaics. Nevertheless, its bandgap (around 1.9–2.3 eV) remains too large for common tandem solar cells. In this work, we report the mechanochemical synthesis of Sn-, Ge-, and Zn-substituted Cs₂AgBiBr₆ in powder form; their bandgaps reach 1.55, 1.80, and 2.02 eV, respectively. These differences are rationalized through density functional theory calculations, demonstrating combined electronic and structural (disorder) effects introduced by the divalent metal-cation substituents. Finally, we present the first vacuum-deposited thin films of the Sn-substituted DP, which also show a notable narrowing of the bandgap, and this paves the way toward its implementation in photovoltaic solar cells.



1. INTRODUCTION

Lead halide perovskites (LHPs) have emerged as promising materials for future photovoltaics and other optoelectronic applications. They follow the general formula APbX₃, where A is a monovalent cation [Cs⁺, CH₃NH₃⁺, or CH(NH₂)₂⁺] and X is a halide anion such as Cl⁻, Br⁻, or I⁻. Despite the well-documented performances of lead halide perovskite-based optoelectronics,^{1,2} the toxicity of Pb²⁺ ions hinders the widespread application of these materials.³ By substituting Pb(II) with a combination of B(I) and B(III) cations, while maintaining the same anion framework (see Figure 1), one can readily form double perovskites (DPs).

Halide double perovskites offer a wide range of properties that can compete directly with those of LHPs, such as their longer recombination lifetime at room temperature, higher

heat and moisture stability, and lower toxicity.⁴ Their chemical formula A₂B⁺B³⁺X₆, containing one monovalent cation (B⁺) and one trivalent cation (B³⁺), shows the large variety of different atomic combinations that can be formed with this stoichiometry. Cs₂NaInCl₆, Cs₂KInCl₆, Cs₂AgInCl₆, Cs₂AgSbCl₆, and Cs₂NaBiCl₆ are just a few examples of reported stable DPs.⁵ Nevertheless, these chloride DPs typically have bandgap energies of >2.5 eV, which are too large for photovoltaic applications.⁶ In this work, we focus on the double perovskite Cs₂AgBiBr₆, with an indirect bandgap of 1.95 eV, which is closer to a useful value in applications as a wide-bandgap absorber in tandem devices.⁴ Indeed, its performance in solar cells has been studied in the literature, but the maximum reported power conversion efficiency (PCE) is only 2.84% with a maximum photocurrent on the order of 5 mA cm⁻².⁷ It has been suggested that this may be overcome by the use of thicker films to increase absorption.⁸ However, Cs₂AgBiBr₆ films have been reported to have a limited charge diffusion length, which in turn limits the performance of such thicker films as photovoltaic absorbers.⁸

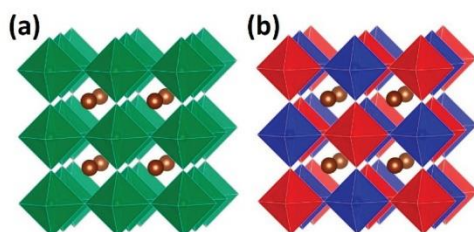


Figure 1. Comparison between the cubic structures of (a) a perovskite AB₂X₆ and (b) a double perovskite A₂B⁺B³⁺X₆.

Received: June 29, 2021
Revised: September 24, 2021
Published: October 8, 2021



A more efficient absorption of visible light (reduction of the bandgap) is required to ensure future applications of double perovskites in optoelectronics. Partial B-site substitutions have been reported as a strategic route for tackling this issue. Karunadasa and co-workers have demonstrated a bandgap narrowing of ~ 0.5 eV by using monovalent and divalent cations with the same ns^2 electronic configuration as Bi(III), namely, Tl(I) and Sn(II), altogether with an induced change in the bandgap nature from indirect to direct.^{9,10} Nevertheless, the addition of the highly toxic Tl element, the slow solution process synthesis, and the lack of a clear substitution mechanism, could hinder the further development of this B-site substitution. Mitzi and co-workers also found a bandgap decrease of ~ 0.3 eV by the addition of Sb(III), another element with an ns^2 valence electron configuration.¹¹ In contrast, addition of In(III), with a different electronic configuration [nd^{10} , same as Ag(I)], was found to increase the bandgap.¹¹ From these results, a phenomenological rule seems to suggest that ns^2 -electronic-configuration substituents (Tl^+ , Sn^{2+} , and Sb^{3+}) cause a decrease in the bandgap of $Cs_2AgBiBr_6$, while nd^{10} substituents lead to a bandgap increase. This observation led us to attempt such bandgap tuning through simpler and faster synthetic methods,¹² along with the introduction of new substituents not previously reported experimentally, in particular Ge^{2+} and Zn^{2+} , with ns^2 and nd^{10} electronic configurations, respectively.

Herein, we report the rapid dry mechanochemical synthesis of Sn^{2+} , Ge^{2+} , and Zn^{2+} -substituted $Cs_2AgBiBr_6$ and their optical and structural characterization. Note that electronic levels directly introduced by the dopants might not be the only effect at play in tuning the absorption of $Cs_2AgBiBr_6$ (the term dopant is used herein in the general sense of a substituent or an additive, without any *a priori* implication for the concentration of free charges or the position of the Fermi level within the bandgap). Indeed, theoretical studies have shown that the degree of order or disorder in the structure, that is, the precise alternation of $[AgBr_6]^{5-}$ and $[BiBr_6]^{3-}$ octahedra or in contrast the existence of segregated $[AgBr_6]^{5-}$ and $[BiBr_6]^{3-}$ domains, can have a strong influence on the bandgap. In particular, Yang et al.¹³ calculated that the bandgap may decrease from 1.93 eV for the fully ordered structure (i.e., perfectly alternating Ag and Bi) to only 0.44 eV for the fully disordered one (i.e., random distribution of Ag and Bi, not fully segregated), with intermediate values closer to those experimentally observed for a partially disordered structure. Furthermore, they showed that the addition of dopants led to a smaller formation energy difference between the ordered and disordered structures. In other words, the lower bandgap observed for doped $Cs_2AgBiBr_6$ could be directly linked to not only electronic effects as previously described, but also to increased structural disorder.

Hence, to rationalize the experimental results obtained with Sn(II), Ge(II), and Zn(II) additives, theoretical calculations are performed in a supercell with a doping ratio of $\sim 15\%$. Our results confirm a favorable neighboring substitution of the B-site doping cations, resulting in a decrease in the bandgap in going from referable $Cs_2AgBiBr_6$ to Ge^{2+} -doped and Sn^{2+} -doped analogues. The mixing of the frontier occupied and unoccupied B^{2+} dopant orbitals in the valence and conduction bands, respectively, accounts for a change in the electronic dimensionality of the double perovskite, which, together with structural octahedral deformations, leads to an indirect–direct transition of the bandgap.

Finally, Sn-based alloys are processed into thin films by single-source vacuum deposition with different substituent loadings. We demonstrate thus the first DP thin films with increased visible absorption, which paves the way for their implementation in photovoltaics and other thin film-based optoelectronic applications.

2. EXPERIMENTAL SECTION

2.1. Materials. Cesium bromide (CsBr, $>99\%$) was purchased from TCI. Bismuth bromide ($BiBr_3$, $\geq 98\%$) and zinc bromide ($ZnBr_2$, 99.999%) were purchased from Sigma-Aldrich. Silver bromide ($AgBr$, $>99.998\%$) and tin(II) bromide ($SnBr_2$, $>99.2\%$) were purchased from Alfa Aesar. Germanium(II) bromide ($GeBr_2$) was purchased from Biosynth. All chemicals were stored in a nitrogen-filled glovebox and used as received without further purification.

2.2. Mechanochemical Synthesis. An experimental procedure similar to that reported in the literature was followed.¹⁴ Binary precursor salts (CsBr, AgBr, and $BiBr_3$ as well as dopants $SnBr_2$, $GeBr_2$, and $ZnBr_2$) were introduced into 10 mL zirconia ball-mill jars with two zirconia beads that are 10 mm in diameter. Powders were maintained in an inert atmosphere, because the jars were closed inside a nitrogen-filled glovebox. Ball-milling (BM) was performed with a MM-400 shaking ball-mill from Retsch, at a frequency of 30 Hz for 1 and 5 h. Pure DP was synthesized from stoichiometric amounts of CsBr, AgBr, and $BiBr_3$. For the doped samples, calculations were taken considering 1 mol of pure DP as the basis; that is, e.g., for the 15% doped samples, 0.15 mol of the dopant was added to 1 mol of $Cs_2AgBiBr_6$ (molar ratio of 1:0.15).

2.3. Thin Film Deposition by Single-Source Vacuum Deposition (SSVD). In a typical deposition, an alumina thermal crucible (Creaphys GmbH) is placed inside a vacuum chamber and loaded with 350 mg of the as-synthesized $Cs_2AgBiBr_6$ powder (termed “DPP”). Then, the chamber was evacuated to a pressure of 8×10^{-6} mbar, and the source is rapidly heated to 550 °C. The deposition is stopped after the complete evaporation of the solid. An average film thickness of 550 nm is deposited, as measured with a mechanical profilometer.

For doped samples, three different starting powders were tested. On one hand, the mechanochemically synthesized 15% $SnBr_2$ -doped double perovskite powder was used (DP:15% $SnBr_2$). On the other hand, for the other compositions, an extra amount of dopant is added and hand mixed with the ball-milled double perovskite powder; i.e., 1 mol of the dopant was hand-mixed inside the evaporation crucible with 0.15 (or 1) mol of DP, and the $Cs_2AgBiBr_6$:dopant molar ratio is 1:0.15 (or 1:1). They are termed in the text “DPP+15% $SnBr_2$ ” or “DPP+100% $SnBr_2$ ”, respectively.

2.4. X-ray Diffraction (XRD) Characterization. X-ray diffraction was measured with a powder diffractometer Empyrean from Panalytical equipped with a Cu $K\alpha$ anode operated at 45 kV and 40 mA. Single scans were acquired in the $2\theta = 8\text{--}60^\circ$ range with a step size of $2\theta = 0.025^\circ$ in Bragg–Brentano geometry in air.

2.5. Optical Characterization. Ultraviolet–visible absorption spectra of the films and powders were recorded using an integrating sphere coupled to an Avantes Avaspec-2048L optical detector (Avantes BV).

2.6. Scanning Electron Microscopy (SEM). SEM images were acquired using a Phenom XL G2Microscope from Thermo Fisher, operating at an acceleration voltage of 10 kV.

2.7. Theoretical Calculations. Theoretical calculations were performed using the density functional theory framework under three-dimensional periodic conditions. The starting crystal structure for double perovskite $Cs_2AgBiBr_6$ was extracted from Materials Project with a cubic crystal system and $Fm\bar{3}m$ space group.¹⁵ Primitive, conventional, and $2 \times 2 \times 2$ lattices were considered in the calculations. In the $2 \times 2 \times 2$ supercell system, subsequent B-site cation substitutions of $1/8Ag^+$ and $1/8Bi^{3+}$ by $1/4Sn^{2+}/Ge^{2+}/Zn^{2+}$ (14% doping concentration) were performed. Minimum-energy crystal structures were obtained by full ion and lattice relaxation at the GGA PBEsol level of theory using a tier 1 numerical atomic orbital (NAO)

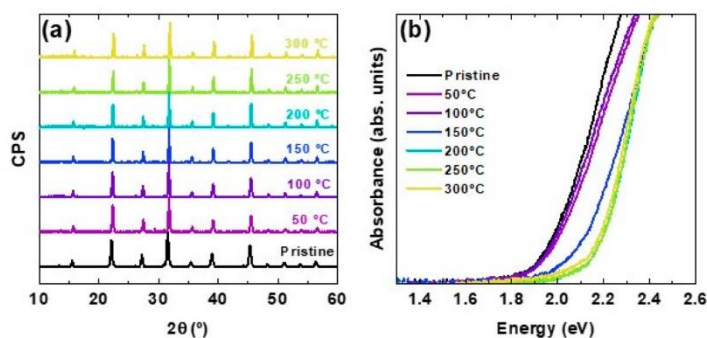


Figure 2. (a) XRD diffractograms of $\text{Cs}_2\text{AgBiBr}_6$ samples after postsynthesis annealing at different temperatures. (b) Ultraviolet–visible absorption onset to estimate the bandgap.

basis set without applying any symmetry constraints. Defect formation energies (DFEs) for other neutral substitutions with or without the formation of vacancies (V) were calculated: $\text{Sn}^{\text{II}}_{\text{Ag}} + V_{\text{Ag}}$, $\text{Sn}^{\text{IV}}_{\text{Bi}} + V_{\text{Ag}}$, and $\text{Sn}^{\text{IV}}_{\text{Ag}} + V_{\text{Bi}}$. The DFE for neutral defects was obtained according to

$$\text{DFE}(X) = E(X) - E(\text{bulk}) - \sum_i n_i \mu_i$$

where $E(X)$ is the energy of the defect supercell, $E(\text{bulk})$ is the energy of the pristine supercell, and n and μ are the number and chemical potential, respectively, of the species added (+) or subtracted (−) from the perfect bulk to form the defect. The sampling k -point grid was set to $6 \times 6 \times 6$, $4 \times 4 \times 4$, and $2 \times 2 \times 2$ for the primitive, conventional, and supercell lattices, respectively. Single-point calculations were further performed at the hybrid HSE06/tier 1 level of theory on the previously GGA PBEsol-optimized crystal structures to obtain the accurate band structures, projected density of states, and bandgap predictions. A general $L-\Gamma-X$ k -path and k -grids up to $8 \times 8 \times 8$ for primitive, $4 \times 4 \times 4$ for conventional, and $3 \times 3 \times 3$ for supercell lattices were selected to explore the first Brillouin zone of the reciprocal space. Relativistic effects were considered by using the atomic ZORA approximation.¹⁶ Crystal structure and frontier crystal orbital representations were visualized through the VESTA software.¹⁷ All of the calculations were performed by means of the efficient, accurate all-electron, full-potential electronic structure FHI-AIMS code package.¹⁶

3. RESULTS AND DISCUSSION

Mechanochemical synthesis of $\text{Cs}_2\text{AgBiBr}_6$ is carried out as described previously.¹⁴ In short, inside a nitrogen-filled glovebox, a stoichiometric amount of CsBr, AgBr, and BiBr_3 is introduced inside a 10 mL zirconia ball-mill jar with two zirconia beads that are 10 mm in diameter. The jars are sealed in nitrogen (see the Experimental Section for more details). After being ground for 1 h, the as-synthesized powder is nearly phase-pure $\text{Cs}_2\text{AgBiBr}_6$ (Figure 2a) with a bandgap of 1.94 eV (Figure 2b). This value is in general agreement with previous literature reports, which present a considerable scattering in values around 1.7–2.3 eV (with most references reporting values in the range of 2.0–2.2 eV).^{4,10,11,18–21} This mismatch of bandgap values for the $\text{Cs}_2\text{AgBiBr}_6$ double perovskite in the literature was previously noticed and studied by Yang and co-workers.¹³ Their first-principles calculations point toward the different arrangement of Ag^+ and Bi^{3+} ions as the cause of the bandgap variation. Upon introduction of different levels of cation disorder on the sublattice of Ag–Bi, the band alignment of the whole structure is modified, going from a wider indirect bandgap for the highly ordered structure to a narrower direct

bandgap for the disordered-cation substructure. The ordering of the structure may be tuned by synthetic conditions.^{21,22} Herein, the rapid dry ball-milling mechanochemical approach employed is hypothesized to lead to a partially disordered structure, according to the relatively low bandgap value of 1.94 eV with regard to most experimental reports.

When the as-synthesized powders are thermally annealed at different temperatures for 15 min, the absorption edge is found to blue-shift by ≤ 250 meV (Figure 2b). These results suggest that, as the annealing temperature increases, the double perovskite structure undergoes a conversion from a less ordered structure to a higher-order arrangement of the cations. These changes, which are likely to occur at the atomic scale, cannot be detected by X-ray diffraction within the limits of our instrumentation. In contrast, the similar diffraction pattern for all samples presented in Figure 2a demonstrates the stability of the $\text{Cs}_2\text{AgBiBr}_6$ DP without any noticeable degradation into other binary or ternary phases.

These results highlight the fact that, without any alloying or doping with extrinsic elements, the bandgap of $\text{Cs}_2\text{AgBiBr}_6$ can be tuned by synthesis and postsynthesis conditions. Nevertheless, even after a long milling process of 5 h, it appears to be difficult to reach bandgap values below approximately 1.8 eV (see Figure S1). Thus, to obtain narrower bandgap energies, we focused on the incorporation of extra ions into the double perovskite structure. In this case, we incorporated Sn^{2+} , Ge^{2+} , and Zn^{2+} in the mechanochemical synthesis of $\text{Cs}_2\text{AgBiBr}_6$ and evaluated their effect on the optical absorption of the final compound.

In accordance with previous results with different additives,^{9–11} we observe a trend in the bandgap shift according to the electronic configuration of the additive (ns^2 for Sn^{2+} and Ge^{2+} or nd^{10} for Zn^{2+}), in view of the different onset of the ultraviolet–visible (UV–vis) absorption spectra presented in Figure 3. Upon incorporation of small amounts of Sn(II), the absorption of the double perovskite can be significantly red-shifted. Following the previously optimized procedure for the $\text{Cs}_2\text{AgBiBr}_6$ dry mechanochemical synthesis (see Experimental Section for more details), Sn is incorporated into the double perovskite structure and modifies its optical properties, as one can see by the different colors of the powders (Figure S2). In Figure 3a, the red-shift in the UV–vis absorption is clearly observed, reducing the bandgap from 1.94 eV for the pure DP to 1.55 eV for the highly substituted samples (see Table S1). It is worth mentioning that the bandgap values have been extracted from the Tauc plot,

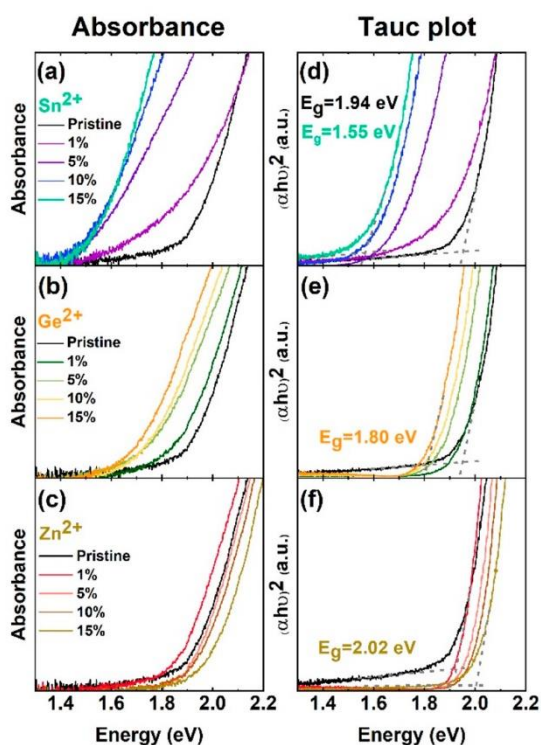


Figure 3. (a–c) Absorbance spectra and (d–f) corresponding Tauc plots of pristine and metal-substituted samples with different loadings as indicated in the legend. Bandgap energies can be estimated by a linear extrapolation of the Tauc plots, as shown in panels d–f. For the sake of simplicity, this extrapolation and estimated bandgap values are only given for the pristine (d) and most substituted samples (d–f), but all values are listed in Tables S1–S3. Tauc plots are derived considering a direct bandgap, which appears to be more accurate than considering an indirect one (Figure S3) and is also supported by theoretical calculations (Figure S11).

because the direct linear extrapolation of the absorbance spectra may be misleading (Figure 3d–f). Frequently, doped materials show sub-band gap absorption states that might have a negative influence in the estimation of the bandgap directly from the UV–vis spectra. In this case, a Tauc plot considering a direct allowed transition has been used to determine the bandgap energies. The choice of a direct transition is based on several reasons. (i) The Tauc plot of pristine $\text{Cs}_2\text{AgBiBr}_6$ with an indirect transition gives rise to a similar bandgap value compared with that of the direct transition (Figure S3). (ii) For the doped species, the Tauc plot considering an indirect transition does not show the expected linear behavior (Figure S3), which can be considered as experimental evidence of a direct bandgap. (iii) As we will discuss below, theoretical calculations confirm not only the reduction in the bandgap but also the transition from indirect to direct upon doping.

In the same line, the addition of small amounts of Ge(II) also caused a red-shift in the absorption of the double perovskite (Figure 3b). In this case, the bandgap modification is progressive and smoother than for Sn-substituted samples, reaching a bandgap of 1.80 eV (see Figure 3e and Table S2), ideal for the fabrication of tandem solar cells with silicon. This result is also in line with previous calculations in which a large

reduction in the bandgap was predicted by Sn(II) or Ge(II) doping.²³ On the contrary, upon incorporation of ZnBr_2 , the absorption onset is slightly blue-shifted compared to that of $\text{Cs}_2\text{AgBiBr}_6$, and the bandgap increases to 2.02 eV for the sample with the highest level of ZnBr_2 incorporation (Figure 3c and Table S3).

Notwithstanding the changes in the optical properties, the final structure of the double perovskite is maintained after the incorporation of the additives, without noticeable byproduct phases or particular broadening and/or narrowing of the diffraction peaks in the XRD characterization (Figures S4–S6).

To gain more insight into the structural and electronic effects upon doping, we performed a series of theoretical calculations based on density functional theory. In the primitive unit cell (Figure S8), the reference double perovskite $\text{Cs}_2\text{AgBiBr}_6$ is predicted with an indirect X–L bandgap of 2.15 eV at the HSE06 level (Figure S9 and Table S4), in relatively good accord with the experimental value of 1.94 eV and with recently reported data.²³ The valence band maximum (VBM) is described mainly by the p orbitals of Br, whereas the conduction band minimum (CBM) is predominantly contributed by the p orbitals of Bi (Figure S10). An extended supercell made by $2 \times 2 \times 2$ primitive unit cells was modeled to assess the effect of B-cation substitution in a 14% ratio (see Experimental Section for details), similar to the highest level of doping experimentally achieved (15%). We considered two doping motifs by substituting either neighboring or distant Ag^+ and Bi^{3+} atoms (Figure 4 and Table S5). Other types of charge-compensating substitutions ($\text{Sn}^{\text{II}}_{\text{Ag}} + \text{V}_{\text{Ag}}$, $\text{Sn}^{\text{IV}}_{\text{Bi}} + \text{V}_{\text{Ag}}$, and $\text{Sn}^{\text{IV}}_{\text{Ag}} + \text{V}_{\text{Bi}}$) were theoretically assessed and found to be higher in energy (Table S6).

Theoretical calculations at the HSE06 level indicate that the “neighboring” substitution is preferred over the “separated”

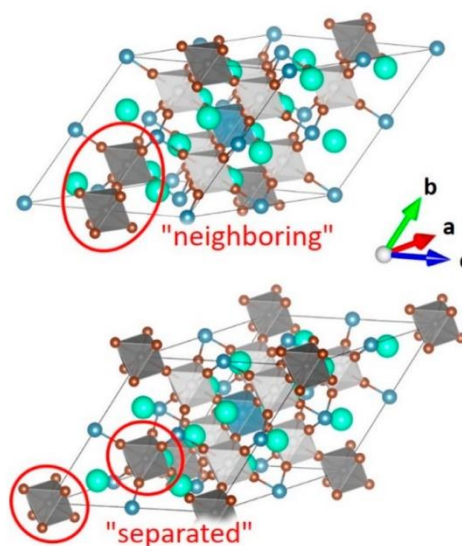


Figure 4. Extended supercells with “neighboring” and “separated” B-cation substitutions in double perovskite $\text{Cs}_2\text{Ag}_{1-a}\text{Bi}_{1-a}\text{X}_{2a}\text{Br}_6$, where $X = \text{Sn, Ge, or Zn}$ and $a = 1/8$. Color coding: light green for Cs, dark blue for Bi (coordination octahedra not shown for the sake of clarity), brown for Br, dark gray for substituted B-cation octahedra, and light gray for Ag-cation octahedra.

disposition, with energy differences of 0.07, 0.18, and 0.51 eV for Sn²⁺, Ge²⁺, and Zn²⁺ doping, respectively. These results are in good accord with a recent theoretical study in which the thermodynamic stability of Sn²⁺/Ge²⁺ B-cation substitution is assessed in the conventional unit cell of Cs₂AgBiBr₆.²³ With a focus on the most stable “neighboring” substituted double perovskites, band structure calculations on the supercell show a significant decrease in the bandgap in going from pristine Cs₂AgBiBr₆ (2.13 eV) to Ge²⁺-doped (1.81 eV) and Sn²⁺-doped (1.63 eV) structures (Figure 5), in very good

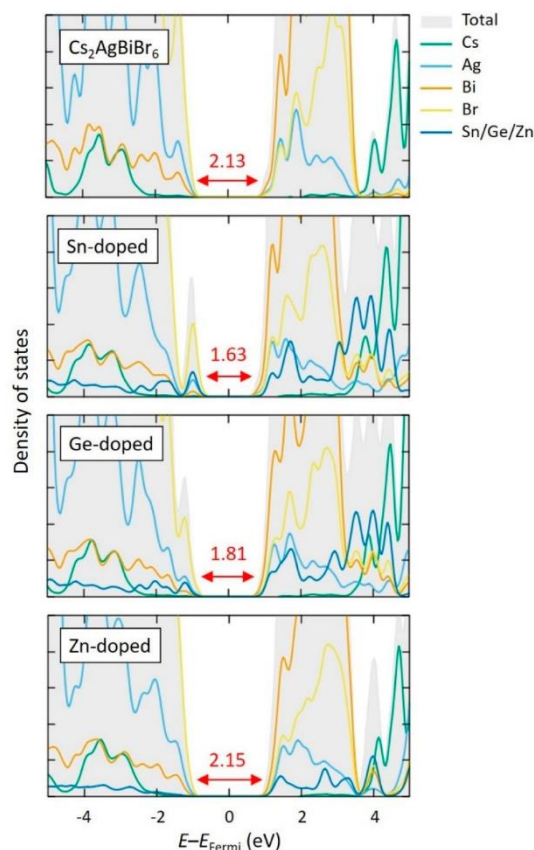


Figure 5. Atom-projected density of states calculated for the supercell of Cs₂AgBiBr₆ and its doped analogues at the HSE06 level. The bandgap is indicated in electronvolts.

correlation with the experimental results. Although the major contribution to the VBM (Br-p) and CBM (Bi-p) does not change with respect to the reference Cs₂AgBiBr₆, the s and p orbitals of Sn and Ge significantly participate in the frontier bands of the doped material. This can be seen from the density of states (Figure 5 and Figures S12–S14), crystal orbital topologies (Figure 6 and Figure S10), and Mulliken-projected band structures (Figure S11). Importantly, the nature of the bandgap changes from indirect (X–L) to direct (Γ–Γ) upon doping (Figures S9 and S11), which can be explained by the mixing of the s orbital of the doping element (Sn or Ge) with the Br p orbital in the VBM, and of the Sn/Ge p orbital with the Bi p orbital in the CBM (see Figure 6 for the case of Sn²⁺ and Figure S15 for Ge²⁺), in accord with previous

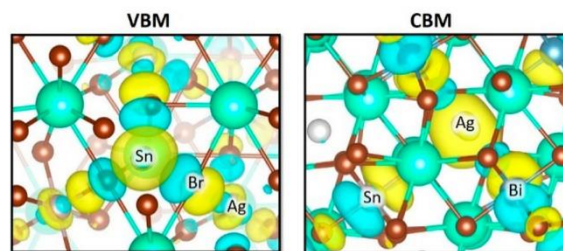


Figure 6. Frontier crystal orbitals corresponding to the VBM and CBM calculated at the HSE06 level for the Sn²⁺-doped double perovskite. Color coding: light green for Cs, light gray for Ag, blue-gray for Bi, brown for Br, and yellow and turquoise for crystal orbital phases (isovalue of 0.04).

suggestions.²³ Moreover, a significant distortion along with a tilting of the B-site octahedra is predicted upon doping (see Figures S16 and S17). The reduction of the bandgap found experimentally and confirmed theoretically after ns² B-site doping therefore implies a significant geometry deformation accompanied by a change in the electronic dimensionality of the double perovskite, rather than a simple inclusion of frontier, discrete defect states by Sn²⁺ or Ge²⁺.²⁴

In contrast to ns² doping, nd¹⁰ Zn²⁺ B-cation substitution leads to a negligible change in the bandgap (2.15 eV) with respect to Cs₂AgBiBr₆ (Figure 5). In this case, the relatively deep energy levels of nd¹⁰ Zn²⁺ do not interact with the VBM, whose nature is described by the Br p and Ag d orbitals (Figure 5), as in the case of the undoped DP. The unoccupied Zn 4s⁰ orbitals are located slightly higher in energy from the CBM and weakly interact with the Bi p and Ag s orbitals (Figure S18). The Zn–Br distances are significantly distorted out of a perfect octahedron (Figure S17); however, this geometry deformation does not introduce frontier defect states within the bandgap.

Considering the experimental and theoretical results reported so far, Sn stands out as the best option to significantly reduce the bandgap of Cs₂AgBiBr₆. However, the implementation of these materials in most optoelectronic devices such as solar cells or light-emitting diodes requires their deposition as thin films. Single-source vacuum deposition (SSVD) has been demonstrated to be a fast and reproducible method compatible with a wide range of materials for obtaining thin, smooth, and homogeneous films.^{25–28} In this technique, the presynthesized powder materials are placed inside a ceramic crucible in a vacuum chamber. When the crucible is heated at a prefixed temperature under high-vacuum conditions, the materials sublime and deposit on top of a substrate, placed right above the material source. Eventually, thin films with the same composition as the starting materials are deposited onto the substrates.

To the best of our knowledge, SSVD has been employed successfully by others to deposit pure, wide-bandgap, Cs₂AgBiBr₆, but it has never been used to prepare thin films of the doped, low-bandgap compositions.^{29,30} We first optimized the conditions for the deposition of the undoped DP presynthesized by dry ball-milling (see Experimental Section for further details). As-deposited films do not show the expected diffractogram and optical absorption of Cs₂AgBiBr₆ (Figure S19). Similar to what was described in previous reports, we also observed that the as-prepared films presented XRD peaks corresponding to undesirable side phases such as Cs₃Bi₂Br₉, with a preferential orientation along the c-

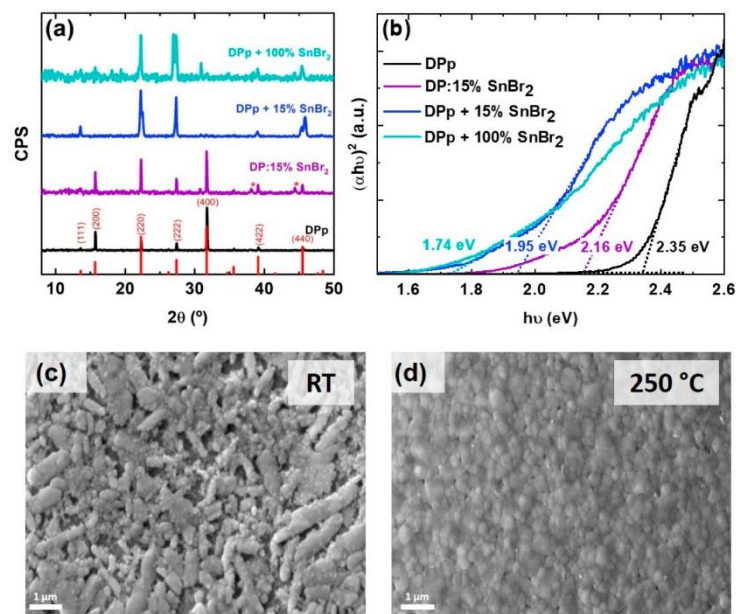


Figure 7. (a) XRD diffractograms of SSVD thin films of pristine and Sn-doped $\text{Cs}_2\text{AgBiBr}_6$ samples after annealing at 250°C . Red asterisks indicate the interfering peaks from the Al platform of the XRD setup. DPp refers to the deposition of pure ball-milled $\text{Cs}_2\text{AgBiBr}_6$, DP:15% SnBr_2 to ball-milled doped $\text{Cs}_2\text{AgBiBr}_6$:15% SnBr_2 , DPp+15% SnBr_2 to pure ball-milled $\text{Cs}_2\text{AgBiBr}_6$ with an extra 15% of SnBr_2 added and manually mixed in the crucible, and DPp+100% SnBr_2 to pure ball-milled $\text{Cs}_2\text{AgBiBr}_6$ with an extra 100% of SnBr_2 added and manually mixed in the crucible. (b) Tauc plots [derived from absorbance spectra (Figure S21)] of post-annealed Sn-doped thin films considering a direct allowed transition. (c) SEM images of pristine DP thin films at room temperature and (d) annealed at 250°C (scale bar of $1\ \mu\text{m}$).

axis as one can see by the main peaks at $2\theta = 8.7^\circ$ and 26.3° corresponding to the (001) and (003) planes, respectively (Figure S19a).^{29,31} This is also in accordance with the observed wide bandgap (Figure S19b). After being annealed at a high temperature (250°C), these unwanted byproducts vanish to yield the expected $\text{Cs}_2\text{AgBiBr}_6$ phase (Figure 7a; black diffractogram termed “BM DPp”). This transformation is also linked to important changes in morphology, as observed by SEM (Figure 7c,d). The as-deposited film shows a heterogeneous morphology with anisotropic domains of different sizes. After annealing, the morphology becomes much more homogeneous, with close-packed grains or domains $\sim 500\ \text{nm}$ in typical size. High-resolution X-ray photoelectron spectra of Cs 3d, Ag 3d, Bi 4f, and Br 3d signals are presented in Figure S20. Quantitative analysis of the thin film, based on these spectra, yields atomic percentages of 20.3%, 10.4%, 9.2%, and 60.1% for Cs, Ag, Bi, and Br, respectively. This highlights the nearly stoichiometric transfer of the preformed $\text{Cs}_2\text{AgBiBr}_6$ material by SSVD. Indeed, within instrumental and analysis error, the values are very close to the expected composition. Thin films of the pristine double perovskite present a bandgap of 2.35 eV (Figure 7b), in agreement with previous reports of this material.^{32,33}

Finally, we tested the SSVD of Sn-substituted DP. The SSVD of presynthesized 15% Sn-doped powder (DP:15% SnBr_2) after annealing at 250°C led to a slight red-shift of the absorption onset in regard to the pristine composition (Figure 7b and Figure S21). Nevertheless, according to the XRD diffractograms, the overall structure is kept constant, following the same pattern as the annealed pure double perovskite thin films (Figure 7a).

To achieve thin films with a narrower bandgap, more SnBr_2 was added to the pure DP inside the evaporation crucible (this is, without previously ball-milling these mixtures), we explored two different ratios (see Experimental Section). When 15% SnBr_2 was added to the nondoped DP (DPp+15% SnBr_2), there is a further red-shift of the absorption onset of the thin films, achieving a bandgap of 1.95 eV (Figure 7b). Elemental analysis derived from XPS (Figure S22) reveals that in both cases the molar fraction of Sn(II) present in the films is similar and around 5% (independent of whether 15% SnBr_2 is added before or after ball-milling). However, the bandgap shift is accompanied by changes in crystallinity (Figure 7a). Indeed, the diffractogram of this sample with SnBr_2 added during the evaporation corresponds to the expected $\text{Cs}_2\text{AgBiBr}_6$ double perovskite phase, albeit with a preferential orientation perpendicular to the (220) and (222) planes (see Figure S23). If the amount of SnBr_2 added is increased to a DP:Sn molar ratio of 1:1 (DPp+100% SnBr_2), a thin film with a 1.74 eV bandgap was obtained after annealing (Figure 7b) with a crystallinity similar to that of the 15% added film previously discussed (Figure 7a). Elemental and chemical analysis (Figure S22) shows that this drastic addition of 100% in the evaporation crucible leads to an increase in the tin atomic percentage to only 9.5%. Hence, it seems that the process is somehow limited and excess SnBr_2 is lost in the evaporation, not incorporated into the crystalline film. It is also worth mentioning that such an important addition of SnBr_2 leads to the formation of different Sn species, as evidenced by the secondary, low-binding energy component in the XPS Sn $3d_{5/2}$ spectra (see Figure S22). These results demonstrate that it is possible to obtain homogeneous thin films with the double perovskite crystal structure of $\text{Cs}_2\text{AgBiBr}_6$ and a tunable

bandgap through the insertion of tin bromide in a fully dry process.

4. CONCLUSIONS

We have studied the bandgap tuning of the $\text{Cs}_2\text{AgBiBr}_6$ double perovskite synthesized by solvent-free approaches through two different routes: (i) via postsynthesis thermal annealing and (ii) via the introduction of different dopants in the structure. The first method demonstrated that an increase in the annealing temperature leads to a widening of the bandgap, from 1.94 eV for the pristine form to 2.16 eV when annealing at 300 °C. The reason for this phenomenon may reside in the increase in the Ag–Bi lattice ordering upon annealing, which triggers an increase in the bandgap of the double perovskite. In contrast, the incorporation of SnBr_2 and GeBr_2 into the DP yielded a remarkable red-shift in the absorption onset (1.55 and 1.80 eV, respectively). The addition of ZnBr_2 , instead, induced a slight increase in the bandgap. The underlying reason for these changes was studied through density functional theory calculations, indicating that Sn^{2+} and Ge^{2+} change the electronic dimensionality of the double perovskite by mixing their occupied s orbitals in the VBM and their unoccupied p orbitals in the CBM. This, in combination with structural octahedral deformations, leads to a significant reduction of the bandgap, in agreement with the experimental results, and to an indirect-to-direct transition in the nature of the gap. Finally, Sn-doped DP thin films were deposited by single-source vacuum deposition. Different dopant concentrations were studied, revealing the possibility of tuning the absorption properties in thin films. These results pave the way to the implementation of cation-substituted $\text{Cs}_2\text{AgBiBr}_6$ thin films in next-generation optoelectronic devices.

■ ASSOCIATED CONTENT

SI Supporting Information

The Supporting Information is available free of charge at <https://pubs.acs.org/doi/10.1021/acs.chemmater.1c02236>.

XRD diffractograms after annealing; estimated bandgap values for pristine and doped samples; XRD and UV–vis absorption spectra of DP ball-milled for 5 h; pictures of Sn-doped samples; Tauc plots of doped powders considering an indirect bandgap; XRD diffractograms of doped samples; UV–vis absorption spectra of DP doped with Sn^{4+} and Ge^{4+} ; theoretical calculations, including representations of unit cells, bandgap values, band structures, density of states, frontier crystal orbital representations, and structural deformation analysis; XPS, XRD, and UV–vis absorption spectra of SSVD pristine and doped DP; and crystal orientation of $\text{Cs}_2\text{AgBiBr}_6$ (PDF)

■ AUTHOR INFORMATION

Corresponding Author

Francisco Palazón – Instituto de Ciencia Molecular (ICMol),
Universidad de Valencia, 46980 Paterna, Spain;
orcid.org/0000-0002-1503-5965;
Email: francisco.palazon@uv.es

Authors

Paz Sebastián-Luna – Instituto de Ciencia Molecular (ICMol),
Universidad de Valencia, 46980 Paterna, Spain;
orcid.org/0000-0001-6992-199X

Joaquín Calbo – Instituto de Ciencia Molecular (ICMol),
Universidad de Valencia, 46980 Paterna, Spain;
orcid.org/0000-0003-4729-0757

Nicolás Albiach-Sebastián – Instituto de Ciencia Molecular
(ICMol), Universidad de Valencia, 46980 Paterna, Spain

Michele Sessolo – Instituto de Ciencia Molecular (ICMol),
Universidad de Valencia, 46980 Paterna, Spain;
orcid.org/0000-0002-9189-3005

Enrique Orti – Instituto de Ciencia Molecular (ICMol),
Universidad de Valencia, 46980 Paterna, Spain;
orcid.org/0000-0001-9544-8286

Henk J. Bolink – Instituto de Ciencia Molecular (ICMol),
Universidad de Valencia, 46980 Paterna, Spain;
orcid.org/0000-0001-9784-6253

Complete contact information is available at:
<https://pubs.acs.org/10.1021/acs.chemmater.1c02236>

Notes

The authors declare no competing financial interest.

■ ACKNOWLEDGMENTS

This work has received funding from the Spanish Ministry of Science and Innovation and European Feder Funds (Projects RTI2018-095362-A-I00, PGC2018-099568-B-I00, PID2020-119748GA-I00, PCI2019-111829-2, and CEX2019-000919-M) and the Generalitat Valenciana (IDIFEDER/2018/061 and PROMETEO/2020/077). P.S.-L. thanks the Spanish Ministry of Universities for her predoctoral grant (FPU18/01732). F.P. and M.S. thank the Spanish Ministry of Science for their Juan de la Cierva and Ramón y Cajal contracts, respectively.

■ REFERENCES

- (1) Jeevaraj, M.; Sudhakar, S.; Kumar, M. K. Evolution of Stability Enhancement in Organo-Metallic Halide Perovskite Photovoltaics: A Review. *Mater. Today Commun.* **2021**, 102159.
- (2) Xiang, W.; Liu, S.; Tress, W. A Review on the Stability of Inorganic Metal Halide Perovskites: Challenges and Opportunities for Stable Solar Cells. *Energy Environ. Sci.* **2021**, 2090–2113.
- (3) Li, J.; Cao, H. L.; Jiao, W.; Bin; Wang, Q.; Wei, M.; Cantone, L.; Lü, J.; Abate, A. Biological Impact of Lead from Halide Perovskites Reveals the Risk of Introducing a Safe Threshold. *Nat. Commun.* **2020**, 11 (1), 310.
- (4) Slavney, A. H.; Hu, T.; Lindenberg, A. M.; Karunadasa, H. I. A Bismuth-Halide Double Perovskite with Long Carrier Recombination Lifetime for Photovoltaic Applications. *J. Am. Chem. Soc.* **2016**, 138 (7), 2138–2141.
- (5) Tang, H.; Xu, Y.; Hu, X.; Hu, Q.; Chen, T.; Jiang, W.; Wang, L.; Jiang, W. Lead-Free Halide Double Perovskite Nanocrystals for Light-Emitting Applications: Strategies for Boosting Efficiency and Stability. *Adv. Sci.* **2021**, 8, 2004118.
- (6) Adjogri, S. J.; Meyer, E. L. A Review on Lead-Free Hybrid Halide Perovskites as Light Absorbers for Photovoltaic Applications Based on Their Structural, Optical, and Morphological Properties. *Molecules* **2020**, 25, 5039.
- (7) Yang, X.; Chen, Y.; Liu, P.; Xiang, H.; Wang, W.; Ran, R.; Zhou, W.; Shao, Z. Simultaneous Power Conversion Efficiency and Stability Enhancement of $\text{Cs}_2\text{AgBiBr}_6$ Lead-Free Inorganic Perovskite Solar Cell through Adopting a Multifunctional Dye Interlayer. *Adv. Funct. Mater.* **2020**, 30 (23), 2001557.
- (8) Longo, G.; Mahesh, S.; Buizza, L. R. V.; Wright, A. D.; Ramadan, A. J.; Abdi-jalebi, M.; Nayak, P. K.; Herz, L. M.; Snaith, H. J. Understanding the Performance-Limiting Factors of $\text{Cs}_2\text{AgBiBr}_6$ Double-Perovskite Solar Cells. *ACS Energy Lett.* **2020**, 5, 2200–2207.

- (9) Slavney, A. H.; Leppert, L.; Bartesaghi, D.; Gold-Parker, A.; Toney, M. F.; Savenije, T. J.; Neaton, J. B.; Karunadasa, H. I. Defect-Induced Band-Edge Reconstruction of a Bismuth-Halide Double Perovskite for Visible-Light Absorption. *J. Am. Chem. Soc.* **2017**, *139* (14), 5015–5018.
- (10) Lindquist, K. P.; Mack, S. A.; Slavney, A. H.; Leppert, L.; Gold-Parker, A.; Stebbins, J. F.; Salleo, A.; Toney, M. F.; Neaton, J. B.; Karunadasa, H. I. Tuning the Bandgap of $\text{Cs}_2\text{AgBiBr}_6$ through Dilute Tin Alloying. *Chem. Sci.* **2019**, *10* (45), 10620–10628.
- (11) Du, K. Z.; Meng, W.; Wang, X.; Yan, Y.; Mitzi, D. B. Bandgap Engineering of Lead-Free Double Perovskite $\text{Cs}_2\text{AgBiBr}_6$ through Trivalent Metal Alloying. *Angew. Chem., Int. Ed.* **2017**, *56* (28), 8158–8162.
- (12) Palazon, F.; El Ajjouri, Y.; Bolink, H. J. Making by Grinding: Mechanochemistry Boosts the Development of Halide Perovskites and Other Multinary Metal Halides. *Adv. Energy Mater.* **2020**, *10* (13), 1902499.
- (13) Yang, J.; Zhang, P.; Wei, S. H. Band Structure Engineering of $\text{Cs}_2\text{AgBiBr}_6$ Perovskite through Order-Disordered Transition: A First-Principle Study. *J. Phys. Chem. Lett.* **2018**, *9* (1), 31–35.
- (14) Rodkey, N.; Kaal, S.; Sebastia-Luna, P.; Birkhölzer, Y. A.; Ledinsky, M.; Palazon, F.; Bolink, H. J.; Morales-Masis, M.; et al. Pulsed Laser Deposition of $\text{Cs}_2\text{AgBiBr}_6$: From Mechanothesized Powders to Dry, Single-Step Deposition. *Chem. Mater.* **2021**, *33*, 7417–7422.
- (15) Jain, A.; Ong, S. P.; Hautier, G.; Chen, W.; Richards, W. D.; Dacek, S.; Cholia, S.; Gunter, D.; Skinner, D.; Ceder, G. Commentary: The Materials Project: A Materials Genome Approach to Accelerating Materials Innovation. *APL Mater.* **2013**, *1* (1), 011002.
- (16) Blum, V.; Gehrke, R.; Hanke, F.; Havu, P.; Havu, V.; Ren, X.; Reuter, K.; Scheffler, M. Ab Initio Molecular Simulations with Numeric Atom-Centered Orbitals. *Comput. Phys. Commun.* **2009**, *180* (11), 2175–2196.
- (17) Momma, K.; Izumi, F. VESTA 3 for Three-Dimensional Visualization of Crystal, Volumetric and Morphology Data. *J. Appl. Crystallogr.* **2011**, *44* (6), 1272–1276.
- (18) Smith, M. D.; Connor, B. A.; Karunadasa, H. I. Tuning the Luminescence of Layered Halide Perovskites. *Chem. Rev.* **2019**, *119* (5), 3104–3139.
- (19) Jiang, Y.; Li, K.; Wu, X.; Zhu, M.; Zhang, H.; Zhang, K.; Wang, Y.; Loh, K. P.; Shi, Y.; Xu, Q.-H. In Situ Synthesis of Lead-Free Halide Perovskite $\text{Cs}_2\text{AgBiBr}_6$ Supported on Nitrogen-Doped Carbon for Efficient Hydrogen Evolution in Aqueous HBr Solution. *ACS Appl. Mater. Interfaces* **2021**, *13* (8), 10037–10046.
- (20) Ghasemi, M.; Zhang, L.; Yun, J. H.; Hao, M.; He, D.; Chen, P.; Bai, Y.; Lin, T.; Xiao, M.; Du, A.; et al. Dual-Ion-Diffusion Induced Degradation in Lead-Free $\text{Cs}_2\text{AgBiBr}_6$ Double Perovskite Solar Cells. *Adv. Funct. Mater.* **2020**, *30* (42), 2002342.
- (21) Ji, F.; Klarbring, J.; Wang, F.; Ning, W.; Wang, L.; Yin, C.; Figueroa, J. S. M.; Christensen, C. K.; Etter, M.; Ederth, T.; et al. Lead-Free Halide Double Perovskite $\text{Cs}_2\text{AgBiBr}_6$ with Decreased Band Gap. *Angew. Chem., Int. Ed.* **2020**, *59* (35), 15191–15194.
- (22) Kleibecker, J. E.; Choi, E.-M.; Jones, E. D.; Yu, T.-M.; Sala, B.; MacLaren, B. A.; Kepaptsoglou, D.; Hernandez-Maldonado, D.; Ramasse, Q. M.; Jones, L.; et al. Route to Achieving Perfect B-Site Ordering in Double Perovskite Thin Films. *NPG Asia Mater.* **2017**, *9* (7), e406–e406.
- (23) Ma, X.; Li, Z.; Yang, J. Efficient Direct Band Gap Photovoltaic Material Predicted Via Doping Double Perovskites $\text{Cs}_2\text{AgBiX}_6$ ($X = \text{Cl}, \text{Br}$). *J. Phys. Chem. C* **2021**, *125*, 10868–10875.
- (24) Xiao, Z.; Meng, W.; Wang, J.; Mitzi, D. B.; Yan, Y. Searching for Promising New Perovskite-Based Photovoltaic Absorbers: The Importance of Electronic Dimensionality. *Mater. Horiz.* **2017**, *4* (2), 206–216.
- (25) Sebastia-Luna, P.; Navarro-Alapont, J.; Sessolo, M.; Palazon, F.; Bolink, H. J. Solvent-Free Synthesis and Thin-Film Deposition of Cesium Copper Halides with Bright Blue Photoluminescence. *Chem. Mater.* **2019**, *31* (24), 10205–10210.
- (26) El Ajjouri, Y.; Palazon, F.; Sessolo, M.; Bolink, H. J. Single-Source Vacuum Deposition of Mechanothesized Inorganic Halide Perovskites. *Chem. Mater.* **2018**, *30*, 7423–7427.
- (27) Crane, M. J.; Kroupa, D. M.; Roh, J. Y.; Anderson, R. T.; Smith, M. D.; Gamelin, D. R. Single-Source Vapor Deposition of Quantum-Cutting $\text{Yb}^{3+}:\text{CsPb}(\text{Cl}_{1-x}\text{Br}_x)_3$ and Other Complex Metal-Halide Perovskites. *ACS Appl. Energy Mater.* **2019**, *2* (6), 4560–4565.
- (28) Longo, G.; Gil-Escrig, L.; Degen, M. J.; Sessolo, M.; Bolink, H. J. Perovskite Solar Cells Prepared by Flash Evaporation. *Chem. Commun.* **2015**, *51* (34), 7376–7378.
- (29) Fan, P.; Peng, H.-X.; Zheng, Z.-H.; Chen, Z.-H.; Tan, S.-J.; Chen, X.-Y.; Luo, Y.-D.; Su, Z.-H.; Luo, J.-T.; Liang, G.-X. Single-Source Vapor-Deposited $\text{Cs}_2\text{AgBiBr}_6$ Thin Films for Lead-Free Perovskite Solar Cells. *Nanomaterials* **2019**, *9* (12), 1760.
- (30) Pantaler, M.; Fettkenhauer, C.; Nguyen, H. L.; Anusca, I.; Lupascu, D. C. Deposition Routes of $\text{Cs}_2\text{AgBiBr}_6$ Double Perovskites for Photovoltaic Applications. *MRS Adv.* **2018**, *3* (32), 1819–1823.
- (31) Yang, B.; Chen, J.; Hong, F.; Mao, X.; Zheng, K.; Yang, S.; Li, Y.; Pullerits, T.; Deng, W.; Han, K. Lead-Free, Air-Stable All-Inorganic Cesium Bismuth Halide Perovskite Nanocrystals. *Angew. Chem., Int. Ed.* **2017**, *56* (41), 12471–12475.
- (32) Steele, J. A.; Puech, P.; Keshavarz, M.; Yang, R.; Banerjee, S.; Debroye, E.; Kim, C. W.; Yuan, H.; Heo, N. H.; Vanacken, J.; et al. Giant Electron-Phonon Coupling and Deep Conduction Band Resonance in Metal Halide Double Perovskite. *ACS Nano* **2018**, *12* (8), 8081–8090.
- (33) Pantaler, M.; Cho, K. T.; Queloz, V. I. E.; García Benito, I.; Fettkenhauer, C.; Anusca, I.; Nazeeruddin, M. K.; Lupascu, D. C.; Grancini, G. Hysteresis-Free Lead-Free Double-Perovskite Solar Cells by Interface Engineering. *ACS Energy Lett.* **2018**, *3* (8), 1781–1786.

Supporting Information for:

**Tuning the Optical Absorption of Sn-, Ge-, and Zn-
Substituted Cs₂AgBiBr₆ Double Perovskites: Structural and
Electronic Effects**

Paz Sebastián-Luna, Joaquín Calbo, Nicolás Albiach-Sebastián, Michele Sessolo,
Francisco Palazón*, Enrique Ortí and Henk J. Bolink

Instituto de Ciencia Molecular (ICMol), Universidad de Valencia, C/ Catedrático J.
Beltrán 2, 46980 Paterna, Spain

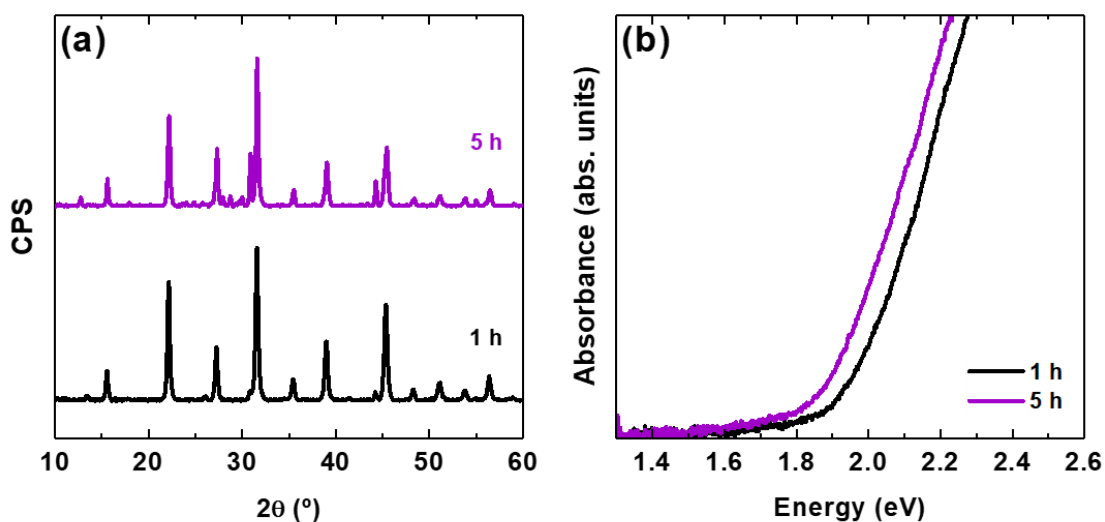


Figure S1. (a) XRD diffractograms of $\text{Cs}_2\text{AgBiBr}_6$ samples ball-milled during 1 h and 5 h. (b) UV-Vis absorption onset to estimate the bandgap.

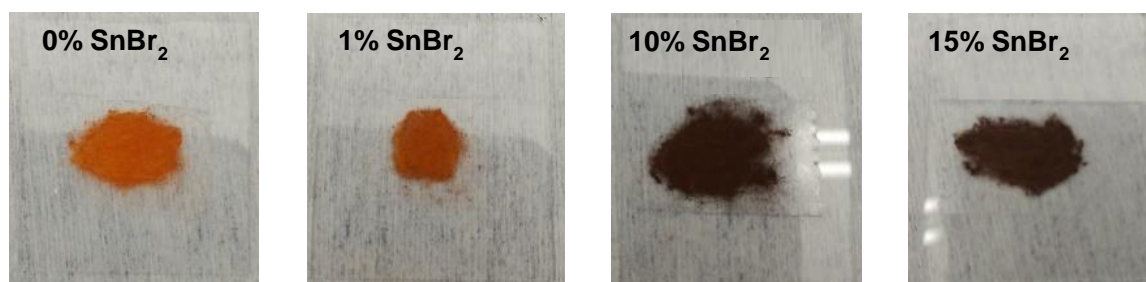


Figure S2. Color change of the ball-milled $\text{Cs}_2\text{AgBiBr}_6$ powders with extra- SnBr_2 added. An increase in the Sn content provokes a darkening of the powders, red-shifting their bandgap.

Table S1. Bandgap values linearly-extrapolated from the Tauc plot with direct transition of SnBr_2 -doped samples.

Sample	Bandgap energy (eV)
Pristine	1.94
1%	1.86
5%	1.66
10%	1.59
15%	1.55

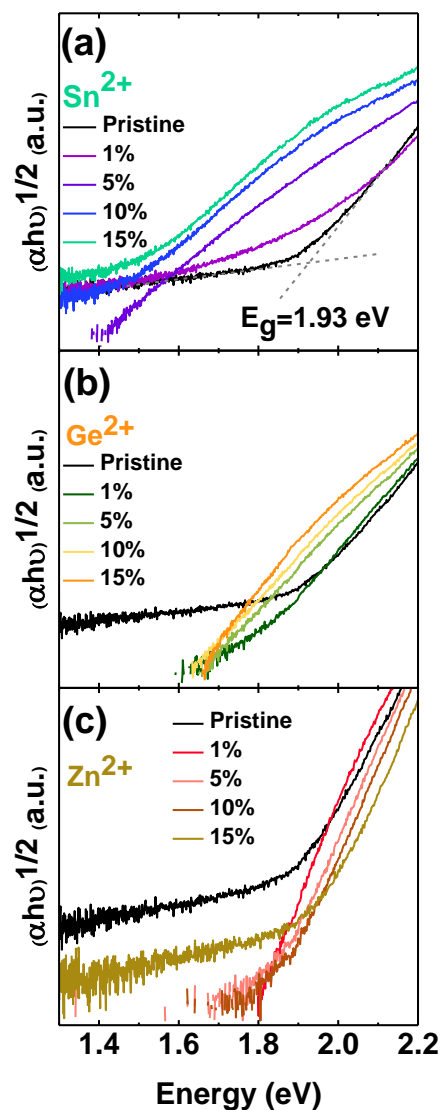


Figure S3. Tauc plots for the Sn^{2+} -, Ge^{2+} -, and Zn^{2+} -doped powders considering an indirect transition. The estimated bandgap for pristine $\text{Cs}_2\text{AgBiBr}_6$ is given. For all other samples, considering a direct transition (**Figure 3d-f** in main text) appears to be more accurate for the bandgap determination. This hypothesis is also verified by theoretical calculations, which show an indirect-to-direct transition with additives (see **Figures S9-S11** and main text for discussion).

Table S2. Bandgap values linearly-extrapolated from the Tauc plot with direct transition of GeBr₂-doped samples.

Sample	Bandgap energy (eV)
Pristine	1.94
1%	1.93
5%	1.86
10%	1.84
15%	1.80

Table S3. Bandgap values linearly-extrapolated from the Tauc plot with direct transition of ZnBr₂-doped samples.

Sample	Bandgap energy (eV)
Pristine	1.94
1%	1.92
5%	1.95
10%	1.98
15%	2.02

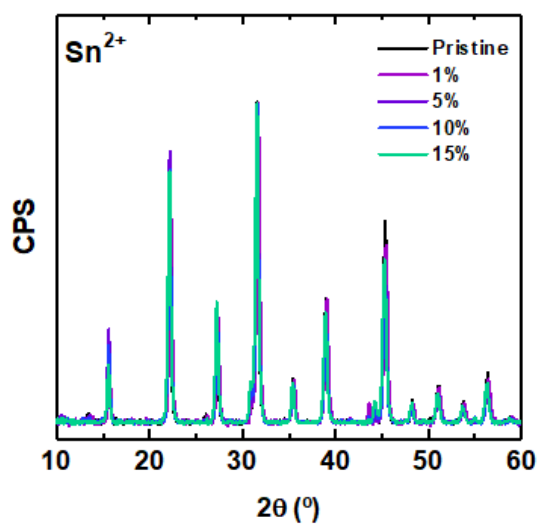


Figure S4. XRD diffractograms of as-synthesized SnBr₂-added Cs₂AgBiBr₆ powders.

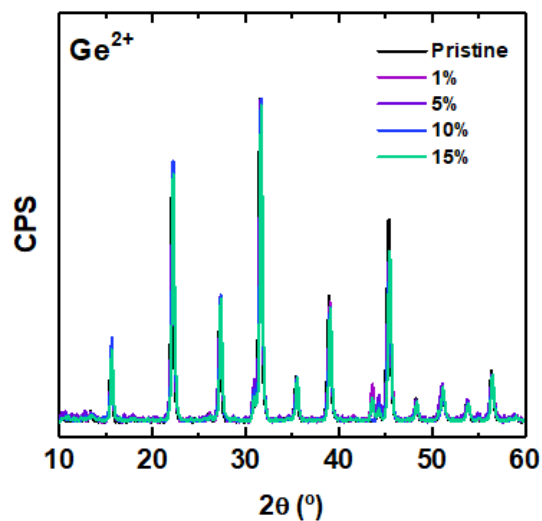


Figure S5. XRD diffractograms of as-synthesized GeBr₂-added Cs₂AgBiBr₆ powders.

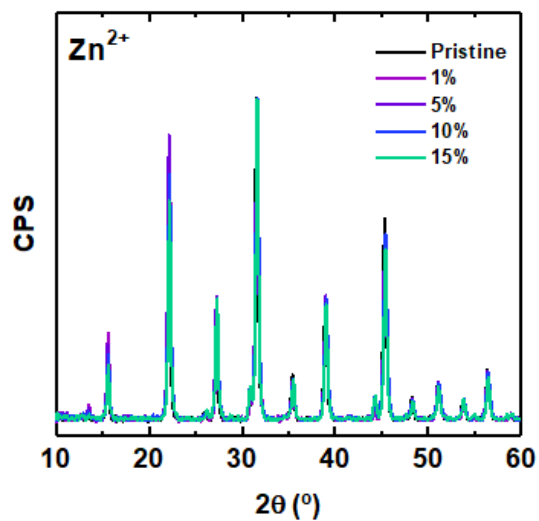


Figure S6. XRD diffractograms of as-synthesized ZnBr₂-added Cs₂AgBiBr₆ powders.

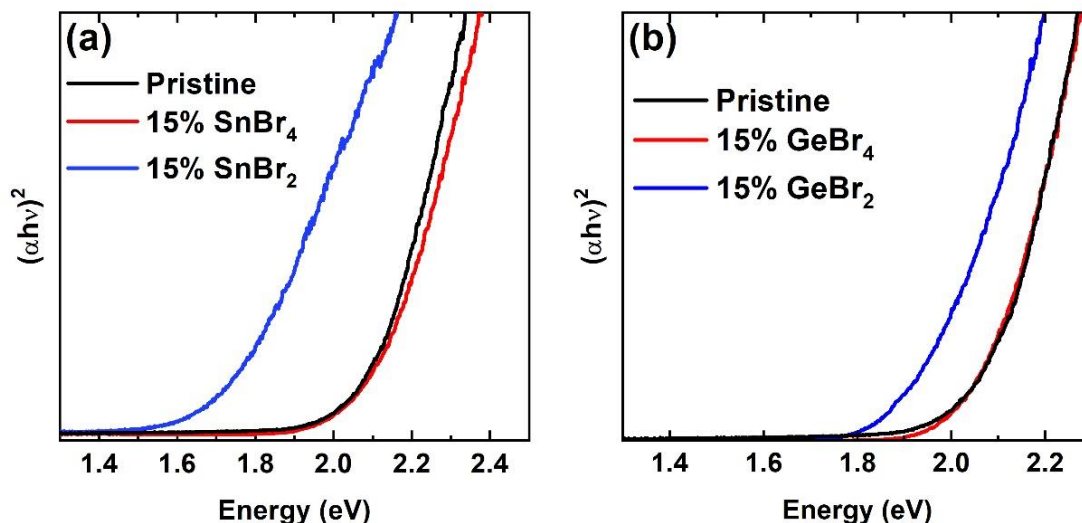


Figure S7. Tauc plots of pristine DP as well as samples prepared with 15% MBr_2 and MBr_4 additives ($M = \text{Sn}$ and Ge). Addition of $M(\text{IV})$ -based additives does not lead to a shift in bandgap, contrary to the addition of $M(\text{II})$ -based additives.

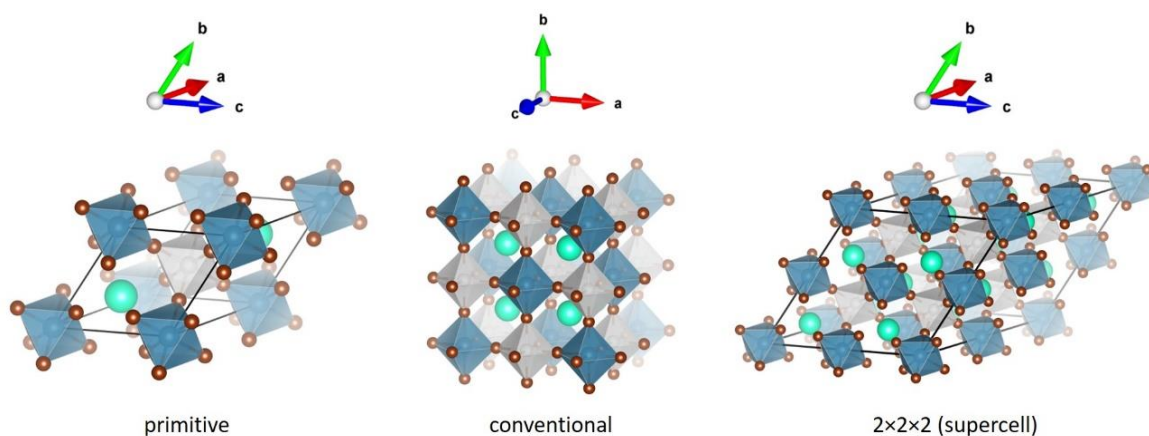


Figure S8. Primitive, conventional, and $2 \times 2 \times 2$ (supercell) lattices modelled for geometry and electronic structure calculations of $\text{Cs}_2\text{AgBiBr}_6$, with a total of 10, 40, and 80 atoms, respectively.

Table S4. Bandgap convergence as a function of unit cell and k-point sampling grid for $\text{Cs}_2\text{AgBiBr}_6$. The k-grid used in the full ion and lattice relaxation procedure for each unit cell is indicated in bold.

Unit cell (k-grid)	Bandgap (eV)
Primitive ($2 \times 2 \times 2$)	2.16
Primitive ($3 \times 3 \times 3$)	2.74
Primitive ($4 \times 4 \times 4$)	2.10
Primitive ($6 \times 6 \times 6$)	2.15

Primitive ($8 \times 8 \times 8$)	2.15
Conventional ($2 \times 2 \times 2$)	1.96
Conventional ($3 \times 3 \times 3$)	2.21
Conventional ($4 \times 4 \times 4$)	1.96
Supercell ($2 \times 2 \times 2$)	2.14
Supercell ($3 \times 3 \times 3$)	2.13

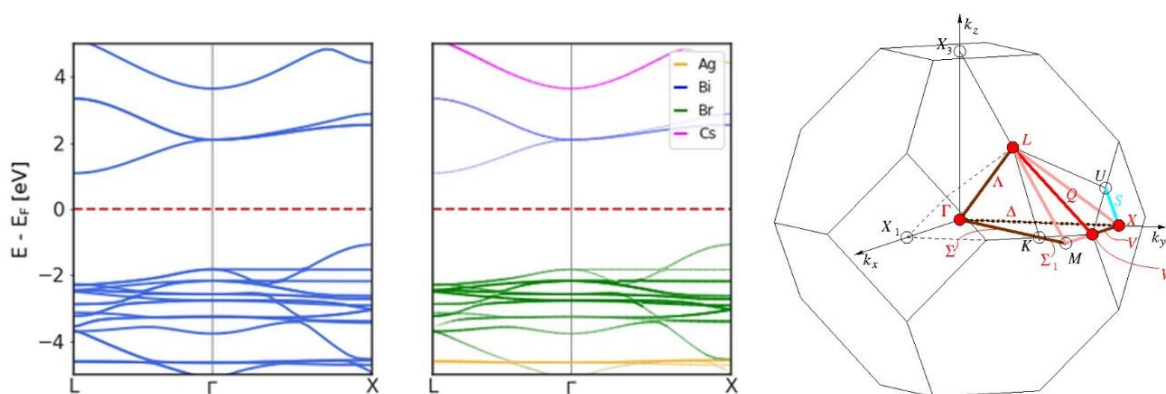


Figure S9. Band structure, Mulliken-projected band structure, and first Brillouin zone (from left to right) for the primitive unit cell of $\text{Cs}_2\text{AgBiBr}_6$.

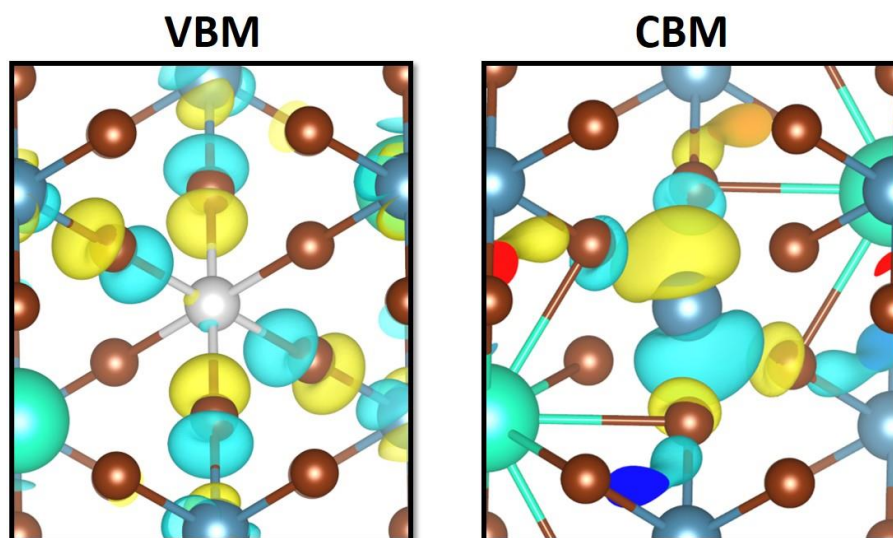


Figure S10. Frontier crystal orbitals corresponding to the valence band maximum (VBM) and conduction band minimum (CBM) calculated at the HSE06 level for the $\text{Cs}_2\text{AgBiBr}_6$ double perovskite. Color coding: light green for Cs, light grey for Ag, blue-grey for Bi, brown for Br, and yellow and turquoise for crystal orbital phases.

Table S5. Relative stability of “neighbouring” and “separated” doping in B-cation substituted Cs₂AgBiBr₆ double perovskites.

Substitution	Relative energy (eV)
Sn ²⁺ “neighbouring”	0.000
Sn ²⁺ “separated”	0.072
Ge ²⁺ “neighbouring”	0.000
Ge ²⁺ “separated”	0.176
Zn ²⁺ “neighbouring”	0.000
Zn ²⁺ “separated”	0.511

Table S6. Defect formation energy calculated for the different substitutions with Sn.

Substitution	Defect formation energy (eV)
Sn ^{II} _{Ag} + Sn ^{II} _{Bi} "neighbouring"	0.62
Sn ^{II} _{Ag} + Sn ^{II} _{Bi} "separated"	0.69
Sn ^{II} _{Ag} + V _{Ag}	2.43
Sn ^{IV} _{Bi} + V _{Ag} "neighbouring"	1.41
Sn ^{IV} _{Bi} + V _{Ag} "separated"	1.45
Sn ^{IV} _{Ag} + V _{Bi} "neighbouring"	3.28
Sn ^{IV} _{Ag} + V _{Bi} "separated"	3.69

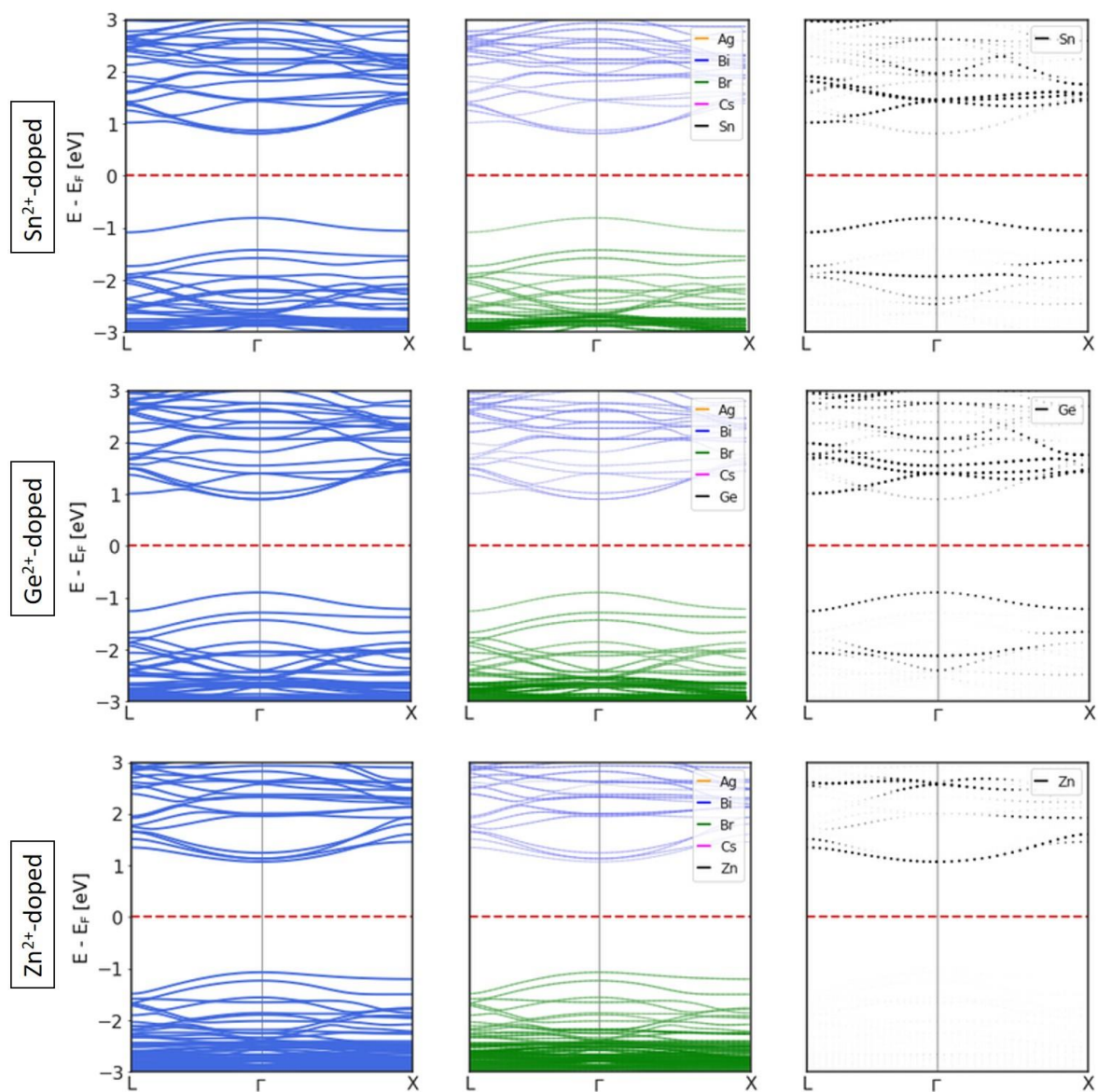


Figure S11. Band structure, Mulliken-projected band structure, and doping B-cation contribution to the band structure (from left to right) for the supercells of doped double perovskites.

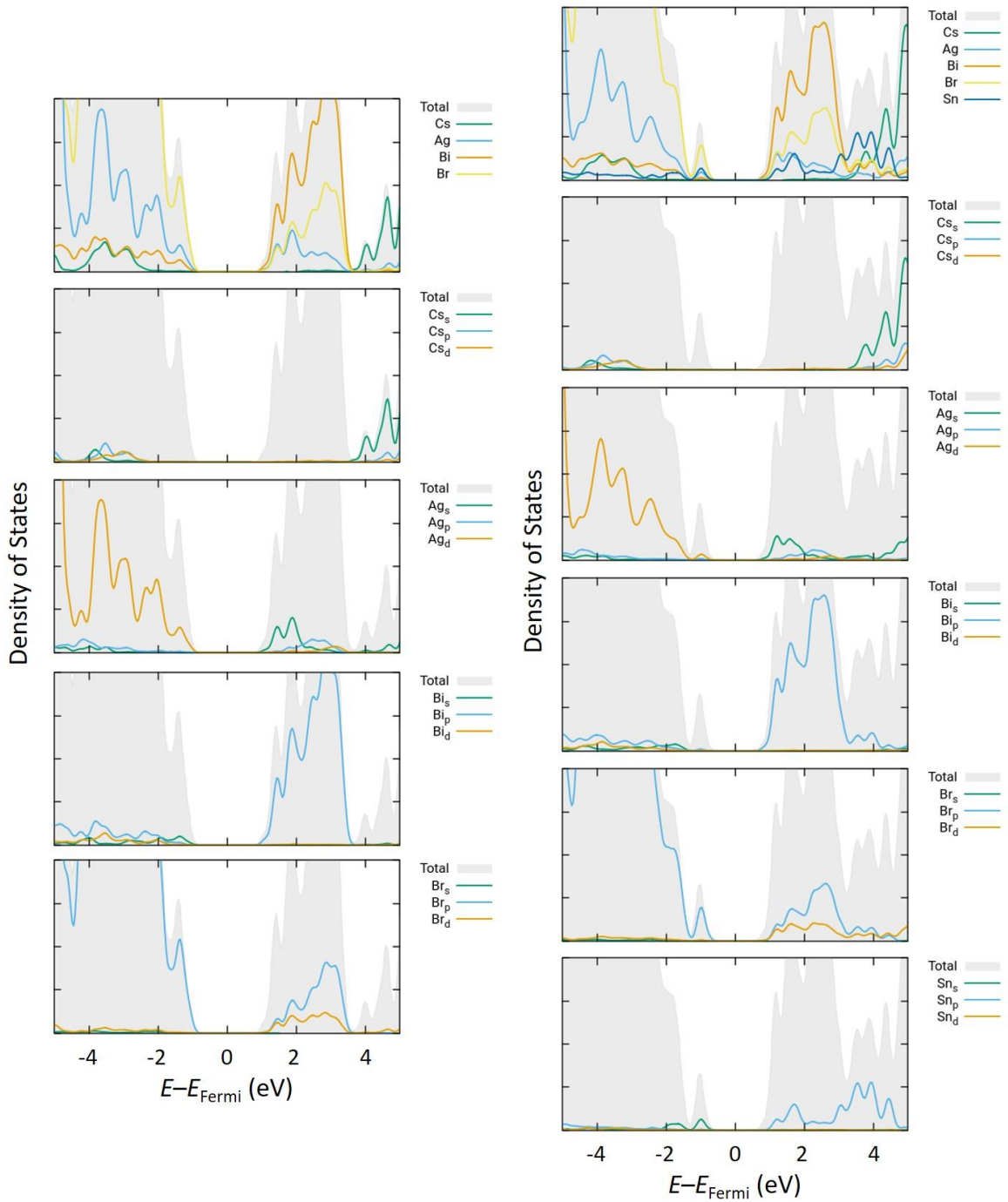


Figure S12. Atom- and angular momentum-projected density of states calculated for pristine $\text{Cs}_2\text{AgBiBr}_6$ (left) and Sn^{2+} “neighbouring”-substituted (right) double perovskites.

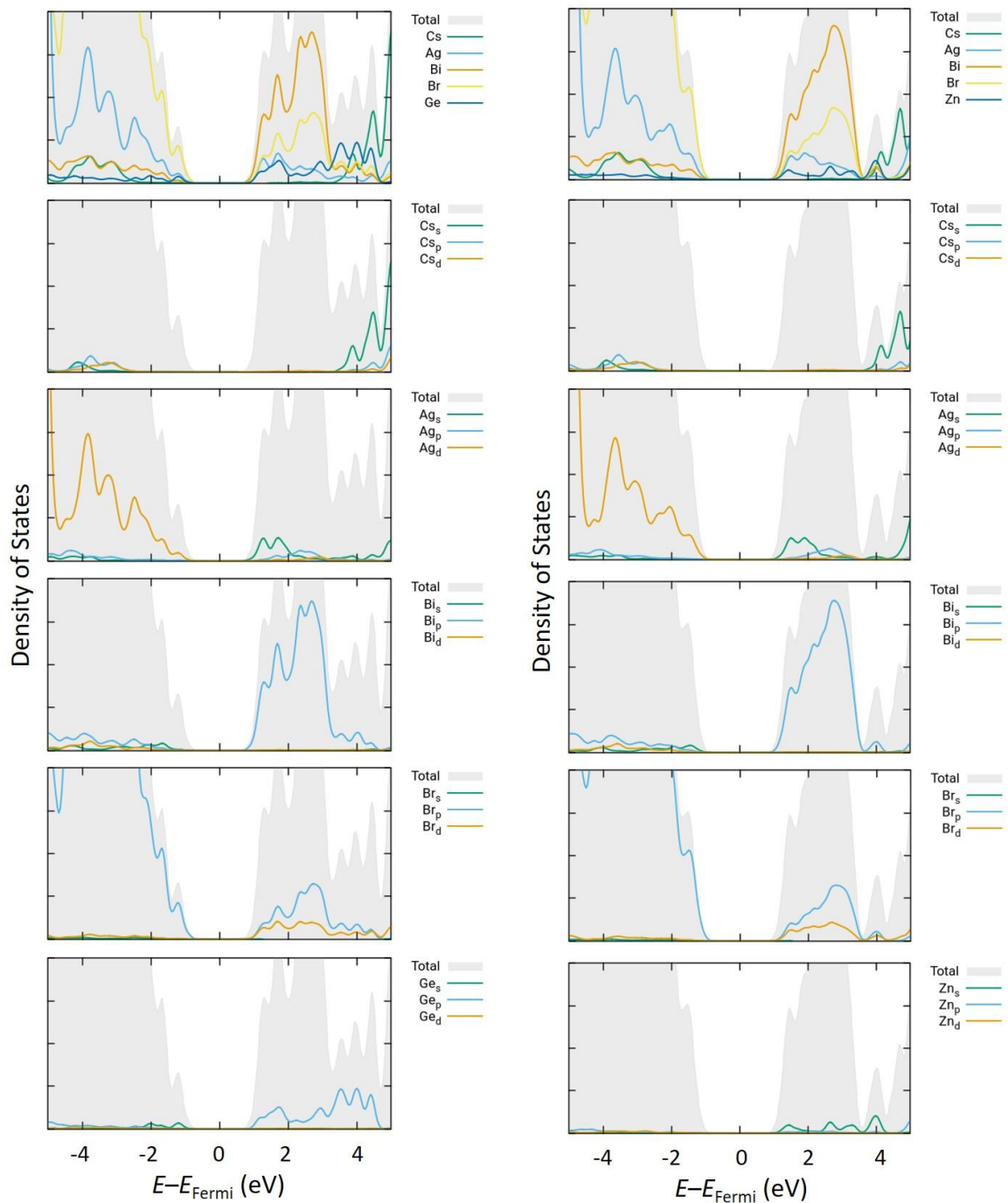


Figure S13. Atom- and angular momentum-projected density of states calculated for Ge^{2+} “neighbouring”-substituted (left) and Zn^{2+} “neighbouring”-substituted (right) double perovskites.

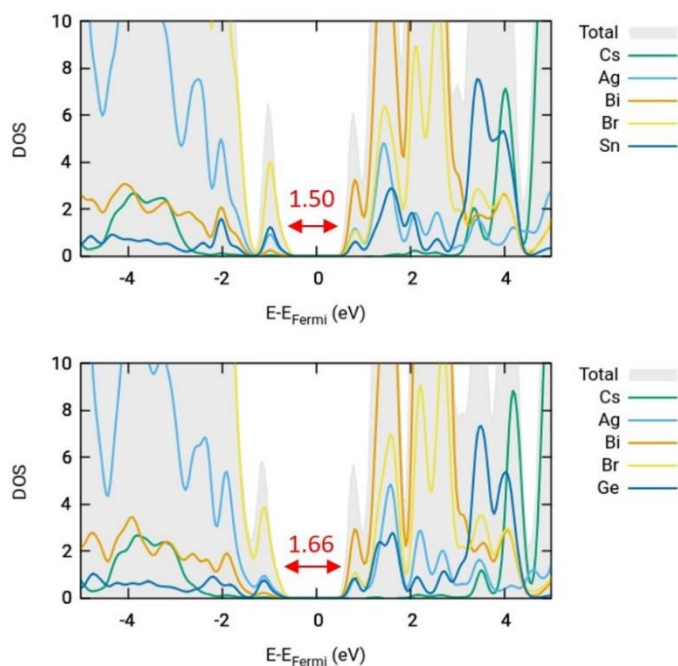


Figure S14. Atom-projected density of states calculated for Sn^{2+} “separated” substituted (top) and Ge^{2+} “separated” substituted (bottom) double perovskites. The bandgap is indicated in eV.

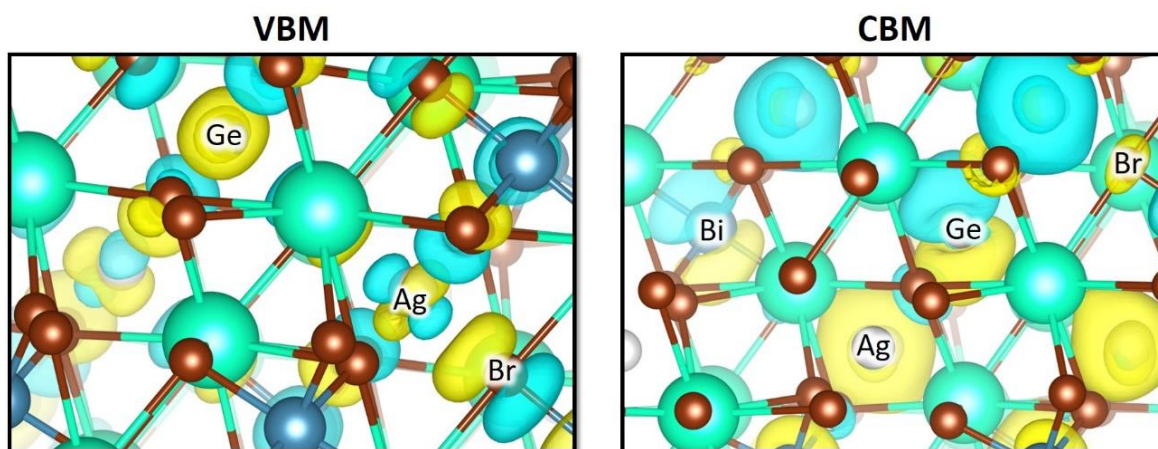


Figure S15. Frontier crystal orbitals of the VBM and CBM calculated at the HSE06 level for Ge^{2+} -doped double perovskite. Color coding: Cs in light green, Ag in light grey, Bi in blue-grey, Br in brown, and crystal orbital phases in yellow and turquoise (isovalue = 0.04).

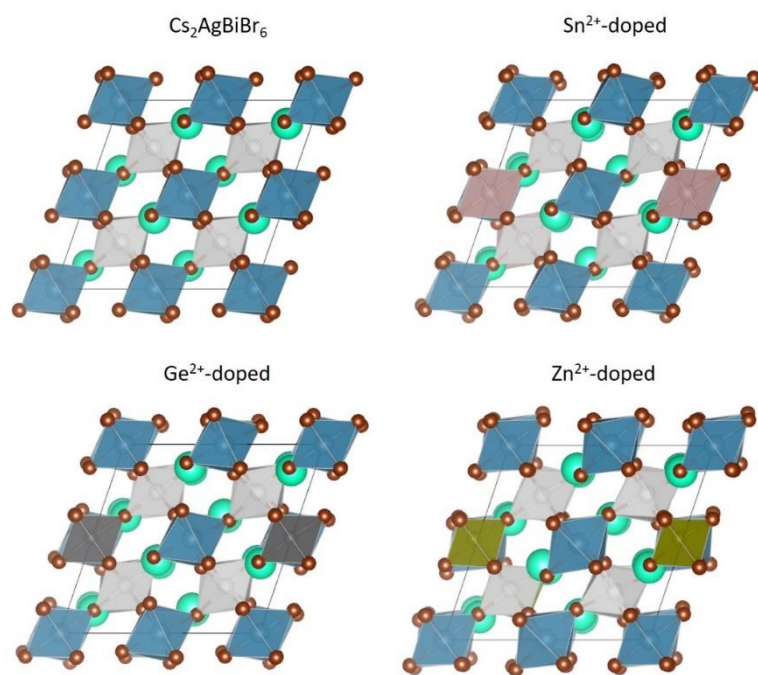


Figure S16. Minimum-energy crystal structure calculated at the PBEsol level for the supercell of $\text{Cs}_2\text{AgBiBr}_6$ and “neighbouring”-doped analogues.

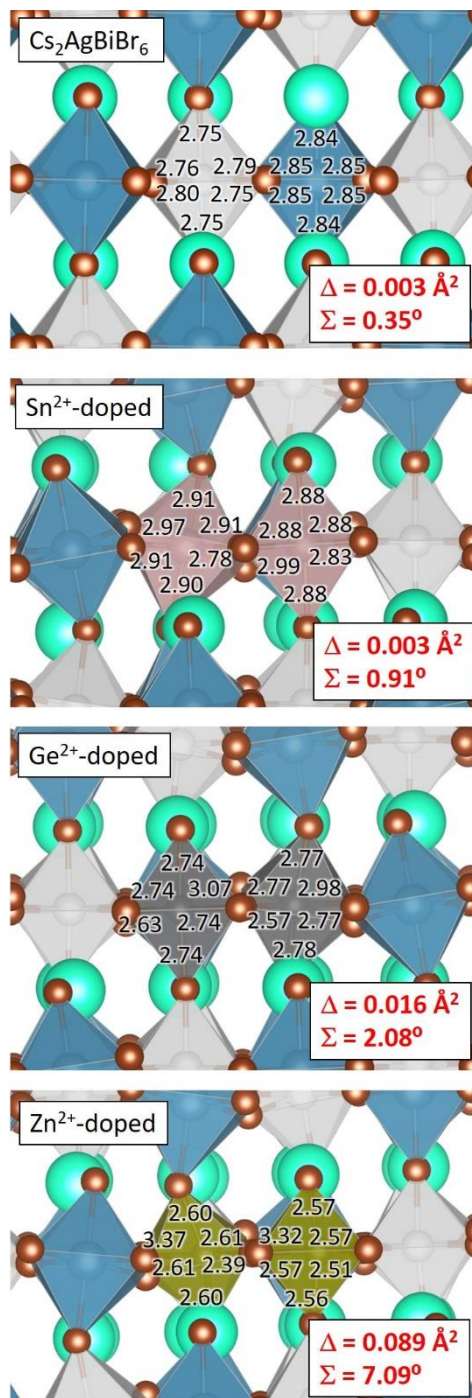


Figure S17. Octahedral B-cation to Br distances (in Å) for the minimum-energy crystal structures calculated at the PBEsol level for the supercell of Cs₂AgBiBr₆ and “neighbouring”-doped analogues. The octahedral distortion parameters Δ and Σ are calculated as $\Delta = (\Delta_{\text{Oh},1} + \Delta_{\text{Oh},2})/2$, where $\Delta_{\text{Oh},x} = 1/6 \cdot \sum((d_i - d)/d)^2$, d_i = B-cation–Br distance, d = B-cation–Br mean distance, and $\Sigma = (\Sigma_{\text{Oh},1} + \Sigma_{\text{Oh},2})/2$, where $\Sigma_{\text{Oh},x} = 1/12 \cdot \sum|\phi_i - 90^\circ|$, ϕ_i = Br–B-cation–Br angle.

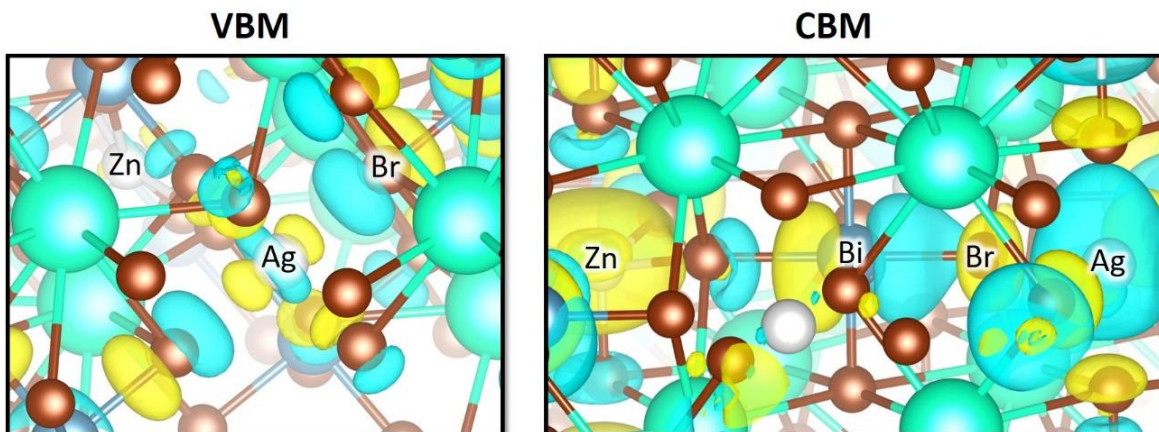


Figure S18. Frontier crystal orbitals of the VBM and CBM calculated at the HSE06 level for Zn^{2+} -doped double perovskite. Color coding: Cs in light green, Ag in light grey, Bi in blue-grey, Br in brown, and crystal orbital phases in yellow and turquoise (isovalue = 0.04).

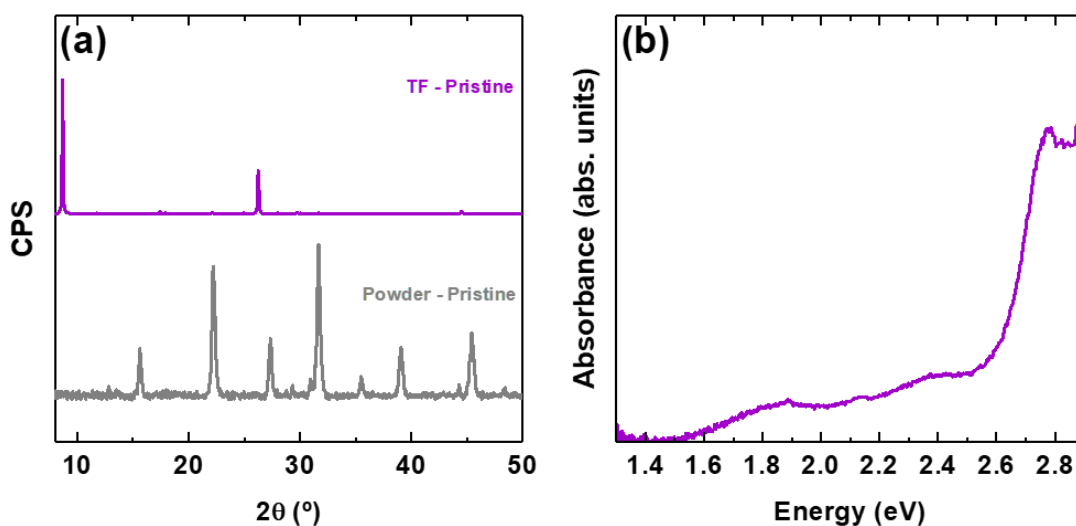


Figure S19. XRD diffractogram (a) and absorbance (b) of SSVD thin film (TF) as-deposited $\text{Cs}_2\text{AgBiBr}_6$ (without annealing), showing a predominance of $\text{Cs}_3\text{Bi}_2\text{Br}_9$ phase. More details in the main text.

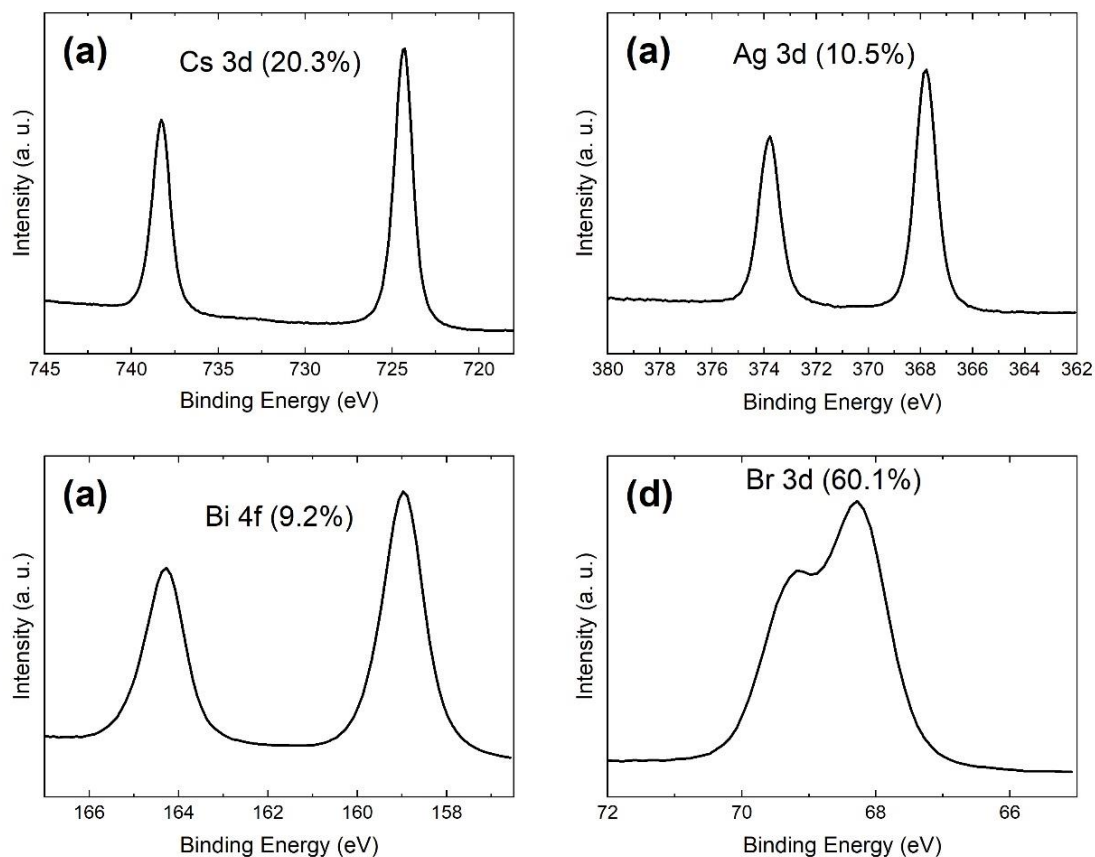


Figure S20. XPS spectra of $\text{Cs}_2\text{AgBiBr}_6$ thin film prepared by SSVD. Derived atomic percentages of each element are indicated in the legend showing a very close match with the expected stoichiometry.

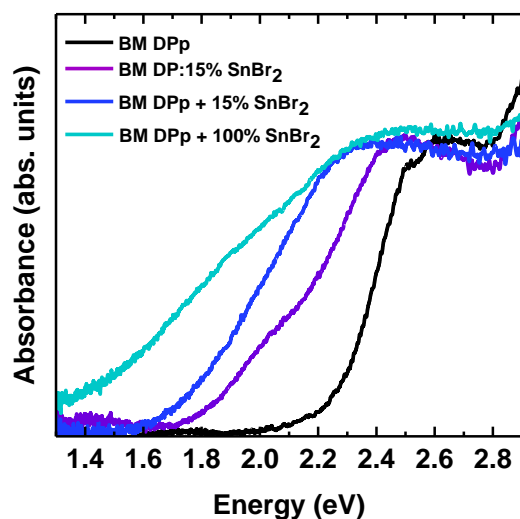


Figure S21. UV-Vis absorbance spectra of SSVD thin films. Tauc plots presented in main text (**Figure 7b**) are derived from these spectra.

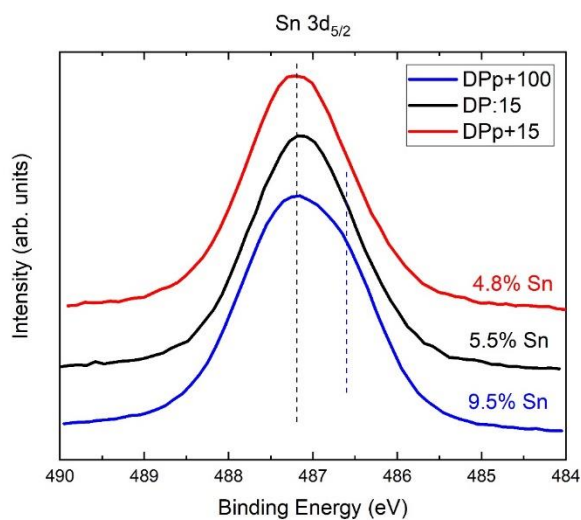


Figure S22. XPS Sn $3d_{5/2}$ spectra of SSVD thin films. Resulting atomic fraction of Sn in the thin films is indicated in the figure in each case. The exact oxidation state or more precisely chemical bonding of Sn is difficult to determine. Nevertheless, an obvious secondary component at lower binding energy appears when an excess of 100% is added (blue curve and dashed line), which is not present in the lower-loading Sn samples (red and black curves).

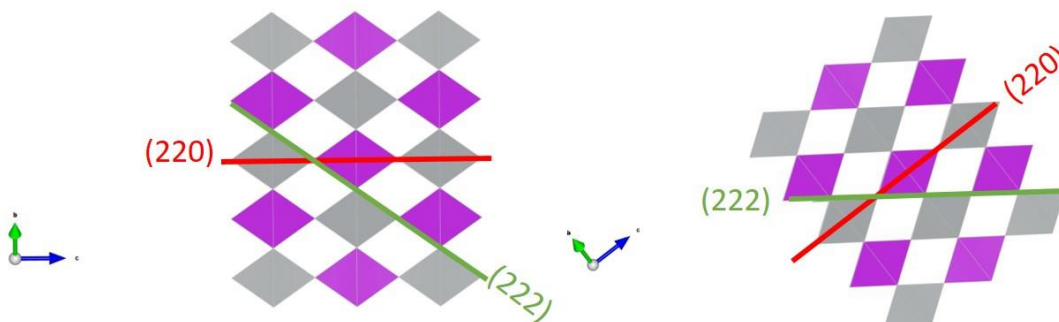


Figure S23. $\text{Cs}_2\text{AgBiBr}_6$ crystal structure oriented with (220) and (222) planes perpendicular to the substrate.

Appendix C

Article: Vacuum Deposited Cesium Tin Iodide Thin
Films with Tunable Thermoelectric Properties

Vacuum-Deposited Cesium Tin Iodide Thin Films with Tunable Thermoelectric Properties

Paz Sebastia-Luna, Unnati Pokharel, Bas A. H. Huisman, L. Jan Anton Koster, Francisco Palazon,* and Henk J. Bolink*



Cite This: *ACS Appl. Energy Mater.* 2022, 5, 10216–10223



Read Online

ACCESS |



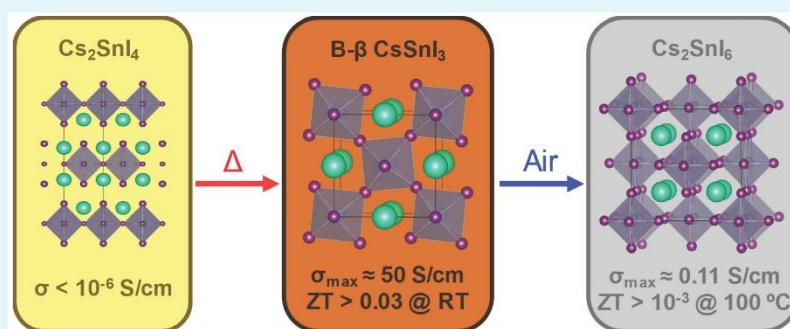
Metrics & More



Article Recommendations



Supporting Information



ABSTRACT: Most current thermoelectric materials have important drawbacks, such as toxicity, scarceness, and peak operating temperatures above 300 °C. Herein, we report the thermoelectric properties of different crystalline phases of Sn-based perovskite thin films. The 2D phase, Cs₂SnI₄, is obtained through vacuum thermal deposition and easily converted into the black β phase of CsSnI₃ (B-β CsSnI₃) by annealing at 150 °C. B-β CsSnI₃ is a p-type semiconductor with a figure of merit (*ZT*) ranging from 0.021 to 0.033 for temperatures below 100 °C, which makes it a promising candidate to power small electronic devices such as wearable sensors which may be interconnected in the so-called Internet of Things. The B-β phase is stable in nitrogen, whereas it spontaneously oxidizes to Cs₂SnI₆ upon exposure to air. Cs₂SnI₆ shows a negative Seebeck coefficient and an ultralow thermal conductivity. However, the *ZT* values are 1 order of magnitude lower than for B-β CsSnI₃ due to a considerably lower electrical conductivity.

KEYWORDS: thermoelectrics, perovskite, tin, thin film, conductivity, Seebeck, room temperature

INTRODUCTION

Thermoelectric generators (TEGs) represent a very promising source of renewable energy, as they directly convert (waste) heat into electricity.^{1,2} Thermoelectric materials are typically characterized by the figure of merit (*ZT*)

$$ZT = \frac{S^2 \sigma}{\kappa} T \quad (1)$$

which depends on the following key parameters: *S* is the Seebeck coefficient, σ is the electrical conductivity, κ is the thermal conductivity, and *T* is the absolute temperature. Thus, to maximize the *ZT* value of a given material, a large Seebeck coefficient, a high electrical conductivity, and a low thermal conductivity are required.^{2,3} Among the most widely used thermoelectric materials, we find Bi₂Te₃, Sb₂Te₃, and SnSe, with the latter exhibiting a *ZT* of 3.1 (at 798 K), the highest reported value so far.^{2,4,5} Nevertheless, the scarceness, toxicity, and high fabrication costs of these materials, especially for tellurides, represent a huge hindrance in their further

development.^{6,7} Besides, most of them are used in a single crystal state,^{2,4} which limits their integration in different device architectures. Another major bottleneck comes from the temperature where their operational peak is reached, usually above 300 °C.⁸ It is paramount to decrease this minimum temperature required to widen the possible applications of TEGs and make them a suitable power source for the Internet of Things (IoT) and its many derivatives in industry, agriculture, and wearable healthcare devices.⁹ Because the majority of these applications require room or moderate temperatures, TE materials with good performance below 100 °C are needed.¹⁰

Received: June 20, 2022

Accepted: July 18, 2022

Published: July 26, 2022

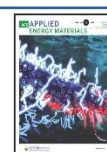


Table 1. Existing Different Phases and Structures of the Cs–Sn–I System, Their Crystal Structures, and Ambient Conditions for Each Phase Transition^a

Phase	B- α CsSnI ₃	B- β CsSnI ₃	B- γ CsSnI ₃	Y CsSnI ₃	Cs ₂ SnI ₆
Crystal structure					
Crystal system	Cubic	Tetragonal	Orthorhombic	Orthorhombic	Cubic
Stability conditions	T > 425 K Air/N ₂	350 < T < 425 K Air/N ₂	300 K N ₂	300 K Air (\approx sec)	300 K Air (\approx hours)

^aTransition temperatures are taken from the literature.^{20,21}

Organic semiconductors such as poly(3,4-ethylene-dioxythiophene) (PEDOT) or doped fullerene derivatives with oligoethylene-glycol (OEG) side chains have been proposed for near room temperature TE.^{1,11} While these are undoubtedly interesting alternatives, the use of such organic semiconductors presents additional challenges: given the large size of the organic dopants (necessary to enhance electrical conductivity and hence ZT), their incorporation into the host material without disrupting the packing and creating additional energetic disorder is challenging.¹¹ Furthermore, polymers are unsuitable for high-purity thin film deposition methods based on vacuum sublimation. Hence, inorganic TE materials operating near room temperature are sought after. Currently, some inorganic materials, such as Ag₂Se or Cu₂Se, have shown good prospects for room temperature applications, but a fine-tuning of the stoichiometry and deposition conditions is needed to achieve the best efficiencies, a process that can be costly and time-consuming.^{12,13} In the search for alternative materials that are easy to process, metal halide perovskites, such as CH₃NH₃PbI₃, FASnI₃, or CsSnI₃, have emerged in recent years as potential thermoelectric materials. Indeed, ultralow thermal conductivity and acceptable Seebeck coefficients have been demonstrated.^{14–16} Sn-based halide perovskites surpass their Pb counterparts in thermoelectric performance because of the self-oxidation of Sn²⁺ to Sn⁴⁺, acting as a self-doping mechanism that enhances their electrical conductivity.¹⁶ Besides, their toxicity is reduced due to the absence of Pb in their composition. In this work, we focus herein on CsSnI₃, which furthermore does contain Cs instead of an organic cation, offering much higher thermal stability than organic–inorganic perovskites.¹⁷ It must be noted that Cs is up to 3 orders of magnitude more abundant on the earth's crust than Bi or Te, which are common elements for current thermoelectrics.¹⁰ In fact, Cs is one of the most “under-produced” elements with scope for increased production.¹⁸ With regards to toxicity, cesium has 40 known isotopes, of which radioactive ¹³⁷Cs is the most toxic and dangerous. In this work, we use its most stable isotope, ¹³³Cs, with a much lower toxicity.¹⁹ Therefore, CsSnI₃ emerges as a promising alternative to most current thermoelectric compounds such as PbTe, Bi₂Te₃, or Sb₂Te₃ with regards to element abundance and toxicity.

CsSnI₃ is known to have four different polymorphs, two of them existing at room temperature (Table 1):^{20,21} a yellow phase, Y CsSnI₃, with an orthorhombic one-dimensional double-chain structure and an orthorhombic three-dimensional

perovskite that is black in color, B- γ CsSnI₃. On the basis of the literature, annealing Y CsSnI₃ to 150 °C under an inert atmosphere yields a black cubic perovskite (B- α), which upon cooling back below 150 °C transforms into a black tetragonal phase (B- β) and into the black orthorhombic phase B- γ when it is cooled below 80 °C. Exposing B- γ CsSnI₃ to air for a short period of time triggers the transformation into Y CsSnI₃, as this is the species that is thermodynamically more stable at ambient conditions.^{20,21} Eventually, upon prolonged exposure to air, Y CsSnI₃ evolves to Cs₂SnI₆, a vacancy-ordered double perovskite that contains oxidized Sn⁴⁺ rather than Sn²⁺ ions.²² Previous reports have studied the thermoelectric properties of CsSnI₃ thin films. Saini et al. prepared films grown by the solution process in DMSO:DMF mixtures and using toluene as antisolvent, followed by thermal annealing reaching a ZT of 0.137 at room temperature.²³ Kontos et al. studied the effect of SnF₂ doping onto spin-coated CsSnI₃ films, revealing a change in the electrical resistance upon the exposure to air of the samples.²¹ In the same line, Liu et al. reached a ZT around 0.14 in SnCl₂-doped CsSnI₃ films deposited by a sequential evaporation method.²⁴ Nevertheless, this performance is only achieved upon the introduction of additional SnCl₂ into the structure and after exposure of the films to air and humidity for 6 min, while a longer exposure time was found to diminish the ZT again.²⁴ Kanatzidis and co-workers studied the thermal and transport properties of a series of CsSnBr_{3-x}I_x perovskites, obtaining a ZT for CsSnI₃ of 0.025 at 300 K that reaches a maximum of 0.15 at 550 K. These results were achieved with bulk (6 × 6 × 1.5 mm) crystals sintered at 923 K for periods of more than 24 h.²⁵ In summary, these results demonstrate the potential of CsSnI₃ thin films for TE. However, the aforementioned protocols include complex solvent processing, need of external dopants or additives, and high-temperature synthesis and/or are very sensitive to air and humidity. More robust and simpler routes are therefore sought after.

Here, we focus our research on the study of vacuum deposition of CsSnI₃ thin films via single source thermal evaporation of presynthesized dry powders. Thermal vacuum deposition shows better thickness control, higher throughput, and higher reproducibility compared to solution processing.^{26,27} Remarkably, the as-synthesized film presents the two-dimensional structure characteristic of Cs₂SnI₆, a species reported only theoretically so far. Its electrical conductivity detected is very low but can be increased by several orders of magnitude upon annealing and consequent conversion to B- β CsSnI₃, achieving a maximum ZT of 0.033.

RESULTS AND DISCUSSION

Following the procedure described in the [Experimental Methods](#), synthesis of the CsSnI_3 was performed via dry mechanochemical synthesis by ball-milling under nitrogen, thus preventing oxidation and degradation of Sn(II) in contact with the atmosphere. The synthesized CsSnI_3 is a black powder with a complex X-ray diffraction pattern (see [Figure S1](#)). When this diffraction pattern is compared with the known patterns for the yellow phase (γ CsSnI_3 , Inorganic Crystal Structure Database code 262927) and the black gamma phase (β - γ CsSnI_3 , ICSD code 262926), it can be deduced that our as-synthesized powder is a mixture of these two phases.

Once the powders were formed, thin films with thicknesses of few hundred nanometers (see the [Experimental Methods](#) for more details) were deposited via single-source vacuum deposition (SSVD) inside a high-vacuum chamber. SSVD has been previously shown by us and others to be a fast and reproducible method for depositing pure, stoichiometric materials.^{28–30} In our case, the SSVD of the ball-milled CsSnI_3 did not lead directly to the deposition of any of the previously mentioned CsSnI_3 phases, as the XRD diffractogram does not match with any of them ([Figure 1a](#)). On the contrary,

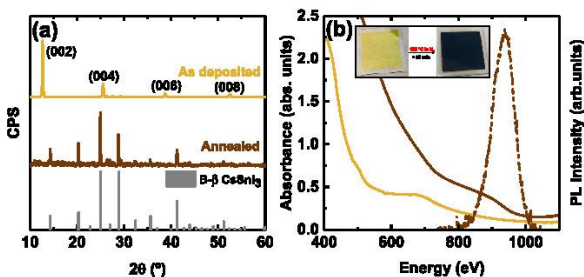


Figure 1. (a) XRD diffractograms and (b) absorbance (solid lines) and photoluminescence (dashed line) spectra of SSVD thin films as-deposited and annealed for 25 min at 150 °C. Panel a shows the ICSD pattern for the black beta phase of CsSnI_3 (code 262925) and the predicted main crystalline structure for both films. Predicted XRD planes of as-deposited thin films were obtained from the fit presented in [Figure S2](#).

the few and equally spaced peaks present are reminiscent of a 2D material. Indeed the main diffractogram signals can be well matched with a 2D phase isostructural to $\text{Cs}_2\text{Pb}(\text{I}_{0.5}\text{Cl}_{0.5})_4$ ([Figure S2](#)).³¹ Thus, it is reasonable to ascribe this signal to the

crystallization of the 2D phase Cs_2SnI_4 ([Figure S2](#)), whose main diffraction peaks correspond to the (00*l*) planes. To the best of our knowledge, this phase has only been theoretically reported because of its high instability.^{32,33} Indeed, we attempted the mechanochemical synthesis of Cs_2SnI_4 , but a mixture of γ CsSnI_3 and β - γ CsSnI_3 was formed instead ([Figure S3](#)). The formation route of Cs_2SnI_4 upon the sublimation of CsSnI_3 powder still remains unclear to us. We hypothesize that even if the 2D phase is unstable, the high energies supplied by the evaporation process allowed its formation. However, we cannot rule out the coexistence of Cs_2SnI_4 in the thin films together with CsSnI_3 phases. Indeed, minor peaks around $2\theta = 27.6^\circ$ and $2\theta = 29.2^\circ$ do not match the 2D structure and suggest traces of γ CsSnI_3 and β - γ CsSnI_3 ([Figure S2](#)). The preferential deposition of Cs_2SnI_4 took place in a reproducible manner at several evaporation batches of ball-milled CsSnI_3 ([Figure S4](#)), with slight differences in the presence of side phases that could be linked to variations in the air exposure. Elemental analysis by energy dispersive X-ray spectroscopy (EDX) shows a molar ratio of Cs:Sn:I 1:1.5:3.1, very close to the stoichiometry expected for a CsSnI_3 -derived phase (1:1:3) with an excess of Sn ascribed to indium tin oxide (ITO) substrate. The absorption spectrum ([Figure 1b](#)) confirms the presence of at least two different species with different absorption intensities. The Tauc plot derived from the absorption spectrum reveals two bandgaps of 2.45 and 1.42 eV which are ascribed to γ CsSnI_3 (indirect transition) and Cs_2SnI_4 (direct transition) phases, respectively, very similar to the literature references ([Figure S5](#)).^{32,34}

A preliminary study of the electrical properties of the 2D phase revealed a very low conductivity ([Figure S6](#)). Such a low conductivity is detrimental for thermoelectric use, as it would lead to a very low ZT value. However, it was possible to convert the poorly conductive Cs_2SnI_4 into the more conductive black beta phase of CsSnI_3 (β - γ CsSnI_3) by thermal annealing at 150 °C under an inert atmosphere ([Figure 1a](#)). [Figure S7](#) shows the XRD patterns resulting from *in situ* annealing of Cs_2SnI_4 thin films up to 150 °C. Cs_2SnI_4 undergoes a gradual conversion to CsSnI_3 , for which 25 min of annealing is required to form a pure black beta phase of CsSnI_3 . This transformation is further evidenced by the increase in optical absorption of the thin film in the 500–950 nm region ([Figure 1b](#)), causing a darkening of the film (note that both absorption spectra in [Figure 1b](#) are obtained from the same film—same thickness—and hence absorbance units directly relate to absorption coefficient of the given

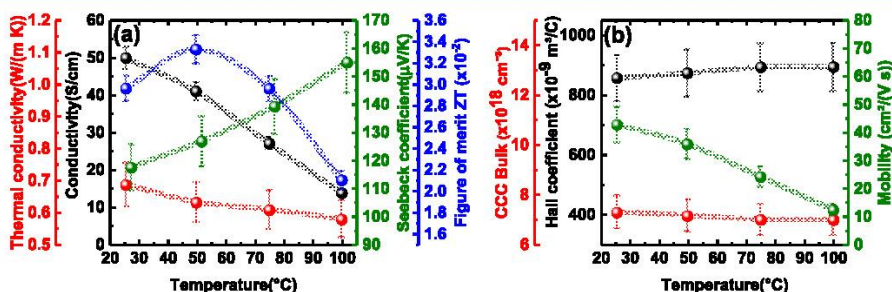


Figure 2. (a) Temperature dependence of electrical conductivity, σ (black line), thermal conductivity, κ (red line), Seebeck coefficient, S (green line), and figure of merit, ZT (blue line) of β - γ CsSnI_3 . (b) Temperature dependence of Hall coefficient (black line), charge carrier concentration of the bulk, CCC (red line), and charge mobility (green line) of β - γ CsSnI_3 . Errors bars come from measurement of film thickness and the deviation of the equipment (see the [Experimental Methods](#)). The ZT and charge mobility error bars originate from the combination of these errors.

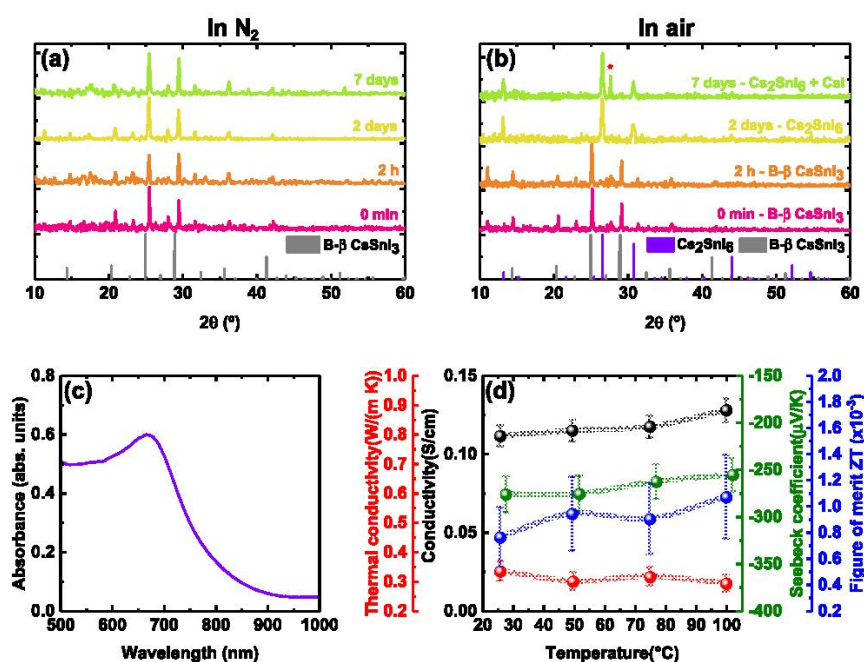


Figure 3. XRD diffractograms of the evolution of Cs_2SnI_6 thin films exposed to (a) air and (b) N_2 for 1 week. The red asterisk stands for the main XRD peak of CsI , a byproduct of the degradation. (c) UV–vis absorbance spectrum of Cs_2SnI_6 . (d) Temperature dependence of electrical conductivity, σ (black line), thermal conductivity, κ (red line), Seebeck coefficient, S (green line), and figure of merit, ZT (blue line), of Cs_2SnI_6 thin films. See the error bar calculation in Figure 2a.

phase). The shift toward higher wavelengths translates into a narrowing of the bandgap. Assuming a direct bandgap for this material, we obtain a value of 1.30 eV from the absorption spectrum (see the Tauc plot in Figure S8). Contrary to Cs_2SnI_4 where no photoluminescence (PL) was detected, $\text{B-}\beta$ CsSnI_3 shows infrared emission with the maximum at 937 nm (1.32 eV). This implies that there is only a very small Stokes shift. Both the bandgap deduced from absorption and the maximum of the PL emission are in agreement with values reported previously.^{21,22,34,35} These properties make $\text{B-}\beta$ CsSnI_3 also interesting for alternative applications such as a light absorber for solar cells or as the emitter for near-infrared light-emitting diodes.^{36,37}

The thermoelectric performance of $\text{B-}\beta$ CsSnI_3 thin-films was then studied under an inert atmosphere through temperature-dependent measurements ranging from 25 to 100 °C (Figure 2a) with an integrated thin film analyzer from Linseis (see the Experimental Methods).³⁸ The electrical conductivity (σ) decreases with increasing temperature as expected for bandlike charge transport. A maximum conductivity of 50 ± 3 S/cm at room temperature is obtained. This is 7 orders of magnitude higher than the conductivity of the phase that was formed prior to annealing the film, Cs_2SnI_4 . Hall effect measurements (Figure 2b) show that the $\text{B-}\beta$ CsSnI_3 thin-films are a p-type semiconductor (positive Hall coefficient) with a charge carrier concentration (CCC) around $7 \times 10^{18} \text{ cm}^{-3}$ and hole mobility of $42 \pm 6 \text{ cm}^2 \text{ V}^{-1} \text{ s}^{-1}$ at room temperature. A temperature increase causes a sharp decrease in the charge carrier mobility in line with the observed decrease in the electrical conductivity, whereas the carrier concentration remains virtually constant. It is known that the origin of the p-type conduction of $\text{B-}\beta$ CsSnI_3 arises from its ability to accommodate Sn^{4+} ions and Sn vacancies due to oxidation,

which effectively acts as self-doping and hence transit to a hole-doped state.³⁹ When increasing the temperature, holes delocalize and molecular vibrations increase to achieve a metal-like behavior translating into a decrease in the electrical conductivity.^{20,25,40} Thus, the mean free path of electrons is reduced, and their mobility is also decreased. While this behavior is typical of a metal and not of an intrinsic semiconductor, we should stress that CsSnI_3 is effectively a self-doped semiconductor (not a metal, as it clearly presents a bandgap of 1.3 eV as shown in Figure 1). In the words of Chung et al.,²⁰ “although stoichiometric CsSnI_3 is a semiconductor, the material is prone to intrinsic defects associated with Sn vacancies. This creates highly mobile holes which cause the materials to appear metallic.” We hypothesize that as no phase transition took place here upon heating and samples were stored in nitrogen during measurement, the formation of new Sn^{4+} centers is avoided, so the carrier concentration is kept constant. These findings were previously reported by others as they did not consider phase transitions upon heating $\text{B-}\beta$ CsSnI_3 to have an effect on the charge transport properties.²⁰

On the other hand, the ultralow thermal conductivity (κ) detected in the whole range of temperatures is consistent with the ultralow lattice thermal conductivity reported for most halide perovskites.^{14,41} The cause of this phenomenon is ascribed to the phonon–phonon scattering inside the crystal lattice, which intensifies by increasing the temperature, hindering the thermal transport (decreasing κ).^{17,24,25} Such low thermal conductivities are beneficial for the thermoelectric performance and are found in other materials such MAPbI_3 or SnSe , whose ZT is one of the highest reported so far.^{15,42}

The positive Seebeck coefficient, S , as shown in Figure 2a, confirms that $\text{B-}\beta$ CsSnI_3 is a p-type semiconductor, consistent

Table 2. Comparison of Maximum Electrical Conductivity (σ_{\max}), Thermal Conductivity (κ_{\max}), Seebeck Coefficient (S_{\max}), and Figure of Merit ZT (ZT_{\max}) for the Three Species Studied in This Work^a

phase	σ_{\max} (S/cm)	κ_{\max} (W/m·K)	S_{\max} (μ V/K)	ZT_{\max}
Cs ₂ SnI ₄	2.47×10^{-6} at 25 °C	ND	ND	ND
B- β CsSnI ₃	50 ± 3 at 25 °C	0.69 ± 0.07 at 25 °C	154 ± 11 at 100 °C	0.0333 ± 0.0013 at 50 °C
Cs ₂ SnI ₆	0.128 ± 0.007 at 100 °C	0.33 ± 0.03 at 25 °C	-255 ± 18 at 100 °C	0.0011 ± 0.0003 at 100 °C

^aTemperatures at which they are achieved are given. ND stands for nondetected.

with our Hall effect measurements and in corroboration with findings from others.^{20,43} S steadily rises up to $154 \pm 11 \mu$ V/K with increasing temperature, which agrees with the decrease in electrical conductivity and is comparable to other Sn-based perovskites.^{3,2,5} A similar value for S was determined independently with a different characterization methodology (see Figure S9 and the Experimental Methods). The thermoelectric figure of merit, ZT , for our thin films (thickness = 300 nm) of B- β CsSnI₃ ranges from 0.021 to 0.033 in the temperature range studied (room temperature to 100 °C) and reaches its maximum (0.0333 ± 0.0013) at 50 °C, which is relevant for applications near room temperature.

When the B- β CsSnI₃ thin film is kept in an inert atmosphere (Figure 3a), the black beta phase is preserved for at least 7 days. However, as mentioned, B- β CsSnI₃ spontaneously evolves to Cs₂SnI₆ upon exposure to air in 2 days or less (Figure 3b). This phase change is accompanied by a decrease in the film homogeneity and the formation of pinholes spread all over the film surface, as SEM images evidence (Figure S10). The poor morphology is likely attributed to an irregular oxidation from B- β CsSnI₃ to Cs₂SnI₆, which could be avoided by controlling the atmosphere composition and deposition process.^{44,45} After 1 week in air we observe the formation of some small amount of CsI, indicating some degradation of this Cs₂SnI₆ structure and a low stability of the phase upon exposure to air for long periods. In contrast, Figure S11 shows that the XRD diffraction pattern after heating to 150 °C in ambient conditions remains unchanged, revealing the high thermal stability of Cs₂SnI₆. This finding was previously confirmed by other authors who performed thermogravimetric analysis (TGA), showing no decomposition until 515 K.⁴⁶

The conversion of B- β CsSnI₃ to Cs₂SnI₆ leads to a change of the optical properties of the thin films. The shape and the intensity of the optical absorbance are completely different from the B- β CsSnI₃ phase (Figure 3c). The absorption spectra has an overall strongly reduced absorbance compared to that of the B- β CsSnI₃ phase.^{47,48} A direct bandgap of 1.49 eV can be estimated from the Tauc plot (Figure S12), in line with previous reports for this phase.^{22,49,50} No significant PL was detected for this material, which could be ascribed to a high nonradiative recombination rate of the films induced by the formation of trap states.^{44,48,51}

Figure 3d shows the temperature dependence of the thermoelectric performance of Cs₂SnI₆ thin films. We observe a conductivity around 0.1 S/cm in the whole temperature range, in line with other reported values.⁴⁵ This is 2 orders of magnitude lower than that observed previously for B-beta CsSnI₃ (Figure 2). An ultralow thermal conductivity is also found for Cs₂SnI₆, together with a negative Seebeck coefficient over the whole range of temperatures, indicating that electrons are the dominant charge carriers (n-type conduction). The n-type character of the compound comes from the presence of iodine vacancies and tin interstitials inside the lattice, defects

easily formed in this double perovskite.^{46,51} With our home-built setup, measurements run on a different day and on a different sample yielded a Seebeck coefficient at 25 °C of -514μ V/K (Figure S13), which is considerably higher in absolute value, although in the same order of magnitude as what was obtained from the analysis using the thin-film analyzer. We hypothesize that the difference of Seebeck values arises from a dissimilar oxidation level of the layers. It seems plausible that variations in the atmosphere, for example, oxygen concentration, moisture, or temperature, during the oxidation of B- β CsSnI₃ to Cs₂SnI₆ may cause a different degree of oxidation affecting the charge transport mechanisms and, thus, the thermoelectric performance. We should also note that the oxidation in air from CsSnI₃ to Cs₂SnI₆ is likely accompanied by formation of SnO₂ which may be amorphous and hence not detected here by XRD. It is possible that this side-product also affects the overall thermoelectric properties of the film. Anyhow, the low electrical conductivity (2 orders of magnitude lower than that of B- β CsSnI₃) leads to ZT values around 1×10^{-3} in the 25–100 °C range. The improvement of the electrical conductivity is thus paramount to boost the possibilities in TE of this material.

CONCLUSIONS

In conclusion, we report the thermal deposition of Cs₂SnI₄ directly from the SSVD of ball-milled CsSnI₃ powder. Absorption spectra of these thin films reveal the presence of the 2D perovskite ($E_g = 1.42$ eV) together with traces of Y CsSnI₃ ($E_g = 2.45$ eV). Their electrical conductivity is found to be extremely low but rises almost 7 orders of magnitude after annealing for 25 min at 150 °C, when the B- β CsSnI₃ phase is formed. B- β CsSnI₃ shows ultralow thermal conductivity and p-type conduction corroborated from Seebeck and Hall measurements. Its electrical conductivity decreases when increasing the temperature, caused by the reduction in charge mobility. In the temperature range studied (RT–100 °C) and without exposure to air or further external doping, the maximum ZT achieved is 0.0333 ± 0.0013 at 50 °C. The black beta phase is conserved in nitrogen for more than 7 days but oxidizes into Cs₂SnI₆ upon exposure to air for a few hours. Cs₂SnI₆ has a lower electrical conductivity, an ultralow thermal conductivity, and a larger absolute Seebeck coefficient, reaching a ZT of 0.0011 ± 0.0003 (100 °C) (see Table 2 for summarized maximum values achieved). Hence, both B- β CsSnI₃ and Cs₂SnI₆ show potential for implementation in low-temperature operating TEGs when the conductivity of these materials can be controllably improved.

EXPERIMENTAL METHODS

Materials. Cesium iodide (CsI, >99%) was purchased from TCI. Tin(II) iodide (SnI₂, 99.999%) was purchased from Alfa Aesar. All chemicals were stored in a nitrogen-filled glovebox and used as received without further purification.

Mechanochemical Synthesis. Stoichiometric amounts of CsI and SnI₂ were introduced inside a 10 mL zirconia ball-mill jar with two zirconia beads of 10 mm diameter inside a nitrogen-filled glovebox. Ball-milling (BM) was performed with a MM-400 shaking ball-mill from Retsch at a frequency of 30 Hz for 30 min.

Thin-Film Deposition by Single-Source Vacuum Deposition (SSVD). In a typical deposition, an alumina thermal crucible (Creaphys GmbH) was placed inside a vacuum chamber, and the as-synthesized CsSnI₃ powder was loaded. Then, the chamber was evacuated to a pressure of 7×10^{-6} mbar, and the source was rapidly heated to 500 °C. The deposition was stopped after the complete evaporation of the solid. The sample film thickness was measured with a mechanical profilometer (Ambios XP200). Results shown in the main text are obtained from thin films of B-β CsSnI₃ and Cs₂SnI₆ with a film thickness of 210 nm ($\pm 0.5\%$) and 540 nm ($\pm 0.2\%$), respectively. The reason a thicker film was deposited to evaluate Cs₂SnI₆ is that the conductivity is lower than for CsSnI₃, and therefore the overall conductance of the film falls below the limit of detection of the instrumental setup if a 210 nm film is employed. The thickness evaluation is performed on the relevant phase right before thermoelectric characterization to ensure accurate conductivity assessment. It must be noted, however, that the 540 nm thickness of the Cs₂SnI₆ film is obtained from a precursor B-β CsSnI₃ film of 515 nm, meaning that an $\approx 5\%$ thickness increase occurs upon phase transition.

XRD Characterization. X-ray diffraction was measured with a powder diffractometer (Empyrean from Panalytical) equipped with a Cu K α anode operated at 45 kV and 40 mA. Single scans were acquired in the $2\theta = 8^\circ$ – 60° range with a step size of $2\theta = 0.01^\circ$ in Bragg–Brentano geometry in air. A sealed dome sample holder (Anton Paar) was used for measurements in N₂.

Optical Characterization. UV–vis absorption spectra of the films are acquired in a transmission configuration coupled to an Avantes Avaspec-2048L optical detector (Avantes BV). Photoluminescence measurements were performed inside a nitrogen-filled glovebox by using a MatchBox laser as an excitation source at 515 nm coupled to an Avantes Avaspec-2048L optical detector. For a typical analysis, one scan with an integration time of 3 s was collected.

Scanning Electron Microscopy (SEM). SEM images were obtained by using a Phenom XL G2Microscope from Thermo Fisher at an operating acceleration voltage of 10 kV. EDX data were acquired with a Hitachi S-4800 scanning electron microscope.

Thermoelectric Property Measurements. The electrical conductivity, thermal conductivity, Seebeck coefficient, and Hall effect were measured simultaneously on the same sample by using a thin film analyzer (TFA) from Linseis. The operation mechanism of this equipment is described elsewhere.³⁸ A home-built setup was employed to measure the Seebeck coefficient of B-β CsSnI₃ and Cs₂SnI₆ thin films for comparison. The Seebeck coefficients of samples processed under the same conditions were measured with both setups to compare values.⁵² All measurements were performed under an inert atmosphere. For error bar calculation, we have incorporated the error of the equipment provided by the manufacturer and the thickness measurement into consideration. Final errors are $\pm 10\%$ for thermal conductivity, $\pm 6\%$ for electrical conductivity, $\pm 7\%$ for the Seebeck coefficient, and $\pm 9\%$ for the Hall coefficient. ZT and charge mobility errors are calculated from the combination of these errors.

■ ASSOCIATED CONTENT

Supporting Information

The Supporting Information is available free of charge at <https://pubs.acs.org/doi/10.1021/acsaem.2c01936>.

XRD diffractograms of as-synthesized CsSnI₃; fitted XRD diffractogram, Tauc plot and J – V curve of Cs₂SnI₄ thin films; XRD diffractograms of different batches and annealing effect on Cs₂SnI₄ and conversion to B-β CsSnI₃; Tauc plot and Seebeck coefficient calculation of

B-β CsSnI₃ thin films; XRD diffractograms of annealing effect on Cs₂SnI₆; Tauc plot and Seebeck coefficient calculation of Cs₂SnI₆ thin films; SEM images of Cs₂SnI₄, B-β CsSnI₃, and Cs₂SnI₆ thin films (PDF)

■ AUTHOR INFORMATION

Corresponding Authors

Francisco Palazon – Instituto de Ciencia Molecular, ICMol, Universidad de Valencia, 46980 Paterna, Spain; Departamento de Ingeniería Química y Ambiental, Universidad Politécnica de Cartagena, 30202 Cartagena, Spain; orcid.org/0000-0002-1503-5965; Email: francisco.palazon@uv.es

Henk J. Bolink – Instituto de Ciencia Molecular, ICMol, Universidad de Valencia, 46980 Paterna, Spain; orcid.org/0000-0001-9784-6253; Email: henk.bolink@uv.es

Authors

Paz Sebastia-Luna – Instituto de Ciencia Molecular, ICMol, Universidad de Valencia, 46980 Paterna, Spain; orcid.org/0000-0001-6992-199X

Unnati Pokharel – Zernike Institute for Advanced Materials, University of Groningen, 9747 AG Groningen, The Netherlands; orcid.org/0000-0003-4783-6406

Bas A. H. Huisman – Instituto de Ciencia Molecular, ICMol, Universidad de Valencia, 46980 Paterna, Spain; orcid.org/0000-0002-3553-3398

L. Jan Anton Koster – Zernike Institute for Advanced Materials, University of Groningen, 9747 AG Groningen, The Netherlands; orcid.org/0000-0002-6558-5295

Complete contact information is available at: <https://pubs.acs.org/doi/10.1021/acsaem.2c01936>

Notes

The authors declare no competing financial interest.

■ ACKNOWLEDGMENTS

The research leading to these results has received funding from the European Research Council (ERC) under the European Union's Horizon 2020 research and innovation programme (Grant Agreement No. 834431). The authors acknowledge support from the Comunitat Valenciana (IDIFEDER/2018/061 and PROMETEU/2020/077) as well as by the Ministry of Science and Innovation (MCIN) and the Spanish State Research Agency (AEI) (Project PCI2019-111829-2 funded by MCIN/AEI/10.13039/501100011033) and by the European Union (Project CEX2019-000919-M) funded by MCIN/AEI/10.13039/501100011033 Dutch Research Council (NWO, FOM Focus Group "Next Generation Organic Photovoltaics"). P.S. thanks the Spanish Ministry of Universities for her predoctoral grant (FPU18/01732 and EST19/00295). F.P. acknowledges funding from the Ramón y Cajal program of the Spanish Ministry of Science (RYC2020-028803-I).

■ REFERENCES

- (1) Beretta, D.; Neophytou, N.; Hodges, J. M.; Kanatzidis, M. G.; Narducci, D.; Martin-Gonzalez, M.; Beekman, M.; Balke, B.; Cerretti, G.; Tremel, W.; Zevalkink, A.; Hofmann, A. I.; Müller, C.; Dörfling, B.; Campoy-Quiles, M.; Caironi, M. Thermoelectrics: From History, a Window to the Future. *Mater. Sci. Eng. R* 2019, 138, 210–255.

- (2) Snyder, G. J.; Toberer, E. S. Complex Thermoelectric Materials. *Nat. Mater.* **2008**, *7*, 105–114.
- (3) Wu, T.; Gao, P. Development of Perovskite-Type Materials for Thermoelectric Application. *Materials (Basel)* **2018**, *11* (6), 999.
- (4) Zhou, C.; Lee, Y. K.; Yu, Y.; Byun, S.; Luo, Z. Z.; Lee, H.; Ge, B.; Lee, Y. L.; Chen, X.; Lee, J. Y.; Cojocaru-Mirădin, O.; Chang, H.; Im, J.; Cho, S. P.; Wuttig, M.; Dravid, V. P.; Kanatzidis, M. G.; Chung, I. Polycrystalline SnSe with a Thermoelectric Figure of Merit Greater than the Single Crystal. *Nat. Mater.* **2021**, *20*, 1378–1384.
- (5) Ao, D. W.; Liu, W. D.; Chen, Y. X.; Wei, M.; Jabar, B.; Li, F.; Shi, X. L.; Zheng, Z. H.; Liang, G. X.; Zhang, X. H.; Fan, P.; Chen, Z. G. Novel Thermal Diffusion Temperature Engineering Leading to High Thermoelectric Performance in Bi₂Te₃-Based Flexible Thin-Films. *Adv. Sci.* **2022**, *9* (5), 2103547.
- (6) Shie, M. D.; Deeds, F. E. The Importance of Tellurium as a Health Hazard in Industry. A Preliminary Report. *Public Health Rep.* **1920**, *35* (16), 939–954.
- (7) Vávrová, S.; Struhárňanská, E.; Tuřňa, J.; Stuchlík, S. Tellurium: A Rare Element with Influence on Prokaryotic and Eukaryotic Biological Systems. *Int. J. Mol. Sci.* **2021**, *22*, 5924.
- (8) Yan, Q.; Kanatzidis, M. G. High-Performance Thermoelectrics and Challenges for Practical Devices. *Nat. Mater.* **2021**.
- (9) Jaziri, N.; Boughamoura, A.; Müller, J.; Mezghani, B.; Tounsi, F.; Ismail, M. A Comprehensive Review of Thermoelectric Generators: Technologies and Common Applications. *Energy Reports* **2020**, *6* (7), 264–287.
- (10) Caballero-Calero, O.; Ares, J. R.; Martín-González, M. Environmentally Friendly Thermoelectric Materials: High Performance from Inorganic Components with Low Toxicity and Abundance in the Earth. *Adv. Sustain. Syst.* **2021**, *5* (11), 2100095.
- (11) Liu, J.; Qiu, L.; Portale, G.; Torabi, S.; Stuart, M. C. A.; Qiu, X.; Koopmans, M.; Chiechi, R. C.; Hummelen, J. C.; Anton Koster, L. J. Side-Chain Effects on N-Type Organic Thermoelectrics: A Case Study of Fullerene Derivatives. *Nano Energy* **2018**, *52*, 183–191.
- (12) Zheng, Z. H.; Zhang, D. L.; Jabar, B.; Chen, T. B.; Nisar, M.; Chen, Y. F.; Li, F.; Chen, S.; Liang, G. X.; Zhang, X. H.; Fan, P.; Chen, Y. X. Realizing High Thermoelectric Performance in Highly (001)-Textured Flexible Cu₂Se Thin Film for Wearable Energy Harvesting. *Mater. Today Phys.* **2022**, *24*, 100659.
- (13) Zheng, Z. H.; Zhang, D. L.; Niu, J. Y.; Shi, X. L.; Chen, T. B.; Chen, Y. F.; Li, F.; Liang, G. X.; Chen, Y. X.; Fan, P.; Chen, Z. G. Achieving Ultrahigh Power Factor in N-Type Ag₂Se Thin Films by Carrier Engineering. *Mater. Today Energy* **2022**, *24*, 100933.
- (14) Pisoni, A.; Jačimović, J.; Barišić, O. S.; Spina, M.; Gaál, R.; Forró, L.; Horváth, E. Ultra-Low Thermal Conductivity in Organic-Inorganic Hybrid Perovskite CH₃NH₃PbI₃. *J. Phys. Chem. Lett.* **2014**, *5*, 2488–2492.
- (15) Haque, M. A.; Kee, S.; Villalva, D. R.; Ong, W.; Baran, D. Halide Perovskites: Thermal Transport and Prospects for Thermoelectricity. *Adv. Sci.* **2020**, *7*, 1903389.
- (16) Zheng, L.; Zhu, T.; Li, Y.; Wu, H.; Yi, C.; Zhu, J.; Gong, X. Enhanced Thermoelectric Performance of F4-TCNQ Doped FASnI₃ Thin Films. *J. Mater. Chem. A* **2020**, *8*, 25431–25442.
- (17) Qian, F.; Hu, M.; Gong, J.; Ge, C.; Zhou, Y.; Guo, J.; Chen, M.; Ge, Z.; Padture, N. P.; Zhou, Y.; Feng, J. Enhanced Thermoelectric Performance in Lead-Free Inorganic CsSn_{1-x}GexI₃ Perovskite Semiconductors. *J. Phys. Chem. C* **2020**, *124* (22), 11749–11753.
- (18) Vesborg, P. C. K.; Jaramillo, T. F. Addressing the Terawatt Challenge: Scalability in the Supply of Chemical Elements for Renewable Energy. *RSC Adv.* **2012**, *2* (21), 7933–7947.
- (19) Aaseth, J.; Nurchi, V. M.; Andersen, O. Medical Therapy of Patients Contaminated with Radioactive Cesium or Iodine. *Biomolecules* **2019**, *9* (12), 856.
- (20) Chung, I.; Song, J.-H.; Im, J.; Androulakis, J.; Malliakas, C. D.; Li, H.; Freeman, A. J.; Kenney, J. T.; Kanatzidis, M. G. CsSnI₃: Semiconductor or Metal? High Electrical Conductivity and Strong Near-Infrared Photoluminescence from a Single Material. High Hole Mobility and Phase-Transitions. *J. Am. Chem. Soc.* **2012**, *134*, 8579–8587.
- (21) Kontos, A. G.; Kaltzoglou, A.; Siranidi, E.; Palle, D.; Angeli, G. K.; Arfanis, M. K.; Psycharis, V.; Raptis, Y. S.; Kamitsos, E. I.; Trikalitis, P. N.; Stoumpos, C. C.; Kanatzidis, M. G.; Falaras, P. Structural Stability, Vibrational Properties, and Photoluminescence in CsSnI₃ Perovskite upon the Addition of SnF₂. *Inorg. Chem.* **2017**, *56*, 84–91.
- (22) Qiu, X.; Cao, B.; Yuan, S.; Chen, X.; Qiu, Z.; Jiang, Y.; Ye, Q.; Wang, H.; Zeng, H.; Liu, J.; Kanatzidis, M. G. From Unstable CsSnI₃ to Air-Stable Cs₂SnI₆: A Lead-Free Perovskite Solar Cell Light Absorber with Bandgap of 1.48 eV and High Absorption Coefficient. *Sol. Energy Mater. Sol. Cells* **2017**, *159*, 227–234.
- (23) Saini, S.; Baranwal, A. K.; Yabuki, T.; Hayase, S.; Miyazaki, K. Growth of Halide Perovskites Thin Films for Thermoelectric Applications. *MRS Adv.* **2019**, *4*, 1719–1725.
- (24) Liu, T.; Zhao, X.; Li, J.; Liu, Z.; Liscio, F.; Milita, S.; Schroeder, B. C.; Fenwick, O. Enhanced Control of Self-Doping in Halide Perovskites for Improved Thermoelectric Performance. *Nat. Commun.* **2019**, *10* (1), 1–9.
- (25) Xie, H.; Hao, S.; Bao, J.; Slade, T. J.; Snyder, G. J.; Wolverton, C.; Kanatzidis, M. G. All-Inorganic Halide Perovskites as Potential Thermoelectric Materials: Dynamic Cation off-Centering Induces Ultralow Thermal Conductivity. *J. Am. Chem. Soc.* **2020**, *142* (20), 9553–9563.
- (26) Momblona, C.; Gil-Escrig, L.; Bandiello, E.; Hutter, E. M.; Sessolo, M.; Lederer, K.; Blochwitz-Nimoth, J.; Bolink, H. J. Efficient Vacuum Deposited P-i-n and n-i-p Perovskite Solar Cells Employing Doped Charge Transport Layers. *Energy Environ. Sci.* **2016**, *9*, 3456–3463.
- (27) Gil-Escrig, L.; Momblona, C.; Forgács, D.; Pla, S.; Fernández-Lázaro, F.; Sessolo, M.; Sastre-Santos, A.; Bolink, H. J. Interface Engineering in Efficient Vacuum Deposited Perovskite Solar Cells. *Org. Electron.* **2016**, *37*, 396–401.
- (28) Chen, M.; Ju, M. G.; Garces, H. F.; Carl, A. D.; Ono, L. K.; Hawash, Z.; Zhang, Y.; Shen, T.; Qi, Y.; Grimm, R. L.; Pacifici, D.; Zeng, X. C.; Zhou, Y.; Padture, N. P. Highly Stable and Efficient All-Inorganic Lead-Free Perovskite Solar Cells with Native-Oxide Passivation. *Nat. Commun.* **2019**, *10* (16), 1–8.
- (29) El Ajjouri, Y.; Palazon, F.; Sessolo, M.; Bolink, H. J. Single-Source Vacuum Deposition of Mechanosynthesized Inorganic Halide Perovskites. *Chem. Mater.* **2018**, *30*, 7423–7427.
- (30) Fan, P.; Gu, D.; Liang, G. X.; Luo, J. T.; Chen, J. L.; Zheng, Z. H.; Zhang, D. P. High-Performance Perovskite CH₃NH₃PbI₃ Thin Films for Solar Cells Prepared by Single-Source Physical Vapour Deposition. *Sci. Rep.* **2016**, *6*, 29910.
- (31) Li, J.; Yu, Q.; He, Y.; Stoumpos, C. C.; Niu, G.; Trimarchi, G. G.; Guo, H.; Dong, G.; Wang, D.; Wang, L.; Kanatzidis, M. G. Cs₂PbI₂Cl₂, All-Inorganic Two-Dimensional Ruddlesden-Popper Mixed Halide Perovskite with Optoelectronic Response. *J. Am. Chem. Soc.* **2018**, *140*, 11085–11090.
- (32) Yang, J.-H.; Yuan, Q.; Yakobson, B. I. Chemical Trends of Electronic Properties of Two-Dimensional Halide Perovskites and Their Potential Applications for Electronics and Optoelectronics. *J. Phys. Chem. C* **2016**, *120*, 24682–24687.
- (33) Bala, A.; Deb, A. K.; Kumar, V. Atomic and Electronic Structure of Two-Dimensional Inorganic Halide Perovskites A_{n+1}M_nX_{3n+1} (n = 1–6, A = Cs, M = Pb and Sn, and X = Cl, Br, and I) from Ab Initio Calculations. *J. Phys. Chem. C* **2018**, *122*, 7464–7473.
- (34) Zhang, J.; Yu, C.; Wang, L.; Li, Y.; Ren, Y.; Shum, K. Energy Barrier at the N719-Dye/CsSnI₃ Interface for Photogenerated Holes in Dye-Sensitized Solar Cells. *Sci. Rep.* **2015**, *4*, 6954.
- (35) Kong, Q.; Lee, W.; Lai, M.; Bischak, C. G.; Gao, G.; Wong, A. B.; Lei, T.; Yu, Y.; Wang, L.-W.; Ginsberg, N. S.; Yang, P. Phase-Transition-Induced p-n Junction in Single Halide Perovskite Nanowire. *Proc. Natl. Acad. Sci. U. S. A.* **2018**, *115* (36), 8889–8894.
- (36) Ye, T.; Wang, K.; Hou, Y.; Yang, D.; Smith, N.; Magill, B.; Yoon, J.; Mudiyansele, R. R. H. H.; Khodaparast, G. A.; Wang, K.; Priya, S. Ambient-Air-Stable Lead-Free CsSnI₃ Solar Cells with Greater than 7.5% Efficiency. *J. Am. Chem. Soc.* **2021**, *143*, 4319–4328.

- (37) Hong, W.-L.; Huang, Y.-C.; Chang, C.-Y.; Zhang, Z.-C.; Tsai, H.-R.; Chang, N.-Y.; Chao, Y.-C. Efficient Low-Temperature Solution-Processed Lead-Free Perovskite Infrared Light-Emitting Diodes. *Adv. Mater.* **2016**, *28*, 8029–8036.
- (38) Linseis, V.; Völklein, F.; Reith, H.; Nielsch, K.; Woias, P. Advanced Platform for the In-Plane ZT Measurement of Thin Films. *Rev. Sci. Instrum.* **2018**, *89*, 015110.
- (39) Stoumpos, C. C.; Malliakas, C. D.; Kanatzidis, M. G. Semiconducting Tin and Lead Iodide Perovskites with Organic Cations: Phase Transitions, High Mobilities, and near-Infrared Photoluminescent Properties. *Inorg. Chem.* **2013**, *52* (15), 9019–9038.
- (40) Takahashi, Y.; Hasegawa, H.; Takahashi, Y.; Inabe, T. Hall Mobility in Tin Iodide Perovskite $\text{CH}_3\text{NH}_3\text{SnI}_3$: Evidence for a Doped Semiconductor. *J. Solid State Chem.* **2013**, *205*, 39–43.
- (41) Ye, T.; Wang, X.; Li, X.; Yan, A. Q.; Ramakrishna, S.; Xu, J. Ultra-High Seebeck Coefficient and Low Thermal Conductivity of a Centimeter-Sized Perovskite Single Crystal Acquired by a Modified Fast Growth Method. *J. Mater. Chem. C* **2017**, *5*, 1255–1260.
- (42) Zhao, L. D.; Lo, S. H.; Zhang, Y.; Sun, H.; Tan, G.; Uher, C.; Wolverton, C.; Dravid, V. P.; Kanatzidis, M. G. Ultralow Thermal Conductivity and High Thermoelectric Figure of Merit in SnSe Crystals. *Nature* **2014**, *508*, 373–377.
- (43) Lee, W.; Li, H.; Wong, A. B.; Zhang, D.; Lai, M.; Yu, Y.; Kong, Q.; Lin, E.; Urban, J. J.; Grossman, J. C.; Yang, P. Ultralow Thermal Conductivity in All-Inorganic Halide Perovskites. *Proc. Natl. Acad. Sci. U. S. A.* **2017**, *114* (33), 8693–8697.
- (44) López-Fraguas, E.; Masi, S.; Mora-Seró, I. Optical Characterization of Lead-Free Cs_2SnI_6 Double Perovskite Fabricated from Degraded and Reconstructed CsSnI_3 Films. *ACS Appl. Energy Mater.* **2019**, *2* (12), 8381–8387.
- (45) Guo, F.; Lu, Z.; Mohanty, D.; Wang, T.; Bhat, I. B.; Zhang, S.; Shi, S.; Washington, M. A.; Wang, G. C.; Lu, T. M. A Two-Step Dry Process for Cs_2SnI_6 Perovskite Thin Film. *Mater. Res. Lett.* **2017**, *5* (8), 540–546.
- (46) Bhui, A.; Ghosh, T.; Pal, K.; Singh Rana, K.; Kundu, K.; Soni, A.; Biswas, K. Intrinsically Low Thermal Conductivity in the N-Type Vacancy-Ordered Double Perovskite Cs_2SnI_6 : Octahedral Rotation and Anharmonic Rattling. *Chem. Mater.* **2022**, *34* (7), 3301–3310.
- (47) Koyanagi, T.; Kapil, G.; Ogomi, Y.; Yoshino, K.; Shen, Q.; Toyoda, T.; Murakami, T. N.; Segawa, H.; Hayase, S. Hot-Injection and Ultrasonic Irradiation Syntheses of Cs_2SnI_6 Quantum Dot Using Sn Long-Chain Amino-Complex. *J. Nanoparticle Res.* **2020**, *22*, 69.
- (48) Lee, B.; Shin, B.; Park, B. Uniform Cs_2SnI_6 Thin Films for Lead-Free and Stable Perovskite Optoelectronics via Hybrid Deposition Approaches. *Electron. Mater. Lett.* **2019**, *15*, 192–200.
- (49) Qiu, X.; Jiang, Y.; Zhang, H.; Qiu, Z.; Yuan, S.; Wang, P.; Cao, B. Lead-Free Mesoscopic Cs_2SnI_6 Perovskite Solar Cells Using Different Nanostructured ZnO Nanorods as Electron Transport Layers. *Phys. Status Solidi RRL* **2016**, *10* (8), 587–591.
- (50) El Ajjouri, Y.; Locardi, F.; Gelvez-Rueda, M. C.; Prato, M.; Sessolo, M.; Ferretti, M.; Grozema, F. C.; Palazon, F.; Bolink, H. J. Mechanochemical Synthesis of Sn(II) and Sn(IV) Iodide Perovskites and Study of Their Structural, Chemical, Thermal, Optical, and Electrical Properties. *Energy Technol.* **2020**, *8* (4), 1900788.
- (51) Xiao, Z.; Zhou, Y.; Hosono, H.; Kamiya, T. Intrinsic Defects in a Photovoltaic Perovskite Variant Cs_2SnI_6 . *Phys. Chem. Chem. Phys.* **2015**, *17*, 18900–18903.
- (52) Liu, J.; Qiu, L.; Portale, G.; Koopmans, M.; ten Brink, G.; Hummelen, J. C.; Koster, L. J. A. N-Type Organic Thermoelectrics: Improved Power Factor by Tailoring Host-Dopant Miscibility. *Adv. Mater.* **2017**, *29* (36), 1701641.

Supporting Information:

Vacuum Deposited Cesium Tin Iodide Thin Films with Tunable Thermoelectric Properties

Paz Sebastián-Luna,^a Unnati Pokharel,^b Bas A. H. Huisman,^a L. Jan Anton Koster,^b
Francisco Palazón,^{*a,c} and Henk J. Bolink,^{*a}

^a Instituto de Ciencia Molecular, ICMol, Universidad de Valencia, 46980 Paterna, Spain

^b Zernike Institute for Advanced Materials, University of Groningen, 9747 AG Groningen,
The Netherlands

^c Departamento de Ingeniería Química y Ambiental, Universidad Politécnica de Cartagena,
30202 Cartagena, Spain

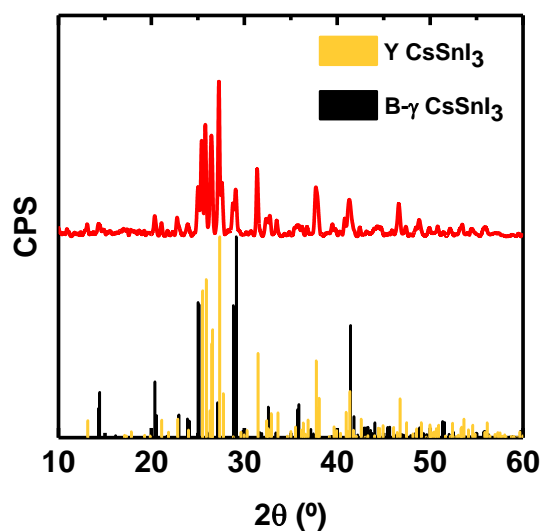


Figure S1. XRD diffractogram of as-synthesized CsSnI_3 powder by dry mechanochemistry together with the Inorganic Crystal Structure Database patterns of yellow phase (Y CsSnI_3 , ICSD code 262927) and the black gamma phase ($\text{B-}\gamma \text{ CsSnI}_3$, ICSD code 262926).

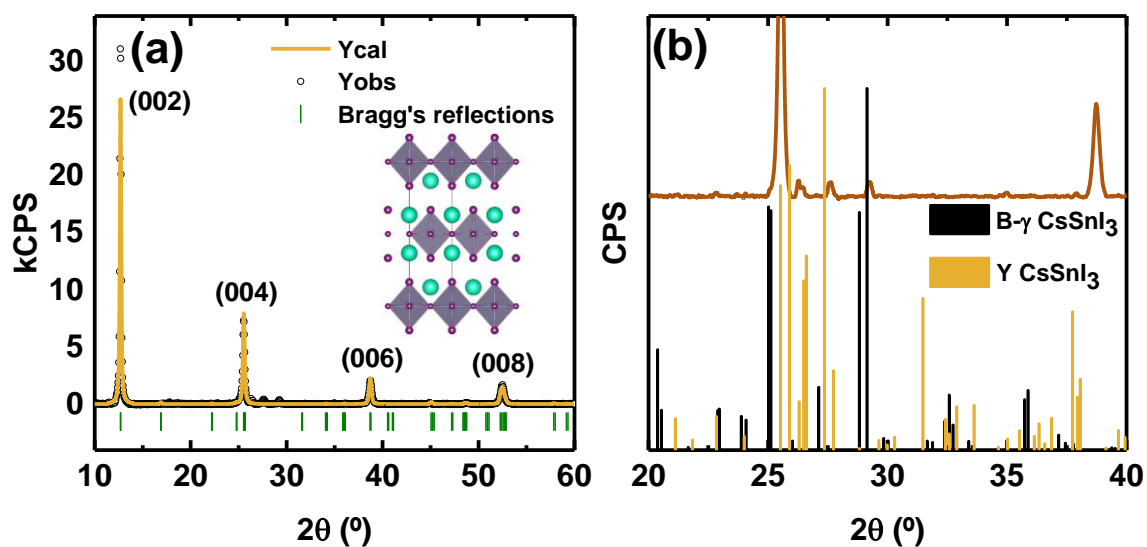


Figure S2. (a) Experimental (open circles) and fitted (yellow line) diffractograms of as-deposited Cs_2SnI_4 thin-films showing planes with preferential orientation (bold). Calculated Bragg's reflections position in green. Inset with the expected crystallographic structure of Cs_2SnI_4 is given. (b) Zoomed area of as-deposited Cs_2SnI_4 thin-film together with the Inorganic Crystal Structure Database patterns of yellow phase (Y CsSnI_3 , ICSD code 262927) and the black gamma phase ($\text{B-}\gamma \text{ CsSnI}_3$, ICSD code 262926).

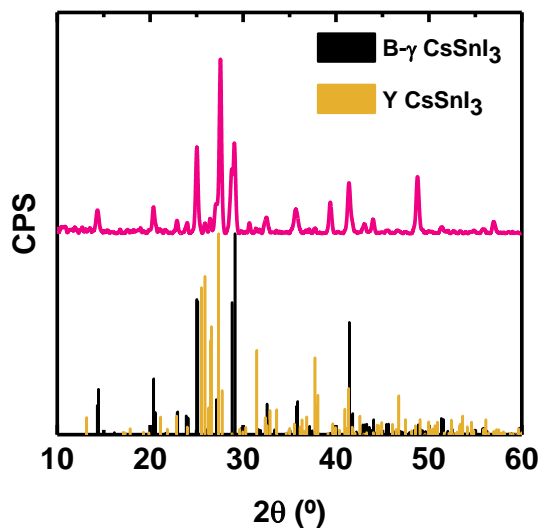


Figure S3. XRD diffractogram of as-synthesized Cs_2SnI_4 powder by dry mechanochemistry. As-synthesized powder is a mixture of yellow phase (Y CsSnI_3 , ICSD code 262927) and the black gamma phase (B- γ CsSnI_3 , ICSD code 262926), as clearly indicated in the data.

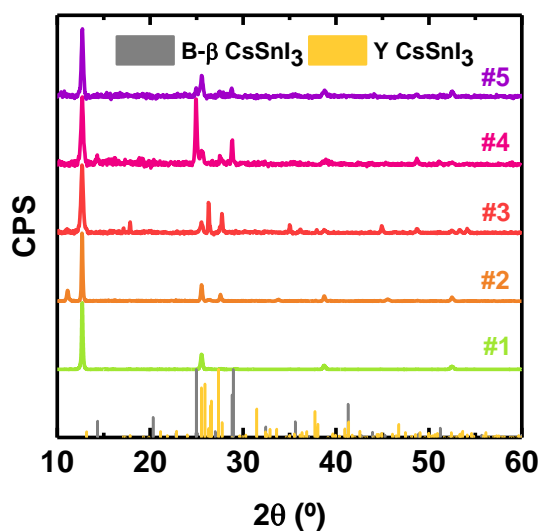


Figure S4. XRD diffractogram of as-deposited Cs_2SnI_4 thin-films from different deposition batches together with the Inorganic Crystal Structure Database patterns of yellow phase (Y CsSnI_3 , ICSD code 262927) and the black beta phase (B- β CsSnI_3 , ICSD code 262925).

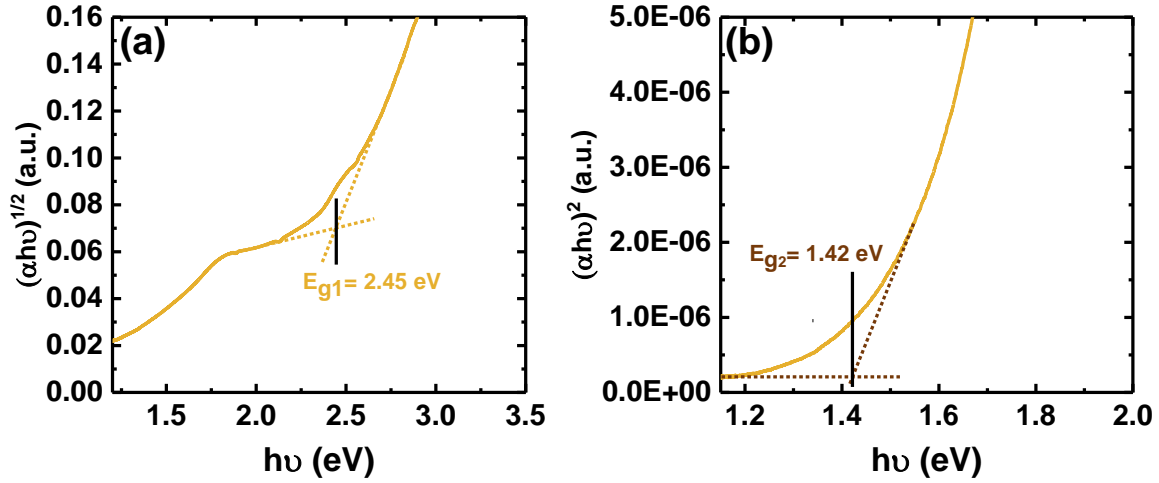


Figure S5. Tauc plot of as-deposited SSVD CsSnI₃ thin films considering (a) an indirect and (b) direct transition. E_{g1} is ascribed to the yellow phase of CsSnI₃ and E_{g2} , to Cs₂SnI₄.

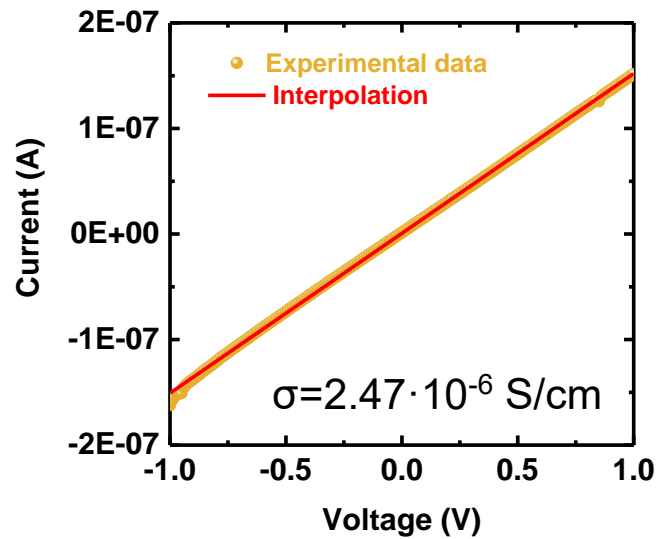


Figure S6. Current vs voltage curve of Cs₂SnI₄ (yellow line) to determine the electrical conductivity. Red line represents the linear interpolation of the JV curve. According to Ohm's law (**Equation S1**), it is possible to calculate the electrical conductivity from the slope of the linear plot.

$$I = \frac{1}{R} V = \sigma V \quad \text{Eq. S1}$$

Where I stands for current intensity, R electrical resistance, V voltage and σ electrical conductivity.

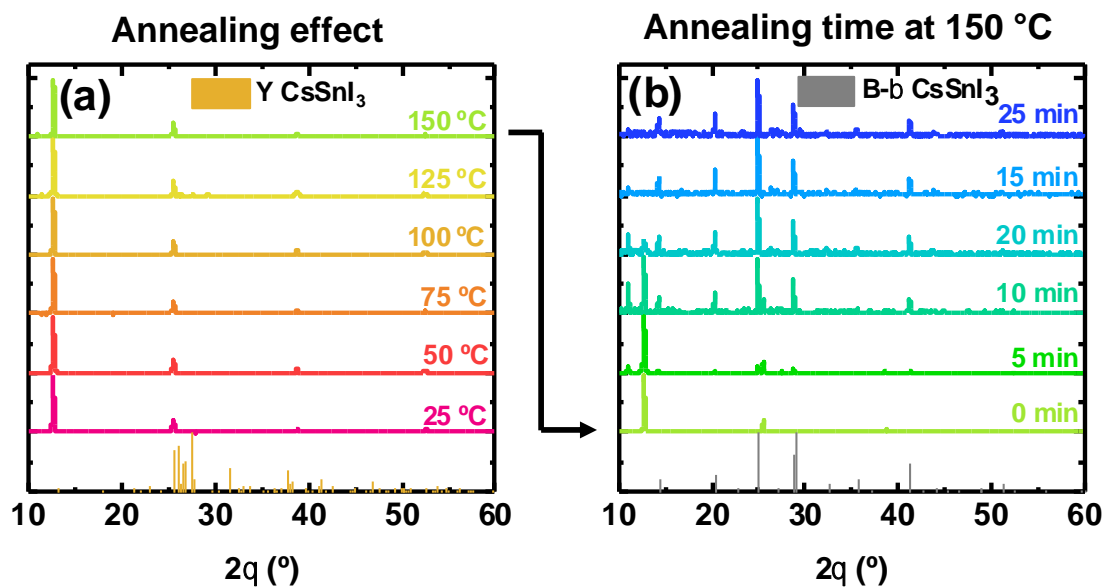


Figure S7. XRD diffractograms of (a) in-situ annealing of Cs_2SnI_4 thin films up to 150 °C and (b) effect of the annealing time at 150 °C until it is fully converted into the black beta phase of CsSnI_3 .

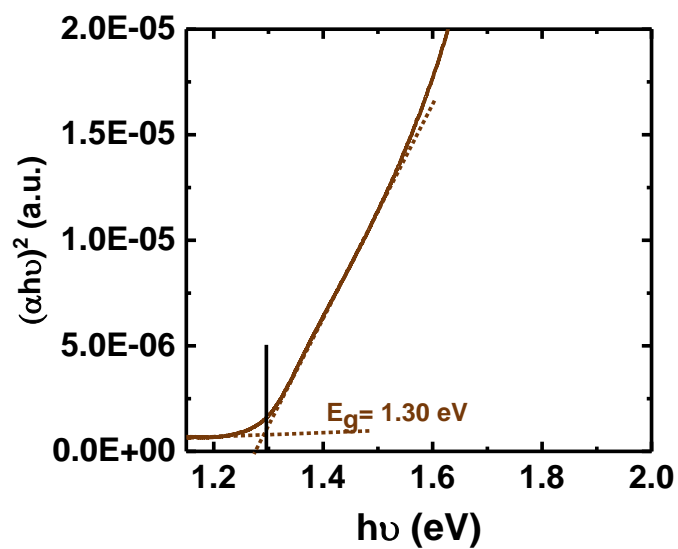


Figure S8. Tauc plot of β - β CsSnI_3 thin films considering a direct transition. A bandgap of 1.30 eV is estimated.

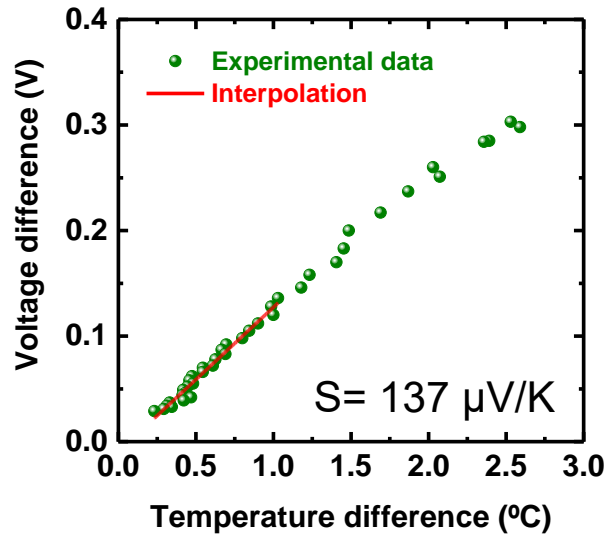


Figure S9. Thermoelectric voltage vs. temperature difference for B- β CsSnI₃ thin films at room temperature. The sign and the value of the Seebeck coefficient are given by **Equation S2**.

$$S = - \frac{\Delta V}{\Delta T} \quad \text{Eq. S2}$$

Where ΔV stands for difference in thermal voltage and ΔT , temperature difference.

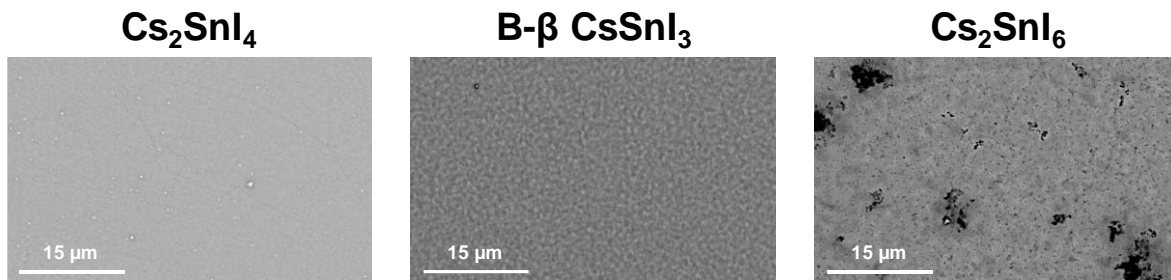


Figure S10. SEM images of Cs₂SnI₄, B- β CsSnI₃ and Cs₂SnI₆ thin films at 10,000x magnification.

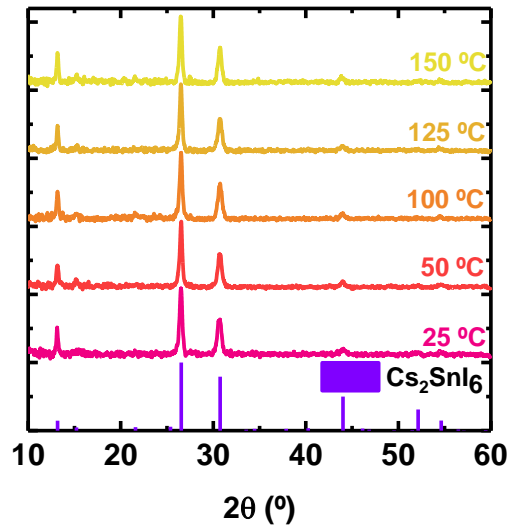


Figure S11. XRD diffractograms of in-situ annealed Cs₂SnI₆ thin films up to 150 °C.

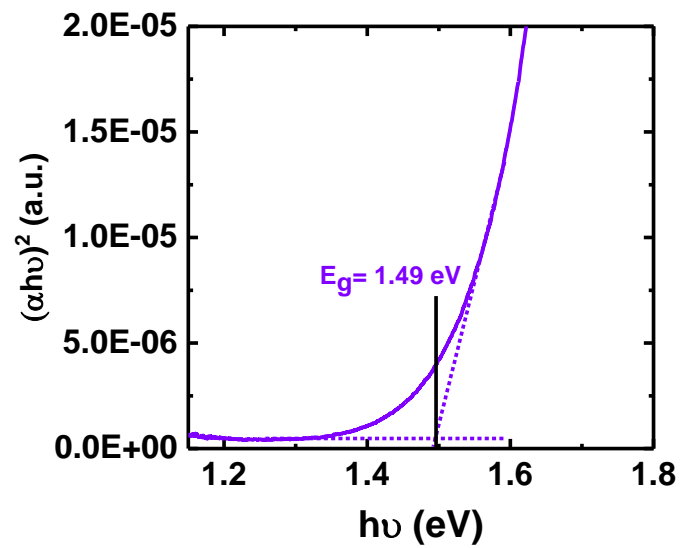


Figure S12. Tauc plot of Cs₂SnI₆ thin films considering a direct transition. A bandgap of 1.49 eV is estimated.

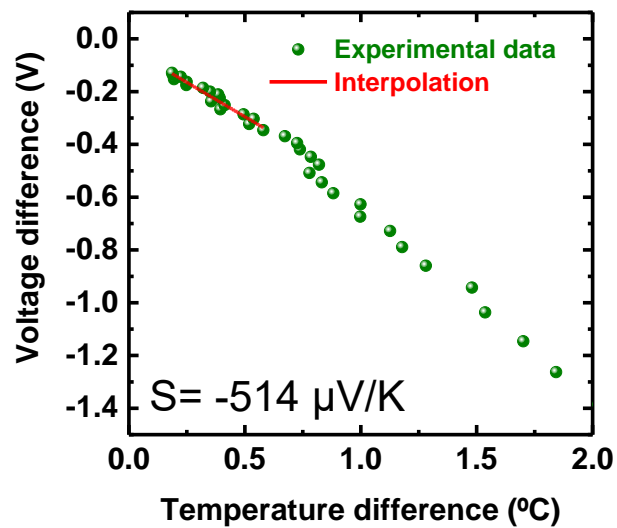


Figure S13. Thermoelectric voltage vs. temperature difference for Cs_2SnI_6 at room temperature. The sign and the value of the Seebeck coefficient are given by **Eq. S2**.

Appendix D

Bibliography

- (1) NASA - Global Climate Change. The effects of climate change. <https://climate.nasa.gov/effects/>
- (2) European Commission. Consequences of climate change. https://ec.europa.eu/clima/climate-change/consequences-climate-change_en
- (3) Ritchie, H.; Roser, M.; Rosado, P. CO₂ and greenhouse gas emissions. <https://ourworldindata.org/greenhouse-gas-emissions>
- (4) Ritchie, H.; Roser, M.; Rosado, P. Energy - Our World in Data. <https://ourworldindata.org/energy-mix>
- (5) Eurostat. Energy statistics - an overview. https://ec.europa.eu/eurostat/statistics-explained/index.php?title=Energy_statistics_-_an_overview
- (6) Huen, P.; Daoud, W. A. Advances in Hybrid Solar Photovoltaic and Thermoelectric Generators. *Renew. Sustain. Energy Rev.* **2017**, *72*, 1295–1302.
- (7) Jaziri, N.; Boughamoura, A.; Müller, J.; Mezghani, B.; Tounsi, F.; Ismail, M. A Comprehensive Review of Thermoelectric Generators: Technologies and Common Applications. *Energy Reports* **2020**, *6* (7), 264–287.
- (8) Eurostat. Energy consumption in households. https://ec.europa.eu/eurostat/statistics-explained/index.php?title=Energy_consumption_in_households&oldid=569853
- (9) Beretta, D.; Neophytou, N.; Hodges, J. M.; Kanatzidis, M. G.; Narducci, D.; Martin-Gonzalez, M.; Beekman, M.; Balke, B.; Cerretti, G.; Tremel, W.; Zevalkink, A.; Hofmann, A. I.; Müller, C.; Dörfling, B.; Campoy-Quiles, M.; Caironi, M. Thermoelectrics: From History, a Window to the Future. *Mater. Sci. Eng. R* **2019**, *138*, 210–255.
- (10) Nayak, P. K.; Mahesh, S.; Snaith, H. J.; Cahen, D. Photovoltaic Solar Cell Technologies: Analysing the State of the Art. *Nat. Rev. Mater.* **2019**, *4* (4), 269–285.
- (11) Kitai, A. Chapter 5: Light Emitting Diodes. In *Principles of Solar Cells, LEDs and Diodes*; John Wiley & Sons, Ltd, 2011; pp 215–252.
- (12) Nardelli, A.; Deuschle, E.; de Azevedo, L. D.; Pessoa, J. L. N.; Ghisi, E. Assessment of Light Emitting Diodes Technology for General Lighting: A Critical Review. *Renew. Sustain. Energy Rev.* **2017**, *75*, 368–379.
- (13) Kalyani, N. T.; Swart, H.; Dhoble, S. J.; Kalyani, N. T.; Swart, H.; Dhoble, S. J. Chapter 4: Artificial Lighting: Origin—Impact and Future Perspectives. In *Principles and Applications of Organic Light Emitting Diodes (OLEDs)*; Woodhead Publishing, 2017; pp 87–113.
- (14) Schubert, E. F. Light-Emitting Diodes. In *Wiley Encyclopedia of Electrical and Electronics Engineering*; Webster, J., Ed.; John Wiley & Sons, Ltd, 2014.
- (15) Godlewski, J.; Obarowska, M. Organic Light Emitting Devices. *Opto-Electronics Rev.* **2007**, *15* (4), 179–183.
- (16) Bizzarri, C.; Spuling, E.; Knoll, D. M.; Volz, D.; Bräse, S. Sustainable Metal Complexes for Organic Light-Emitting Diodes (OLEDs). *Coord. Chem. Rev.* **2018**, *373*, 49–82.

- (17) Knupfer, M. Exciton Binding Energies in Organic Semiconductors. *Appl. Phys. A* **2003**, *77* (5), 623–626.
- (18) Cinquino, M.; Prontera, C. T.; Pugliese, M.; Giannuzzi, R.; Taurino, D.; Gigli, G.; Maiorano, V. Light-Emitting Textiles: Device Architectures, Working Principles, and Applications. *Micromachines* **2021**, *12* (6), 652.
- (19) Zou, S.; Liu, Y.; Li, J.; Liu, C.; Feng, R.; Jiang, F.; Li, Y.; Song, J.; Zeng, H.; Hong, M.; Chen, X. Stabilizing Cesium Lead Halide Perovskite Lattice through Mn(II) Substitution for Air-Stable Light-Emitting Diodes. *J. Am. Chem. Soc.* **2017**, *139* (33), 11443–11450.
- (20) Will, P.-A.; Reineke, S. Organic Light-Emitting Diodes. In *Handbook of Organic Materials for Electronic and Photonic Devices*; Woodhead Publishing, 2019; pp 695–726.
- (21) Zhang, L.; Liu, Y.; Yang, Z.; Liu, S. (Frank). Two Dimensional Metal Halide Perovskites: Promising Candidates for Light-Emitting Diodes. *J. Energy Chem.* **2019**, *37*, 97–110.
- (22) Veldhuis, S. A.; Boix, P. P.; Yantara, N.; Li, M.; Sum, T. C.; Mathews, N.; Mhaisalkar, S. G. Perovskite Materials for Light-Emitting Diodes and Lasers. *Adv. Mater.* **2016**, *28* (32), 6804–6834.
- (23) You, P.; Tang, G.; Yan, F. Two-Dimensional Materials in Perovskite Solar Cells. *Mater. Today Energy* **2019**, *11*, 128–158.
- (24) Zhang, W.; Tao, K.; Ji, C.; Sun, Z.; Han, S.; Zhang, J.; Wu, Z.; Luo, J. (C₆H₁₃N)₂BiI₅: A One-Dimensional Lead-Free Perovskite-Derivative Photoconductive Light Absorber. *Inorg. Chem.* **2018**, *57* (8), 4239–4243.
- (25) American Chemical Society. How a Solar Cell Works. <https://www.acs.org/content/acs/en/education/resources/highschool/chemmatters/past-issues/archive-2013-2014/how-a-solar-cell-works.html>
- (26) TU Delft OpenCourseWare. Solar Energy: The Working Principle of a Solar Cell.
- (27) Kour, R.; Arya, S.; Verma, S.; Gupta, J.; Bandhoria, P.; Bharti, V.; Datt, R.; Gupta, V. Potential Substitutes for Replacement of Lead in Perovskite Solar Cells: A Review. *Glob. Challenges* **2019**, *3*, 1900050.
- (28) Longo, G.; Gil-Escrig, L.; Degen, M. J.; Sessolo, M.; Bolink, H. J. Perovskite Solar Cells Prepared by Flash Evaporation. *Chem. Commun.* **2015**, *51* (34), 7376–7378.
- (29) Li, G.; Shittu, S.; Diallo, T. M. O.; Yu, M.; Zhao, X.; Ji, J. A Review of Solar Photovoltaic-Thermoelectric Hybrid System for Electricity Generation. *Energy* **2018**, *158*, 41–58.
- (30) Guechi, N.; Bouhemadou, A.; Bin-Omran, S.; Bourzami, A.; Louail, L. Elastic, Optoelectronic and Thermoelectric Properties of the Lead-Free Halide Semiconductors Cs₂AgBiX₆ (X = Cl, Br): Ab Initio Investigation. *J. Electron. Mater.* **2018**, *47* (2), 1533–1545.
- (31) Wu, T.; Gao, P. Development of Perovskite-Type Materials for Thermoelectric Application. *Materials (Basel)*. **2018**, *11* (6), 999.

- (32) Snyder, G. J.; Toberer, E. S. Complex Thermoelectric Materials. *Nat. Mater.* **2008**, *7* (2), 105–114.
- (33) Arar, S. Thermocouple Principles—the Seebeck Effect and Seebeck Coefficient - Technical Articles. <https://www.allaboutcircuits.com/technical-articles/thermocouple-principles-seebeck-effect-seebeck-voltage-seebeck-coefficients/>
- (34) Haque, M. A.; Kee, S.; Villalva, D. R.; Ong, W.; Baran, D. Halide Perovskites: Thermal Transport and Prospects for Thermoelectricity. *Adv. Sci.* **2020**, *7* (10), 1903389.
- (35) Thermoelectrics. Northwestern Materials Science and Engineering. Thermoelectric Properties of Materials. <http://thermoelectrics.matsci.northwestern.edu/thermoelectrics/index.html>
- (36) Lindemuth, J. Hall Mobility Measurement of Solar Cell Material. *Magn. Technol. International* **2012**, 36–39.
- (37) Stranks, S. D.; Hoyer, R. L. Z.; Di, D.; Friend, R. H.; Deschler, F. The Physics of Light Emission in Halide Perovskite Devices. *Adv. Mater.* **2019**, *31* (47), 1803336.
- (38) Yang, T. C.-J.; Fiala, P.; Jeangros, Q.; Ballif, C. High-Bandgap Perovskite Materials for Multijunction Solar Cells. *Joule* **2018**, *2* (8), 1421–1436.
- (39) Sun, J.; Yang, J.; Lee, J. I.; Cho, J. H.; Kang, M. S. Lead-Free Perovskite Nanocrystals for Light-Emitting Devices. *J. Phys. Chem. Lett.* **2018**, *9* (7), 1573–1583.
- (40) Asim, N.; Sopian, K.; Ahmadi, S.; Saeedfar, K.; Alghoul, M. A.; Saadatian, O.; Zaidi, S. H. A Review on the Role of Materials Science in Solar Cells. *Renew. Sustain. Energy Rev.* **2012**, *16* (8), 5834–5847.
- (41) National Renewable Energy Laboratory (NREL). Best Research-Cell Efficiency Chart.
- (42) Lei, H.; Chen, J.; Tan, Z.; Fang, G. Review of Recent Progress in Antimony Chalcogenide-Based Solar Cells: Materials and Devices. *Sol. RRL* **2019**, *3* (6), 1–27.
- (43) Park, N.-G.; Grätzel, M.; Miyasaka, T. *Organic-Inorganic Halide Perovskite Photovoltaics*; Springer, 2016.
- (44) World Health Organization. Lead poisoning. <https://www.who.int/news-room/fact-sheets/detail/lead-poisoning-and-health>
- (45) Wang, R.; Wang, J.; Tan, S.; Duan, Y.; Wang, Z.-K.; Yang, Y. Opportunities and Challenges of Lead-Free Perovskite Optoelectronic Devices. *Trends Chem.* **2019**, *1* (4), 368–379.
- (46) Kour, R.; Arya, S.; Verma, S.; Gupta, J.; Bandhoria, P.; Bharti, V.; Datt, R.; Gupta, V. Potential Substitutes for Replacement of Lead in Perovskite Solar Cells: A Review. *Glob. Challenges* **2019**, *3* (11), 1900050.
- (47) Zhou, C.; Lee, Y. K.; Yu, Y.; Byun, S.; Luo, Z. Z.; Lee, H.; Ge, B.; Lee, Y. L.; Chen, X.; Lee, J. Y.; Cojocaru-Mirédin, O.; Chang, H.; Im, J.; Cho, S. P.; Wuttig, M.; Dravid, V. P.; Kanatzidis, M. G.; Chung, I. Polycrystalline SnSe with a Thermoelectric Figure of Merit Greater than the Single Crystal. *Nat. Mater.* **2021**, *20*, 1378–1384.

- (48) Ao, D. W.; Liu, W. Di; Chen, Y. X.; Wei, M.; Jabar, B.; Li, F.; Shi, X. L.; Zheng, Z. H.; Liang, G. X.; Zhang, X. H.; Fan, P.; Chen, Z. G. Novel Thermal Diffusion Temperature Engineering Leading to High Thermoelectric Performance in Bi₂Te₃-Based Flexible Thin-Films. *Adv. Sci.* **2022**, *9* (5), 2103547.
- (49) Shie, M. D.; Deeds, F. E. The Importance of Tellurium as a Health Hazard in Industry. A Preliminary Report. *Public Health Rep.* **1920**, *35* (16), 939–954.
- (50) Vávrová, S.; Struhárňanská, E.; Turňa, J.; Stuchlík, S. Tellurium: A Rare Element with Influence on Prokaryotic and Eukaryotic Biological Systems. *Int. J. Mol. Sci.* **2021**, *22*, 5924.
- (51) Yan, Q.; Kanatzidis, M. G. High-Performance Thermoelectrics and Challenges for Practical Devices. *Nat. Mater.* **2021**.
- (52) Caballero-Calero, O.; Ares, J. R.; Martín-González, M. Environmentally Friendly Thermoelectric Materials: High Performance from Inorganic Components with Low Toxicity and Abundance in the Earth. *Adv. Sustain. Syst.* **2021**, *5* (11), 2100095.
- (53) Liu, J.; Qiu, L.; Portale, G.; Torabi, S.; Stuart, M. C. A.; Qiu, X.; Koopmans, M.; Chiechi, R. C.; Hummelen, J. C.; Anton Koster, L. J. Side-Chain Effects on n-Type Organic Thermoelectrics: A Case Study of Fullerene Derivatives. *Nano Energy* **2018**, *52*, 183–191.
- (54) Zheng, Z. H.; Zhang, D. L.; Jabar, B.; Chen, T. B.; Nisar, M.; Chen, Y. F.; Li, F.; Chen, S.; Liang, G. X.; Zhang, X. H.; Fan, P.; Chen, Y. X. Realizing High Thermoelectric Performance in Highly (010)-Textured Flexible Cu₂Se Thin Film for Wearable Energy Harvesting. *Mater. Today Phys.* **2022**, *24*, 100659.
- (55) Zheng, Z. H.; Zhang, D. L.; Niu, J. Y.; Shi, X. L.; Chen, T. B.; Chen, Y. F.; Li, F.; Liang, G. X.; Chen, Y. X.; Fan, P.; Chen, Z. G. Achieving Ultrahigh Power Factor in n-Type Ag₂Se Thin Films by Carrier Engineering. *Mater. Today Energy* **2022**, *24*, 100933.
- (56) Vaquero, P. Chapter 1: Synthesis and Property Measurements of Thermoelectric Materials. In *Inorganic Thermoelectric Materials: From Fundamental Concepts to Materials Design*; Royal Society of Chemistry, 2021; pp 1–52.
- (57) Anastas, P.; Eghbali, N. Green Chemistry: Principles and Practice. *Chem. Soc. Rev.* **2010**, *39* (1), 301–312.
- (58) Palazon, F.; El Ajjouri, Y.; Bolink, H. J. Making by Grinding: Mechanochemistry Boosts the Development of Halide Perovskites and Other Multinary Metal Halides. *Adv. Energy Mater.* **2019**, 1902499.
- (59) El Ajjouri, Y.; Chirvony, V. S.; Vassilyeva, N.; Sessolo, M.; Palazon, F.; Bolink, H. J. Low-Dimensional Non-Toxic A₃Bi₂X₉ Compounds Synthesized by a Dry Mechanochemical Route with Tunable Visible Photoluminescence at Room Temperature. *J. Mater. Chem. C* **2019**, *7*, 6236–6240.
- (60) El Ajjouri, Y.; Chirvony, V. S.; Sessolo, M.; Palazon, F.; Bolink, H. J. Incorporation of Potassium Halides in the Mechanochemical Synthesis of Inorganic Perovskites: Feasibility and Limitations of Ion-Replacement and Trap Passivation. *RSC Adv.* **2018**, *8* (72), 41548–41551.

- (61) Protesescu, L.; Yakunin, S.; Nazarenko, O.; Dirin, D. N.; Kovalenko, M. V. Low-Cost Synthesis of Highly Luminescent Colloidal Lead Halide Perovskite Nanocrystals by Wet Ball Milling. *ACS Appl. Nano Mater.* **2018**, *1* (3), 1300–1308.
- (62) Sessolo, M.; Gil-Escrig, L.; Longo, G.; Bolink, H. J. Perovskite Luminescent Materials. *Top. Curr. Chem.* **2016**, *374* (4), 52.
- (63) Momblona, C.; Gil-Escrig, L.; Bandiello, E.; Hutter, E. M.; Sessolo, M.; Lederer, K.; Blochwitz-Nimoth, J.; Bolink, H. J. Efficient Vacuum Deposited p-i-n and n-i-p Perovskite Solar Cells Employing Doped Charge Transport Layers. *Energy Environ. Sci.* **2016**, *9*, 3456–3463.
- (64) Liu, M.; Johnston, M. B.; Snaith, H. J. Efficient Planar Heterojunction Perovskite Solar Cells by Vapour Deposition. *Nature* **2013**, *501* (7467), 395–398.
- (65) El Ajjouri, Y.; Palazon, F.; Sessolo, M.; Bolink, H. J. Single-Source Vacuum Deposition of Mechanosynthesized Inorganic Halide Perovskites. *Chem. Mater.* **2018**, *30*, 7423–7427.
- (66) Retsch GmbH. Mixer Mill MM 400 - RETSCH - powerful grinding by impact and friction. <https://www.retsch.com/products/milling/ball-mills/mixer-mill-mm-400/function-features/>
- (67) Engberg, S.; Martinho, F.; Gansukh, M.; Protti, A.; Küngas, R.; Stamate, E.; Hansen, O.; Canulescu, S.; Schou, J. Spin-Coated $\text{Cu}_2\text{ZnSnS}_4$ Solar Cells: A Study on the Transformation from Ink to Film. *Sci. Rep.* **2020**, *10*, 20749.
- (68) Sanders, S.; Stümmeler, D.; Pfeifer, P.; Ackermann, N.; Simkus, G.; Heuken, M.; Baumann, P. K.; Vescan, A.; Kalisch, H. Chemical Vapor Deposition of Organic-Inorganic Bismuth-Based Perovskite Films for Solar Cell Application. *Sci. Rep.* **2019**, *9*, 9774.
- (69) Fan, P.; Peng, H.-X.; Zheng, Z.-H.; Chen, Z.-H.; Tan, S.-J.; Chen, X.-Y.; Luo, Y.-D.; Su, Z.-H.; Luo, J.-T.; Liang, G.-X. Single-Source Vapor-Deposited $\text{Cs}_2\text{AgBiBr}_6$ Thin Films for Lead-Free Perovskite Solar Cells. *Nanomaterials* **2019**, *9* (12), 1760.
- (70) Fan, P.; Gu, D.; Liang, G. X.; Luo, J. T.; Chen, J. L.; Zheng, Z. H.; Zhang, D. P. High-Performance Perovskite $\text{CH}_3\text{NH}_3\text{PbI}_3$ Thin Films for Solar Cells Prepared by Single-Source Physical Vapour Deposition. *Sci. Rep.* **2016**, *6*, 29910.
- (71) Liang Tan, W.; McNeill, C. R. X-Ray Diffraction of Photovoltaic Perovskites: Principles and Applications. *Appl. Phys. Rev.* **2022**, *9* (2), 021310.
- (72) Raval, N.; Maheshwari, R.; Kalyane, D.; Youngren-Ortiz, S. R.; Chougule, M. B.; Tekade, R. K. Chapter 10: Importance of Physicochemical Characterization of Nanoparticles in Pharmaceutical Product Development. In *Basic Fundamentals of Drug Delivery*; Academic Press, 2019; pp 369–400.
- (73) Stevie, F. A.; Donley, C. L. Introduction to X-Ray Photoelectron Spectroscopy. *J. Vac. Sci. Technol. A* **2020**, *38* (6), 063204.
- (74) Baer, D. R.; Thevuthasan, S. Chapter 16: Characterization of Thin Films and Coatings. In *Handbook of Deposition Technologies for Films and Coatings*; William Andrew Publishing, 2010; pp 749–864.

- (75) Abdi-Jalebi, M.; Ibrahim Dar, M.; Sadhanala, A.; Johansson, E. M. J.; Pazoki, M. Chapter 3: Optical Absorption and Photoluminescence Spectroscopy. In *Characterization Techniques for Perovskite Solar Cell Materials*; Elsevier, 2019; pp 49–79.
- (76) Mann, S. A.; Sciacca, B.; Zhang, Y.; Wang, J.; Kontoleta, E.; Liu, H.; Garnett, E. C. Integrating Sphere Microscopy for Direct Absorption Measurements of Single Nanostructures. *ACS Nano* **2017**, *11* (2), 1412–1418.
- (77) Thermo Fisher Scientific. Principles of Scanning Electron Microscopy. <https://www.thermofisher.com/es/es/home/materials-science/learning-center/applications/scanning-electron-microscope-sem-electron-column.html>
- (78) Thermo Fisher Scientific. Electrons in SEM. <https://www.thermofisher.com/es/es/home/materials-science/learning-center/applications/sem-electrons.html>
- (79) Thermo Fisher Scientific. Scanning Electron Microscopes. <https://www.thermofisher.com/es/es/home/materials-science/learning-center/applications/what-is-scanning-electron-microscopy.html>
- (80) Thermo Fisher Scientific. EDX Analysis with a Scanning Electron Microscope (SEM): How Does it Work? <https://www.thermofisher.com/es/es/home/global/forms/industrial/edx-analysis-sem.html>
- (81) Linseis Messgeräte GmbH. TFA: Instruction Manual. p 84.
- (82) Linseis, V.; Völklein, F.; Reith, H.; Nielsch, K.; Woias, P. Advanced Platform for the In-Plane ZT Measurement of Thin Films. *Rev. Sci. Instrum.* **2018**, *89*, 015110.
- (83) Dörfling, B.; Zapata-Arteaga, O.; Campoy-Quiles, M. A Setup to Measure the Seebeck Coefficient and Electrical Conductivity of Anisotropic Thin-Films on a Single Sample. *Rev. Sci. Instrum.* **2020**, *91* (10), 105111.
- (84) Linseis Messgeraete GmbH. 3 omega measurement technique. <https://www.linseis.com/en/methods/3-omega-method/>
- (85) Leijtens, T.; Bush, K. A.; Prasanna, R.; McGehee, M. D. Opportunities and Challenges for Tandem Solar Cells Using Metal Halide Perovskite Semiconductors. *Nat. Energy* **2018**, *3*, 828–838.
- (86) Xing, J.; Zhao, Y.; Askerka, M.; Quan, L. N.; Gong, X.; Zhao, W.; Zhao, J.; Tan, H.; Long, G.; Gao, L.; Yang, Z.; Voznyy, O.; Tang, J.; Lu, Z. H.; Xiong, Q.; Sargent, E. H. Color-Stable Highly Luminescent Sky-Blue Perovskite Light-Emitting Diodes. *Nat. Commun.* **2018**, *9* (1), 1–8.
- (87) Xu, L. J.; Sun, C. Z.; Xiao, H.; Wu, Y.; Chen, Z. N. Green-Light-Emitting Diodes Based on Tetrabromide Manganese(II) Complex through Solution Process. *Adv. Mater.* **2017**, *29* (10), 2–6.
- (88) Li, X.; Zhong, X.; Hu, Y.; Li, B.; Sheng, Y.; Zhang, Y.; Weng, C.; Feng, M.; Han, H.; Wang, J. Organic-Inorganic Copper(II)-Based Material: A Low-Toxic, Highly Stable Light Absorber for Photovoltaic Application. *J. Phys. Chem. Lett.* **2017**, *8* (8), 1804–1809.

- (89) Jun, T.; Sim, K.; Iimura, S.; Sasase, M.; Kamioka, H.; Kim, J.; Hosono, H. Lead-Free Highly Efficient Blue-Emitting Cs₃Cu₂I₅ with 0D Electronic Structure. *Adv. Mater.* **2018**, *30* (43), 0–11.
- (90) Roccanova, R.; Yangui, A.; Nhalil, H.; Shi, H.; Du, M.-H.; Saparov, B. Near-Unity Photoluminescence Quantum Yield in Blue-Emitting Cs₃Cu₂Br_{5-x}I_x (0 ≤ x ≤ 5). *ACS Appl. Electron. Mater.* **2019**, *1* (3), 269–274.
- (91) Danckwerts, P. V. Colloidal Synthesis and Optical Properties of All-Inorganic Low-Dimensional Cesium Copper Halide Nanocrystals. *Chem. Eng. Sci.* **1962**, *17* (11), 955.
- (92) Zhang, Z.-X.; Li, C.; Lu, Y.; Tong, X.-W.; Liang, F.-X.; Zhao, X.-Y.; Wu, D.; Xie, C.; Luo, L.-B. Sensitive Deep Ultraviolet Photodetector and Image Sensor Composed of Inorganic Lead-Free Cs₃Cu₂I₅ Perovskite with Wide Bandgap. *J. Phys. Chem. Lett.* **2019**, *10*, 5343–5350.
- (93) Rosales, B. A.; Wei, L.; Vela, J. Synthesis and Mixing of Complex Halide Perovskites by Solvent-Free Solid-State Methods. *J. Solid State Chem.* **2018**.
- (94) Ajjouri, Y. El; Locardi, F.; Gélvez-Rueda, M. C.; Prato, M.; Sessolo, M.; Ferretti, M.; Grozema, F. C.; Palazon, F.; Bolink, H. J. Mechanochemical Synthesis of Sn(II) and Sn(IV) Iodide Perovskites and Study of Their Structural, Chemical, Thermal, Optical, and Electrical Properties. *Energy Technol.* **2020**, *8* (4), 1900788.
- (95) Hong, Z.; Tan, D.; John, R. A.; Tay, Y. K. E.; Ho, Y. K. T.; Zhao, X.; Sum, T. C.; Mathews, N.; García, F.; Soo, H. Sen. Completely Solvent-Free Protocols to Access Phase-Pure, Metastable Metal Halide Perovskites and Functional Photodetectors from the Precursor Salts. *iScience* **2019**, *16*, 312–325.
- (96) Palazon, F.; El Ajjouri, Y.; Sebastia-Luna, P.; Lauciello, S.; Manna, L.; Bolink, H. J. Mechanochemical Synthesis of Inorganic Halide Perovskites: Evolution of Phase-Purity, Morphology, and Photoluminescence. *J. Mater. Chem. C* **2019**, *7* (37), 11406–11410.
- (97) Crane, M. J.; Kroupa, D. M.; Roh, J. Y.; Anderson, R. T.; Smith, M. D.; Gamelin, D. R. Single-Source Vapor Deposition of Quantum-Cutting Yb³⁺:CsPb(Cl_{1-x}Br_x)₃ and Other Complex Metal-Halide Perovskites. *ACS Appl. Energy Mater.* **2019**, *2* (6), 4560–4565.
- (98) Le Bail, A. Whole Powder Pattern Decomposition Methods and Applications: A Retrospection. *Powder Diffr.* **2005**, *20* (4), 316–326.
- (99) Thompson, P., Cox, D.E., Hasting, J. B. Rietveld Refinement of Deybe-Scherrer Synchrotron X-Ray Data from Al₂O₃. *Jorunal Apply Crystallogr.* **1987**, *20*, 79–83.
- (100) Horiba Scientific. What is Fluorescence Spectroscopy? <https://www.horiba.com/pol/scientific/technologies/fluorescence-spectroscopy/fluorescence-spectroscopy/>
- (101) Edinburgh Instruments. What are Absorption, Excitation and Emission Spectra? <https://www.edinst.com/blog/what-are-absorption-excitation-and-emission-spectra/>

- (102) Evident - Olympus LS. Fluorescence Excitation & Emission | Emission Spectrums. <https://www.olympus-lifescience.com/en/microscope-resource/primer/lightandcolor/fluoroexcitation/>
- (103) Sierra-Ávila, R.; Pérez-Alvarez, M.; Cadenas-Pliego, G.; Ávila-Orta, C. A.; Betancourt-Galindo, R.; Jiménez-Regalado, E.; Jiménez-Barrera, R. M.; Martínez-Colunga, J. G. Synthesis of Copper Nanoparticles Coated with Nitrogen Ligands. *J. Nanomater.* **2014**, *2014*, 1–8.
- (104) Vo Van, K.; Habashi, F. Identification and Thermal Stability of Copper(1) Sulfate. *Can. J. Chem.* **1972**, *50*, 3872.
- (105) Li, J.; Shacham-Diamand, Y.; Mayer, J. W. Copper Deposition and Thermal Stability Issues in Copper-Based Metallization for ULSI Technology. *Mater. Sci. Reports* **1992**, *9*, 1–51.
- (106) Cheng, P.; Sun, L.; Feng, L.; Yang, S.; Yang, Y.; Zheng, D.; Zhao, Y.; Sang, Y.; Zhang, R.; Wei, D.; Deng, W.; Han, K. Colloidal Synthesis and Optical Properties of All-Inorganic Low-Dimensional Cesium Copper Halide Nanocrystals. *Angew. Chemie - Int. Ed.* **2019**.
- (107) Zhang, Z.; Li, C.; Lu, Y.; Tong, X.; Liang, F.-X.; Zhao, X.; Wu, D.; Xie, C.; Luo, L. Sensitive Deep Ultraviolet Photodetector and Image Sensor Composed of Inorganic Lead-Free Cs₃Cu₂I₅ Perovskite with Wide Bandgap. *J. Phys. Chem. Lett.* **2019**, *10*, 5343-5350.
- (108) Mykhalichko, B.; Davydov, V. N.; Aksel'rud, L. G. Synthesis and Structure of Cs₃Cu₂Cl₅. *Russ. J. Inorg. Chem.* **1997**, *42* (7), 1125–1127.
- (109) Groeneveld, B. G. H. M.; Duim, H.; Kahmann, S.; De Luca, O.; Tekelenburg, E. K.; Kamminga, M. E.; Protesescu, L.; Portale, G.; Blake, G. R.; Rudolf, P.; Loi, M. A. Photochromism in Ruddlesden–Popper Copper-Based Perovskites: A Light-Induced Change of Coordination Number at the Surface. *J. Mater. Chem. C* **2020**, *8* (43), 15377–15384.
- (110) Smail, R. B.; Jezorek, R. L.; Lejnieks, J.; Enayati, M.; Grama, S.; Monteiro, M. J.; Percec, V. Acetone–Water Biphasic Mixtures as Solvents for Ultrafast SET-LRP of Hydrophobic Acrylates. *Polym. Chem* **2017**, *8*, 3102.
- (111) Barnes, J. C.; Hume, D. N. Copper(II) Bromide Complexes. I. A Spectrophotometric Study. *Inorg. Chem.* **1963**, *2* (3), 444–448.
- (112) Margolis, L. A.; Schaeffer, R. W.; Yoder, C. H. The Synthesis and Analysis of Copper(I) Iodide. A First-Year Laboratory Project. *J. Chem. Educ.* **2009**, *78* (2), 235.
- (113) Burdett, J. K.; Sevov, S. Stability of the Oxidation States of Copper. *J. Am. Chem. Soc.* **1995**, *117* (51), 12788–12792.
- (114) Sharma, V. K.; Millero, F. J. Determining the Stability Constant of Copper(I) Halide Complexes from Kinetic Measurements. *Inorg. Chem.* **1988**, *27* (18), 3256–3259.
- (115) Ahrland, S.; Rawsthorne, J.; Haaland, A.; Jerslev, B.; Schäffer, C. E.; Sunde, E.; Sørensen, N. A. The Stability of Metal Halide Complexes in Aqueous Solution. VII. The Chloride Complexes of Copper(I). *Acta Chem. Scand.* **1970**, *24*, 157–172.

- (116) Chemistry LibreTexts. P1: Standard Reduction Potentials by Element. https://chem.libretexts.org/Ancillary_Materials/Reference/Reference_Tables/Electrochemistry_Tables/P1%3A_Standard_Reduction_Potentials_by_Element
- (117) Biesinger, M. C.; Lau, L. W. M.; Gerson, A. R.; Smart, R. S. C. Resolving Surface Chemical States in XPS Analysis of First Row Transition Metals, Oxides and Hydroxides: Sc, Ti, V, Cu and Zn. *Appl. Surf. Sci.* **2010**, *257* (3), 887–898.
- (118) Shin, J.; Kim, M.; Jung, S.; Kim, C. S.; Park, J.; Song, A.; Chung, K. B.; Jin, S. H.; Lee, J. H.; Song, M. Enhanced Efficiency in Lead-Free Bismuth Iodide with Post Treatment Based on a Hole-Conductor-Free Perovskite Solar Cell. *Nano Res.* **2018**, *11* (12), 6283–6293.
- (119) Johansson, M. B.; Zhu, H.; Johansson, E. M. J. Extended Photo-Conversion Spectrum in Low-Toxic Bismuth Halide Perovskite Solar Cells. *J. Phys. Chem. Lett.* **2016**, *7* (17), 3467–3471.
- (120) Lian, L.; Zheng, M.; Zhang, P.; Zheng, Z.; Du, K.; Lei, W.; Gao, J.; Niu, G.; Zhang, D.; Zhai, T.; Jin, S.; Tang, J.; Zhang, X.; Zhang, J. Photophysics in Cs₃Cu₂X₅ (X=Cl, Br, I): Highly Luminescent Self-Trapped Excitons from Local Structure Symmetrization. *Chem. Mater.* **2020**, *32* (8), 3462–3468.
- (121) Li, Q.; Chen, Z.; Yang, B.; Tan, L.; Xu, B.; Han, J.; Zhao, Y.; Tang, J.; Quan, Z. Pressure-Induced Remarkable Enhancement of Self-Trapped Exciton Emission in One-Dimensional CsCu₂I₃ with Tetrahedral Units. *J. Am. Chem. Soc.* **2020**, *142* (4), 1786–1791.
- (122) Qi, H.; Wang, S.; Jiang, X.; Fang, Y.; Wang, A.; Shen, H.; Du, Z. Research Progress and Challenges of Blue Light-Emitting Diodes Based on II–VI Semiconductor Quantum Dots. *J. Mater. Chem. C* **2020**, *8* (30), 10160–10173.
- (123) Feezell, D.; Nakamura, S. Invention, Development, and Status of the Blue Light-Emitting Diode, the Enabler of Solid-State Lighting. *Comptes Rendus Phys.* **2018**, *19* (3), 113–133.
- (124) Palazon, F.; Pérez-del-Rey, D.; Dänekamp, B.; Dreessen, C.; Sessolo, M.; Boix, P. P.; Bolink, H. J. Room-Temperature Cubic Phase Crystallization and High Stability of Vacuum-Deposited Methylammonium Lead Triiodide Thin Films for High-Efficiency Solar Cells. *Adv. Mater.* **2019**, *1902692*, 1–6.
- (125) Jeevaraj, M.; Sudhakar, S.; Kumar, M. K. Evolution of Stability Enhancement in Organometallic Halide Perovskite Photovoltaics-a Review. *Mater. Today Commun.* **2021**, *27*, 102159.
- (126) Xiang, W.; Liu, S.; Tress, W. A Review on the Stability of Inorganic Metal Halide Perovskites: Challenges and Opportunities for Stable Solar Cells. *Energy Environ. Sci.* **2021**, *14* (4), 2090–2113.
- (127) Li, J.; Cao, H. L.; Jiao, W. Bin; Wang, Q.; Wei, M.; Cantone, I.; Lü, J.; Abate, A. Biological Impact of Lead from Halide Perovskites Reveals the Risk of Introducing a Safe Threshold. *Nat. Commun.* **2020**, *11*, 310.

- (128) Slavney, A. H.; Hu, T.; Lindenberg, A. M.; Karunadasa, H. I. A Bismuth-Halide Double Perovskite with Long Carrier Recombination Lifetime for Photovoltaic Applications. *J. Am. Chem. Soc.* **2016**, *138* (7), 2138–2141.
- (129) Tang, H.; Xu, Y.; Hu, X.; Hu, Q.; Chen, T.; Jiang, W.; Wang, L.; Jiang, W. Lead-Free Halide Double Perovskite Nanocrystals for Light-Emitting Applications: Strategies for Boosting Efficiency and Stability. *Adv. Sci.* **2021**, 2004118.
- (130) Adjogri, S. J.; Meyer, E. L. A Review on Lead-Free Hybrid Halide Perovskites as Light Absorbers for Photovoltaic Applications Based on Their Structural, Optical, and Morphological Properties. *Molecules* **2020**, *25* (21), 5039.
- (131) Yang, X.; Chen, Y.; Liu, P.; Xiang, H.; Wang, W.; Ran, R.; Zhou, W.; Shao, Z. Simultaneous Power Conversion Efficiency and Stability Enhancement of Cs₂AgBiBr₆ Lead-Free Inorganic Perovskite Solar Cell through Adopting a Multifunctional Dye Interlayer. *Adv. Funct. Mater.* **2020**, *30* (23), 2001557.
- (132) Longo, G.; Mahesh, S.; Buizza, L. R. V.; Wright, A. D.; Ramadan, A. J.; Abdi-jalebi, M.; Nayak, P. K.; Herz, L. M.; Snaith, H. J. Understanding the Performance-Limiting Factors of Cs₂AgBiBr₆ Double-Perovskite Solar Cells. *ACS Energy Lett.* **2020**, *5*, 2200–2207.
- (133) Slavney, A. H.; Leppert, L.; Bartesaghi, D.; Gold-Parker, A.; Toney, M. F.; Savenije, T. J.; Neaton, J. B.; Karunadasa, H. I. Defect-Induced Band-Edge Reconstruction of a Bismuth-Halide Double Perovskite for Visible-Light Absorption. *J. Am. Chem. Soc.* **2017**, *139* (14), 5015–5018.
- (134) Lindquist, K. P.; Mack, S. A.; Slavney, A. H.; Leppert, L.; Gold-Parker, A.; Stebbins, J. F.; Salleo, A.; Toney, M. F.; Neaton, J. B.; Karunadasa, H. I. Tuning the Bandgap of Cs₂AgBiBr₆ through Dilute Tin Alloying. *Chem. Sci.* **2019**, *10* (45), 10620–10628.
- (135) Du, K. Z.; Meng, W.; Wang, X.; Yan, Y.; Mitzi, D. B. Bandgap Engineering of Lead-Free Double Perovskite Cs₂AgBiBr₆ through Trivalent Metal Alloying. *Angew. Chemie - Int. Ed.* **2017**, *56* (28), 8158–8162.
- (136) Yang, J.; Zhang, P.; Wei, S. H. Band Structure Engineering of Cs₂AgBiBr₆ Perovskite through Order-Disordered Transition: A First-Principle Study. *J. Phys. Chem. Lett.* **2018**, *9* (1), 31–35.
- (137) Rodkey, N.; Kaal, S.; Sebastia-Luna, P.; Birkhölzer, Y. A.; Ledinsky, M.; Palazon, F.; Bolink, H. J.; Morales-Masis, M. Pulsed Laser Deposition of Cs₂AgBiBr₆: From Mechanochemically Synthesized Powders to Dry, Single-Step Deposition. *Chem. Mater.* **2021**, *33* (18), 7417–7422.
- (138) Jain, A.; Ong, S. P.; Hautier, G.; Chen, W.; Richards, W. D.; Dacek, S.; Cholia, S.; Gunter, D.; Skinner, D.; Ceder, G.; Persson, K. A. Commentary: The Materials Project: A Materials Genome Approach to Accelerating Materials Innovation. *APL Mater.* **2013**, *1* (1).
- (139) Blum, V.; Gehrke, R.; Hanke, F.; Havu, P.; Havu, V.; Ren, X.; Reuter, K.; Scheffler, M. Ab Initio Molecular Simulations with Numeric Atom-Centered Orbitals. *Comput. Phys. Commun.* **2009**, *180* (11), 2175–2196.

- (140) Momma, K.; Izumi, F. VESTA 3 for Three-Dimensional Visualization of Crystal, Volumetric and Morphology Data. *J. Appl. Crystallogr.* **2011**, *44* (6), 1272–1276.
- (141) Smith, M. D.; Connor, B. A.; Karunadasa, H. I. Tuning the Luminescence of Layered Halide Perovskites. *Chem. Rev.* **2019**, *119* (5), 3104–3139.
- (142) Jiang, Y.; Li, K.; Wu, X.; Zhu, M.; Zhang, H.; Zhang, K.; Wang, Y.; Loh, K. P.; Shi, Y.; Xu, Q.-H. In Situ Synthesis of Lead-Free Halide Perovskite Cs₂AgBiBr₆ Supported on Nitrogen-Doped Carbon for Efficient Hydrogen Evolution in Aqueous HBr Solution. *ACS Appl. Mater. Interfaces* **2021**, *13* (8), 10037–10046.
- (143) Ghasemi, M.; Zhang, L.; Yun, J. H.; Hao, M.; He, D.; Chen, P.; Bai, Y.; Lin, T.; Xiao, M.; Du, A.; Lyu, M.; Wang, L. Dual-Ion-Diffusion Induced Degradation in Lead-Free Cs₂AgBiBr₆ Double Perovskite Solar Cells. *Adv. Funct. Mater.* **2020**, 2002342.
- (144) Ji, F.; Klarbring, J.; Wang, F.; Ning, W.; Wang, L.; Yin, C.; Figueroa, J. S. M.; Christensen, C. K.; Etter, M.; Ederth, T.; Sun, L.; Simak, S. I.; Abrikosov, I. A.; Gao, F. Lead-Free Halide Double Perovskite Cs₂AgBiBr₆ with Decreased Band Gap. *Angew. Chemie Int. Ed.* **2020**, *59*, 1–5.
- (145) Kleibecker, J. E.; Choi, E.-M.; Jones, E. D.; Yu, T.-M.; Sala, B.; MacLaren, B. A.; Kepaptsoglou, D.; Hernandez-Maldonado, D.; Ramasse, Q. M.; Jones, L.; Barthel, J.; MacLaren, I.; MacManus-Driscoll, J. L. Route to Achieving Perfect B-Site Ordering in Double Perovskite Thin Films. *NPG Asia Mater.* **2017**, *9*, e406.
- (146) Ma, X.; Li, Z.; Yang, J. Efficient Direct Band Gap Photovoltaic Material Predicted Via Doping Double Perovskites Cs₂AgBiX₆ (X = Cl, Br). *J. Phys. Chem. C* **2021**, *125* (20), 10868–10875.
- (147) Xiao, Z.; Meng, W.; Wang, J.; Mitzi, D. B.; Yan, Y. Searching for Promising New Perovskite-Based Photovoltaic Absorbers: The Importance of Electronic Dimensionality. *Mater. Horizons* **2017**, *4* (2), 206–216.
- (148) Sebastia-Luna, P.; Navarro-Alapont, J.; Sessolo, M.; Palazon, F.; Bolink, H. J. Solvent-Free Synthesis and Thin-Film Deposition of Cesium Copper Halides with Bright Blue Photoluminescence. *Chem. Mater.* **2019**, *31* (24), 10205–10210.
- (149) Crane, M. J.; Kroupa, D. M.; Roh, J. Y.; Anderson, R. T.; Smith, M. D.; Gamelin, D. R. Single-Source Vapor Deposition of Quantum-Cutting Yb³⁺:CsPb(Cl_{1-x}Br_x)₃ and Other Complex Metal-Halide Perovskites. *ACS Appl. Energy Mater.* **2019**, *2* (6), 4560–4565.
- (150) Pantaler, M.; Fettkenhauer, C.; Nguyen, H. L.; Anusca, I.; Lupascu, D. C. Deposition Routes of Cs₂AgBiBr₆ Double Perovskites for Photovoltaic Applications. *MRS Adv.* **2018**, *3* (32), 1819–1823.
- (151) Yang, B.; Chen, J.; Hong, F.; Mao, X.; Zheng, K.; Yang, S.; Li, Y.; Pullerits, T.; Deng, W.; Han, K. Lead-Free, Air-Stable All-Inorganic Cesium Bismuth Halide Perovskite Nanocrystals. *Angew. Chemie* **2017**, *129*, 12645–12649.
- (152) Steele, J. A.; Puech, P.; Keshavarz, M.; Yang, R.; Banerjee, S.; Debroye, E.; Kim, C. W.; Yuan, H.; Heo, N. H.; Vanacken, J.; Walsh, A.; Hofkens, J.; Roeffaers, M. B. J. Giant Electron-

Phonon Coupling and Deep Conduction Band Resonance in Metal Halide Double Perovskite. *ACS Nano* **2018**, *12* (8), 8081–8090.

(153) Pantaler, M.; Cho, K. T.; Queloz, V. I. E.; Benito, I. G.; Fettkenhauer, C.; Anusca, I.; Nazeeruddin, M. K.; Lupascu, D. C.; Grancini, G. Hysteresis-Free Lead-Free Double-Perovskite Solar Cells by Interface Engineering. *ACS Energy Lett.* **2018**, *3* (8), 1781–1786.

(154) Pisoni, A.; Jaćimović, J.; Barišić, O. S.; Spina, M.; Gaál, R.; Forró, L.; Horváth, E. Ultra-Low Thermal Conductivity in Organic-Inorganic Hybrid Perovskite $\text{CH}_3\text{NH}_3\text{PbI}_3$. *J. Phys. Chem. Lett.* **2014**, *5*, 2488–2492.

(155) Zheng, L.; Zhu, T.; Li, Y.; Wu, H.; Yi, C.; Zhu, J.; Gong, X. Enhanced Thermoelectric Performance of F_4 -TCNQ Doped FASnI_3 Thin Films. *J. Mater. Chem. A* **2020**, *8*, 25431–25442.

(156) Qian, F.; Hu, M.; Gong, J.; Ge, C.; Zhou, Y.; Guo, J.; Chen, M.; Ge, Z.; Padture, N. P.; Zhou, Y.; Feng, J. Enhanced Thermoelectric Performance in Lead-Free Inorganic $\text{CsSn}_{1-x}\text{Ge}_x\text{I}_3$ Perovskite Semiconductors. *J. Phys. Chem. C* **2020**, *124* (22), 11749–11753.

(157) Vesborg, P. C. K.; Jaramillo, T. F. Addressing the Terawatt Challenge: Scalability in the Supply of Chemical Elements for Renewable Energy. *RSC Adv.* **2012**, *2* (21), 7933–7947.

(158) Aaseth, J.; Nurchi, V. M.; Andersen, O. Medical Therapy of Patients Contaminated with Radioactive Cesium or Iodine. *Biomolecules* **2019**, *9* (12), 856.

(159) Chung, I.; Song, J.-H.; Im, J.; Androulakis, J.; Malliakas, C. D.; Li, H.; Freeman, A. J.; Kenney, J. T.; Kanatzidis, M. G. CsSnI_3 : Semiconductor or Metal? High Electrical Conductivity and Strong Near-Infrared Photoluminescence from a Single Material. High Hole Mobility and Phase-Transitions. *J. Am. Chem. Soc.* **2012**, *134*, 8579–8587.

(160) Kontos, A. G.; Kaltzoglou, A.; Siranidi, E.; Palles, D.; Angeli, G. K.; Arfanis, M. K.; Psycharis, V.; Raptis, Y. S.; Kamitsos, E. I.; Trikalitis, P. N.; Stoumpos, C. C.; Kanatzidis, M. G.; Falaras, P. Structural Stability, Vibrational Properties, and Photoluminescence in CsSnI_3 Perovskite upon the Addition of SnF_2 . *Inorg. Chem.* **2017**, *56*, 84–91.

(161) Qiu, X.; Cao, B.; Yuan, S.; Chen, X.; Qiu, Z.; Jiang, Y.; Ye, Q.; Wang, H.; Zeng, H.; Liu, J.; Kanatzidis, M. G. From Unstable CsSnI_3 to Air-Stable Cs_2SnI_6 : A Lead-Free Perovskite Solar Cell Light Absorber with Bandgap of 1.48 eV and High Absorption Coefficient. *Sol. Energy Mater. Sol. Cells* **2017**, *159*, 227–234.

(162) Saini, S.; Baranwal, A. K.; Yabuki, T.; Hayase, S.; Miyazaki, K. Growth of Halide Perovskites Thin Films for Thermoelectric Applications. *MRS Adv.* **2019**, *4*, 1719–1725.

(163) Liu, T.; Zhao, X.; Li, J.; Liu, Z.; Liscio, F.; Milita, S.; Schroeder, B. C.; Fenwick, O. Enhanced Control of Self-Doping in Halide Perovskites for Improved Thermoelectric Performance. *Nat. Commun.* **2019**, *10* (1), 1–9.

(164) Xie, H.; Hao, S.; Bao, J.; Slade, T. J.; Snyder, G. J.; Wolverton, C.; Kanatzidis, M. G. All-Inorganic Halide Perovskites as Potential Thermoelectric Materials: Dynamic Cation off-Centering Induces Ultralow Thermal Conductivity. *J. Am. Chem. Soc.* **2020**, *142* (20), 9553–9563.

- (165) Gil-Escrig, L.; Momblona, C.; Forgács, D.; Pla, S.; Fernández-Lázaro, F.; Sessolo, M.; Sastre-Santos, Á.; Bolink, H. J. Interface Engineering in Efficient Vacuum Deposited Perovskite Solar Cells. *Org. Electron.* **2016**, *37*, 396–401.
- (166) Liu, J.; Qiu, L.; Portale, G.; Koopmans, M.; ten Brink, G.; Hummelen, J. C.; Koster, L. J. A. n-Type Organic Thermoelectrics: Improved Power Factor by Tailoring Host-Dopant Miscibility. *Adv. Mater.* **2017**, *29* (36), 1701641.
- (167) Chen, M.; Ju, M. G.; Garces, H. F.; Carl, A. D.; Ono, L. K.; Hawash, Z.; Zhang, Y.; Shen, T.; Qi, Y.; Grimm, R. L.; Pacifici, D.; Zeng, X. C.; Zhou, Y.; Padture, N. P. Highly Stable and Efficient All-Inorganic Lead-Free Perovskite Solar Cells with Native-Oxide Passivation. *Nat. Commun.* **2019**, *10* (16), 1–8.
- (168) Li, J.; Yu, Q.; He, Y.; Stoumpos, C. C.; Niu, G.; Trimarchi, G. G.; Guo, H.; Dong, G.; Wang, D.; Wang, L.; Kanatzidis, M. G. Cs₂PbI₂Cl₂, All-Inorganic Two-Dimensional Ruddlesden-Popper Mixed Halide Perovskite with Optoelectronic Response. *J. Am. Chem. Soc.* **2018**, *140*, 11085–11090.
- (169) Yang, J.-H.; Yuan, Q.; Yakobson, B. I. Chemical Trends of Electronic Properties of Two-Dimensional Halide Perovskites and Their Potential Applications for Electronics and Optoelectronics. *J. Phys. Chem. C* **2016**, *120*, 24682–24687.
- (170) Bala, A.; Deb, A. K.; Kumar, V. Atomic and Electronic Structure of Two-Dimensional Inorganic Halide Perovskites A_{n+1}M_nX_{3n+1} (n = 1–6, A = Cs, M = Pb and Sn, and X = Cl, Br, and I) from Ab Initio Calculations. *J. Phys. Chem. C* **2018**, *122*, 7464–7473.
- (171) Zhang, J.; Yu, C.; Wang, L.; Li, Y.; Ren, Y.; Shum, K. Energy Barrier at the N719-Dye/CsSnI₃ Interface for Photogenerated Holes in Dye-Sensitized Solar Cells. *Sci. Rep.* **2014**, *4*, 6954.
- (172) Kong, Q.; Lee, W.; Lai, M.; Bischak, C. G.; Gao, G.; Wong, A. B.; Lei, T.; Yu, Y.; Wang, L.-W.; Ginsberg, N. S.; Yang, P. Phase-Transition-Induced p-n Junction in Single Halide Perovskite Nanowire. *Proc. Natl. Acad. Sci.* **2018**, *115* (36), 8889–8894.
- (173) Ye, T.; Wang, K.; Hou, Y.; Yang, D.; Smith, N.; Magill, B.; Yoon, J.; Mudiyansele, R. R. H. H.; Khodaparast, G. A.; Wang, K.; Priya, S. Ambient-Air-Stable Lead-Free CsSnI₃ Solar Cells with Greater than 7.5% Efficiency. *J. Am. Chem. Soc.* **2021**, *143*, 4319–4328.
- (174) Hong, W.-L.; Huang, Y.-C.; Chang, C.-Y.; Zhang, Z.-C.; Tsai, H.-R.; Chang, N.-Y.; Chao, Y.-C. Efficient Low-Temperature Solution-Processed Lead-Free Perovskite Infrared Light-Emitting Diodes. *Adv. Mater.* **2016**, *28*, 8029–8036.
- (175) Stoumpos, C. C.; Malliakas, C. D.; Kanatzidis, M. G. Semiconducting Tin and Lead Iodide Perovskites with Organic Cations: Phase Transitions, High Mobilities, and near-Infrared Photoluminescent Properties. *Inorg. Chem.* **2013**, *52* (15), 9019–9038.
- (176) Takahashi, Y.; Hasegawa, H.; Takahashi, Y.; Inabe, T. Hall Mobility in Tin Iodide Perovskite CH₃NH₃SnI₃: Evidence for a Doped Semiconductor. *J. Solid State Chem.* **2013**, *205*, 39–43.

- (177) Ye, T.; Wang, X.; Li, X.; Yan, A. Q.; Ramakrishna, S.; Xu, J. Ultra-High Seebeck Coefficient and Low Thermal Conductivity of a Centimeter-Sized Perovskite Single Crystal Acquired by a Modified Fast Growth Method. *J. Mater. Chem. C* **2017**, *5*, 1255–1260.
- (178) Zhao, L. D.; Lo, S. H.; Zhang, Y.; Sun, H.; Tan, G.; Uher, C.; Wolverton, C.; Dravid, V. P.; Kanatzidis, M. G. Ultralow Thermal Conductivity and High Thermoelectric Figure of Merit in SnSe Crystals. *Nature* **2014**, *508*, 373–377.
- (179) Lee, W.; Li, H.; Wong, A. B.; Zhang, D.; Lai, M.; Yu, Y.; Kong, Q.; Lin, E.; Urban, J. J.; Grossman, J. C.; Yang, P. Ultralow Thermal Conductivity in All-Inorganic Halide Perovskites. *Proc. Natl. Acad. Sci. U. S. A.* **2017**, *114* (33), 8693–8697.
- (180) López-Fraguas, E.; Masi, S.; Mora-Seró, I. Optical Characterization of Lead-Free Cs₂SnI₆ Double Perovskite Fabricated from Degraded and Reconstructed CsSnI₃ Films. *ACS Appl. Energy Mater.* **2019**, *2* (12), 8381–8387.
- (181) Guo, F.; Lu, Z.; Mohanty, D.; Wang, T.; Bhat, I. B.; Zhang, S.; Shi, S.; Washington, M. A.; Wang, G. C.; Lu, T. M. A Two-Step Dry Process for Cs₂SnI₆ Perovskite Thin Film. *Mater. Res. Lett.* **2017**, *5* (8), 540–546.
- (182) Bhui, A.; Ghosh, T.; Pal, K.; Singh Rana, K.; Kundu, K.; Soni, A.; Biswas, K. Intrinsically Low Thermal Conductivity in the n-Type Vacancy-Ordered Double Perovskite Cs₂SnI₆: Octahedral Rotation and Anharmonic Rattling. *Chem. Mater.* **2022**, *34* (7), 3301–3310.
- (183) Koyanagi, T.; Kapil, G.; Ogomi, Y.; Yoshino, K.; Shen, Q.; Toyoda, T.; Murakami, T. N.; Segawa, H.; Hayase, S. Hot-Injection and Ultrasonic Irradiation Syntheses of Cs₂SnI₆ Quantum Dot Using Sn Long-Chain Amino-Complex. *J. Nanoparticle Res.* **2020**, *22*, 69.
- (184) Lee, B.; Shin, B.; Park, B. Uniform Cs₂SnI₆ Thin Films for Lead-Free and Stable Perovskite Optoelectronics via Hybrid Deposition Approaches. *Electron. Mater. Lett.* **2019**, *15*, 192–200.
- (185) Qiu, X.; Jiang, Y.; Zhang, H.; Qiu, Z.; Yuan, S.; Wang, P.; Cao, B. Lead-Free Mesoscopic Cs₂SnI₆ Perovskite Solar Cells Using Different Nanostructured ZnO Nanorods as Electron Transport Layers. *Phys. Status Solidi RRL* **2016**, *10* (8), 587–591.
- (186) Xiao, Z.; Zhou, Y.; Hosono, H.; Kamiya, T. Intrinsic Defects in a Photovoltaic Perovskite Variant Cs₂SnI₆. *Phys. Chem. Chem. Phys.* **2015**, *17*, 18900–18903.

Appendix E

List of Abbreviations

BE	Binding Energy
BM	Ball Milling
BSE	Backscattered Electrons
CIGS	Copper Indium Gallium Selenide
CZTS	Copper Zinc Tin Sulfide
DMF	Dimethyl Formamide
DMSO	Dimethyl Sulfoxide
DP	Double Perovskite
EDX	Energy-dispersive X-Ray
EIL	Electron Injection Layer
EQE	External Quantum Efficiency
ETL	Electron-Transport Layer
EU	European Union
HIL	Hole Injection Layer
HOMO	Highest Occupied Molecular Orbital
HTL	Hole-Transport Layer
ICSD	Inorganic Crystal Structure Database
ICMol	Instituto de Ciencia Molecular
IoT	Internet of Things
ITO	Indium Tin Oxide
KE	Kinetic Energy
LED	Light-Emitting Diode
LHP	Lead Halide Perovskite
LUMO	Lowest Unoccupied Molecular Orbital
MCS	Mechanochemical Synthesis
MMH	Multinary Metal Halide
NIR	Near Infrared
OEG	Oligoethylene–glycol
OLED	Organic Light-Emitting Diode
PCE	Power Conversion Efficiency
PEDOT	Poly(3,4-ethylenedioxythiophene)
PeLED	Perovskite Light Emitting Diode
PL	Photoluminescence
PLD	Pulsed Laser Deposition

PLE	Photoluminescence Excitation
PLQY	Photoluminescence Quantum Yield
QLED	Quantum Light-Emitting Diode
SE	Secondary Electrons
SEM	Scanning Electron Microscopy
SSVD	Single-source Vacuum Deposition
STE	Self-Trapped Exciton
TCO	Transparent Conductive Oxide
TE	Thermoelectric
TEG	Thermoelectric Generator
TGA	Thermogravimetric Analysis
UE	Unió Europea
UV-Vis	Ultraviolet-Visible
WPPD	Whole Powder Pattern Decompositions
XPS	X-Ray Photoelectron Spectroscopy
XRD	X-Ray Diffraction

Appendix F

Index of Figures, Tables and Equations

Index of Figures

Figure 1.1. Device architecture and working mechanism of (a) an organic LED (OLED) and (b) inorganic LED. Illustrations are adapted from literature.¹⁸

Figure 1.2. Basic working mechanism of a solar cell. (1) Generation of an electron and a hole upon the absorption of a photon. (2) A potential loss mechanism occurs when electrons and holes recombine. However, it is unlikely in efficient solar cells (3) Diffusion and drift of electrons and holes through the charge selective layers. (4) Extracted electrons travel through an external circuit generating a current. (5) Electrons that have passed through the circuit recombine with holes. Illustration adapted from literature.²⁶

Figure 1.3. Schematic diagram of (a) planar n-i-p and (b) planar p-i-n solar cell architectures (not to scale). Yellow arrows indicate the direction of the sunlight.

Figure 1.4. Schematic diagram of a thermoelectric device. Illustration adapted from literature.³²

Figure 1.5. Illustration of an n-type semiconductor subjected to a temperature difference to show how electrons diffuse from the hot side to the cold side. Illustration adapted from literature.³³

Figure 1.6. Illustration of the compromise between Seebeck coefficient, electrical conductivity, thermal conductivity and thermal conductivity to achieve a high ZT. Illustration adapted from literature.³⁴

Figure 1.7. Schematic structure of ABX₃ perovskite.

Figure 1.8. Efficiency chart of the most common photovoltaic technologies over the last decades. Illustration taken from literature.⁴¹

Figure 2.1. (a) 10 mL zirconia ball mill jar with two 10 mm zirconia beads and Teflon O-ring. (b) Mixer Mill MM-400 from Retsch. Picture taken from reference.⁶⁶

Figure 2.2. Schematic diagram of spin coating technique.

Figure 2.3. Basic components of the evaporator used for SSVD.

Figure 2.4. Schematic diagram of diffraction of X-rays according to Bragg's law. The illustration is adapted from reference.⁷¹

Figure 2.5. (a) Schematic diagram of the photoemission process that takes place in XPS. The illustration is adapted from reference.⁷⁴ (b) Schematic representation on how emitted

electrons interact with the sample depending on how deep they are generated. The illustration is adapted from reference.⁷³

Figure 2.6. Schematic diagram of (a) integrating sphere and (b) transmission setup used for UV-Vis absorbance.

Figure 2.7. Jablonski diagram of fluorescence showing the radiative and non-radiative processes that can take place after the photon absorption.

Figure 2.8. Schematic diagram of a measurement chip where the material has been deposited as thin film (grey area) and electrodes are labelled. The illustration is adapted from reference.⁸¹

Figure 2.9. Configuration of the measurement chip for a Seebeck coefficient measurement. The illustration is adapted from reference.⁸¹

Figure 2.10. Layout of the measurement chip for the Hall coefficient calculation. The illustration is adapted from reference.⁸¹

Figure 3.1. Crystal structures of $\text{Cs}_3\text{Cu}_2\text{Br}_5$ (left) and CsCu_2Br_3 (right), created with VESTA software based on crystallographic information files obtained in the Inorganic Crystal Structure Database (refs: 150297 and 49613). Green balls represent Cs^+ ions and blue polygons represent CuBr_4 tetrahedra.

Figure 3.2. (a) XRD data (open circles) and fits (solid-colored lines) of different CsCu_2X_3 compounds. (b) Unit cell volume as derived from fits.

Figure 3.3. Thermogravimetric analysis (TGA) of the pure-halide CsCu_2X_3 compounds.

Figure 3.4. (a) XRD data (open circles) and fit (solid-colored lines) of different $\text{Cs}_3\text{Cu}_2\text{X}_5$ compounds. (b) Unit cell volume as derived from the fit.

Figure 3.5. Comparison of the colour of the powders for $\text{Cs}_3\text{Cu}_2\text{X}_5$ when they are kept inside a nitrogen filled glovebox (up) and when they are exposed to air and moisture for 24 h (down).

Figure 3.6. XRD of the as-prepared powders from ball milling synthesis for pure-halide $\text{Cs}_3\text{Cu}_2\text{X}_5$ compounds. Non-exposed to air powders are presented with a straight line and the exposed ones, with a dashed line.

Figure 3.7. Thermogravimetric analysis (TGA) of the pure-halide $\text{Cs}_3\text{Cu}_2\text{X}_5$ compounds when they are kept inside a nitrogen filled glovebox. A special zoom is presented in the zone of first weight loss for chloride compound, which could correspond with the formation of Cu_2O .

Figure 3.8. (a) Scheme of Jahn-Teller distortion on ground state and excited state of Cu(I)- d^{10} and Cu(II)- d^9 , respectively. Structure distortion for a generic ML_4 tetrahedral is shown. (b) Diagram for the STE formation on $Cs_3Cu_2X_5$. Pictures have been extracted from literature.⁸⁹

Figure 3.9. PLE (left) and PL (right) spectra of different $Cs_3Cu_2X_5$. X given in the legend. For $Cs_3Cu_2(Cl_{0.75}Br_{0.25})_5$ excitation spectrum corresponding to 516 nm emission and corresponding emission spectrum are presented as dashed lines, whereas excitation spectrum corresponding to emission at 450 nm and corresponding emission spectrum are presented as solid lines.

Figure 3.10. Characterization of SSVD $Cs_3Cu_2I_5$ thin film. (a) X-ray diffractogram with Le Bail fit in green. For an easy comparison, data and fit from bulk powder (see Figure 3.4) is reproduced here in red. (b) Scanning electron microscopy image. Scale bar is 1 micron (see lower magnifications in Figure S30). (c) Photoluminescence excitation and emission spectra in green. For an easy comparison, data from bulk powder (see Figure 3.9) is reproduced here in red.

Figure 4.1. Comparison between the cubic structures of a perovskite $AB^{2+}X_3$ (a) and a double perovskite $A_2B^+B^{3+}X_6$ (b).

Figure 4.2. XRD diffractograms of $Cs_2AgBiBr_6$ samples after post-synthesis annealing at different temperatures (a), and UV-Vis absorption onset to estimate the bandgap (b).

Figure 4.3. (a) XRD diffractograms of $Cs_2AgBiBr_6$ samples ball-milled during 1 h and 5 h. (b) UV-Vis absorption onset to estimate the bandgap.

Figure 4.4. UV-Vis absorption onset to estimate the bandgap of $SnBr_2$ - (a), $GeBr_2$ - (b), and $ZnBr_2$ - (c) doped double perovskite. Panels (d, e, f) show the Tauc plot considering a direct allowed transition for the aforementioned dopants, respectively. The estimated bandgaps for the pristine and 15%-doped species are given.

Figure 4.5. Cells with “neighboring” and “separated” B-cation substitutions in the double perovskite $Cs_2Ag_{(1-a)}Bi_{(1-a)}X_{2a}Br_6$ where X = Sn, Ge, Zn and $a = \frac{1}{8}$. Color coding: Cs in light green, Bi in dark blue (coordination octahedra are not shown for clarity), Br in brown, substituted B-cation octahedra in dark gray, and Ag-cation octahedra in light gray.

Figure 4.6. Atom-projected density of states calculated for the supercell of $Cs_2AgBiBr_6$ and its doped analogues. The bandgap is indicated in eV.

Figure 4.7. XRD diffractogram (a) and absorbance (b) of SSVD thin film (TF) as-deposited $\text{Cs}_2\text{AgBiBr}_6$ (without annealing), showing a predominance of $\text{Cs}_3\text{Bi}_2\text{Br}_9$ phase. More details in the main text.

Figure 4.8. (a) XRD diffractograms of SSVD thin films of pristine and Sn-doped $\text{Cs}_2\text{AgBiBr}_6$ samples after annealing at 250 °C. Red asterisks indicate the interfering peaks from the Al platform of the XRD setup. “BM DPp” refers to the deposition of pure ball-milled $\text{Cs}_2\text{AgBiBr}_6$; “BM DP:15% SnBr_2 ” to ball-milled doped $\text{Cs}_2\text{AgBiBr}_6$:15% SnBr_2 ; “BM DPp+15% SnBr_2 ” to pure ball-milled $\text{Cs}_2\text{AgBiBr}_6$ with an extra 15% of SnBr_2 added and manually mixed in the crucible; “BM DPp+100% SnBr_2 ” to pure ball-milled $\text{Cs}_2\text{AgBiBr}_6$ with an extra 100% of SnBr_2 added and manually mixed in the crucible. (b) Tauc plot of post-annealed Sn-doped thin-films considering a direct allowed transition. (c) SEM images of pristine DP thin-films at room temperature and (d) annealed at 250 °C (scale 1 μm).

Figure 5.1. (a) XRD diffractograms and (b) absorbance (solid lines) and photoluminescence (dashed line) spectra of SSVD thin-films as-deposited and annealed for 25 min at 150 °C. Panel (a) shows the ICSD pattern for black beta phase of CsSnI_3 (code 262925) and the predicted main crystalline structure for both films. Predicted XRD planes of as-deposited thin-films were obtained from the fit presented in Figure S2.

Figure 5.2. XRD diffractograms of (a) in-situ annealing of Cs_2SnI_4 thin films up to 150 °C and (b) effect of the annealing time at 150 °C until it is fully converted into the black beta phase of CsSnI_3 .

Figure 5.3. (a) Temperature dependence of electrical conductivity, σ (black line), thermal conductivity, κ (red line), Seebeck coefficient, S (green line) and figure-of-merit, ZT (blue line) of B- β CsSnI_3 . (b) Temperature dependence of Hall coefficient (black line), charge carrier concentration of the bulk, n (red line) and charge mobility (green line) of B- β CsSnI_3 . Errors bars come from measurement of film thickness and the deviation of the equipment (see Experimental Section). ZT and charge mobility error bars are originated from the combination of these errors.

Figure 5.4. XRD diffractograms of the evolution of Cs_2SnI_6 thin films exposed to (a) air and (b) N_2 for 1 week. Red asterisk stands for the main XRD peak of CsI , a by-product of the degradation. (c) UV-Vis absorbance spectrum of Cs_2SnI_6 . (d) Temperature dependence of electrical conductivity, σ (black line), thermal conductivity, κ (red line), Seebeck coefficient,

S (green line) and figure-of-merit, ZT (blue line) of Cs_2SnI_6 thin films. See error bar calculation in Figure 5.3a.

Figure 5.5. SEM images of Cs_2SnI_4 , B- β CsSnI_3 and Cs_2SnI_6 thin films at 10,000x magnification. Insets with the appearance of each thin film are included.

Index of Tables

Table 1.1. Summary of relevant properties that a material (or thin film) should meet for different applications. “Yes” implies that the property is important for the given application.

Table 3.2. Lattice parameters derived from Le Bail fits of CsCu_2X_3 compounds (space group = $Cmcm$). Please note that the results are expressed without taking into account the number of significant digits.

Table 3.2. Lattice parameters derived from Le Bail fits of $\text{Cs}_3\text{Cu}_2\text{X}_5$ compounds (space group = $Pnma$ for all compounds except for $\text{Cs}_3\text{Cu}_2\text{X}_5$ for which $Cmcm$ is assumed).

Table 3.3. PLQY and λ_{em} for $\text{Cs}_3\text{Cu}_2\text{X}_5$ compounds freshly prepared, exposed to air for 24 h, and thermally annealed. For mixed-halide compounds, as no benefit was observed for freshly prepared samples, stability in air or upon annealing was not assessed.

Table 5.1. Existing Different Phases and Structures of the Cs–Sn–I System, Their Crystal Structures, and Ambient Conditions for Each Phase Transition.^a

Table 5.2. Comparison of maximum electrical conductivity (σ_{max}), thermal conductivity (κ_{max}), Seebeck coefficient (S_{max}), and figure-of-merit ZT (ZT_{max}) for the three species studied in this work.^a

Index of Equations

Equation 1.1. Thermoelectric figure-of-merit, ZT .

Equation 1.2. Definition of electrical conductivity, σ .

Equation 1.3. Definition of charge carrier concentration, n .

Equation 1.4. Definition of charge mobility, μ .

Equation 1.5. Definition of thermal conductivity, κ .

Equation 2.1. Bragg's law.

Equation 2.2. Calculation of the binding energy, BE .

Equation 2.3. Lambert-Beer law.

Equation 2.4. Relationship between absorbance and transmittance.

Equation 2.5. Definition of Seebeck coefficient, S .

Equation 2.6. Definition of thermal conductivity, κ .

Appendix G

List of Publications

Included in this PhD thesis:

1. **Paz Sebastián-Luna**, Javier Navarro-Alapont, Michele Sessolo, Francisco Palazón*, and Henk J. Bolink. Solvent-Free Synthesis and Thin-Film Deposition of Cesium Copper Halides with Bright Blue Photoluminescence. *Chemistry of Materials*, **2019**, 31 (24), 10205–10210.
<https://doi.org/10.1021/acs.chemmater.9b03898>
2. **Paz Sebastián-Luna**, Joaquín Calbo, Nicolás Albiach-Sebastián, Michele Sessolo, Francisco Palazón, Enrique Ortí, Henk J Bolink. Tuning the Optical Absorption of Sn-, Ge-, and Zn-Substituted Cs₂AgBiBr₆ Double Perovskites: Structural and Electronic Effects. *Chemistry of Materials*, **2021**, 33 (20), 8028-8035.
<https://doi.org/10.1021/acs.chemmater.1c02236>
3. **Paz Sebastián-Luna**, Unnati Pokharel, Bas A. H. Huisman, L. Jan Anton Koster, Francisco Palazón, Henk J Bolink. Vacuum-Deposited Cesium Tin Iodide Thin Films with Tunable Thermoelectric Properties. *ACS Applied Energy Materials*, **2022**, 5 (8), 10216-10223.
<https://doi.org/10.1021/acsaem.2c01936>

Other publications:

4. Francisco Palazón, Yousra El Ajjouri, **Paz Sebastián-Luna**, Simone Lauciello, Liberato Manna, Henk J Bolink. Mechanochemical Synthesis of Inorganic Halide Perovskites: Evolution of Phase-purity, Morphology, and Photoluminescence. *Journal of Materials Chemistry C*, **2019**, 7, 11406-11410.
<https://doi.org/10.1039/C9TC03778K>
5. **Paz Sebastián-Luna**, María C Gélvez-Rueda, Chris Dreesen, Michele Sessolo, Ferdinand C Grozema, Francisco Palazón, Henk J Bolink. Potential and limitations of CsBi₃I₁₀ as a photovoltaic material. *Journal of Materials Chemistry A*, **2020**, 8 (31), 15670-15674.
<https://doi.org/10.1039/D0TA02237C>

6. Nathan Rodkey, Stan Kaal, **Paz Sebastia-Luna**, Yorick A Birkholzer, Martin Ledinsky, Francisco Palazon, Henk J Bolink, Monica Morales-Masıs. Pulsed Laser Deposition of Cs₂AgBiBr₆: from Mechanochemically Synthesized Powders to Dry, Single-Step Deposition. *Chemistry of Materials*, **2021**, 33 (18), 7417–7422.
<https://doi.org/10.1021/acs.chemmater.1c02054>
7. **Paz Sebastia-Luna**, Michele Sessolo, Francisco Palazon, Henk J Bolink. Low temperature, vacuum-processed bismuth triiodide solar cells with organic small-molecule hole transport bilayer. *Energy Technology*, **2021**, 9 (12), 2100661.
<https://doi.org/10.1002/ente.202100661>
8. Oleksandr Stroyuk, Oleksandra Raievska, **Paz Sebastia-Luna**, Bas AH Huisman, Christian Kupfer, Anastasia Barabash, Jens Hauch, Henk J Bolink, Christoph J Brabec. Highly Luminescent Transparent Cs₂Ag_xNa_{1-x}Bi_yIn_{1-y}Cl₆ Perovskite Films Produced by Single-Source Vacuum Deposition. *ACS Materials Lett.* **2023**, 5 (2), 596–602.
<https://doi.org/10.1021/acsmaterialslett.3c00034>

Acknowledgements

*“Que a veces no puedo dormir
Y mirando hacia el techo me quedo pensando
Qué lentas que pasan las horas
Qué rápido pasan los años.”*
La Oreja de Van Gogh

Posiblemente esta sea la parte que más me ha costado escribir de toda la tesis. En fin, allá vamos.

En primer lugar, me gustaría agradecer a mis dos directores de tesis, Henk Bolink y Francisco Palazón todo el apoyo que me habéis dado durante estos años. To Henk for letting me be part of his research group since I arrived at ICMol, guiding me, offering me advice from his experience and, above all, putting up with my continuous complaints about the mess in the lab (uff, how annoying I have been with this). I can only thank you for trusting me from the beginning and helping me to grow and get to where I am now. Thank you.

A Paco, mi supervisor fugado, como yo le llamo, por estar ahí día tras día, ayudándome, resolviendo todas mis dudas, por muy tontas que fuesen, y siempre darme la mejor de las respuestas y animándome a seguir. El camino no ha sido fácil pero siempre tenías palabras de ánimo para mí para seguir adelante. No sabes cuánto valoro toda la paciencia que has tenido conmigo y con todos mis continuos cambios de planes, tienes el cielo ganado por ello! Ha sido un placer haber trabajado codo a codo contigo todos estos años y haberme contagiado de tu inconformismo y ese espíritu luchador incansable por hacer avanzar la ciencia y nuestros derechos laborales. Sigue así, vas a ser un gran ejemplo para tus futur@s doctorand@s!

Otra parte fundamental de esta tesis han sido mis compañeros de grupo, tanto actuales como pasados, pero, sin lugar a duda, hay tres personas que la han hecho inmejorable: Isidora, Arghanoon y Lucía.

Isidora, mi serbia favorita, llevamos juntas en el grupo desde casi el primer día, más de cuatro años contigo que se me han pasado volando. No sé ni cómo explicar el apoyo tan grande que has sido para mí y que quiero que sigas siendo en mi vida. Me ha encantado ir contigo a prácticamente todas las conferencias; ensayar tus interminables presentaciones (creo que la del guanidinium la puedo hacer yo ya); rellenar 800 millones de papeles para extranjería y demás burocracia; contarnos nuestros dramas; rescatarte de cuasi cualquier situación (incluso de puertas automáticas) y compartir contigo todo este tiempo. Se queda pendiente ese viaje a Belgrado que tanto has mencionado! Mi hija en el grupo, como nosotras decimos, te mereces lo mejor y espero estar a tu lado para verlo! Волим те!

Arghanoon, although you can call her Argha, my gossip partner, the biggest fan of lemons and earrings, destiny brought us together as desk mates and since then you have earned a place in my heart. I admire your perseverance, your fighting spirit and your courage for having given a voice and a face to the struggle of the people of Iran, especially women. My most sincere appreciation, I will be there for whatever you need me (even if that includes

begging an embassy to give you a visa or screaming for candies at Christmas parades). I'm keeping you as a friend and can't wait to see what the future holds for you, دارم دوستت!

Lucía, posiblemente la persona más activa y entusiasta que he conocido, de verdad que sigo sin saber de dónde sacas la energía para llegar a todo y siempre con una sonrisa. Te admiro por no haber perdido la esperanza conmigo y haberme seguido propuesto planes, a pesar de que mi yo gruñón y vago decía siempre que no. Prueba de ello son las clases de pole dance y telas aéreas que nos llevamos... menudo cuadro somos, más vale que nos dediquemos a la ciencia porque en la gimnasia artística no tenemos mucho futuro... Seguiremos comentando *realities* cutres y quejándonos de todo un poco, va en nuestros genes. Tus innumerables audios cotilleando y quejándote a partes iguales me dan la vida, me encanta esta nueva Lucía en modo Destroyer. Conociéndote, conseguirás todo lo que te propongas y más. Te quiero!

Isabella, you have been the latest addition to the office and you have brought that touch of tenderness and sweetness that we needed. Lots of encouragement with your PhD! I'll miss our office so much! Chris, siempre me ha fascinado todo lo que sabes, no entiendo cómo puedes saber de absolutamente todo (aunque tú digas que no)! Ya he perdido la cuenta de todas las veces que te he preguntado dudas (y tú a mí, eh) y siempre me has dado la respuesta que buscaba. Te admiro y te deseo toda la suerte del mundo en tus siguientes pasos! Bas, the party leader by excellence and my most frequent collaborator, how can we be so unlucky to always be in charge of updating Quartzzy? I think it has become one of my worst nightmares. The materials I have spelled out for you in my own way because, according to you, "a physicist doesn't have to know about chemical things". Good thing we always got a bit of humor out of it! I will always remember you as the biggest hater of Spanish food (I'm sorry you have no culinary taste XD). Abhi, I have loved getting to know you more over the years. Always with words of encouragement and good vibes from early in the morning. Whenever you want, we'll do the happy dance and fist bump again! "La tía rosa" wishes you all the best!

Oh Nathan, I think I have loved and hated you in equal parts over the years. Even though I had a hard time understanding you at first (and still do), I have laughed a lot with you and your crazy ideas. When I thought you couldn't surprise us anymore, you still did: your haircuts, your obsession for climbing everything around you, all the junk you put in the GB F, the odyssey with the posters in Boston in short, I don't know how you are still alive! If I were you, I would start writing the thesis now, if you take as long as with the draft of the antiperovskite... you won't be on time!

Mención especial también a Lidón y Kassio, dos de las personas más trabajadoras del grupo. Os agradezco todo lo que me habéis enseñado en el grupo y los buenos momentos juntos. Creo que incluso echaré de menos llevar los residuos y los interminables repartos de evaporadoras. Bueno, en verdad no, pero a vosotros muchísimo! Cristina, cada vez que me acuerdo lo bien que me lo pasé contigo en la sesión de posters de Boston, me río como el primer día. Se nos quedan pendientes unos bailes en la feria de Córdoba! Fede, tu alegría y buen rollo son contagiosos! Siempre ahí con una sonrisa para animar el día, se te echará de menos! Michele, no te libras. Seré breve y concisa, como acostumbras: gracias!

Agradecer también a todos los antiguos miembros y las nuevas incorporaciones del grupo: Lorenzo, Dani T, Manu, Joost, Jons, Michele F (*aka* Michelino), Javi, Sofía, Inma, Sang, Laura, Dani P, etc. Por supuesto, no puedo olvidarme de Jorge Ferrando, por siempre estar ahí cuando le necesitamos con cualquier problema que surge, por tonto que sea, y solucionarlo enseguida! Sin ti el *belljar* no existiría! Muchas gracias, Jorge! Muchas gracias también al resto de personal del ICMol por todos estos años!

I would like to thank Prof. Jan Anton Koster for allowing me to spend a few months in his group at the University of Groningen. And, also, to Unnati, for helping me since I arrived in the group and making my stay there much more bearable! It was an experience that I will take with me for life!

Y, por último, agradecer a mi familia, mis padres y hermanas, por todo el cariño y apoyo que me han dado y estar ahí siempre a mi lado. Inés y Emma, ahora me tendréis que llamar “doctora tía Paz” (qué bien suena, no?). Me habéis preguntado millones de veces de qué va mi tesis y qué hago en mi trabajo, pues aquí lo tenéis. Suerte para entenderla!

Blai, no sé suficientes palabras para agradecerte la paciencia que has tenido conmigo desde que decidí empezar la tesis, consolarme cuando más abajo estaba y darme fuerza para seguir. Sé que soy pesada y que las gracias no hay que darlas, pero igualmente lo hago. Gran parte del mérito de esta tesis también es tuyo.

Después de leer estos agradecimientos, que casi parecen sacados de una telenovela, si crees que me he olvidado de ti, date por agradecido también!